



**HAL**  
open science

# Gravity currents from non-axisymmetric releases

Nadim Zgheib

► **To cite this version:**

Nadim Zgheib. Gravity currents from non-axisymmetric releases. Fluids mechanics [physics.class-ph]. Institut National Polytechnique de Toulouse - INPT; University of Florida, 2015. English. NNT : 2015INPT0034 . tel-04233233

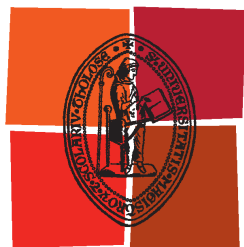
**HAL Id: tel-04233233**

**<https://theses.hal.science/tel-04233233>**

Submitted on 9 Oct 2023

**HAL** is a multi-disciplinary open access archive for the deposit and dissemination of scientific research documents, whether they are published or not. The documents may come from teaching and research institutions in France or abroad, or from public or private research centers.

L'archive ouverte pluridisciplinaire **HAL**, est destinée au dépôt et à la diffusion de documents scientifiques de niveau recherche, publiés ou non, émanant des établissements d'enseignement et de recherche français ou étrangers, des laboratoires publics ou privés.



Université  
de Toulouse

# THÈSE

En vue de l'obtention du

## DOCTORAT DE L'UNIVERSITÉ DE TOULOUSE

Délivré par :

Institut National Polytechnique de Toulouse (INP Toulouse)

Discipline ou spécialité :

Dynamique des fluides

---

Présentée et soutenue par :

M. NADIM ZGHEIB

le vendredi 13 mars 2015

Titre :

DYNAMIQUE DES COURANTS DE GRAVITE NON-AXISYMETRIQUES

---

Ecole doctorale :

Mécanique, Energétique, Génie civil, Procédés (MEGeP)

Unité de recherche :

Institut de Mécanique des Fluides de Toulouse (I.M.F.T.)

Directeur(s) de Thèse :

M. OLIVIER EIFF

M. SIVARAMAKRISHNAN BALACHANDAR

Rapporteurs :

M. ANDREW OOI, UNIVERSITE DE MELBOURNE

M. TIAN-JAN HSU, UNIVERSITY OF DELAWARE

Membre(s) du jury :

M. OLIVIER THUAL, INP TOULOUSE, Président

M. ALEXANDRU SHEREMET, UNIVERSITE DE FLORIDE, Membre

M. SIVARAMAKRISHNAN BALACHANDAR, UNIVERSITE DE FLORIDE, Membre

M. THOMAS BONOMETTI, INP TOULOUSE, Membre

## RESUME

Les courants de gravité, écoulements issus de la présence d'un contraste de densité dans un fluide ou de la présence de fluides de densités différentes, sont rencontrés dans de nombreuses situations naturelles ou industrielles. Quelques exemples de courants de gravité sont les avalanches, les marées noires et les courants de turbidité. Certains courants de gravité peuvent représenter un danger pour l'homme ou l'environnement, il est donc nécessaire de comprendre et de prédire leur dynamique. Cette thèse a pour objectif d'étudier l'évolution de courants de gravité de masse fixée, et notamment l'influence d'une forme initiale non-axisymétrique sur la dynamique, effet jusque-là peu abordé dans la littérature. Pour cela, une large gamme de paramètres est couverte, incluant le rapport de masse volumique entre le fluide ambiant et le fluide dans le courant, le rapport de forme initiale, la forme de la section horizontale de la colonne de fluide (circulaire, rectangulaire ou en forme de croix), le nombre de Reynolds (couvrant jusqu'à 4 ordres de grandeur) et la nature du fluide lourd (salin ou chargé en particules). Deux campagnes d'expériences ont été menées et complétées par des simulations numériques hautement résolues. Le résultat majeur est que la propagation du courant et le dépôt de particules (lorsque particules il y a) sont fortement influencés par la forme initiale de la colonne de fluide. Dans le cas de la colonne initialement rectangulaire le courant se propage plus vite et dépose plus de particules dans la direction initialement de plus courte dimension. Ce comportement non-axisymétrique est observé dans une large gamme des paramètres étudiés ici. Pourtant les modèles analytiques existants et notamment le modèle dit de boîte (box model) qui prédit avec succès le comportement des courants de gravité/turbidité dans les cas plan et axisymétrique ne sont pas capables de reproduire ce phénomène. C'est pourquoi

une extension du box model a été développée ici, et est en mesure de décrire la dynamique de courants de gravité de masse fixée dont la forme initiale est arbitraire. Le cas plus général d'un courant de gravité évoluant sur un plan incliné a été abordé et une dynamique intéressante a été observée.

## ABSTRACT

Gravity currents are buoyancy driven flows that appear in a variety of situations in nature as well as industrial applications. Typical examples include avalanches, oil spills, and turbidity currents. Most naturally occurring gravity currents are catastrophic in nature, and therefore there is a need to understand how these currents advance, the speeds they can attain, and the range they might cover. This dissertation will focus on the short and long term evolution of gravity currents initiated from a finite release. In particular, we will focus attention to hitherto unaddressed effect of the initial shape on the dynamics of gravity currents. A range of parameters is considered, which include the density ratio between the current and the ambient (heavy, light, and Boussinesq currents), the initial height aspect ratio (height/radius), different initial cross-sectional geometries (circular, rectangular, plus-shaped), a wide range of Reynolds numbers covering 4 orders of magnitude, as well as conservative scalar and non-conservative (particle-driven) currents. A large number of experiments have been conducted with the abovementioned parameters, some of these experiments were complemented with highly-resolved direct numerical simulations. The major outcome is that the shape of the spreading current, the speed of propagation, and the final deposition profile (for particle-driven currents) are significantly influenced by the initial geometry, displaying substantial azimuthal variation. Especially for the rectangular cases, the current propagates farther and deposits more particles along the initial minor axis of the rectangular cross section. This behavior pertaining to non-axisymmetric release is robust, in the sense that it is observed for the aforementioned range of parameters, but nonetheless cannot be predicted by current theoretical models such as the box model, which has been proven to work in the context of planar and axisymmetric releases. To

that end, we put forth a simple analytical model (an extension to the classical box model), well suited for accurately capturing the evolution of finite volume gravity current releases with arbitrary initial shapes. We further investigate the dynamics of a gravity current resulting from a finite volume release on a sloping boundary where we observe some surprising features.

## REMERCIEMENTS

I would like to start by thanking my parents for their never-ending love and support and for providing me with the best education I could ask for. I am thankful for my sister's guidance and grateful for my brother for being a great role model and making it possible for me to attend grad school.

It has been a wonderful journey. I had the pleasure and privilege of working with two great advisors, Prof. Balachandar and Prof. Bonometti, on some very interesting projects. Whether at University of Florida (UF) or Institut de Mécanique des Fluides de Toulouse (IMFT), they have been very generous with their time.

I am grateful to the joint PhD committee members for their constructive feedback. I would like to express my gratitude to Prof. O. Thual for making sure the PhD defense went as smoothly as possible at IMFT. I would like to express my thanks to Professors, H. Fan, D. Legendre, A. Sheremet, and L. Ukeiley for fruitful interactions following my PhD proposal. I am grateful to Prof. A. Ooi for a productive collaboration that resulted in an additional chapter to my thesis. I would like to acknowledge Prof. T. Hsu for his in-depth remarks of the thesis.

I was fortunate to be part of a dynamic and supportive group while at UF and IMFT. I would like to express my thanks to Mrugesh Shringarpure for his invaluable help with the spectral code. I would also like to acknowledge Georges Akiki, Subramanian Annamalai, Yue "Stanley" Ling, and Manoj Parmar for fruitful discussions and help with various topics.

I would like to express my sincere gratitude to Sébastien Cazin for help in setting up the experiments at IMFT and spending significant time to get me up to speed on post-processing. I would like to express my thanks to Hervé Ayroles for his assistance

during my 2014 visit to IMFT. I would like to acknowledge the members of group OTE, specifically Serge Font and Sylvain Belliot for their valuable day to day support with the experimental setup. I am deeply grateful to Sylvie Senny for her help during all the visits to IMFT. I would like to express my appreciation to Laurent Lacaze and Matthieu Mercier for their valuable ideas and advice in the various aspects of the experiments. I am grateful to Cécile Molles for her help in sieving the particles.

Finally I would like to acknowledge funding support from the UF Graduate School and PIRE NSF, as well as IMFT, INPT, and the French Embassy in Miami (for the Chateaubriand Fellowship) for support while at IMFT.

## SOMMAIRE

1	INTRODUCTION .....	10
1.1	Classification of Gravity Currents.....	11
1.1.1	Finite vs Continuous Release.....	11
1.1.2	Source of Current-Ambient Density Difference.....	11
1.1.4	Geometric Constraints.....	13
1.2	Classical Approaches .....	14
1.2.1	Laboratory Experiments .....	14
1.2.2	Numerical Simulations.....	15
1.2.3	Theoretical Models .....	15
1.3	Present Interest and Contributions .....	16
2	METHODOLOGY .....	25
2.1	Experiments.....	25
2.1.1	Setup.....	25
2.1.2	Measurements.....	27
2.1.3	Image Processing.....	29
2.2	Direct Numerical Simulations.....	30
2.3	Extended Box Model.....	32
2.3.1	Initial Condition.....	35
2.3.2	Time Integration and Spatial Discretization .....	37
3	LONG-LASTING EFFECT OF INITIAL CONFIGURATION IN GRAVITATIONAL SPREADING OF MATERIAL FRONTS .....	46
3.1	Background.....	46
3.2	Non-Circular Spreading of Density Currents.....	47
3.3	A New Model for the Prediction of the Propagation of Non-Circular Density Flows .....	53
3.4	Summary and Discussion .....	56
4	DIRECT NUMERICAL SIMULATION OF CYLINDRICAL PARTICLE-LADEN GRAVITY CURRENTS .....	66
4.1	Background.....	66
4.2	Mathematical Formulation.....	69
4.3	Results.....	71
4.3.1	Three-Dimensional Structures.....	71
4.3.2	One-Dimensional Time Evolution .....	73
4.3.2	Front Location .....	73
4.3.3	Deposition .....	74
4.3.4	Wall Shear-Stress and Near-Wall Dynamics .....	76
4.3.5	Conclusions and Recommendations .....	77

5	DYNAMICS OF NON-CIRCULAR FINITE RELEASE GRAVITY CURRENTS .....	87
5.1	Background.....	87
5.2	Experimental and Numerical Procedures.....	92
5.2.1	Experimental Setup .....	92
5.2.2	Preliminary Verifications .....	94
5.2.3	Numerical Procedure.....	96
5.3	High-Reynolds Number Boussinesq Density Currents.....	97
5.3.1	Self-Similarity of the Front Contour of Non-Circular / Non-Planar Gravity Currents .....	98
5.3.2	Local Front Froude Number of Non-Circular / Non-Planar Gravity Currents .....	101
5.4	Extended Box Model Simulations .....	104
5.4.1	Equations and Assumptions .....	104
5.4.2	Examination of the Extended Box Model.....	106
5.4.3	A Scaling Law for the Final Shape of Non-Circular Gravity Currents.....	109
5.5	Discussion .....	111
5.5.1	Varying Current-to-Ambient Density Ratio.....	112
5.5.2	Turbidity Current.....	112
5.5.3	Effect of Wall Friction.....	113
5.5.4	Influence of the Reynolds Number .....	113
5.5.5	Varying the Vertical and Horizontal Aspect Ratios .....	114
5.5.6	Possible Influence of the Initial Curvature and the Local Instantaneous Curvature .....	115
5.5.7	Vortical Structures of Non-Circular / Non-Planar Gravity Currents .....	116
5.6	Summary and Discussions .....	118
6	PROPAGATION & DEPOSITION OF NON-CIRCULAR FINITE RELEASE PARTICLE-LADEN CURRENTS .....	137
6.1	Background.....	137
6.2	Experiments of Finite-Release Non-Circular Particle-Laden Currents .....	140
6.2.1	Experimental Setup .....	140
6.2.2	Procedure.....	141
6.2.3	Results .....	143
6.2.3.1	Evolution in the horizontal (x,y)-plane .....	143
6.2.3.2	Evolution along the x- and y-axes .....	146
6.2.3.3	Influence of the settling velocity .....	148
6.2.3.4	Influence of the settling velocity .....	149
6.2.3.4	Influence of the initial height aspect ratio .....	149
6.2.3.4	Influence of the lateral boundaries .....	150
6.3	Simulations of Finite-Release Non-Circular Particle-Laden Currents .....	151
6.3.1	Equations and Numerical Setup .....	151
6.3.1	Front Evolution .....	153
6.3.3	Particle Deposition.....	156
6.3.4	Possible Contribution of Bedload Transport .....	158
6.3.5	Possible Contribution of Particle Resuspension .....	161

6.3.5 Vortex Dynamics .....	161
6.4 Conclusion .....	162
7 INVESTIGATION OF FINITE RELEASE GRAVITY CURRENT ON A UNIFORM SLOPE.....	180
7.1 Background.....	180
7.2 Theory and Laboratory Experiments.....	183
7.3 Direct Numerical Simulations of Circular Gravity Currents on an Incline .....	184
7.3.1 Numerical Model .....	184
7.3.2 Initial Condition.....	186
7.4 Structure .....	187
7.5 Front Velocity .....	190
7.6 Mass Redistribution .....	195
7.6.1 Spanwise and Streamwise Average.....	195
7.6.2 Instantaneous Velocity Field.....	196
7.7 Internal Circulation and Froude Number.....	198
7.8 Head and Entrainment.....	200
7.8.1 Defining the Head of the Gravity Current.....	201
7.8.2 Properties of the Head.....	202
7.8.2.1 Geometric Properties and Total Buoyancy.....	202
7.8.2.2 Comparisons with Thermal Theory and Experiments.....	204
7.9 Reynolds Number Dependence.....	205
7.10 Conclusion .....	206
8 CONCLUSIONS AND FUTURE WORK .....	238
APPENDIX: NUMERICAL DETAILS OF THE EXTENDED BOX MODEL .....	244
LIST OF REFERENCES .....	246

## CHAPTER 1 INTRODUCTION

When two fluids of different densities are placed in contact with one another such that the contact interface is parallel to the gravitational field, a predominantly horizontal flow develops (as a result of the hydrostatic pressure difference at the interface) in which the denser of the two fluids (termed heavy fluid) intrudes into its less dense neighbor (termed light fluid) in a ground hugging manner (Figure 1-1). This buoyancy driven flow is termed a gravity current (or density current) and forms the subject of the present thesis.

There are numerous natural flows that fall under the above description, and some of these flows are very common that they have been assigned simplified and perhaps more appropriate labels such as sand storms, avalanches, and oil spills (to name a few). In an attempt to simplify and gain a better understanding of their dynamics, gravity currents have been divided into different categories. These categories may depend on a variety of parameters, which include the type of release, the source of the density difference (the driving force), the extent of the density difference (or density ratio), the geometric confinement or restrictions, etc. Section 1.1 will provide a brief summary for some of these categories of relevant interest to this thesis. Section 1.2 will then elaborate on some of the classical experimental, numerical, and theoretical approaches to this problem. Finally, section 1.3 will discuss the present interests and contributions to the field of gravity currents.

## 1.1 Classification of Gravity Currents

### 1.1.1 Finite vs Continuous Release

A finite release gravity current (Simpson 1972, Huppert & Simpson 1980, Bonnecaze *et al.* 1995, Hacker *et al.* 1996, Gladstone *et al.* 1998, Shin *et al.* 2004, Cantero *et al.* 2007a) corresponds to a scenario where a fixed volume of fluid is suddenly discharged into an ambient environment of different density whereas a continuous release (Garcia and Parker 1993, Hogg *et al.* 2005, Sequeiros *et al.* 2009, Shringarpure *et al.* 2012) usually originates from a large reservoir with a time-dependent flux  $q$  of the form  $q = q_s t^s$  where  $q_s$  is a positive constant,  $t$  stands for time and  $s$  is an exponent either positive (waxing release), negative (waning release), or null (fixed finite-volume release). A finite release is generally observed when the sides of a container suddenly collapse releasing the embodied fluid instantaneously, whereas a continuous release can result from a small rupture along one of the edges of a large container or a pipeline leading to a continuous discharge of material.

### 1.1.2 Source of Current-Ambient Density Difference

The density difference between the two fluids may arise as a consequence of temperature, concentration, or compositional (different fluids altogether) variations, or as a result of suspended particles. The latter type is termed a particle-laden current (Bonnecaze *et al.* 1993, Hallworth & Huppert 1998, Gladstone *et al.* 1998, Necker *et al.* 2002) since the presence of particles gives rise to the excess density and hence the buoyancy driving source. In the case of temperature differences, one may think of a layer of cold (relatively heavy) air sweeping the bottom of a room occupied by warm (relatively light) air. Similarly, when fresh water (relatively light) from a river exits into the ocean (relatively heavy salty water), it flows along the surface, partially due to the

difference in salinity between fresh and salty water. On the other hand, a turbid mixture spreading on the seafloor constitutes an example where the excess density in the current also comes about from the suspension of sediments. The former two examples are homogeneous, scalar driven gravity currents, where the density of both fluids (in the absence of mixing between the current and the ambient fluid) remains unchanged. On the other hand, even in the absence of mixing, the density of a particle-laden current continues to evolve in space and time as a result of the continuous deposition of particles and possible reentrainment back into the flow (if the current is energetic enough).

### **1.1.3 Current to Ambient Density Ratio**

The initial density jump across the interface need not be large, in fact less than a percent difference in density between both fluids is usually sufficient to drive a strong flow. The term Boussinesq flows is commonly used to denote those types of flows resulting from a small density difference between the fluids (Benjamin 1968, Rottman & Simpson 1983, Hartel *et al.* 2000, Marino *et al.* 2005, Ungarish & Zemach 2005). There are some key differences in the structure and shape of a gravity current depending on the initial density ratio between the heavy and light fluids. When the densities of both fluids are comparable, the advancing current senses the presence of the ambient, which imposes a significant resistive force on the intruding current. However, when the density of the current is much larger than that of the ambient (Birman *et al.* 2005, Etienne *et al.* 2005, Lowe *et al.* 2005, Ungarish 2007, Bonometti *et al.* 2008), as in the case of a dam break flow in which water spreads in air, the current does not sense nor perceives any resistance from the surrounding ambient (air in the present example). The presence or absence of a resistive force is manifested by the shape of the gravity current (Figure

1-2). A Boussinesq gravity current usually attains a slug-like shape with a “head” and a “body”, whereas the thickness of a non-Boussinesq current decreases monotonically as we approach the ambient fluid, reaching a minimum value at the front of the current.

#### **1.1.4 Geometric Constraints**

Gravity currents are usually studied in one of two canonical configurations, namely the planar and the axisymmetric setups (Figure 1-3). These configurations are popular and have been widely explored due to their simplicity. They may be easily constructed for experimental and numerical studies, and provide a more manageable challenge for modelling purposes (Shallow Water equations and Box Model). In the planar release case, a flat rectangular gate initially separates a rectangular reservoir of fluid from an ambient of different, usually smaller density. Similarly, at the start of the axisymmetric three-dimensional release, the current is confined inside a hollow circular cylinder at the centre of a large tank containing the ambient fluid (Huppert 1982, Cantero *et al.* 2007), or in an expanding reservoir of relatively small angle of expansion, typically 10-15° (Huppert & Simpson 1980, Cantero *et al.* 2007a). The setups in Figure 1-3 correspond to a finite release scenario. For a continuous release, the gate would be partially lifted, and the trapped fluid would be continuously fed to maintain the desired volumetric discharge rate.

The planar setup may be thought of as a two-dimensional release since the current is confined to move along a specified direction, whereas for the circular release, the current would spread radially outwards (in all directions) but remain axisymmetric because of the initial circular nature of the release.

Gravity currents, when propagating horizontally into their ambient, usually undergo four main stages (Huppert & Simpson 1980). Initially when the current is

released, it accelerates from rest until it reaches a maximum velocity. During this highly transitional phase, termed the acceleration phase, the current undergoes rapid change in its velocity (zero to maximum), and the structure of the release also changes from mostly vertical to horizontal. This phase is often overlooked for three main reasons: (1) it is complex and transitional in nature, (2) it is relatively short lived, and (3) it is presumed to have little effect on the long term dynamics of the current. Following the acceleration phase, the current reaches a steady-state phase referred to as the slumping phase. During this phase, a planar (resp. cylindrical) current advances with a constant (resp. nearly constant) velocity and height (Gladstone 1998). At the end of the slumping phase, the current typically transitions to the inertial self-similar phase where the buoyancy driving force is balanced by the current's inertia. During this phase, the current starts to decelerate as a consequence of its diminishing front height. Finally, as the current's thickness continues to decrease, viscous and/or capillary forces become dominant, and the current evolves into the self-similar viscous/capillary phases.

## **1.2 Classical Approaches**

The study of gravity currents is well developed with research spanning laboratory experiments, numerical simulations, and theoretical models.

### **1.2.1 Laboratory Experiments**

Experiments constitute a very powerful and reliable approach to the study of gravity currents (for example Huppert & Simpson 1980, Bonnetcaze *et al.* 1993, Marino *et al.* 2005). Because of the relative ease and simplicity of conducting self-driven flows, there has been hundreds of experiments reported to date on gravity currents. There are one or two popular quantities that are frequently monitored in experiments, namely the location of the front (from which the front velocity may be derived) and the thickness of

the current at various locations (head, body, tail). In the case of non-conserving currents (particle-laden flows), the final deposition pattern is typically measured as well.

Moreover, depending on the interest of the experimentalists, further specific quantities may be additionally monitored (thickness of the current, ambient entrainment, front instabilities, bottom erosion, etc.).

### **1.2.2 Numerical Simulations**

Quantities such as ambient entrainment, bedload transport, and particle resuspension are difficult and even costly to monitor experimentally. They might require additional resources such as high speed cameras, stress sensors, or relatively expensive fluids. However, these aforementioned quantities, among others, may be calculated numerically with lesser effort and cost (for example Necker *et al.* 2002, Blanchette *et al.* 2005, Cantero *et al.* 2008). It is, in fact, for these hard to observe phenomena that numerical simulations become highly desirable. Fully resolved direct numerical simulations are very accurate but are limited to Reynolds numbers much smaller than what is realized in laboratory experiments and actual environmental or industrial gravity currents. Reynolds averaged and LES approaches have been used for investigating high Reynolds gravity currents (Ooi *et al.* 2007 Paik *et al.* 2009).

### **1.2.3 Theoretical Models**

When numerical simulations become costly, or when fewer details about the flow are needed, researchers may decide to use simpler theoretical models to study gravity currents. These might range in complexity from algebraic equations such as the Box Model (Dade & Huppert 1995, Gladstone *et al.* 1998) to complicated sets of coupled partial differential equations with turbulence closure as well as entrainment and erosion models (such as the three and four equation models of Zeng & Lowe 1997 and Parker

*et al.* 1986). One of the most popular models, however is the one layer, inviscid shallow water equations (Grundy 1986, Bonnetaze *et al.* 1995, Choi & Garcia 1995, Ungarish & Huppert 1998), which are derived from the Euler equations through scaling arguments and vertical integration.

### 1.3 Present Interest and Contributions

This thesis may be summarized by the following fundamental question: If we release a fixed volume of fluid into an ambient of different density, how would the initial shape of the release affect the dynamics of the flow? As we will shortly demonstrate, we find that the manner in which the fluid is released plays an important role in determining how the flow develops. On a horizontal plane the spreading current reaches a non-axisymmetric self-similar shape, whose aspect ratio depends on the shape of the initial release. On a sloping boundary, finite releases tend to evolve to an optimal self-similar shape, whose propagation speed could be substantially higher than for a corresponding planar current.

This dependence on the initial shape of release was first observed in our experiments of saline, Boussinesq currents. We noticed (for non-axisymmetric releases) that regions close to the center of mass of the release advance farther and faster than regions far from the center of release. The difference in velocities along the front was significant, especially for rectangular cross-sections, where the layout of the rectangular release (beyond the self-similar inertial phase of spreading) would resemble an ellipse whose major axis coincided with that of the initial minor axis of the rectangular cross section.

This non-uniform spreading of material fronts is not limited to Boussinesq saline currents. It is of interest to know the influence of various parameters on this preferential

spreading. To that end, we performed a series of experiments and numerical simulations in which we varied multiple parameters, one parameter at a time, to isolate their effect and contribution to this non-uniform flow. In these experiments, we examined the dependence on (1) the current-to-ambient density ratio by considering Boussinesq and non-Boussinesq currents, (2) the wall friction by investigating bottom (no-slip boundary condition) and top (no stress boundary condition) currents, (3) the shape (specifically the cross-section) of the release by considering circular, rectangular, and plus-shaped hollow cylinders, (4) the Reynolds number, which covered 4 orders of magnitude, (5) the local curvature of the release by using a right-angled rectangle and a rounded rectangle (in which the right angles are smoothed), (6) the height aspect ratio (*height/radius*) of the release, which covered a range of [0.25,7], and (7) the presence of relatively heavy particles (particle-laden currents).

Based on the above experiments and simulations, we conclude that the dependence on the initial shape holds for (i) heavy non-Boussinesq bottom currents, (ii) light surface currents, and (iii) particulate turbidity currents. The observed behavior is not influenced by wall friction and is independent of initial height aspect ratio. Only at very low Reynolds number we observe the current to spread to a near axisymmetric shape independent of initial release. Moreover, in the case of particle-laden currents, the final deposition profile of the particles displays substantial azimuthal variation, especially for the rectangular releases where the current deposits noticeably more particles along the initial minor axis of the rectangular cross section (compared with the initial major axis). We have performed a large number of experiments and corresponding very highly resolved direct numerical simulations and have proposed a

simple model to predict the counterintuitive spreading resulting from non-canonical initial releases.

Our simple model is based on the integral box model, which is classically used for predicting the evolution of gravity currents (Huppert & Simpson 1980). Despite the simplicity of the box model, it is able to reproduce the dynamics of axisymmetric and planar releases. However, straightforward application of the Box Model fails for non-axisymmetric releases. According to this model, the height remains uniform along the entire spreading patch, so the speed of propagation remains uniform along the current's front during all the phases of spreading. Using the classical Box Model, an initially non-axisymmetric current inevitably becomes axisymmetric. Similarly, theories based on slumping and self-similar phases also fail to predict the sensitive dependence on the initial shape and the preferential propagation of non-axisymmetric gravity currents for the same reasons. Here, we propose an Extended Box Model based on partitioning of the initial release (into smaller sub-volumes) using geometric rays that are perpendicular to the front. Once the various sub-volumes are obtained, the local fronts are advanced normal to themselves as in the Box Model. This initial partitioning is the key aspect of the present model, since it allows for non-uniform height and speed along the patch's advancing front, during all the phases of spreading. This allows the model to capture the non-axisymmetric propagation of the front.

Unlike planar (two-dimensional) currents that are always unidirectional (do not admit a mean spanwise component of velocity), or axisymmetric currents that are ever diverging, circular releases on sloping boundaries may exhibit nearly unidirectional, diverging, or even converging phases of spreading. Of specific interest is the

converging phase of spreading, which leads to local peaks in buoyancy that translate into a second acceleration phase. Circular releases on sloping boundaries are thus significantly different than planar releases. The formation and evolution of gravity currents under such conditions are not well understood.

This thesis contains 7 chapters other than this introduction. The second chapter elaborates on the methodology, specifically the details behind the experimental and numerical setups as well as the proposed extended box model (EBM). The final chapter 8 will present conclusions and future work. The other 5 chapters are each self-contained and have already appeared as journal articles or will be submitted. They will be briefly described below.

- Chapter 3: In this chapter we present results from laboratory experiments and fully-resolved simulations pertaining to finite release gravity currents with a non-axisymmetric cross-section. First, we demonstrate that, contrary to expectation, the effects of the initial shape influence the current's evolution well into the self-similar phases. Then we identify the physical mechanisms responsible for this dependence and propose a new model capable of capturing the dynamics of such releases. Finally, we show that this dependence on initial configuration is robust for various types of gravity currents (homogeneous and inhomogeneous) over a wide range of parameters such as Reynolds number, density ratio, wall friction and aspect ratio, and discuss the implications for the prediction of the propagation of natural gravity currents as oil spill, turbidity current and debris clouds. This chapter appeared in *Theoretical & Computational Fluid Dynamics* (Zgheib *et al.* 2014).

- Chapter 4: We use highly resolved direct numerical simulations (DNS) to investigate axisymmetric particle-laden gravity currents. We consider the case of a full depth release with monodisperse particles at a dilute concentration where particle-particle interactions may be neglected. The disperse phase is treated as a continuum and a two-fluid formulation is adopted. We present results from two simulations at Reynolds numbers of 3450 and 10000. Our results are in good agreement with previously reported experiments and theoretical models. At early times in the simulations, we observe a set of rolled up vortices that advance at varying speeds. These Kelvin-Helmholtz (K-H) vortex tubes are generated at the surface and exhibit a counter-clockwise rotation. In addition to the K-H vortices, another set of clockwise rotating vortex tubes initiate at the bottom surface and play a major role in the near wall dynamics. These vortex structures have a strong influence on wall shear-stress and deposition pattern. Their relations are explored as well. This Chapter is currently under review for publication in Computers & Fluids.

- Chapter 5: This chapter reports some new aspects of non-axisymmetric gravity currents obtained from laboratory experiments, fully resolved simulations and box models. Following the work of Chapter 3, where we demonstrated that gravity currents initiating from non-axisymmetric cross-sectional geometries do not become axisymmetric, nor do they retain their initial shape during the slumping and inertial phases of spreading, here we show that such non-axisymmetric currents eventually reach a self-similar regime during which (i) the local front propagation scales as  $t^{1/2}$  as in circular releases and (ii) the non-axisymmetric front has a self-similar shape that primarily depends on the aspect ratio of the initial release. Complementary experiments

of non-Boussinesq, top-, and turbidity currents suggest that this dynamics is independent of the density ratio, vertical aspect ratio, wall friction, and Reynolds number provided  $Re$  is large,  $Re \geq O(10^4)$ . The local instantaneous front Froude number obtained from the fully-resolved simulations is compared to existing models of Froude functions. The recently reported extended box model capable of capturing the dynamics of such non-axisymmetric flows is used to propose a scaling law for the self-similar horizontal aspect ratio  $\chi_\infty$  of the propagating front of a gravity current as a function of the initial horizontal aspect ratio  $\chi_0$ . The experimental and numerical results are in good agreement with the proposed scaling law. This Chapter is currently under review for publication in Journal of Fluid Mechanics.

- Chapter 6: The dynamics of non-axisymmetric turbidity currents is considered in this chapter. The study comprises a series of experiments and highly resolved simulations for which a finite volume of particle-laden solution is released into fresh water. A mixture of water and polystyrene particles of diameter  $\tilde{d}_p = 300 \mu\text{m}$  and density  $\tilde{\rho}_c = 1012 \text{ kg/m}^3$  is initially confined in a hollow cylinder at the centre of a large tank filled with fresh water. Cylinders with two different cross sections are examined: a circle and a rounded rectangle in which the sharp corners are smoothed. The time evolution of the front is recorded as well as the spatial distribution of the thickness of the final deposit via the use of a laser triangulation technique. The dynamics of the front and final deposit are significantly influenced by the initial geometry, displaying substantial azimuthal variation especially for the rectangular case where the current extends farther and deposits more particles along the initial minor axis of the rectangular cross section. Several parameters are varied to assess the dependence on the settling velocity, initial

height aspect ratio, and volume fraction. Even though resuspension is not taken into account in our simulations, good agreement with experiments indicates that it does not play an important role in the front dynamics, in terms of velocity and extent of the current. However, wall shear stress measurements show that incipient motion of particles and particle reentrainment do occur in the body of the current and should be accounted for to properly capture the final deposition profile of particles. This Chapter is currently under review for publication in *Physics of Fluids*.

- Chapter 7: In this chapter we report on the dynamics of circular finite-release Boussinesq gravity currents on a uniform slope. The study comprises a series of highly resolved direct numerical simulations for a range of bottom slopes between 5 and 20 degrees. Two Reynolds numbers are considered ( $Re = 1000$  and  $Re = 5000$ ). The temporal evolution of the front is in excellent agreement with previous experiments. One of the most fascinating aspects of this study is the detection of a converging flow towards the centre of the domain. This converging flow is a result of the finite nature of the release coupled with the presence of a sloping boundary and leads to a second acceleration phase in the front velocity of the current. The second acceleration has never been reported in the context of gravity currents. Its significant implications on the short and long term behaviour on the current are discussed. These finite-release currents are invariably dominated by the head where most of the mixing and ambient entrainment occurs. We propose a simple method for defining the head of the current from which we extract various properties including the front Froude number and entrainment coefficient. The Froude number is seen to increase with steeper slopes,

whereas the entrainment coefficient is observed to be weakly dependent on the bottom slope. This Chapter will be submitted to Journal of Fluid Mechanics.

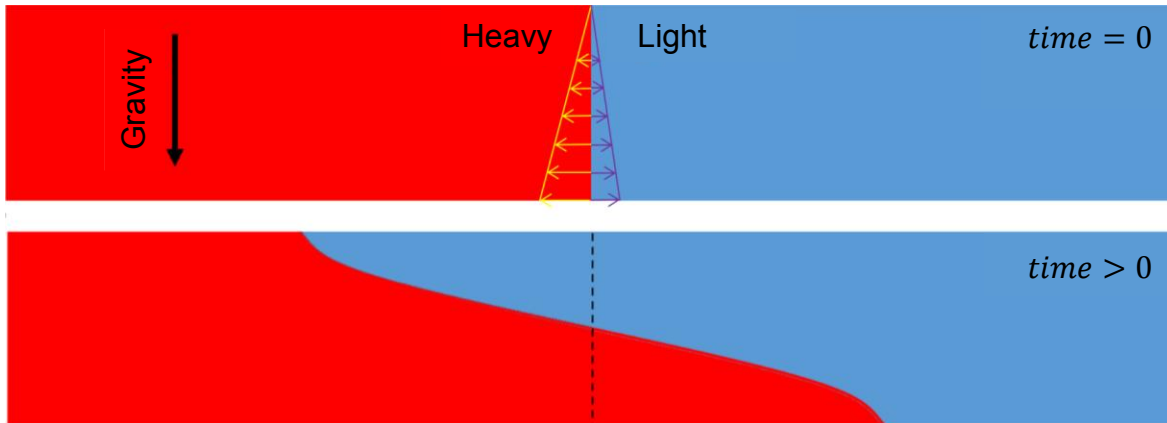


Figure 1-1. Conditions leading to the formation of a gravity current. At  $time = 0$ , a hydrostatic pressure difference is present at the vertical interface. It increases linearly with depth, reaching a maximum at the bottom surface.

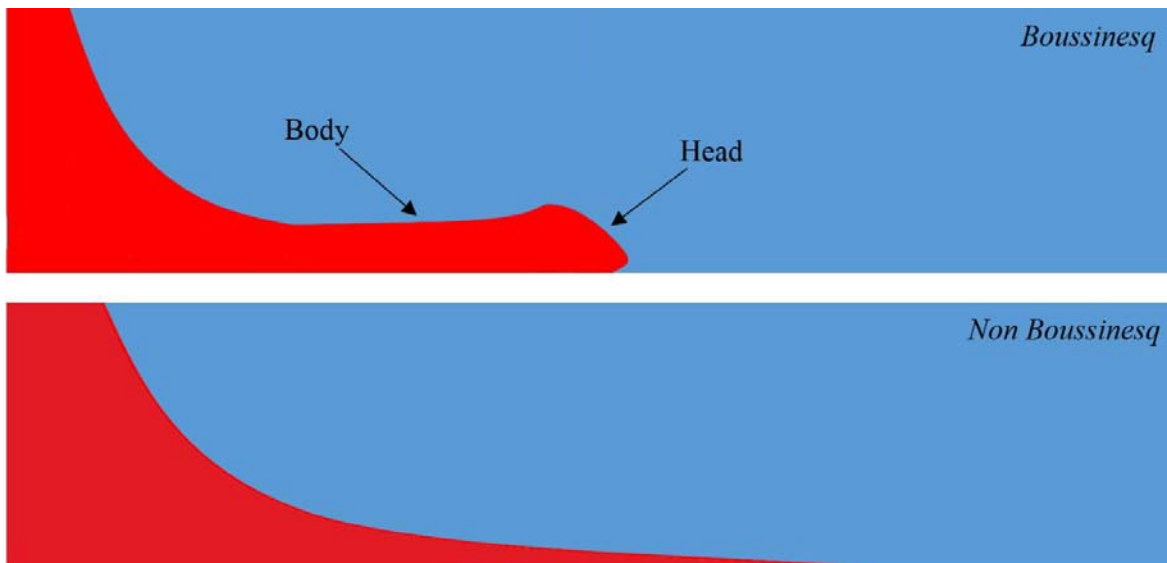


Figure 1-2. Schematic of a Boussinesq (top) and a non Boussinesq (bottom) current.

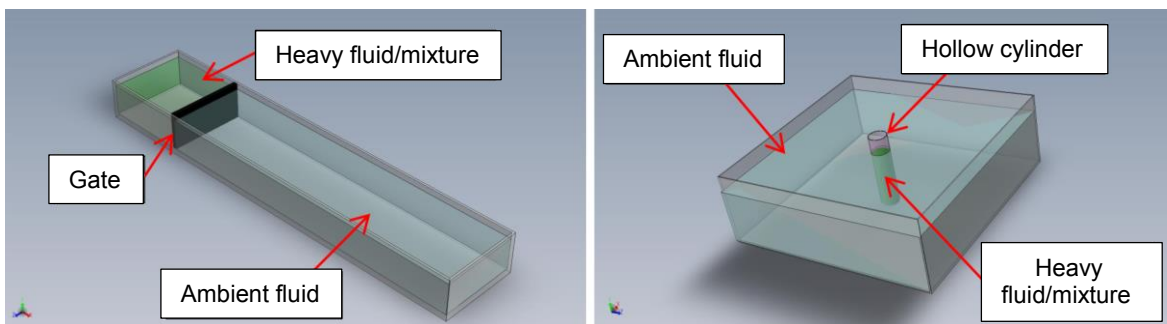


Figure 1-3. Canonical setups: Planar release (left), circular release (right).

## CHAPTER 2 METHODOLOGY

This chapter is arranged into three sections and provides details on the experiments, numerical simulations, and the proposed extended box model. In section §2.1, we elaborate on the experimental setup and discuss how the experiments are performed. We specify the quantities of interest as well as the means of extracting and post-processing the data. Some of the experiments are complemented with direct numerical simulations using a spectral code that has been extensively verified (Cortese & Balachandar 1995, Cantero *et al.* 2007a). Details of the numerical simulations are presented in §2.2. Finally, we elaborate in §2.3 on the proposed extended box model. We present the governing equations and discuss some of the attributes of the model, including the initial partitioning and remapping of Lagrangian points.

### 2.1 Experiments

All experiments were performed at the Institut de Mécanique des Fluides de Toulouse (IMFT) at the experimental facilities of Ondes, Turbulence et Environnement (OTE) group. The details of the experiments are hereby presented.

#### 2.1.1 Setup

A schematic of the setup is shown in Figure 2-1. A hollow cylinder lies at the center of a square transparent tank. The cylinder traps within its walls a fluid or mixture (particles + water) with a different density (typically larger) than the ambient surrounding fluid, which predominantly consisted of tap water. Four cylinders were considered with different cross-sectional shapes: (i) circle (CS), (ii) plus shape (PS), (iii) rounded rectangle (RR), and a true rectangle (TR). The cylinders have roughly the same cross-sectional area (except for the TR, which has the same aspect ratio as that of the RR)

and are depicted in Figure 2-2. Since we are trying to replicate fixed volume gravity currents, it is desired that the contents of the hollow cylinder be instantaneously exposed to the ambient fluid. Therefore, the hollow cylinder must be swiftly lifted (above the water level in the tank) at the time of release. This is achieved via a pulley system (Figure 2-1). Multiple experiments were conducted, the vast majority of those experiments fall under two categories: (1) saline and (2) particle-laden currents.

For saline currents, the tank and the hollow cylinder were simultaneously filled with tap water and salty water, respectively. Simultaneous filling help to minimize leaking (into the tank) by reducing the hydrostatic pressure difference at the interface. The water inside the tank is then given ample time to arrive at a stagnant state. Fluorescent dye (in highly concentrated powder form) is then added to the salty water and stirred to arrive at a homogeneous solution. Finally, the cylinder is swiftly lifted and the current begins to flow. Even though the fluorescent dye may be premixed with the salty water, it is preferable to add it to the solution as close to the time of release as possible. During the time needed for the water inside the tank to stagnate, the dye would diffuse into the tank. If we consider a plan view of the setup, the initial diffusion of the dye would distort the otherwise well-defined cross section of the release (CS, PS, RR, or TR). The distortion could mean more (unnecessary) work later during image processing.

In the case of particle-laden currents, a known amount of particles (polystyrene spheres) is initially poured into the cylinder, and then both the tank and the cylinder are filled with tap water to the desired level. Here again, the water inside the tank must be given ample time to reach a stagnant state before the fluorescent dye is added to the

cylinder. The mixture (water, particles, fluorescent dye) is then vigorously stirred for a few seconds (with a brush) to bring the particles into suspension. The brush is then retracted and the cylinder is quickly lifted. The brush has dimensions of  $4 \times 1$  cm and is connected at its end to a rigid metallic rod. The brush is allowed to sweep the bottom surface (with repetitive vertical gestures) to lift off any particles that have settled out.

The fluorescent dye glows when exposed to black light (or ultraviolet light), a light source whose wavelengths are essentially in the ultraviolet (non-visible) spectrum. Four black light neon tubes are mounted on each side of the tank, with close proximity to the tank bottom surface (the space primarily occupied by the advancing current). For best results, the neon tubes should have similar properties in terms of size, intensity, and wavelength range. A high intensity and a wide range of wavelengths are desirable to strongly illuminate the current and achieve a clear distinction between the current and the ambient with as sharp an interface as possible. Similar properties (among the neon tubes) are also necessary so that the current is equally illuminated and the variations in image intensity are minimal along the interface.

When black light tubes are in use, the experiments must be carried out in a dark room so that only the current becomes visible. Furthermore, if any parts of the structure appear in the images (as a result of the reflected light emitted by the current), they must be covered by a light absorbing material (black tape was found to be useful for these situations). It should be noted that the neon tubes are not shown in the schematic of Figure 2-1.

### **2.1.2 Measurements**

We extract two quantities from the experiments: the location of the front and the thickness of the final deposit (exclusively for particle-laden currents). The front is

extracted from a bottom plan view of the current. This is achieved by placing a mirror (at a 45° angle with the horizontal) directly beneath the tank. A camera is then placed with a line of sight coinciding with the center of the cylinder, such that at time of release, only the cross sections of the various geometries in Figure 2-2 (shown on the right side of the figure) are visible. The vertical sides of the hollow cylinder will not appear in the frame when the camera is perfectly aligned with the center of release.

For particle-laden currents, the thickness of the deposit that results from the settling of particles is of particular interest. At the end of each particle-laden experiment, the tank is slowly drained, and the deposition is allowed to dry off before thickness measurements are undertaken. The height of the deposited sediments is measured with a non-intrusive technique through laser reflection. The basic principle is triangulation.

The laser probe has two main optical elements. The first is a light emitting diode, which projects a visible laser beam on the surface of the targeted element (in this case the deposit) whose elevation needs to be measured. A part of the incident beam is reflected from the surface of the deposit and impacts an ultra-sensitive optical sensor at an angle directly dependent on the distance between the diode and the surface. Before the start of the measurement, the elevation of the light emitting diode from the bottom surface of the tank is measured. Therefore once the distance between the diode and the targeted surface is calculated, the height of the deposit can be straightforwardly inferred by subtracting the latter from the former. The laser has a measuring range of 2 mm with a resolution of 0.5  $\mu\text{m}$  and a spot diameter of 0.1 mm. The measurements are continuous with a frequency of 5000 measurements per second. The 2 mm measuring range begins at a distance of 23 mm from the laser as shown in Figure 2-3.

The laser is mounted on a 2-axis motorized system that guides it over the bottom surface of the tank. The system covers a range of  $800 \times 800$  mm, and depending on the area of the final deposit, the thickness of the sediments was measured every 25 or 50 mm. Since the depth of the deposit at the center of the release can exceed the aforementioned 2 mm measuring range, a micrometer was attached to the laser (inset of Figure 2-1) to allow for controlled vertical displacements.

To account for slight inclination in the tank supporting structure or possible minute height variations caused by the bending of the motorized axis (due to its own weight) as the laser sweeps over the bottom surface, dry measurements of the tank “topography” were computed by displacing a metallic plate of known thickness at various locations in the tank and recording the elevation measured by the laser. These values would then be taken into account when measuring the thickness of the final deposit.

### **2.1.3 Image Processing**

A high resolution camera provides 16-bit grayscale images of size  $2160 \times 2560$  pixels. Images are extracted in digitized form at a frequency of 50 images per second with a pixel intensity range of  $[0,65535]$ . A zero intensity value corresponds to a black pixel, while a 65535 value corresponds to a white pixel. The remaining 65534 values indicate a multitude of gray pixels. A wide pixel intensity range is highly desirable. It allows for a straightforward detection of the front. Consider for example Figure 2-4. On the top, we show a snapshot of a plan view of the current (illuminated, white portion of the image) as it spreads in the ambient fluid (dark background). In the bottom portion of the figure, we plot the pixel intensity along a line parallel to the  $x$ -axis passing through

the center of the release. For the dark background (ambient fluid), the intensity is uniform with an average value of 500, however as we approach the interface the intensity level suddenly rises (within a few pixels) by about an order of magnitude to reach a value close to 5000. This sharp increase in the pixel intensity level allows the front (current-ambient interface) to be readily discerned.

Detection of the front is performed using MATLAB<sup>®</sup> Image Processing Toolbox<sup>™</sup>. The front is determined by setting a threshold value for the pixel intensity. All pixels with an intensity value exceeding the threshold value are considered to belong to the advancing current. All pixels with a lower intensity value (than the threshold value) are not taken into account. The current-ambient interface can be thought of as the outermost iso-contour of the image (where the iso-contour value is the chosen pixel intensity threshold value). The computed location of the front, however is not sensitive to the chosen threshold value because of the order of magnitude sudden jump in pixel intensity at the interface.

The location of the front is first computed in pixels, where each pixel corresponds to a physical length (in microns). This pixel size or length is determined by counting the number of pixels across the length of an object of known dimensions. In the present experiments, each pixel corresponded to 420 microns.

## **2.2 Direct Numerical Simulations**

Details on the numerical code utilized in this thesis are abundant in the literature (Cortese & Balachandar 1995, Cantero *et al.* 2007a). Below we will provide some key details. The interested reader is referred to the aforementioned studies and the papers referenced therein.

The numerical setup is identical to that of the experiments (Figure 2-5). Our focus is to simulate buoyancy driven flows resulting from scalar (homogeneous fluids) and monodisperse particle-laden currents. The particle-laden mixture will be treated as a continuum and a two-fluid formulation is adopted (Scalar gravity currents are a special case of particle-laden currents with zero settling velocity). The code implements an equilibrium Eulerian approach of the two-phase flow equations. The model involves (i) mass (ii) and momentum conservation equations for the continuum fluid phase, (iii) an algebraic equation for the particle phase momentum where the particle velocity is taken to be equal to the local fluid velocity and an imposed settling velocity derived from the Stokes drag force on the particles, (iv) and a transport equation for the density (particle phase concentration). The non-dimensional system of equations read

$$\nabla \cdot \mathbf{u} = 0 \quad (2-1)$$

$$\frac{D\mathbf{u}}{dt} = \phi \mathbf{e}^g - \nabla p + \frac{1}{Re} \nabla^2 \mathbf{u} \quad (2-2)$$

$$\mathbf{u}_p = \mathbf{u} + V_s \mathbf{e}^g \quad (2-3)$$

$$\frac{\partial \phi}{\partial t} + \nabla \cdot (\phi \mathbf{u}_p) = \frac{1}{Sc Re} \nabla^2 \phi. \quad (2-4)$$

In the above, we employ the Boussinesq approximation with the assumption of small density differences between the particle-laden solution and the ambient playing a role only in the buoyancy term of the momentum equation. Unless otherwise stated, all parameters are non-dimensional, however those with an overhead tilde correspond to dimensional quantities. The height  $\tilde{L}_z$  of the domain is taken as the length scale,  $\tilde{U} = \sqrt{\tilde{g}'_0 \tilde{L}_z}$  as the velocity scale,  $\tilde{T} = \tilde{L}_z / \tilde{U}$  as the time scale, ambient density ( $\tilde{\rho}_a$ ) as the density scale, and  $\tilde{\rho}_a \tilde{U}^2$  as the pressure scale. The initial reduced gravitational

acceleration is defined as  $\tilde{g}'_0 = (\tilde{\rho}_p - \tilde{\rho}_a)\phi_0\tilde{g}/\tilde{\rho}_a$ , where  $\tilde{\rho}_p$ ,  $\phi_0$ , and  $\tilde{g}$  represent the dimensional particle density, initial volume fraction of particles in the mixture, and the dimensional gravitational acceleration. We denote by  $\mathbf{u}_p$  and  $\phi$  the velocity and the volume fraction of the particle phase (normalized by the initial volume fraction  $\phi_0$ ), respectively.  $\mathbf{u}$  and  $p$  correspond to the velocity and total pressure of the continuum fluid phase, respectively. The settling velocity  $V_s$  is determined from the Stokes drag force on spherical particles with small particle Reynolds numbers, and  $\mathbf{e}^g$  is a unit vector pointing in the direction of gravity. The Schmidt and Reynolds numbers in (2-4) is defined as

$$Re = \tilde{U}\tilde{L}_z/\tilde{\nu} ; \quad Sc = \tilde{\nu}/\tilde{\kappa} . \quad (2-5)$$

where  $\tilde{\nu}$  and  $\tilde{\kappa}$  represent the kinematic viscosity and the molecular diffusivity of the continuum fluid phase, respectively.

The simulations are carried out inside a rectangular computational domain (Figure 2-5) of dimensions  $L_x \times L_y \times L_z$ . Periodic boundary conditions are imposed along the  $x$  and  $y$  directions. No-slip and free-slip conditions are imposed for the continuous phase along the bottom ( $z = 0$ ) and top ( $z = 1$ ) walls, respectively. Mixed and Neumann boundary conditions are imposed for the particle phase at the top and bottom walls, which translate into zero particle net flux and zero particle resuspension, respectively.

$$\left\{ \text{at } z = 1 \quad \frac{1}{Sc} \frac{\partial \phi}{\partial z} - V_s \phi = 0 \right\}; \quad \left\{ \text{at } z = 0 \quad \frac{\partial \phi}{\partial z} = 0 \right\}. \quad (2-6)$$

### 2.3 Extended Box Model

Gravity currents resulting from planar and cylindrical fixed volume releases will remain planar, and axisymmetric as they spread out. On the other hand, most gravity

currents resulting from non-canonical configurations (non-planar and non-cylindrical) will spread in a manner that greatly depends on the initial shape of release. A simple, widely used, approach such as the box model provides a basic tool to quickly predict the front velocities of gravity currents resulting from canonical setups (planar and axisymmetric). The box model is a bold approximation (Figure 2-6) that assumes a planar (resp. cylindrical) current to advance as a set of height-diminishing rectangles (resp. disks) of length  $x_f(t)$  (resp. radius  $r_f(t)$ ) and height  $h_f(t)$ . Each of these variables (length/radius and height) is a unique function of time  $t$ . They are related by the Froude front condition as well as mass conservation. For a cylindrical current, the box model equations are

$$\frac{dr_f}{dt} = Fr \cdot \sqrt{h_f} \quad (2-7)$$

$$\frac{1}{2}\pi r_f^2 h_f = \text{Initial volume} = \text{constant} \quad (2-8)$$

where  $Fr$  is the Froude function of order unity which depends on the height ratio between the current and the surrounding ambient. The above equations have been rendered non-dimensional using the same length and time scales introduced in the previous section on direct numerical simulations.

The box model is well suited for canonical problems resulting from planar and cylindrical releases, nonetheless, for non-canonical problems, it fails to capture the dependence on the initial shape. The reason for this failure is simple. The box model treats the current as one body as it homogenizes the flow properties (velocity and height) and neglects any spatial variations that might be present. For non-canonical releases, the velocity and height of the release must be allowed to vary along the interface.

The present section will provide details on the proposed extended box model (EBM). First, EBM constitutes a set of coupled algebraic and partial differential equations

$$u_f = Fr \cdot \sqrt{h_f} \quad (2-9)$$

$$\begin{cases} \frac{\partial x_f}{\partial t} = u_f \frac{\partial y_f / \partial s}{\sqrt{(\partial x_f / \partial s)^2 + (\partial y_f / \partial s)^2}} \\ \frac{\partial y_f}{\partial t} = u_f \frac{-\partial x_f / \partial s}{\sqrt{(\partial x_f / \partial s)^2 + (\partial y_f / \partial s)^2}} \end{cases} \quad (2-10a)$$

$$\frac{\partial \sigma}{\partial t} = u_f \quad (2-10b)$$

$$\frac{\partial \sigma h_f}{\partial t} = 0 \quad (2-11)$$

The above set of equations describe the evolution of a gravity current front in the  $x$ - $y$  plane. The independent variables  $s$  and  $t$  represent the distance measured along the circumference of the front and time, respectively. The subscript  $f$  denotes front values, and  $\{x_f(s, t), y_f(s, t)\}$  mark the location of the front in the  $x$ - $y$  plane (Figure 2-7). The height and outward normal velocity of the front correspond to  $h_f(s, t)$  and  $u_f(s, t)$ , respectively. An additional variable, namely the area per arc length  $\sigma(s, t)$  is also used in the model. An integration of  $\sigma(s, t)$  over the entire arc length of the advancing front (perimeter of the current) will yield the total area covered by the platform of the advancing current. All variables are rendered dimensionless using the same scales as in section 2.2. Equations (2-9), (2-10) and (2-11) refer to the Froude front condition, kinematic relations and mass conservation, respectively.

Analytical solutions of (2-9)-(2-11) are not feasible in the case of arbitrary initial patches, however, the system may be solved numerically. Its solution is far easier and faster than the direct numerical simulations discussed in section 2.2. Details about the numerical procedure used for solving (2-9)-(2-11) are hereby presented.

### 2.3.1 Initial Condition

The first step is providing the initial condition for the various variables. We start by defining the shape of the release. Let us consider for example the rounded rectangular shape in Figure 2-2 and discretize the front using a set of equidistant points. The coordinates of these points represent the initial conditions for  $x_f$  and  $y_f$ .

We consider full depth releases (where the initial height of the current inside the hollow cylinder is the same as that of the surrounding ambient), and therefore the initial non-dimensional height is set to unity at the discretized points.

The front velocity is straightforwardly calculated from the height using the Froude condition (2-9). We choose the empirical relation of Huppert-Simpson (1980) for the Froude number function

$$Fr = \min(h_f^{-1/3}, 1.19). \quad (2-12)$$

Finally, the initial condition for  $\sigma$  comes from the partitioning of the initial shape. The initial shape is partitioned geometrically by extending normal (to the front) lines inwards. These normal lines will initiate at the midpoint of each segment connecting 2 consecutive Lagrangian points (Figure 2-8). Because of the point symmetry of the rounded rectangle (RR) (the RR is symmetric w.r.t. the  $x$  and  $y$ -axes), these (normal) lines will intersect the major and minor axes of the RR to form the sub volumes shown in Figure 2-8. Each sub volume has a corresponding segment along the front. The

centers of each of these segments coincide with the Lagrangian points  $\{x_f, y_f\}$ . The initial value of  $\sigma$  may be easily calculated by dividing the surface of each sub volume by the corresponding front segment length

$$\sigma = \frac{Area}{Length}. \quad (2-13)$$

The extended box model generalizes the classical box model (Huppert & Simpson 1980; Dade & Huppert 1995), in several ways. Despite these generalizations, the extended box model involves significant approximations. (H1) The volume of initial release is partitioned geometrically with inward propagating lines (perpendicular to the front) and accordingly different sub-volumes are assigned to the different portions of the front. (H2) As the current propagates, the height of the current is not taken to be a constant over the entire release. It varies along the front depending on the local speed of propagation. (H3) The velocity of propagation is taken to be normal to the front. Since there is variation in the height of the current along the front, it can be expected that there is some tangential flow (tangential velocity) induced by this variation in the current height. However, at the front, since the pressure gradient normal to the front is expected to far exceed the tangential gradient, the current velocity is expected to be predominantly normal to the front. (H4) Finally we assume that even in the present case of non-axisymmetric propagation Huppert-Simpson front relation can be used to express the front velocity in terms of local front height<sup>1</sup>. These assumptions are examined with the help of direct numerical simulations in Chapter 5 section 5.

---

<sup>1</sup> Note that another model of Froude number function could be used without loss of generality

### 2.3.2 Time Integration and Spatial Discretization

Once the initial conditions are known, we march in time using a third order low-storage, explicit Runge-Kutta scheme and an eighth order central finite difference scheme for the spatial derivatives (with periodic boundary conditions). Each time step consists of two stages. The first is an intermediate stage where the governing equations (2-9)-(2-11) are integrated. At the end of this stage, because of the azimuthal variations, the Lagrangian points are no longer equidistant. Each sub-volume associated with a Lagrangian point is then assumed to be homogeneously distributed (along the front) between its two adjacent midpoints (think of volume per unit length along the front).

The second stage involves remapping the non-equidistant Lagrangian points to render them equidistant along the front. This step is necessary, especially in the case of concave corners, as in the plus-configuration for instance, as Lagrangian points may cross each other causing the front to fold on itself. This problem is classically encountered in Lagrangian techniques such as Front Tracking approaches (Unverdi & Tryggvason 1992). Once the points are remapped, new midpoints are calculated and the sub-volumes of the release associated with each new Lagrangian point is computed. Then a step of redistributing the sub-volumes per unit arc length ( $\sigma h_f$ ) is performed, and this step preserves the total volume of the release. Finally  $u_f$  and  $h_f$  are interpolated at the new equi-spaced Lagrangian points.

Let us denote the intermediate stage by \*. Then, if we start with a set of points  $\{(x_f)_i^n, (y_f)_i^n, (u_f)_i^n, (h_f)_i^n, (\sigma)_i^n\}$ , (where superscript  $n$  denotes a (known) quantity at the present time, and subscript  $i$  marks the  $i^{th}$  Lagrangian point), marching in time takes us to the intermediate \* stage

$$\{(x_f)_i^n, (y_f)_i^n, (u_f)_i^n, (h_f)_i^n, (\sigma)_i^n\} \xrightarrow{(2-9)-(2-11)} \{(x_f)_i^*, (y_f)_i^*, (u_f)_i^*, (h_f)_i^*, (\sigma)_i^*\} \quad (2-14)$$

As previously mentioned, the Lagrangian points  $\{(x_f)^*, (y_f)^*\}$  will not necessarily be equidistant along the arc length even when  $\{(x_f)^n, (y_f)^n\}$  are equidistant along the arc length at time  $t_n$ . To render  $\{(x_f)^*, (y_f)^*\}$  equidistant, we first calculate the perimeter of the front (at the intermediate \* stage) by connecting the Lagrangian points with straight segments. From the ratio of the perimeter to the number of points, we compute the required separation distance at the new time step to be  $\Delta^{n+1}$

$$\Delta^{n+1} = \frac{\text{Perimeter}^*}{\text{Number of points}^*} \quad (2-15)$$

A point is then (randomly) fixed and each neighboring point is adjusted along the arc length to arrive at an equidistant set of points (with respect to the front at the intermediate \* stage) with spacing  $\Delta^{n+1}$ .

Once the Lagrangian points are remapped to  $\{(x_f)^{n+1}, (y_f)^{n+1}\}$ , new midpoints are calculated (by again remaining along the arc length of the intermediate stage). Each Lagrangian point now resides at the center of a segment bounded by the newly calculated midpoints. As previously mentioned, each sub-volume (at the intermediate stage), is assumed to be homogeneously distributed (along the front) between its two adjacent midpoints. The task now is to associate a sub-volume to each of the remapped points  $\{(x_f)^{n+1}, (y_f)^{n+1}\}$ . This sub-volume is again bounded by the newly calculated midpoints. This step can be thought of as having an arc composed of multiple segments of different lengths  $l_i$  bounded by the midpoints of the Lagrangian points (Figure 2-9). Each segment is associated to a sub-volume and has a certain (volume per unit length) value ( $K_i$ ). The total volume of the current is recovered from the summation over all

segments  $\sum_{i=1}^N l_i K_i = \text{Initial Volume}$ , where  $N$  is the total number of segments (or number of Lagrangian points).

In a continuous (non-discretized) framework, the volume redistribution step may be described as follows. The volume of a differential element along the front ( $dV$ ) is given by

$$dV = \sigma h_f ds . \quad (2-16)$$

The total volume  $V$  is recovered from a closed line integral along the front

$$V = \oint dV = \oint \sigma h_f ds . \quad (2-17)$$

At the intermediate stage, each (discretized) sub-volume is defined as

$$\Delta V_i^* = \sigma_i^* h_{f_i}^* \Delta s_i^* , \quad (2-18)$$

where  $\Delta s_i^*$  is the length of the segment centered around the Lagrangian point  $p_i^*$  of coordinates  $(x_{f_i}^*, y_{f_i}^*)$ . For the total of the  $N$  segments centered around the  $N$  Lagrangian points, the total volume is the summation

$$V^* = \sum_{i=1}^N \sigma_i^* h_{f_i}^* \Delta s_i^* . \quad (2-19)$$

After remapping of the Lagrangian points, the redistributed sub-volumes become

$$\Delta V_i^{n+1} = (\sigma h_f)_i^{n+1} \Delta s_i^{n+1} , \quad (2-20)$$

where the product  $(\sigma h_f)_i^{n+1}$  is obtained from the intermediate \* stage as follows

$$(\sigma h)_i^{n+1} = \sum_{j=1}^N \alpha_{ij} \sigma_j^* h_{f_j}^* \quad (2-21)$$

where the fraction  $\alpha_{ij}$  is the ratio of the intersection of  $\Delta s_j^*$  and  $\Delta s_j^{n+1}$  divided by the length of  $\Delta s_j^*$

$$\alpha_{ij} = \frac{\Delta s_j^* \cap \Delta s_j^{n+1}}{\Delta s_j^*}. \quad (2-22)$$

Let us consider the simple example shown in Figure 2-9. The boundaries of each segment (Figure 2-9A) can be thought of as the midpoints (thick dashes) of the Lagrangian points at the intermediate stage denoted by the asterisk (\*). When the Lagrangian points are remapped in Figure 2-9B (to render them equidistant), the newly calculated midpoints will mark the new boundaries of the segments at the  $n + 1$  time step. Each segment (at the  $n + 1$  time step) might constitute of different portions of the (non-uniform) segments at the \* stage. At the end of this step, the sub-volumes per unit arc length ( $\sigma h_f$ ) are obtained at the  $n + 1$  time step.

The height at the remapped points ( $h_f^{n+1}$ ) is then found by linear interpolation from the intermediate \* stage, and the velocity is calculated from the Froude condition. Finally, the area per arc length  $\sigma^{n+1}$  is the ratio of  $(\sigma h_f)^{n+1}$  to the interpolated height  $h_f^{n+1}$ .

The extended box model (EBM) is a simple model that is primarily designed to capture the dependence of the flow (front location) on the initial shape of release. It will be shown in the subsequent chapters, that despite its simplicity, it can correctly capture the preferential spreading directions of non-axisymmetric gravity currents.

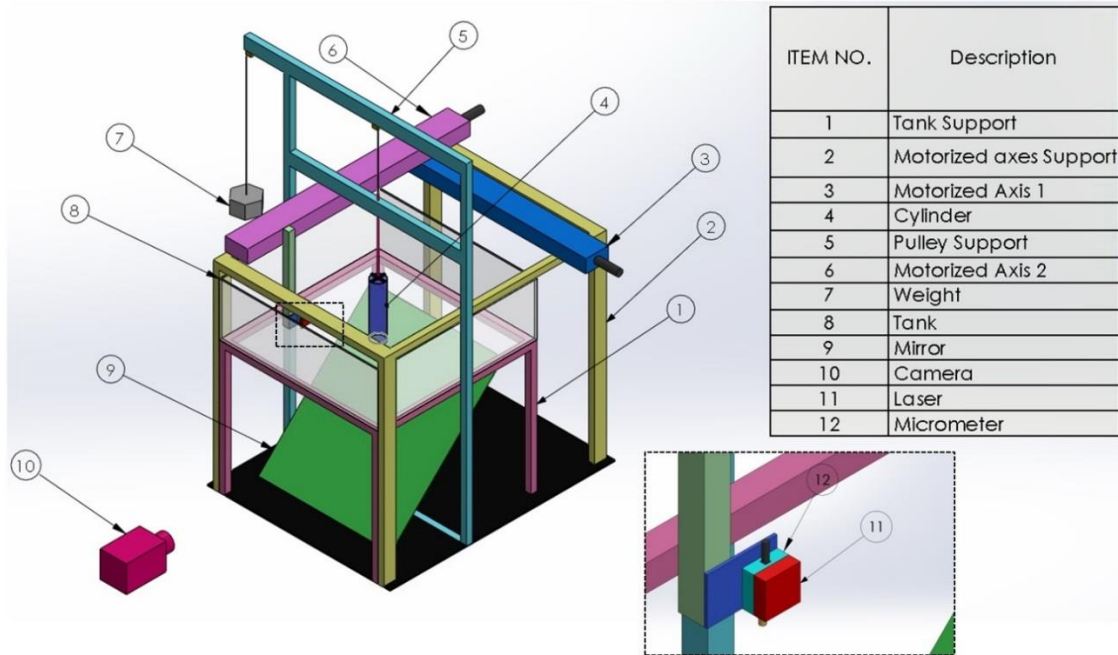


Figure 2-1. Isometric view of experimental setup. For the enlarged view at the bottom right, the tank and the motorized axes support have been hidden to allow for an unobstructed view of the laser.

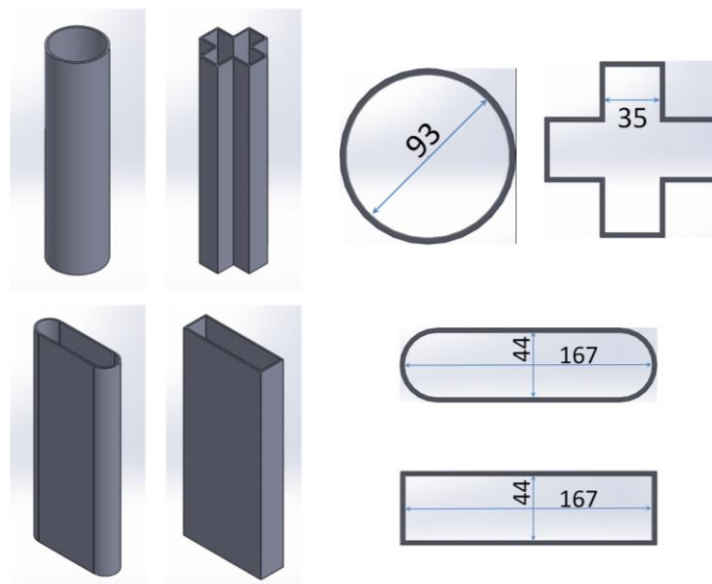


Figure 2-2. Isometric view of the right-angled hollow cylinders. The dimensions of the cross-sections are in mm.

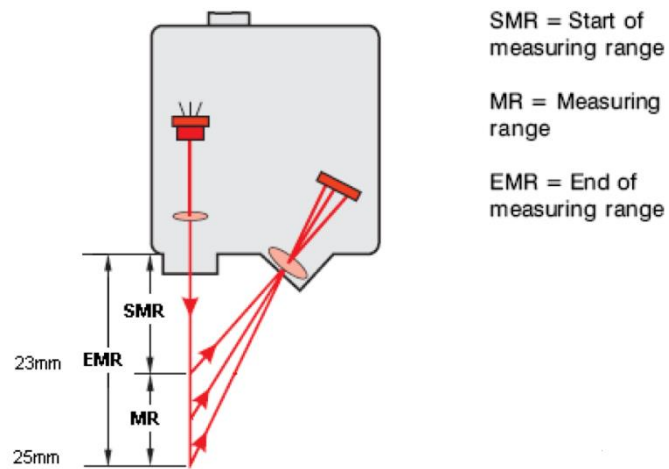


Figure 2-3. Measuring range of laser.

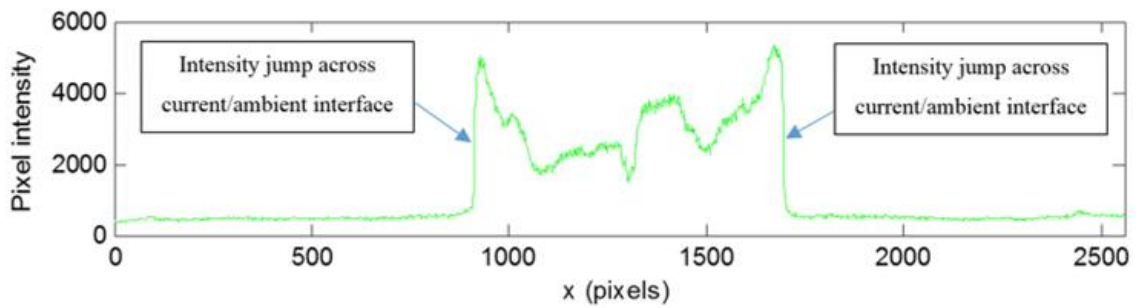
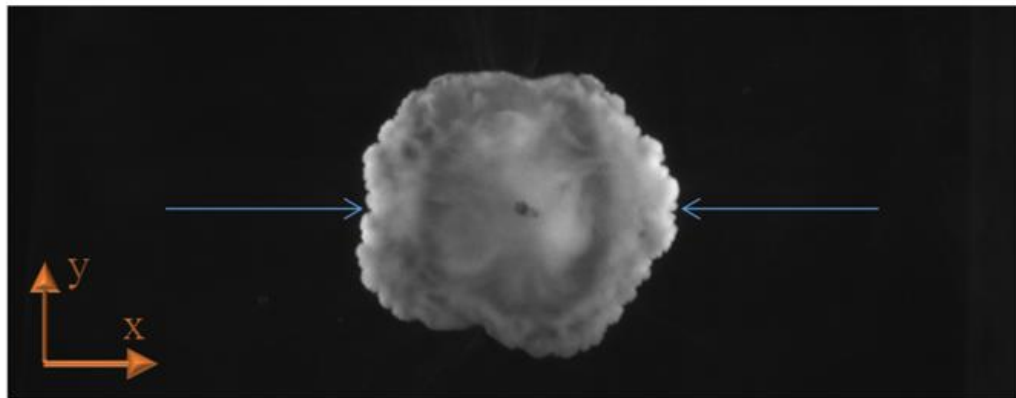


Figure 2-4. The large pixel intensity jump across the interface (close to an order of magnitude) allows the front to be easily identified.

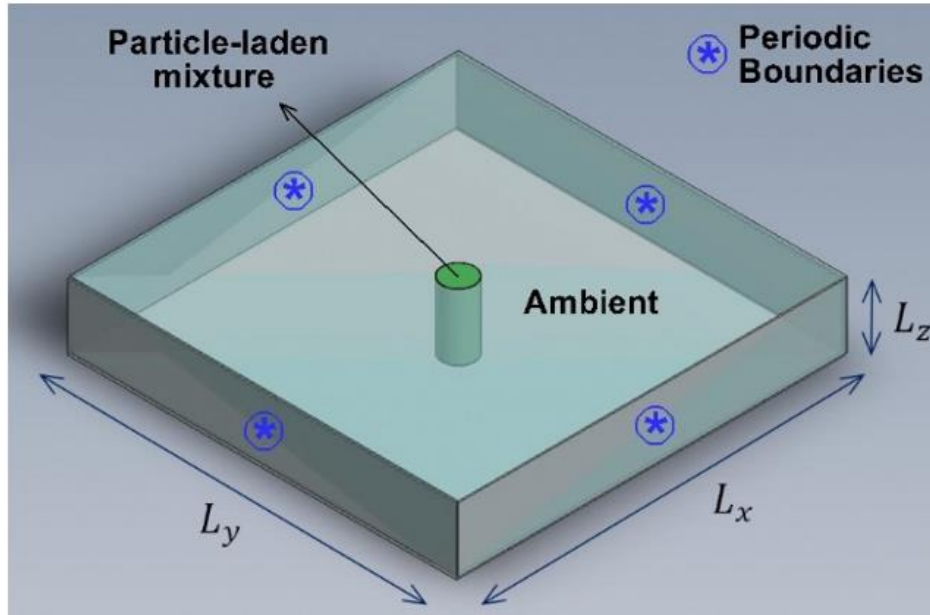


Figure 2-5. Schematic of the numerical domain.

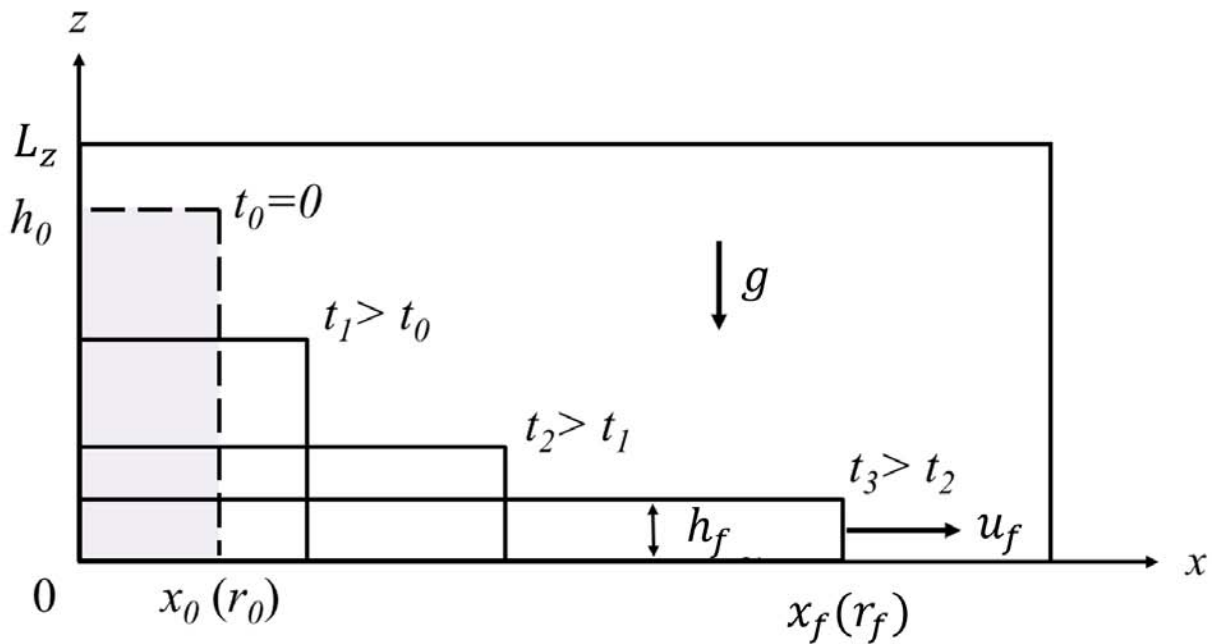


Figure 2-6. Classical box model for planar and cylindrical fixed volume releases

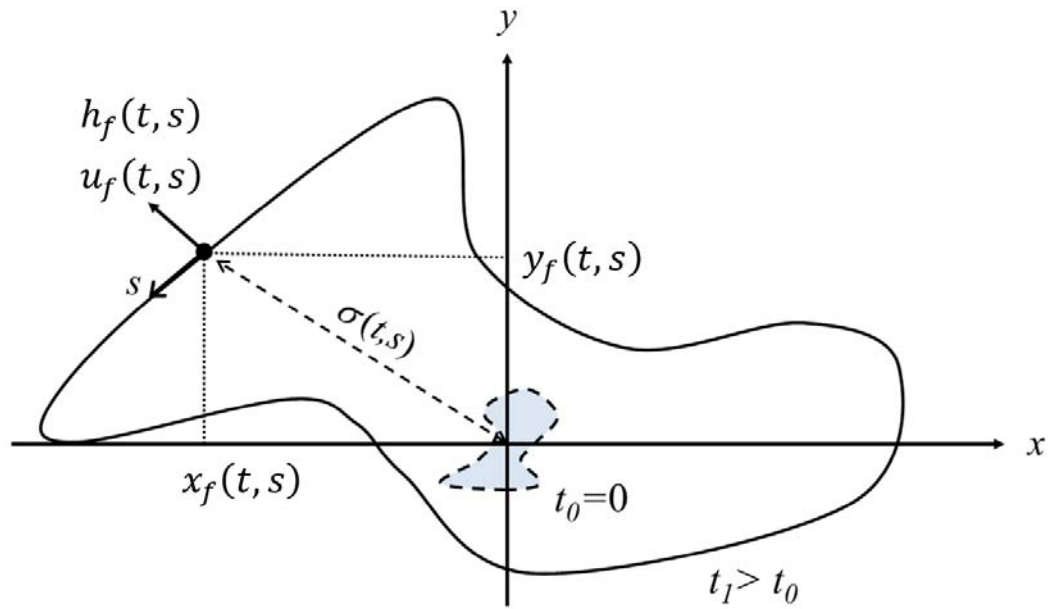


Figure 2-7. Schematic of extended box model.  $(x_f(s, t), y_f(s, t))$  denote the local position,  $h_f(s, t)$  the height,  $u_f(s, t)$  the outward normal velocity of the front and  $\sigma(s, t)$  the area per arc length. The independent variables  $s$  and  $t$  denote the distance measured along the circumference of the front and time, respectively.

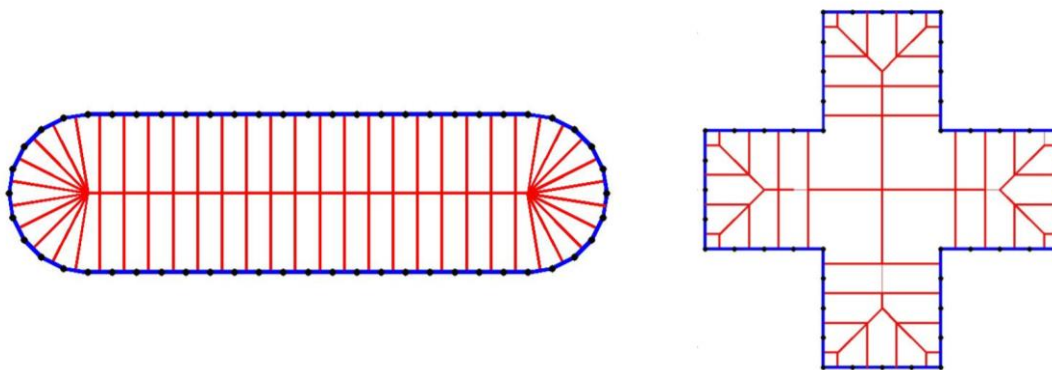


Figure 2-8. Initial partitioning for the EBM for the rounded rectangle (left) and plus shape (right). The equidistant Lagrangian points are shown on the front as black circular disks. Each Lagrangian point is associated with a sub-volume. The sub-volumes are not necessarily equal.

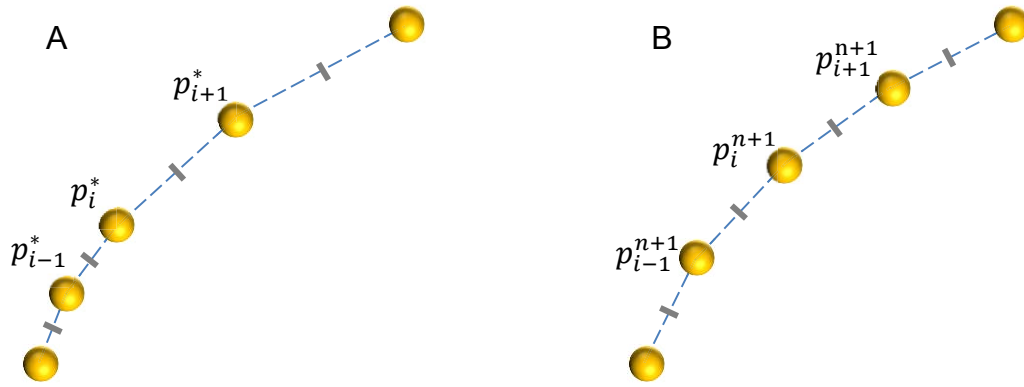


Figure 2-9. Remapping of Lagrangian points and volume redistribution.

CHAPTER 3  
LONG-LASTING EFFECT OF INITIAL CONFIGURATION IN GRAVITATIONAL  
SPREADING OF MATERIAL FRONTS

**3.1 Background**

Consider an accidental collapse or a skilled demolition of a building vertically on itself. The emerging debris cloud will quickly invade a wider region that greatly surpasses the bounds of the demolished building. During the infamous 9/11 attack, the tidal wave of dust and debris enveloped much of the lower Manhattan. The gravitational spreading of these destructive debris clouds, as seen in Figure 3-1, sensitively depends on the building's shape. The non-axisymmetric nature of the resulting lobe-like structure is persistent over a significant time and cannot be predicted by current models. This counter-intuitive behavior of initial condition-dependent spreading of material fronts is not unique to debris clouds, and is applicable to a variety of geophysical flows as demonstrated in this paper. Debris clouds belong to the family of gravity currents which are observed in various natural situations. The manner in which these flows spread has important implications for oil spills (Hoult 1972), accidental toxic gas releases (Britter 1989, Gröbelbauer 1993), fire propagation (Doyle & Carlson 2000), turbidity currents (Meiburg & Kneller 2010), pyroclastic flows (Faillettaz *et al.* 2004), avalanches (Hopfinger 1983, Faillettaz *et al.* 2004) and storms (Hall *et al.* 1976). These flows are driven by a difference in density either stemming from temperature, salinity or suspended sediments.

---

This chapter has been previously published "Zgheib, N., Bonometti, T., & Balachandar, S. 2014. Long-lasting effect of initial configuration in gravitational spreading of material fronts. *Theoretical and Computational Fluid Dynamics*, **28**(5), 521-529."

Predicting the short-time as well as long-time evolution of these material fronts is of crucial interest (Simpson 1982, Huppert 2006). Most real gravity currents are generated by a sudden or continuous release from an arbitrary, often non-circular, source. However, nearly all the prior theoretical, experimental and numerical investigations are based on planar or axisymmetric configurations (von Karman 1940, Benjamin 1968, Huq 1996, Hallworth *et al.* 2001). The underlying (implicit) assumption is that, after a relatively short transitional phase, the material front becomes either planar or axisymmetric. Here we present results from laboratory and numerical experiments that were performed with non-axisymmetric finite initial releases. The most striking feature was that the effect of the initial non-circular shape of the release persists for the whole duration of the observation. This is a unique, but robust, behavior of propagating material fronts, which is quite distinct from propagating informational fronts, such as sound waves and shock fronts, which are well known to quickly become independent of the source shape.

In the present chapter, the physical mechanisms responsible for this peculiar behavior is identified, and a novel model is presented which accounts for the shape of the initial release and predicts the non-axisymmetric propagation of the front of the gravity current. This model when applied to the problem of building demolition captures the time evolution of the observed debris cloud (Figure 3-1).

### **3.2 Non-Circular Spreading of Density Currents**

When a patch of heavy (resp. light) fluid spreads in a lighter (resp. heavier) ambient, it generally goes through successive stages (Huppert 1980, Cantero 2007a), namely an acceleration phase at the end of which the current's front velocity reaches its maximum value, a slumping phase with constant or nearly constant front velocity, and

eventually a phase denoted here as long-time phase where the buoyancy driving force is balanced either by inertia, viscosity or surface tension, respectively. Note that the long-time phase is often referred to as self-similar phase, because it is possible to find an exact long-time similarity solution of the simplified equations of motion (e.g. the shallow-water equations) in some specific configurations as in the planar or axisymmetric case. When a self-similar solution exists, the time evolution of the front height  $h_N$  and front velocity  $u_N$  usually follow the scaling law  $h_N \sim t^\alpha$  and  $u_N \sim t^\beta$  with  $\alpha$  and  $\beta$  being some constants. For instance, in the case of axisymmetric gravity currents, the one-layer shallow-water equations give  $\alpha = -1$  and  $\beta = -1/2$ . The reader is referred to the work (Ungarish 2009, Zemach & Ungarish 2013) for more details about the existence of a similarity solution in various configurations.

While the slumping and self-similar phases have been extensively studied in the past (Hoult 1972, Benjamin 1968, Huppert & Simpson 1980, Rottman & Simpson 1983, Klemp *et al.* 1994, Cantero *et al.* 2007a), the initial acceleration phase has received very little attention (Cantero *et al.* 2007a, Cantero *et al.* 2008b) as initial conditions were believed to be unimportant in the prediction of the long-term dynamics. Here we argue, by means of experiments and fully-resolved simulations that a non-axisymmetric finite-volume release does not reach an axisymmetric shape nor preserve its initial shape for a significant time. In the following we define the “long-time” regime as the regime for which the current has entered a phase for which the local front height and speed obey a scaling law of the form  $h_N \sim t^\alpha$  and  $u_N \sim t^\beta$ , as found for the self-similar (inertial) phase.

The laboratory experiments consist of swiftly releasing a column of dense salty (or turbid) water ( $\rho_c \approx 1100 \text{ kg/m}^3$ ) of height  $h_0$  into a lighter ambient fluid of height  $H$

inside a  $1.2 \times 1.2 \times 0.4\text{m}$  tank, thanks to a hollow cylinder of equivalent radius  $R_0$ . The ambient fluid is either clear water ( $\rho_a \approx 1000 \text{ kg/m}^3$ ) or air ( $\rho_a \approx 1.2\text{kg/m}^3$ ). Unless stated otherwise, we set  $h_0 = H$  (full depth release). Three different cross-sectional shapes are considered: (a) a circular section, (b) a rounded rectangular section, i.e. a rectangle where the two shorter edges are replaced by semi-circles, and (c) a plus-shape section for which concave corners are present (Figure 3-2). Fluorescent dye is added to the fluid inside the cylinder. The front location and the current's height are measured thanks to a mirror placed beneath the tank, which allows for a plan (bottom) view of the front evolution, while the side view of the current provides information about the height's evolution.

Several experiments have been performed for a wide range of Reynolds number  $Re = HU/\nu$  ( $U = \sqrt{g(\rho_c - \rho_a)H/\rho_a}$ ) being the velocity scale,  $g$  the gravitational acceleration, and  $\nu$  the kinematic viscosity of water), initial height aspect ratio  $H/R_0$ , and density ratio  $\rho_c/\rho_a$ . As seen in Table 3-1, the initial aspect ratio based on the local distance from the center of mass is in the range 0.5-8.5, covering both configurations of  $O(10^{-1})$  and  $O(10^1)$  aspect ratio. In all cases, the flow was fully turbulent. The commonly accepted distance of propagation for which transition from the slumping phase to the inertial self-similar phase occurs is about 2 (resp. 5-9) in the cylindrical (resp. planar) configuration (Rottman & Simpson 1983, Cantero *et al.* 2007b). Here the distance of propagation was in the range 7-25, hence the current is likely to enter a regime which resembles the self-similar phase in all cases so the "long-time" regime is reached, as it will be confirmed later (Figures 3-3 and 3-4).

As mentioned above, the behavior of material fronts is in stark contrast to propagation of information (or wave) fronts. For example, an outward propagating sound wave front quickly becomes spherical irrespective of the shape of the source (Lighthill 1978) and the front radius is linearly related to time through sound speed as  $r = c_0 t$  (note that sound intensity distribution depends on the source detail). Similarly a blast wave from a finite source quickly becomes spherical independent of the source shape. Here again the blast radius can be expressed by the power-law (Sachdev 2004)  $r \sim t^{2/5}$ . Although the blast front velocity decreases with time, it remains the same along the entire blast front. Clearly, the propagation of a material front, e.g. gravity currents, cannot be modeled as that of an information front.

The temporal evolution of some axisymmetric and non-axisymmetric gravity currents is presented in Figures 3-2 and 3-4. When the release is non-circular, the current's evolution depends on the initial shape within the time of the observation. For instance, in the case of the gravity current of initial rounded-rectangle cross section, the local front velocity and height at the tips of the initial major (slow) and minor (fast) axes (the marks S and F in Figure 3-7) show large differences in magnitude early after material redistribution (Figures 3-3 and 3-4,  $t > 2$ ). Over time the magnitude of the difference somewhat decreases, but persists up to the end of the experiment/simulation, indicating that the current has not become axisymmetric nor reverted back to its original shape within the limited time of observation. For instance, the patch of heavy fluid of initial rounded-rectangle shape is observed to flip axes, while that of initial plus shape turns into a square.

Initially, the height of the patch is uniform across the surface, and hence, the pressure force is the same along the current's front. As a consequence, just after release, the current rapidly accelerates outward with increasing speed, but initially the current's speed  $u_N$  and height  $h_N$  are independent of the initial shape and are uniform around the circumference of the front (Figures 3-3 and 3-4 for  $t < 1$ ). Upon the release of the heavy fluid inward propagating perturbations initiate at the front, which reflect back at the center of the patch and eventually catch up to the front (Ungarish 2009). During the acceleration phase the heavy material is redistributed within the patch following the direction perpendicular to the initial front. At the end of the redistribution phase, the height  $h_N$  is not uniform along the front of the current (Figure 3-3  $t \approx 2$ ). Since the front velocity  $u_N$  scales as  $\sqrt{h_N}$  (Huppert & Simpson 1980 and Huppert 2006), the speed of propagation is non-uniform along the current's front. This non-uniform circumferential distribution of the heavy fluid within the current, as dictated by the initial shape, remains fixed over time leading to a non-axisymmetric spreading of the current during the slumping and the subsequent spreading phase of the current.

For comparison, the time-dependent solution of the axisymmetric one-layer shallow-water equations (equations 6.24-6.25 in Ungarish 2009) obtained with a finite-difference method similar to that described in appendix 2 of (Ungarish 2009) are plotted in Figures. 3-3B and 3-4B together with the fully-resolved simulation and experimental results. Figure 3-3B shows that the temporal evolution of the local front height of the gravity current of initial rounded-rectangle cross-section roughly follows a slope -1 in log-log representation at times larger than  $t = 5$  approximately. The same trend is observed for the time-dependent solution of the one-layer axisymmetric shallow-water

equations at a somewhat earlier time  $t \approx 3$ . Similarly, the local front speed in Figure 3-4B is observed to roughly follow a slope  $-1/2$ , as clearly seen for the experimental local ‘fast’ front speed. Note that some fluctuations are present in the evolution of the local ‘slow’ front speed, making the comparison more difficult. Comparing the temporal evolution of the local front speed of the non-axisymmetric gravity currents with the time-dependent solution of the one-layer axisymmetric shallow-water equations indicates that the non-axisymmetric gravity currents have entered a long-time phase which resembles the self-similar regime of the axisymmetric configuration, in that the local height and speed roughly follow a law of the type  $h_N \sim t^\alpha$  and  $u_N \sim t^\beta$ , with  $\alpha$  and  $\beta$  being some constants. Note, however, that determining the precise value of  $\alpha$  and  $\beta$ , and the time at which the long-time regime starts is difficult with the present set of experimental and numerical data because of the significant velocity fluctuations observed in Figure 3-4B and the somewhat limited range of parameters investigated here. Larger-size experiments and/or simulations would help to clarify this point.

The dependence of material front propagation on initial condition of release is robust in the sense that the peculiar behavior observed in Figure 3-2 is not restricted to the presently discussed configurations (rounded-rectangle and plus-shaped cross sections; Boussinesq currents of density ratio close to unity). We have conducted many more laboratory and numerical experiments of different non-axisymmetric geometries, density ratios  $\rho_c/\rho_a$  (including Boussinesq homogeneous and turbidity currents  $\rho_c/\rho_a \approx 1$ , heavy currents of dam-break flow type  $\rho_c/\rho_a = O(10^3)$ , and light current  $\rho_c/\rho_a < 1$ ), different aspect-ratio releases (radius to height ratio ranging between 0.5 and 7), varying frictional effects (no-slip/free-slip), and Reynolds numbers (Table 3-1). We found that

provided the Reynolds number is large enough, say  $Re \geq O(10^3)$ , the initial shape of the current always influence the current's continued propagation as well as its preferred asymptotic non-axisymmetric shape for a significant amount of time. Finally, we performed simulations of both full-depth and partial-depth releases (Figure 3-5) and found a qualitative similar dynamics. This indicates that the presently observed behavior is independent of the initial depth ratio. Note that we performed simulations for only two values of  $h_0/H$ . Other experiments or simulations for a wider range of depth ratios would help in quantitatively determining the influence of this parameter on the dynamics of non-cylindrical gravity currents.

### **3.3 A New Model for the Prediction of the Propagation of Non-Circular Density Flows**

This finding has several theoretical implications. The classical Box Model, which is classically used for predicting the evolution of gravity currents (Huppert & Simpson 1980), despite its simplicity, is able to reproduce the dynamics of axisymmetric and planar releases. However, straightforward application of the Box Model fails for non-axisymmetric releases (Figure 3-7). According to this model, the height remains uniform along the entire spreading patch, so the speed of propagation remains uniform along the current's front during all the phases of spreading (recall that the local speed of propagation evolves as the square-root of the local height of the current). Using the classical Box Model, an initially non-axisymmetric current inevitably becomes axisymmetric. Similarly, theories based on slumping and self-similar phases also fail to predict the sensitive dependence on the initial shape and the preferential propagation of non-axisymmetric gravity currents for the same reasons.

Fully-resolved simulations support the experimental findings (Figures. 3-3 and 3-6). The simulations are performed using a spectral code (Cantero *et al.* 2007b) to solve the Navier-Stokes equations using the Boussinesq approximation  $\rho_c/\rho_a \approx 1$ . The numerical domain consists of a Cartesian parallelepiped ( $length \times width \times height = 15 \times 15 \times 1$ ), with a spatial resolution of  $880 \times 880 \times 179$  (140 million degrees of freedom). Boundary conditions are no-slip at the bottom wall, free-slip at the top, and periodic at the sidewalls. The propagation of the current front is visualized via iso-contours of the vertically-averaged dimensionless density field  $\rho = (\rho^* - \rho_a)/(\rho_c - \rho_a) = 0.001$  ( $\rho^*$  is the dimensional local density). Quantitative agreement is found between experiments and fully-resolved simulations. The undulations seen in Figure 3-6 for both simulations and experiments at later times are due to the lobe and cleft instability (Simpson 1972).

Even though such simulations are able to reproduce the peculiar dynamics of non-axisymmetric gravity currents, they are unlikely to be used for rapid prediction, as needed in operational models especially those dealing with the high-Reynolds numbers gravity currents.

Here, we propose an Extended Box Model based on partitioning of the initial release using geometric rays that are perpendicular to the front (Figure 3-7). Once the various sub-volumes are obtained, the local fronts are advanced normal to themselves as in the Box Model. This initial partitioning is the key aspect of the present model, since it allows for non-uniform height and speed along the patch's advancing front, during all the phases of spreading. This allows the model to capture the non-axisymmetric propagation of the front. To be explicit, the formulation of the extended box model

makes use of a Benjamin-type boundary condition (3.1) relating the outward normal front velocity  $u$  to the front height  $h$ , kinematic relations (3.2-3.3) for the advancement of the front position  $(x, y)$  and horizontal area per arc length  $\sigma$ , respectively, and mass conservation (3.4). This results in a system of coupled non-linear PDEs for the unknowns  $u, x, y, \sigma$  and  $h$ , viz

$$u = Fr\sqrt{h} \quad (3-1)$$

$$\frac{\partial\{x, y\}}{\partial t} = u \frac{\{\partial y/\partial s, -\partial x/\partial s\}}{\sqrt{(\partial x/\partial s)^2 + (\partial y/\partial s)^2}} \quad (3-2)$$

$$\frac{\partial\sigma}{\partial t} = u \quad (3-3)$$

$$\frac{\partial(\sigma h)}{\partial t} = 0 \quad (3-4)$$

where, here,  $Fr$  is the Huppert-Simpson Froude number<sup>2</sup>. Note that since the flow is incompressible and entrainment is neglected, the area per arc length  $\sigma$  and the current height  $h$  are such that the total volume  $V$  of the current is given by

$$V = \int_s \sigma h ds \quad (3-5)$$

The independent variables  $s$  and  $t$  denote the curvilinear coordinate along the front and time, respectively.

The solution to (3.1)-(3.4) is far easier and faster than the direct numerical simulations displayed in Figure 3-6a. As shown in Figures 3-1 and 3-7, the solution of the Extended Box Model is capable of capturing the propagation of currents with arbitrary initial forms.

---

<sup>2</sup> Note that another model of Froude number function could be used without losing generality.

At this point, we have shown that (i) fully-resolved simulations and (ii) the proposed extension of the box-model were able to reproduce the observed propagation of non-axisymmetric gravity currents contrary to the classical box-model. It is of major interest, however, to assess the capability of approaches based on the shallow-water equations to reproduce such a dynamics. This would require the development of a numerical approach for solving the two-dimensional one-layer (or better yet two-layer) shallow water-equations as done for example in (La Rocca *et al.* 2008). The development of such an approach is, however, a non-trivial undertaking, which is beyond the scope of the present work. Comparing the present results with a one- and/or two-layer shallow-water approach would allow clarifying the capabilities of shallow-water approaches within the hierarchy of available models for the description of non-axisymmetric gravity currents.

### **3.4 Summary and Discussion**

We have presented results from laboratory experiments and numerical simulations of the propagation of turbulent material fronts stemming from non-axisymmetric finite initial releases. It is found that the effect of the initial non-circular shape of the release persists for the whole duration of the observation. The duration of the experiments was such that the gravity currents have crossed a distance of 12 to 25 times the initial radius, if one considers the equivalent or minimum radius, respectively. This allowed to cover the acceleration phase, the (quasi-)slumping phase and a regime for which the dynamics resembles the self-similar inertial phase predicted by the one-layer axisymmetric shallow-water equations. Finally, we presented a novel model, extending the classical box-model, which accounts for the shape of the initial release and predicts the non-axisymmetric propagation of the front of the gravity current.

It is important to note that the local speed of propagation of a material front generated by the release of a patch of arbitrary shape can vary significantly, thus leading to local “fast fronts” and “slow fronts”. In Figure 3-4, the fastest front is twice as fast as the slowest front during all the observed phases of spreading. Such long-lasting speed variations between the different sections of the front may result in dramatically different front locations that depend on the shape of the initial release. In the context of massive oil spills such as that the Deepwater Horizon oil spill stemming from the explosion of a sea-floor oil gusher in the Gulf of Mexico in April 20, 2010, the flow is likely to remain turbulent for longer times contrary to more moderate oil spills generated by tankers running aground, for which the gravity current is likely to be dominated by viscous and subsequently capillary effects after an hour approximately (Hoult 1972). In the former case, the error made in the estimation of the propagation of the oil spill front, which depends on the nature of initial release, unavoidably decreases the predictive capability of the precise location of impact along the coast. Clearly many other factors such as currents, cross flows, bottom topology, further influence the propagation of non-axisymmetric gravity currents. In light of the present findings, suitable additions to the Extended Box Model described here can help improve the prediction of such gravity currents of arbitrary shapes.

Finally it must be stressed that the present experiments/simulations were done for a limited range of parameters and on a limited spatial domain. The initial shape of the non-cylindrical gravity currents was found to influence the dynamics during the whole but limited duration of observation. For very large domains, however, non-cylindrical finite-release gravity currents are likely to enter, after some time, a regime

where viscous effects are predominant. In that case, viscous diffusion of momentum may homogenize the front height and velocity so that the viscous current may become axisymmetric. More experiments on larger domains are needed to clarify if the presently observed behavior holds for longer distances of propagation and corresponding times than those attained here.



Figure 3-1. Field observations of a non-circular gravity current. Aerial views of (top) a building of square cross-section and (bottom) a T-shaped building being demolished. The structure of the debris cloud is highly dependent on the building's shape. Observe that material very close to the center of the building moves farther out than material located at the building's extremities. The dynamics of the cloud is reasonably well captured by our proposed model, where the front location of the cloud is marked at equal instants of time as blue lines.

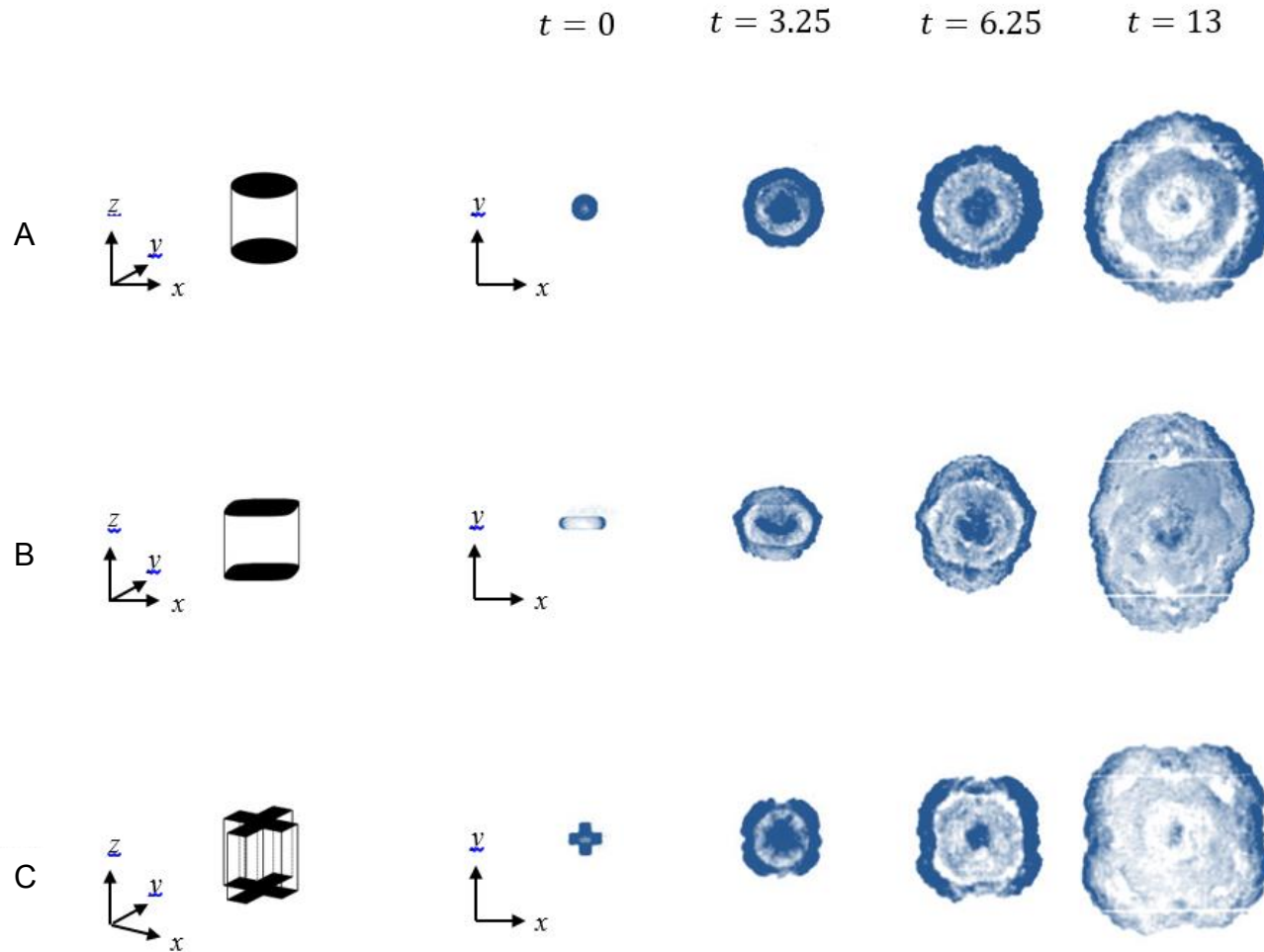


Figure 3-2. Temporal evolution of the experimental collapse of a column of salty water with different cross-sections at the center of a tank containing fresh water ( $H/R_0 = 2$ ,  $Re = 2.8 \times 10^4$ ,  $\rho_c/\rho_a = 1.1$ ). The schemes on the left depict the three-dimensional initial shape of the heavy material in the experiment, namely cylinders of A) circular, B) rounded-rectangle and C) plus-shaped cross sections. Gravity is oriented opposite to  $z$ -axis. Time is scaled by  $T = H/U$  (defined in text).

Table 3-1. Parameters used in the experiments and/or simulations.  $h_0(H)$  is the initial height of the current (ambient),  $R_0$ ,  $R_{min}$ ,  $R_{max}$  are the initial equivalent, minimum, maximum radius of the cross-sectional area of the cylinders,  $L$  is the maximum distance of propagation.

Parameters				
Reynolds	$Re$			
number	[ $7 \times 10^3$ , $10^6$ ]			
Initial depth	$H/h_0$			
ratio	1 - 2			
Initial	$H/R_{max}$	$H/R_0$	$H/R_{min}$	
aspect ratio	0.5	1 - 2 - 4	8.5	
Density	$\rho_c/\rho_a$			
ratio	0.93 - 1.1 - $10^3$			
Distance of	$L/R_{max}$	$L/R_0$	$L/R_{min}$	
propagation	7	12	25	

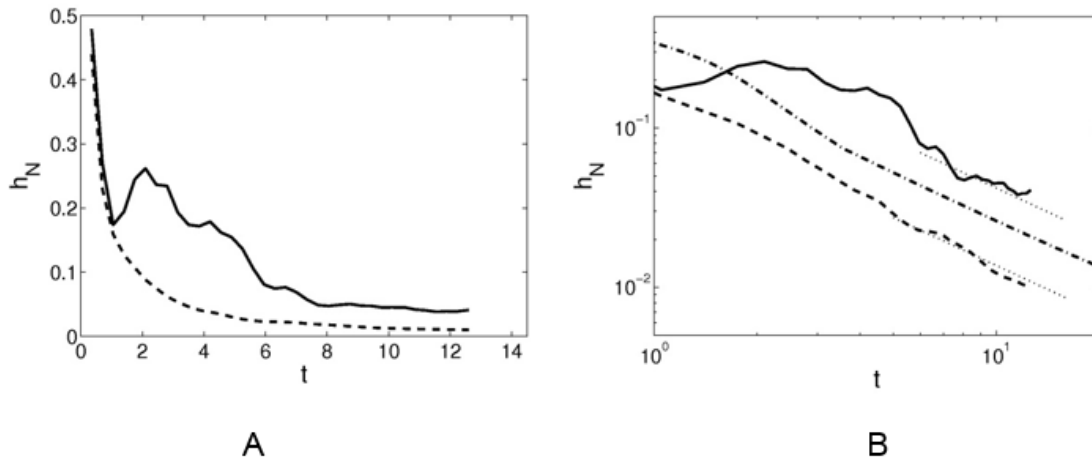


Figure 3-3. Temporal evolution of the local front height in the vertical mid-plane of  $x$ -direction (dashed line) and  $y$ -direction (solid line) of the current of initial rounded-rectangle cross section. A) Results obtained from the fully-resolved simulation with  $H/R_0 = 2$  and  $Re = 8950$ . B) Same as frame a in log-log representation. For comparison, the time-dependent solution of the axisymmetric one-layer shallow-water equations using Huppert & Simpson (1980)'s front condition in the full-depth configuration is shown in frame b (dash-dot line). The dotted lines indicate a slope of -1, as predicted by the self-similar solution of the axisymmetric one-layer shallow-water equations (Ungarish (2009) p122).

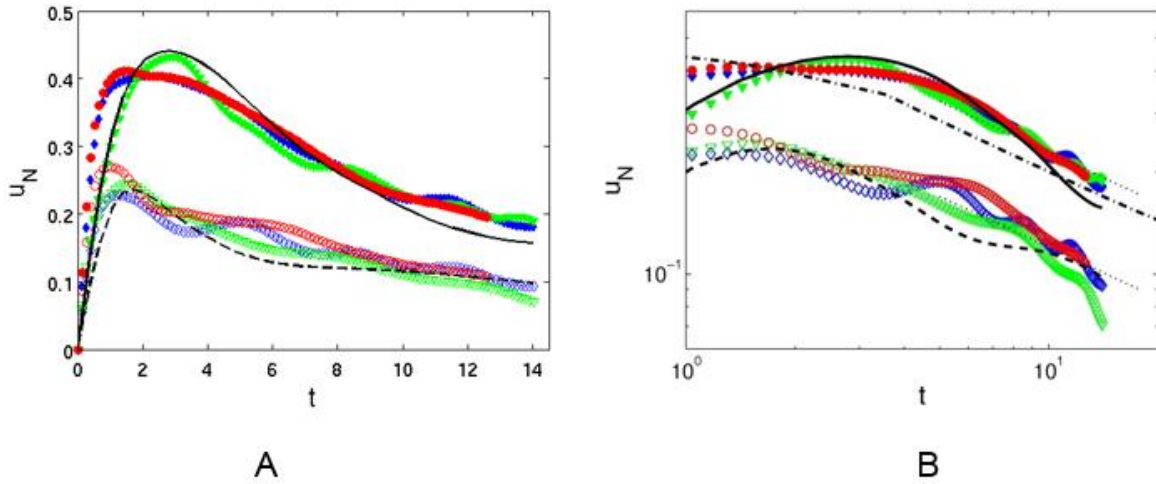


Figure 3-4. Temporal evolution of the local front speed in the vertical mid-plane of  $x$ -direction (lower curves) and  $y$ -direction (upper curves) of the current of initial rounded-rectangle cross section. A) The solid and dashed lines correspond to results obtained from the fully-resolved simulation with  $H/R_0 = 2$  and  $Re = 8950$ , while the symbols are from three experiments for which  $H/R_0 = 2$  and  $Re = 2.8 \times 10^4$ . B) Same as frame A in log-log representation. For comparison, the time-dependent solution of the axisymmetric one-layer shallow-water equations using Huppert & Simpson (1980)'s front condition in the full-depth configuration is shown in frame B (dash-dot line). The dotted lines indicate a slope of  $-1/2$ , as predicted by the self-similar solution of the axisymmetric one-layer shallow-water equations (Ungarish (2009) p122).

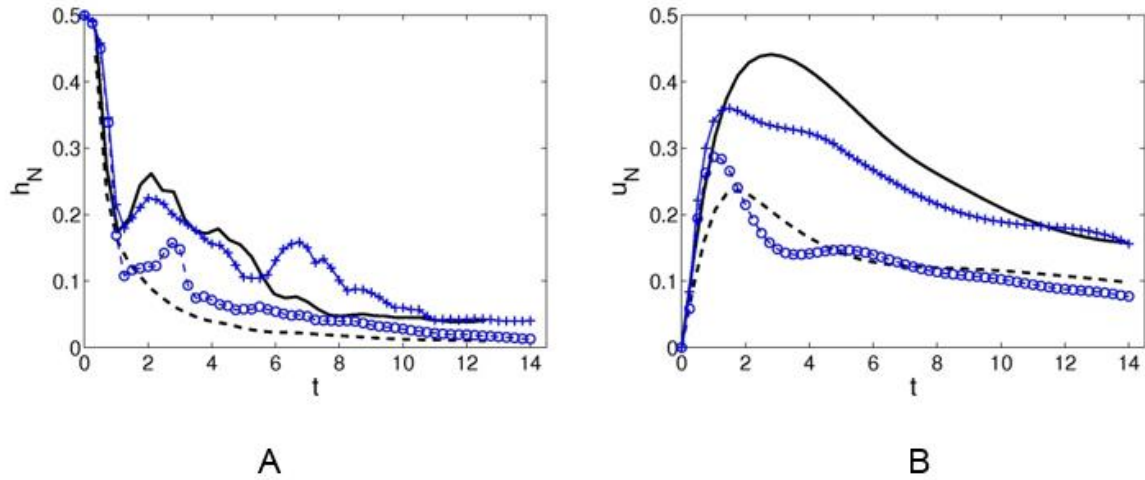


Figure 3-5. Temporal evolution of the local front's height A) and speed B) in the vertical mid-plane of  $x$ -direction (dashed lines) and  $y$ -direction (solid lines) of the current of initial rounded-rectangle cross section for two initial depth ratios, namely a partial-depth release  $h_0 = H/2$  (blue lines with symbols) and a full-depth release  $h_0 = H$  (black lines without symbols). These results are obtained from fully-resolved simulations with  $H/R_0 = 2$  and  $Re = 8950$ .

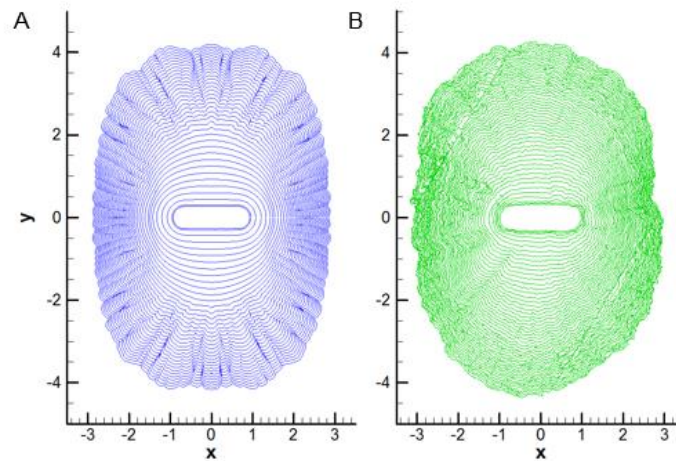


Figure 3-6. Temporal evolution of a non-axisymmetric material front (fully-resolved simulation vs. experiment). The initial cross sectional geometry is a rounded rectangle. A) Numerical simulations with  $Re = 8950$ . Time separation between contours is  $\Delta t = 0.35$  and the final time is  $t_f = 12.6$ ; B) laboratory experiments. Here,  $Re = 28000$ , time separation between contours is  $\Delta t = 0.26$ , and the final time is  $t_f = 12.73$ .

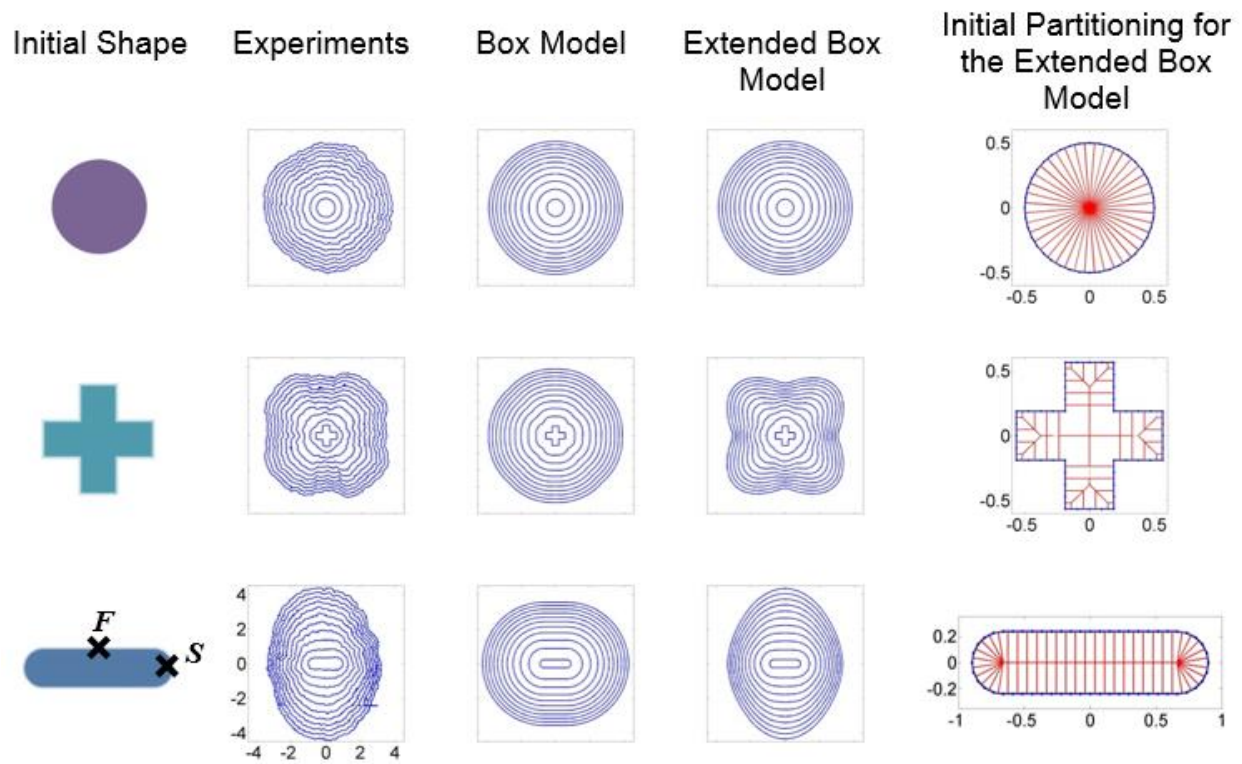


Figure 3-7. Experiments vs. Box Model / Extended Box Model. Front location with a time separation between contours of  $\Delta t = 1.3$ , and a final time of  $t_f = 13$ . In the classical Box Model, as the current propagates, the height is intrinsically averaged over the entire patch of fluid making the propagation inevitably axisymmetric. In the Extended Box Model, the volume of release is initially divided into multiple sub-volumes. The size of each sub-volume depends on the inwardly propagating geometric rays starting from and perpendicular to the current's front. The Extended Box Model is in quantitative agreement with experiments, contrary to the classical Box Model. The marks  $S$  and  $F$  refer to the tips of the initial major (slow) and minor (fast) axes from which the front velocity and height are computed in Figures. 3-3 and 3-4.

## CHAPTER 4 DIRECT NUMERICAL SIMULATION OF CYLINDRICAL PARTICLE-LADEN GRAVITY CURRENTS

### 4.1 Background

Particle driven currents are a special form of gravity currents in which the density difference is caused by the suspension of particles within an interstitial fluid forming the current. If the mixture density of such a suspension is larger than that of the ambient fluid, it will advance primarily horizontally as a turbidity current (Lowe 1982, Gladstone *et al.* 1998). Turbidity currents are inherently more complex than homogeneous conservative currents because the density of the current (and consequently the density difference between the current and the ambient) may vary temporally and spatially as a result of the settling and entrainment of particles. The effective settling speed of particles, for example, may depend on particle Reynolds number, particle flocculation, and interaction with surrounding turbulence. On the other hand, if the current is traveling fast enough over an erodible bed, it may entrain particles causing it to move even faster and consequently entrain more particles in a self-reinforcing cycle.

Particulate gravity currents are observed in many industrial, environmental, and geological situations. Owing to their destructive nature, turbidity currents constitute a major factor in the design of underwater structures such as pipelines and cables (Simpson 1982). In an industrial context, they are essential for transporting sediments that may contain pollutants. Furthermore, they are responsible for the formation of submarine canyons as well as for sedimentation transport into the deep oceans.

Particulate, constant volume releases (Bonnecaze *et al.* 1993, 1995, Hallworth & Huppert 1998, Gladstone *et al.* 1998, Necker *et al.* 2002, Blanchette *et al.* 2005, Cantero *et al.* 2008) have been studied. However, these finite releases are invariably

dominated by fronts. Often in turbidity currents, it is very important to look at the body of the current after the head had long moved away. Experimentally and computationally this is somehow harder to study, and is usually investigated through constant flux currents (Garcia and Parker 1993, Hogg *et al.* 2005, Sequeiros *et al.* 2009, Shringarpure *et al.* 2012). In the present context, we explore a finite-volume cylindrical release of particle-laden fluid in clear ambient surrounding. We wish to identify the dynamics of the current, specifically the three-dimensional layout and vortical structures of the current. Here we are only concerned with deposition and neglect the effects of resuspension. In reality, resuspension of particles may play a role, but the mechanisms of re-suspension are not fully understood and models of resuspension rate remain empirical with large uncertainties (Ziskind *et al.* 1995). In order to make the problem simple and manageable, we look only at the problem of deposition.

Predicting the deposition pattern or the soil erosion resulting from a turbidity current necessitates a good understanding of the mechanism of sediment transport and particle deposition, which are highly dependent on the dynamics of the current, the level of turbulence, and the fluid-particle interaction. As a result, a great level of simplification is generally taken, usually through depth averaging, when studying particulate-driven currents. Some of the models include the Box Model (Bonnecaze *et al.* 1993, Dade & Huppert 1995), which is a simple and fast way to model the extent, speed, and sedimentation pattern of turbidity currents. The Box Model is not directly derived from the Navier-Stokes equations, however it considers the current to evolve with negligible entrainment through a series of height diminishing concentric cylinders for an

axisymmetric lock release configuration. In addition to depth averaging, no radial variation is allowed.

A more complex model is based on the Shallow Water equations (Bonnecaze *et al.* 1995, Ungarish & Huppert 1998, Choi & Garcia 1995), which are derived by vertically averaging the Navier-Stokes equations under the assumption of high length-to-thickness aspect ratio. However, because of the variable volume fraction of the current, an equation of particle conservation is further required. Such models do not usually account for sediment entrainment on the basis that the velocities are insufficient to lift up particles, however the flow is considered to be sufficiently energetic so that turbulent mixing maintains vertically uniform properties.

Most research on axisymmetric particle-laden gravity currents has mainly revolved around the early experiments of Bonnecaze *et al.* (1995) and theoretical models mostly based on the Box Model and Shallow Water equations (Ungarish & Huppert 1998, Gladstone & Woods 2000). Our objective in this study is to pick a scenario that is similar to what has been investigated experimentally but instead examine it through DNS. Highly resolved simulations for cylindrical density-driven finite-release currents have been investigated in the past with results comparing favourably with experiments (Cantero *et al.* 2007a). Here we consider direct numerical simulations of particle-laden currents resulting from the release of an initial cylindrical fluid-particle mixture.

The DNS will allow us to explore the three-dimensional structures of the current from iso-surfaces of density that reveal the three-dimensional outline to iso-surfaces of the swirling strength that show the intensity and structure of the turbulent eddies. These

large scale vortical structures play an important role in the erosion and resuspension of particles by locally modifying the shear stress at the bottom wall. They also play an important role in the deposition of particles by transporting low particle concentration fluid (particle-laden current mixed with ambient) from the current's top layers towards the bottom wall and consequently decreasing the local settling rate. This study will be limited to finite-releases of full-depth cylindrical gravity currents with dilute concentrations of monodisperse particles. The paper is arranged as follows. The mathematical formulation is outlined §4.2. In §4.3, we present our simulation results and compare, where possible, to previous experimental and theoretical data. Finally, main conclusions are given in §4.4 along with recommendations for future work.

## 4.2 Mathematical Formulation

A side view of the problem setup is depicted in Figure 4-1. Initially, a cylindrical gate separates a relatively heavier (compared with the ambient) particle-laden fluid of initial density  $\rho_{c0} = (\rho_p - \rho_a)\phi_0 + \rho_a$  in its interior from the surrounding clear ambient fluid of density  $\rho_a$ . Both fluids are initially at the same level and occupy the entire height of the domain (Figure 4-1). Here,  $\rho_p$  represents the density of suspended particles, and  $\phi_0$  is the initial volume fraction occupied by those particles.

Our focus is to simulate buoyant driven flows with dilute suspensions, where particle-particle interactions may be neglected. We consider monodisperse particles whose size is much smaller than characteristic length scale  $H$  of the problem. The particle-laden solution will be treated as a continuum and a two-fluid formulation is adopted. We follow Cantero *et. al* (2008a) by implementing an Eulerian-Eulerian model of the two-phase flow equations. The model involves (i) mass (ii) and momentum

conservation equations for the continuum fluid phase, (iii) an algebraic equation for the particle phase where the particle velocity is taken to be equal to the local fluid velocity and an imposed settling velocity derived from the Stokes drag force on the particles, (iv) and a transport equation for the volume fraction (particle phase). The non-dimensional system of equations read

$$\nabla \cdot \mathbf{u} = 0 \quad (4-1)$$

$$\frac{D\mathbf{u}}{dt} = \phi \mathbf{e}^g - \nabla p + \frac{1}{Re} \nabla^2 \mathbf{u} \quad (4-2)$$

$$\mathbf{u}_p = \mathbf{u} + \mathbf{u}_s \quad (4-3)$$

$$\frac{\partial \phi}{\partial t} + \nabla \cdot (\phi \mathbf{u}_p) = \frac{1}{Sc Re} \nabla^2 \phi. \quad (4-4)$$

Here  $\mathbf{e}^g$  is a unit vector pointing in the direction of gravity. Unless otherwise stated, all parameters are non-dimensionalized. The height  $H$  of the domain is taken as the length scale,  $U = \sqrt{g'_0 H}$  as the velocity scale,  $T = H/U$  as the time scale,  $\rho_a$  as the density scale, and  $\rho_a U^2$  as the pressure scale. The reduced gravitational acceleration is defined as  $g'_0 = (\rho_p - \rho_a) \phi_0 g / \rho_a$ . We denote by  $\mathbf{u}_p$  and  $\phi$  the velocity and the volume fraction of the particle phase, respectively.  $\mathbf{u}$  and  $p$  correspond to the velocity and total pressure of the continuum fluid phase, respectively. The settling velocity  $\mathbf{u}_s$  is determined from the Stokes drag force on spherical particles with small particle Reynolds numbers. Here, the density of particles is assumed to be appreciably larger than that of the ambient fluid such that the dominant force on the particle is the Stokes drag. The Reynolds and Schmidt numbers in (4-2) and (4-4) are defined as

$$Re = UH/\nu, \quad Sc = \nu/\kappa \quad (4-5)$$

In the above,  $\kappa$  and  $\nu$  represent the molecular diffusivity and kinematic viscosity of the ambient (interstitial) fluid, respectively.

The simulation is carried out inside a rectangular box of dimensions  $L_x \times L_y \times H = 30 \times 30 \times 1$  using a spectral code that has been extensively validated (Cantero *et al.* 2007a,b). Periodic boundary conditions are imposed along the sidewalls for the continuum and particle phases. No-slip and free-slip conditions are imposed for the continuum phase along the bottom and top walls, respectively. Mixed and Neumann boundary conditions are imposed for the particle phase at the top and bottom walls, which translate into zero particle net flux and zero particle resuspension, respectively.

$$\frac{1}{Sc Re} \frac{\partial \phi}{\partial z} - \mathbf{u}_s \phi = 0, \quad \frac{\partial \phi}{\partial z} = 0 \quad (4-6)$$

We present results from two simulations that differ solely by the Reynolds number. The details of the simulations are outlined in Table 4-1. The domain size was chosen for comparison purposes with previous experiments of Bonnecaze *et al.* (1995). We chose a grid resolution of  $680 \times 680 \times 109$  (along the  $x, y$ , and  $z$  directions, respectively) corresponding to over 50 million degrees of freedom. This numerical resolution, for the larger  $Re$  number case of 10000, achieves between 4 and 6 decades of decay in the  $x$ -spectra of density at various instances as shown in Figure 4-2. Similar decay was observed for all other quantities and for the  $y$ -spectra and  $z$ -spectra as well. Thus, the simulations to be discussed here are well resolved.

## 4.3 Results

### 4.3.1 Three-Dimensional Structures

The start of the simulation is initiated by “lifting” the cylindrical gate. The particle-laden solution is heavy and begins to collapse and spread out radially, intruding into the

ambient fluid with a slug-like ground hugging motion. In Figure 4-3, we present iso-surfaces of concentration from the large  $Re$  number simulation of 10000 to help visualize the three-dimensional temporal and spatial structures of the current. Shortly after release ( $t = 2$ ), the front is nearly two-dimensional and the “head” of the current may be recognized by a rolled up vortex tube at the front. At later times ( $t = 4$  and  $t = 6$ ), a pattern of rolled up vortices can be identified. Because of their unequal propagation speeds, some of the relatively faster vortex tubes will catch up with slower tubes ahead and merge to form bigger rolled up vortices (Figure 4-3 at  $t = 4$  and  $t = 6$ ). Furthermore, as the current starts to decelerate, (and because of the no-slip boundary condition at the bottom surface) lobe and cleft structures (Simpson 1972, Hartel et al 2000) begin to emerge rendering the once smooth front more complex and three-dimensional.

The vortical structures identified in Figure 4-3 are the Kelvin-Helmholtz rolled up vortices generated at the current-ambient interface. These vortices exhibit a counter-clockwise rotation and are advected radially outwards by the current. These energetic vortices locally accelerate the flow in the near wall region, and because of the no-slip boundary condition, help to initiate clockwise-rotating vortices at the bottom surface. These bottom vortices are concealed in the iso-surface plots, but may be readily visualized through iso-surface plots of the swirling strength  $\lambda_{ci}$  shown in Figure 4-4. The swirling strength is a good indicator of regions of intense vorticity (Zhou *et. al.* 1999, Chakraborty *et. al.* 2005). It is defined as the absolute value of the imaginary portion of the complex eigenvalue of the velocity gradient tensor.

### 4.3.2 One-Dimensional Time Evolution

In Figure 4-5, we plot the temporal evolution of the mean height  $\bar{h}$  and areal deposit  $\bar{D}$  of the current along the radial direction. These quantities are obtained by averaging along the azimuthal and vertical directions for the density field to calculate  $\bar{h}$ , and integrating in time the tangentially-averaged bottom density section (multiplied by the settling velocity) to obtain  $\bar{D}$

$$\begin{aligned}\bar{h}(r, t) &= \frac{1}{2\pi} \int_0^H \int_0^{2\pi} \rho(r, \theta, z, t) d\theta dz \\ \bar{D}(r, t) &= \frac{1}{2\pi} \int_0^t \int_0^{2\pi} \rho(r, \theta, 0, t) u_s d\theta dt\end{aligned}\tag{4-7}$$

Initially, the areal deposition along the lock length ( $0 \leq r \leq R_0$ ) increases linearly with time up to the point where all the fluid inside the lock has been set in motion ( $t \approx 6$ ). The current is shown to attain the typical slug like shape with an elevated head and a slender body around  $t = 4$ . As seen from Figure 4-6, the effect of sedimentation on the spreading rate of the current is not perceived until enough particles have settled out. This occurs sometime between  $t = 10$  and  $t = 16$ , where the particle-laden current front begins to deviate from the saline current. During that time frame, the current has lost over 45 percent of its total particles (Figure 4-7).

### 4.3.2 Front Location

The front position of the current is shown in Figure 4-6. Because of the axisymmetric nature of spreading, the density field is first averaged in the azimuthal direction. The position of the front is then taken as the location where the vertically averaged density (the current's thickness) drops to a value of 0.01. Our numerical domain was chosen to match the physical setting of experiments reported by

Bonnecaze *et al.* (1995), and their findings are plotted alongside our simulation data in Figure 4-6. Our results for the larger and smaller  $Re$  number simulations are in good agreement with the experiments and the Shallow Water equations-based theoretical model. The larger  $Re$  number case of 10000, which is closer to the  $Re$  number of the experiments of 17000, provides however, slightly better agreement with the experiments and model. In addition to the particle-laden currents, we also show the front location for a saline current experiment carried out by Bonnecaze *et al.* (1995). The saline current experiment serves as a benchmark to identify the time beyond which sedimentation effects influence the front velocity of the particle-laden current.

The aforementioned experiments were carried out in a radial sector tank with monodisperse  $37\ \mu\text{m}$  silicon carbide particles resulting in a non-dimensional settling velocity of  $1.3 \times 10^{-2}$ . The initial reduced gravitational acceleration for the particle-laden and saline currents were  $11\ \text{cm s}^{-2}$  and  $42\ \text{cm s}^{-2}$ , respectively. Despite the difference in the reduced gravitational acceleration, the non-dimensional front positions of these currents will match perfectly until enough particles have settled out and the two curves begin to diverge from one another.

### 4.3.3 Deposition

Of fundamental importance in particle-laden gravity currents is the deposition pattern of sediments. The settling of particles leads to a continuous decrease in the density of the current leading to a decay in the driving force, and eventually causing the current to arrive at a standstill when all the particles have settled out. Figure 4-8 illustrates the temporal evolution of the rate of deposition of suspended particles defined below as

$$\dot{m}(t) = \int_0^{L_y} \int_0^{L_x} \rho(x, y, 0, t) u_s dx dy \quad (4-8)$$

We observe a rise in the sedimentation rate from the time of release up to  $t = 8$  beyond which the particles continue to settle but at a continuously diminishing rate. This behavior of rise and decay in the sedimentation rate has been also observed for planar particle-driven gravity currents (Necker *et al.* 2002).

The local instantaneous deposition rate is strongly affected by the large-scale vortex tubes depicted in Figure 4-4. These tubes create local minima in the instantaneous bottom concentration profile (and hence the instantaneous deposition rate) by transporting low concentration fluid (particle-laden current mixed with the ambient) towards the bottom wall. Consider for instance the 2-dimensional concentration profile on the bottom wall at  $t = 6$  as shown in Figure 4-9. We may readily identify a local minimum at  $r \approx 2.5$ , where the bottom concentration drops by about 14%. The position of this minimum corresponds to the radial location of the vortex tube labeled  $T_3 + T_4$ .

For the sake of comparison with experiments, we plot in Figure 4-10 the areal deposition from both simulations and compare them with Bonnecaze *et al.* (1995) experimental and theoretical final deposition layout. The areal density of deposit of the simulations is taken at  $t = 30$ , at which point over 95% (resp. 91%) of particles have settled for the  $Re = 10000$  (resp.  $Re = 3450$ ) case. The simulation curves are scaled so that the area under the curve is equivalent to that of the experimental results. The simulations as well as the theoretical model indicate that the current's density of deposit increases as we move away from the center and reaches a maximum value close to the position of the gate ( $r = R_0$ ). This is in contrast with the experiments where the density

of deposit decreases monotonically as we move radially outwards. Differences between simulation and experiments are most distinct in the region around the lock. However, for the experiments, the region behind the gate is subject to disturbances from initial stirring in addition to the early sedimentation that initiates before the removal of the gate. The DNS results in Figure 4-10, also reveal a second peak in the amount of deposition at a downstream location from the gate. It should be noted however that the amplitude of these peaks is observed to decrease with increasing Reynolds number. The presence of multiple spikes have also been observed in planar simulations of particle-laden currents (Necker *et al.* 2002).

#### **4.3.4 Wall Shear-Stress and Near-Wall Dynamics**

Exploring the near-wall dynamics of a particulate gravity current is necessary for understanding erosion and resuspension of particles. The wall-shear stress is often used in theoretical models to predict the possibility of sediment entrainment over loose beds (Yalin & Karahan 1979). These bed-shear stresses are closely related to the large scale clockwise rotating vortex tubes discussed in §4.3.1. A two-dimensional contour plot in Figure 4-11 of the wall shear-stress at  $t = 6$  reveals three local minima with a reversal in flow direction (negative wall shear-stress). These local minima correspond to the clockwise rotating vortex tubes sweeping the bottom wall ( $B_1$ ,  $B_2$ , and  $B_3$ ). The vortex tubes  $B_1$  and  $B_3$  are relatively smooth with small variations along the radial direction. Their axisymmetric structure is translated into a smooth shell-like outline in the wall shear-stress contours of Figure 4-11. On the other hand, the hairpin and other small-scale vortical structures forming around  $B_2$  (Figure 4-4) could be the reason behind the square, wavelike pattern at  $r \approx 2.8$  in Figure 4-11. The local minima in the

bottom shear-stress profile of Figure 4-11 are a result of flow reversal due to the aforementioned clockwise vortex tubes rotating at close proximity to the bottom wall. The direction of these vortices and their position with respect to the current is presented in Figure 4-12.

#### **4.3.5 Conclusions and Recommendations**

We presented direct numerical simulation results for a cylindrical, finite-release, particle-laden gravity current. At early times ( $t < 6$ ), the current shows a train of Kelvin-Helmholtz counter-clockwise rotating rolled up tubes that are generated at the current-ambient interface. Below these surface vortex tubes, a set clockwise-rotating eddies initiate from the bottom wall. These large scale vortical structures are difficult to visualize and study experimentally and are unattainable using two-dimensional theoretical models. They are nonetheless very important for studying the erosion, deposition, and resuspension dynamics of particle-laden currents. These vortex tubes may locally modify the bed shear stress and hence could play an important role in particle entrainment and erosion off the bottom wall. Furthermore, by transporting low particle concentration fluid from the surface of the current towards the bottom wall, they locally change the bottom concentration and hence modify the deposition pattern. Our simulations compare favorably with previous experiments (Bonnecaze *et al.* 1995) in terms of the temporal evolution of the front as well as the final deposition pattern.

While this study has focused on particle-laden currents, it would be interesting to run similar simulations, however for density-driven currents (with zero settling velocity). It might be worthwhile to explore the differences in the vortical structure between conservative (density-driven) and non-conservative (particle-laden) currents. Previous studies have considered the differences between the two types of currents. A popular

approach has been to explore the time beyond which the front position of a saline current begins to deviate from that of a turbidity current (Figure 4-6 for example). Other studies have considered the effect on the transition times between the various velocity phases (Necker *et al.* 2002).

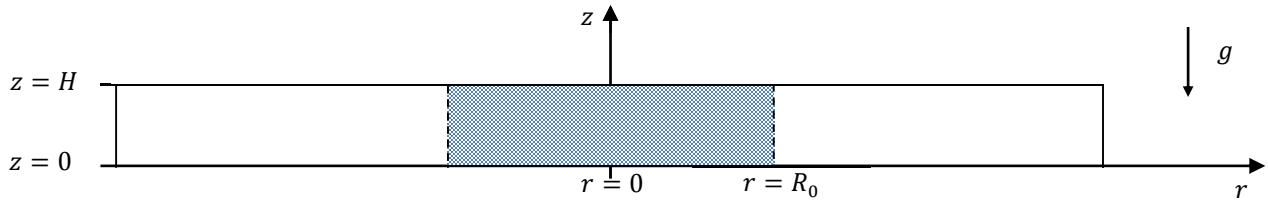


Figure 4-1. Side view of the initial setup of the cylindrical lock-exchange flow inside a rectangular box of size  $L_x \times L_y \times H = 30 \times 30 \times 1$ . Initially, a cylindrical gate of radius  $R_0$  placed at the center of the domain separates particle-laden fluid from the ambient clear fluid. Once the gate is lifted, the simulation starts and the particle-laden fluid begins to intrude horizontally into the ambient.

Table 4-1. Details from the numerical simulations performed for this study.  $Re$ ,  $Sc$ , and  $u_s$  are the Reynolds, Schmidt, and settling velocity defined in §4.2. The simulations ran for  $t_f$  non-dimensional time units.

Domain size	$Re$	$Sc$	$u_s$	Grid Resolution	Time step	$t_f$
$30 \times 30 \times 1$	10,000	1	0.013	$680 \times 680 \times 109$	$2 \times 10^{-3}$	30
$30 \times 30 \times 1$	3,450	1	0.013	$680 \times 680 \times 109$	$2 \times 10^{-3}$	30

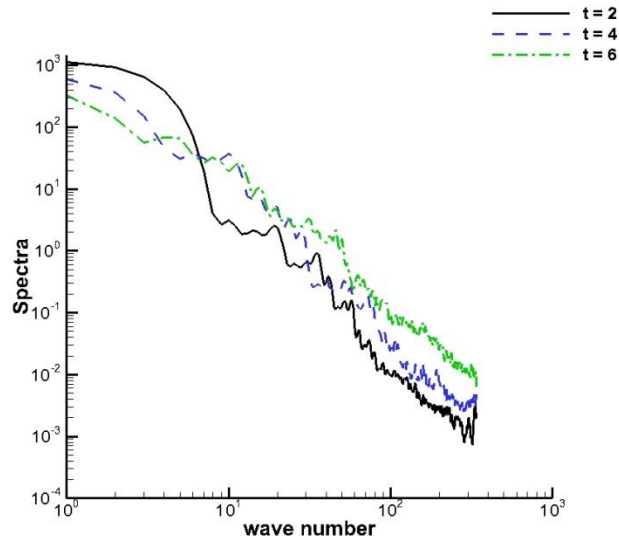


Figure 4-2. Density Spectra as a function of wavenumber along the  $x$ -direction for three different time instances at  $Re = 10000$ .

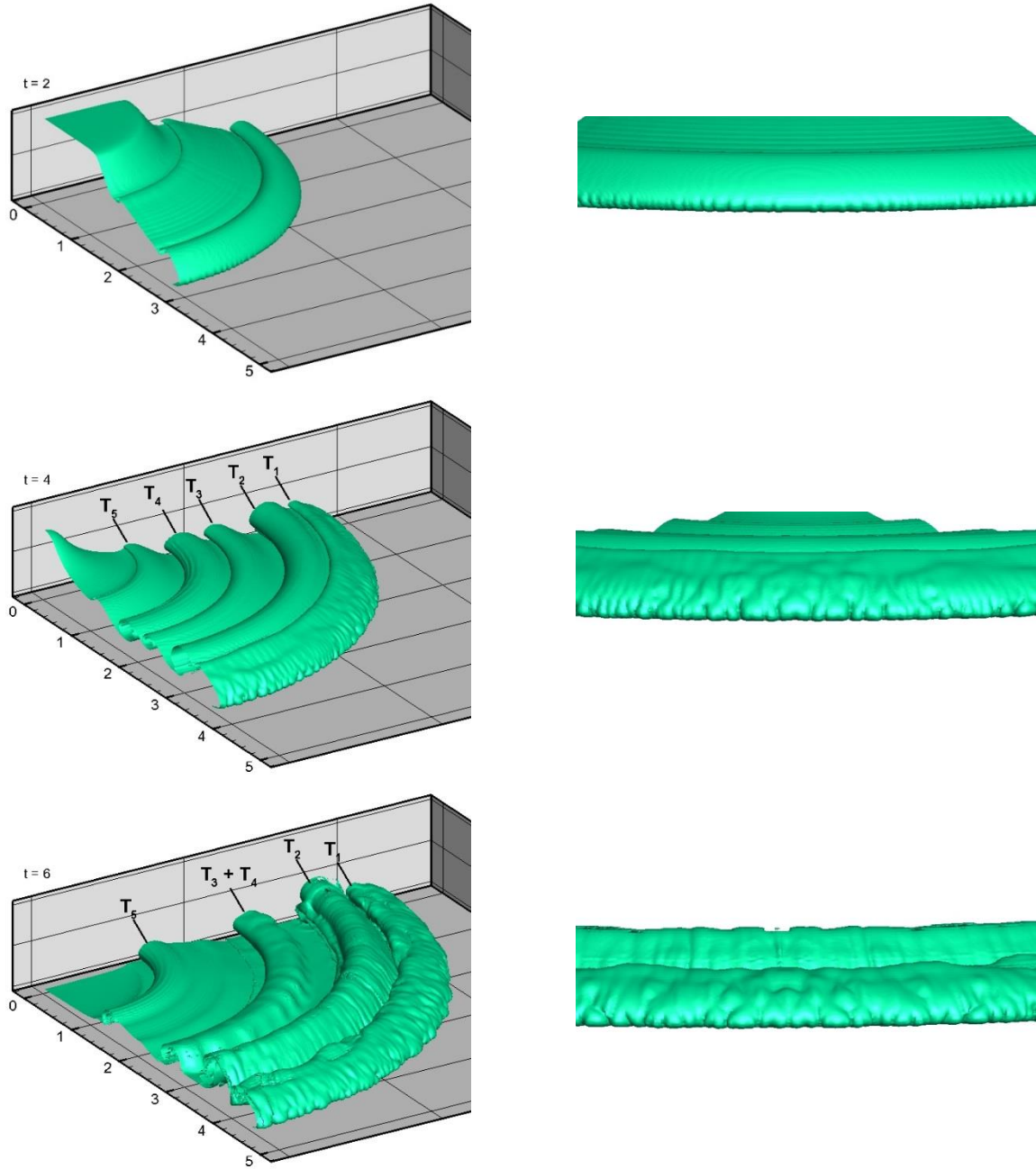


Figure 4-3. Iso-surfaces of density in one quadrant of the computational domain for  $Re = 10000$ . The structure of the current exhibits multiple rolled-vortices with the lobe and cleft instability pattern identifiable at later times ( $t = 6$ ). An iso-value of  $\rho = 0.25$  is employed for all cases. A close up view of the front (on the right) shows its transition from a nearly two-dimensional surface at early times ( $t = 2$ ) to a more complex structure at later times ( $t = 6$ )

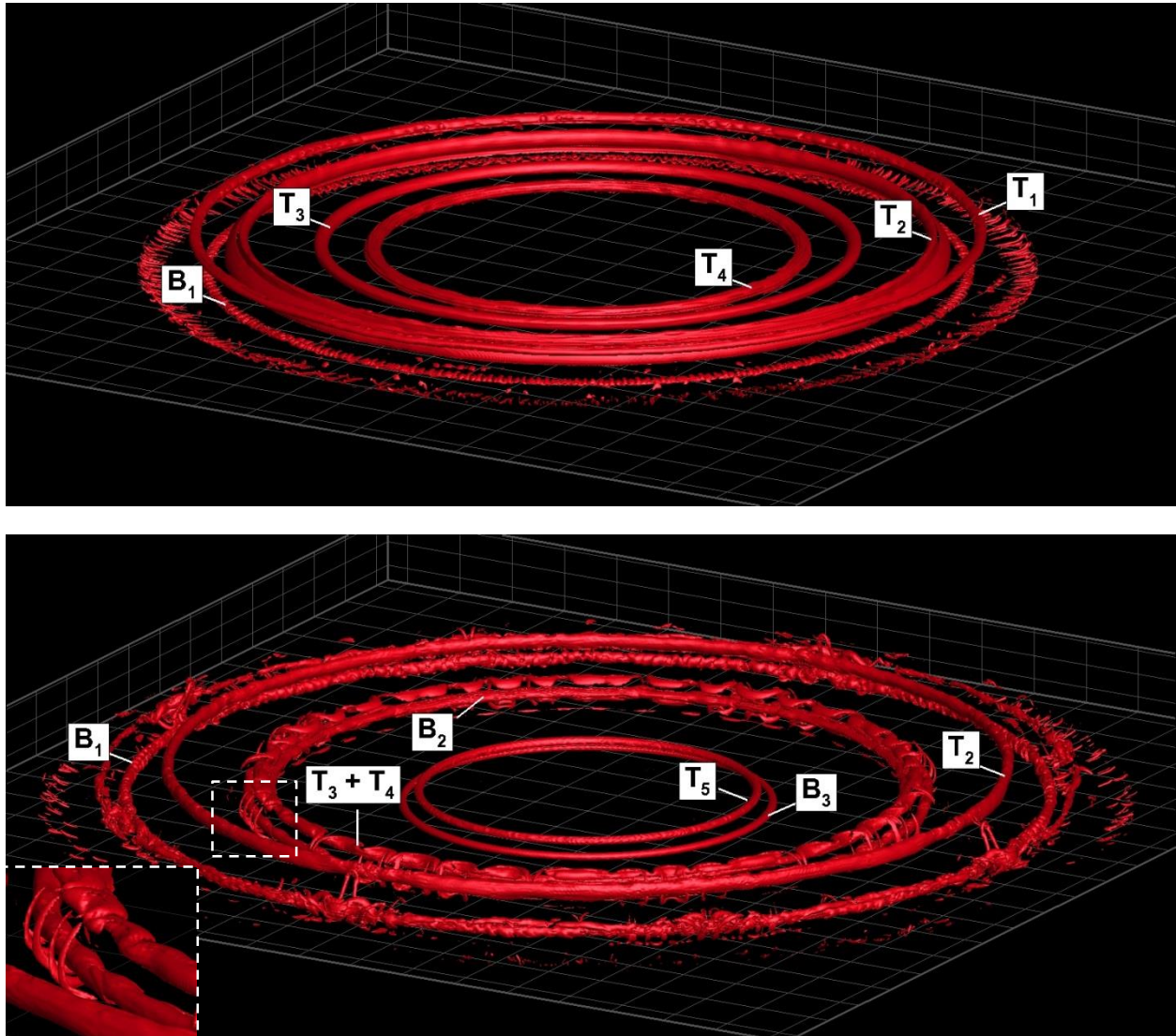


Figure 4-4. Iso-surfaces of  $\lambda_{ci}$  for  $Re = 10000$  with an isovalues of 6 and 8 for  $t = 4$  and  $t = 6$ , respectively. The mean and rms values of  $\lambda_{ci}$  are (0.14, 0.79) for  $t = 4$ , and (0.28, 1.62) for  $t = 6$ . A close-up view at  $t = 6$  shows a set inclined hairpin vortical structures that have formed around the bottom clockwise rotating vortex  $B_2$  in the body of the current.

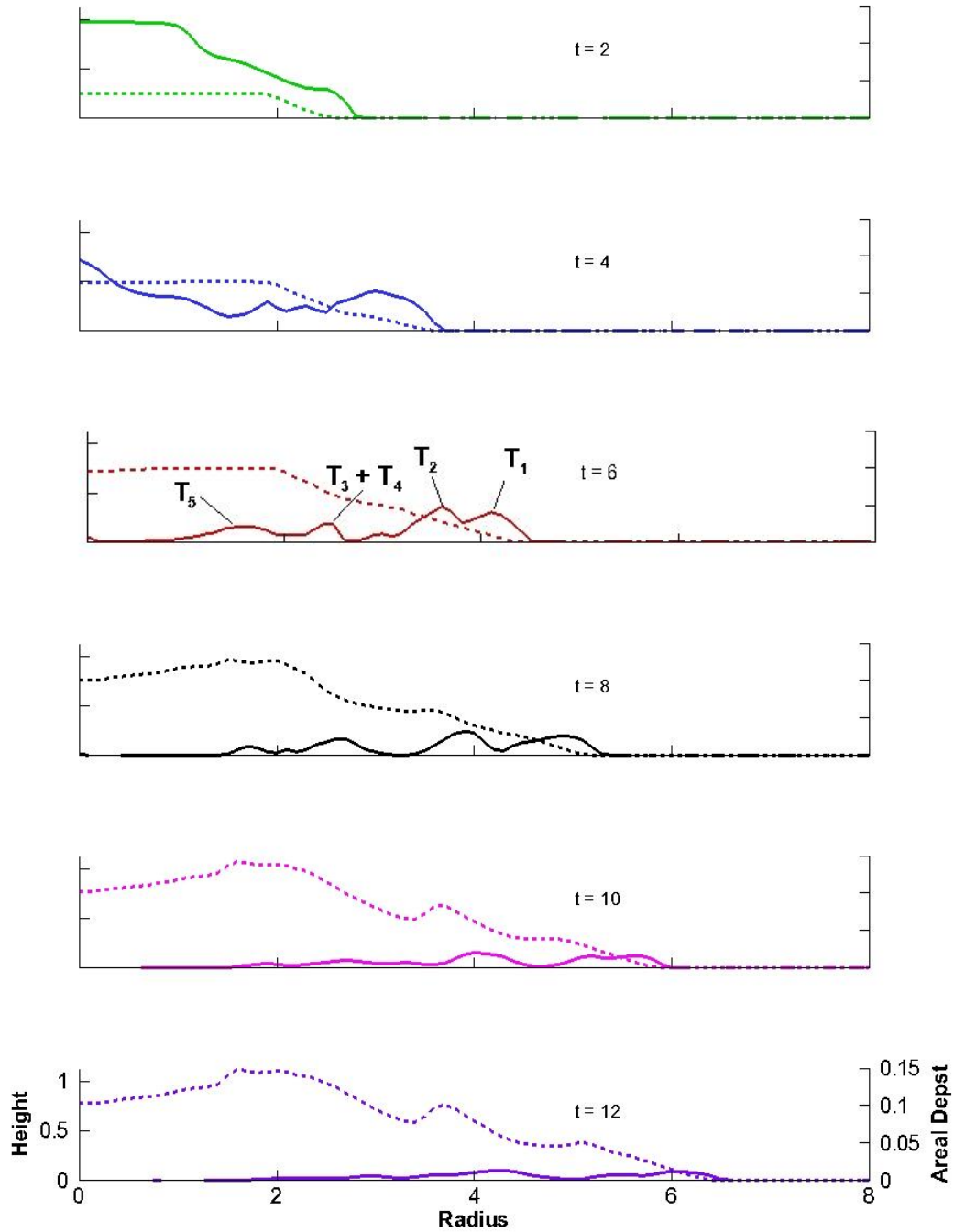


Figure 4-5. Height (solid line) and areal deposit (dashed line) as a function of radius for different times with  $Re = 10000$ . The four peaks in the height profile at  $t = 6$  correspond to the Kelvin-Helmholtz vortices shown in Figure 4-3.

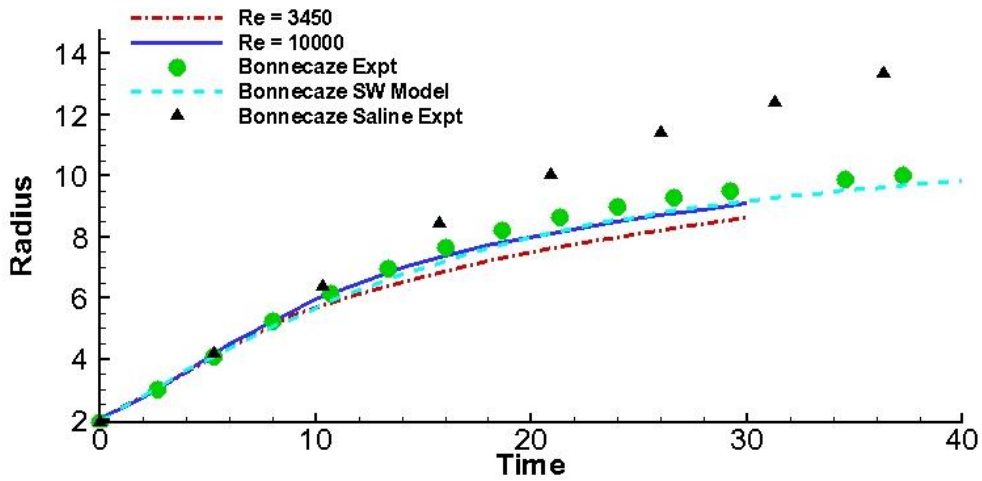


Figure 4-6. Time evolution of the front as a function of time. The solid and dash-dotted lines are from the present simulation. The circular and triangular symbols are from Bonnecaze *et al.* (1995) experiments for particle-laden currents with  $37 \mu\text{m}$ -diameter silicon carbide particles with an initial reduced gravity of  $g'_0 = 11 \text{ cm s}^{-2}$ , and a saline current with  $g'_0 = 42 \text{ cm s}^{-2}$ , respectively. The dashed line is from a Shallow Water equations based theoretical model from Bonnecaze *et al.* (1995).

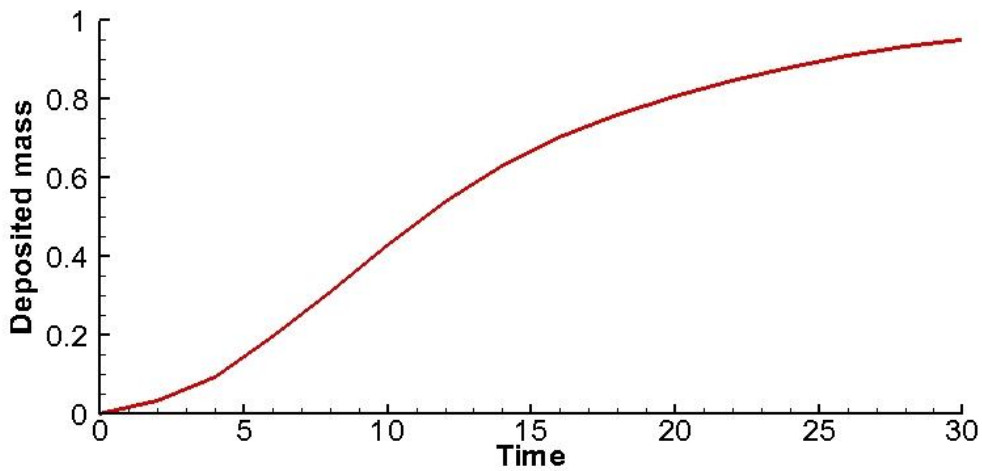


Figure 4-7. Total mass of settled particles as a function of time for  $Re = 10000$ . Results are normalized with the initial mass of suspended particles.

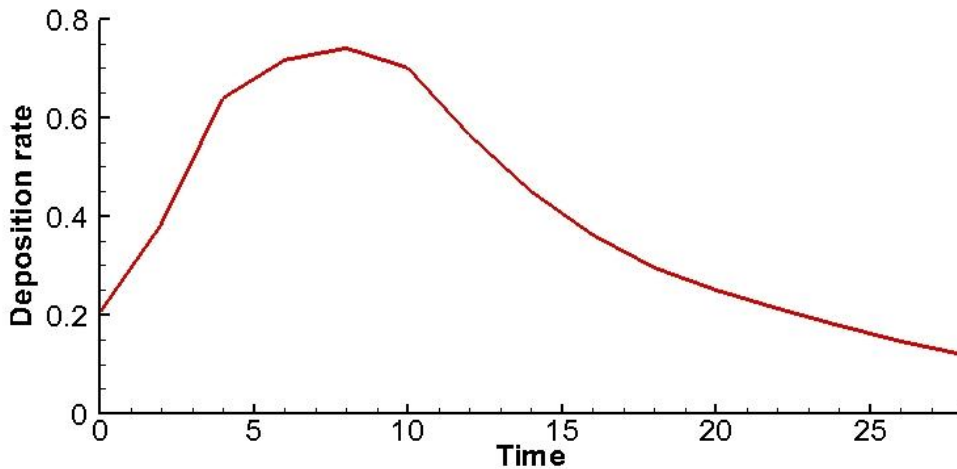


Figure 4-8. Deposition rate versus time at the bottom wall of the domain for  $Re = 10000$ . The sedimentation rate increases from the time of release, attains a maximum value around  $t = 8$  then monotonically diminishes up to the end of the simulation.

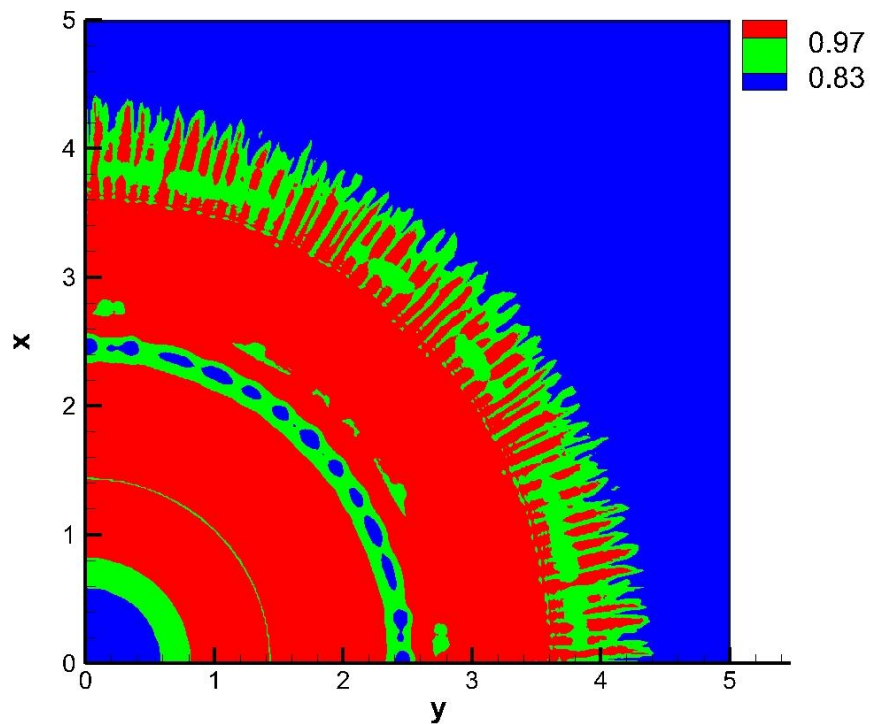


Figure 4-9. Contours of concentration at the bottom wall for  $Re = 10000$  in one quadrant of the computational domain at  $t = 6$ . The large scale vortex tubes transport low concentration fluid (particle-laden fluid mixed with the ambient) from the top of the current towards the bottom wall resulting in a local minimum around  $r = 2.5$ .

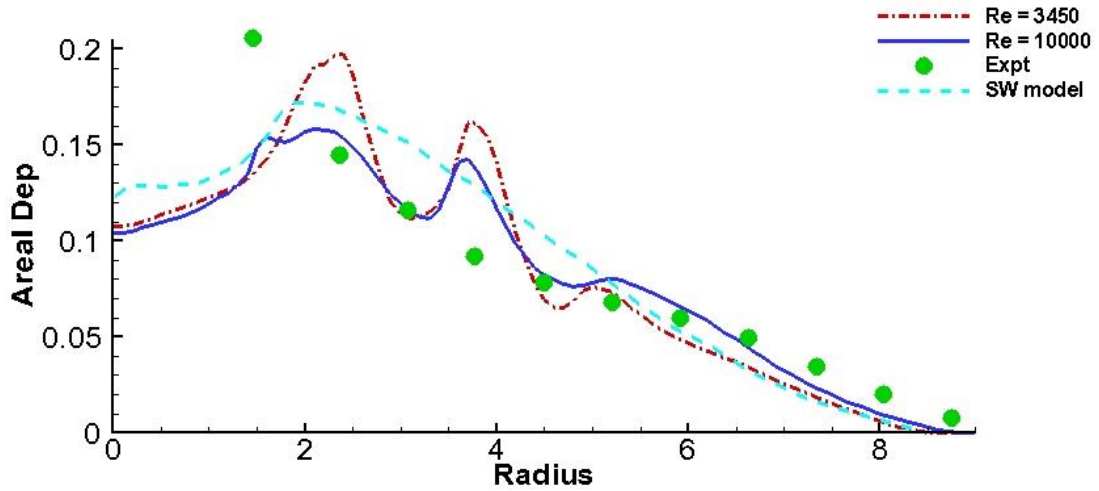


Figure 4-10. Final areal density of deposit from simulation, experiment, and theoretical model. The experiments and theoretical model results are extracted from Bonnecaze *et al.* (1995).

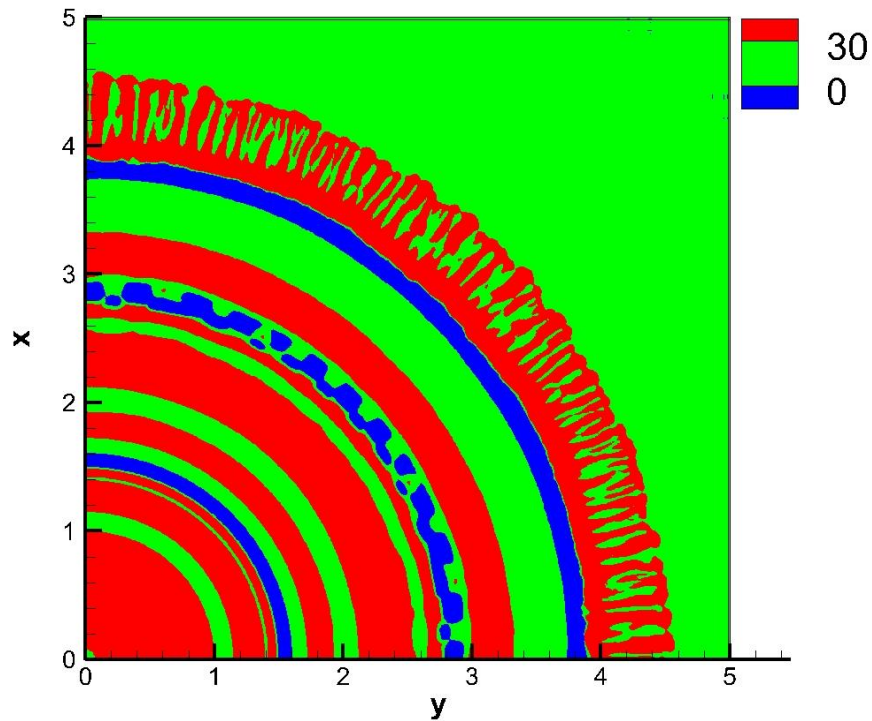


Figure 4-11. Contours of radial bottom shear stress for  $Re = 10000$  in one quadrant of the computational domain at  $t = 6$ . The wall shear stress is strongly affected by the clockwise-rotating bottom vortex tubes shown in Figure 4-4.

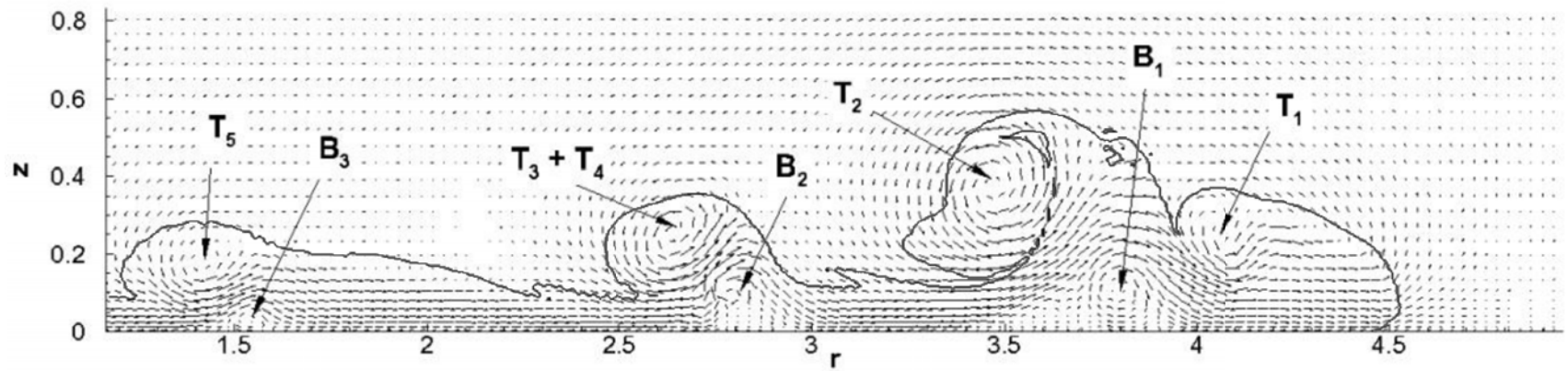


Figure 4-12. Velocity field in a plane passing through the center of the domain at  $t = 6$  for  $Re = 10000$  case. The current layout is visualized by a density contour of  $\rho = 0.05$ . The top (resp. bottom) vortices rotate with a counter-clockwise (resp. clockwise) direction.

## CHAPTER 5 DYNAMICS OF NON-CIRCULAR FINITE RELEASE GRAVITY CURRENTS

### 5.1 Background

Gravity or density currents are horizontal flows generated from a difference in density between two fluids. They encompass a wide variety of environmental and industrial flows that are often catastrophic in nature. Some of the many examples include avalanches (Allen 1982), oil spills (Kubat *et al.* 1998), turbidity currents (Lowe 1982), sand storms (Bagnold 1941), and pyroclastic eruptions (Francis 1993). The density difference can be a result of variations of temperature (a cold breeze of air intruding into a hot ambient), salinity (fresh water from a river draining into the salty dense ocean), or inhomogeneous distribution of particles in suspension (a turbid mixture of fluid-particles advancing into a clear ambient). Depending on the density ratio of the two fluids, gravity currents are categorized as heavy bottom flowing currents, when the intruding fluid is denser than its ambient, and light top flowing currents, when the intruding fluid is lighter than its surrounding ambient. Furthermore, gravity currents can be simplified as Boussinesq (heavy or light) currents when the density difference is much smaller than the current and the ambient densities.

Gravity currents, when propagating horizontally into their ambient, usually undergo four main stages (Huppert & Simpson 1980). Initially when the current is released, it accelerates from rest until it reaches a maximum velocity. During this highly transitional phase, termed the acceleration phase, the current undergoes rapid change in its velocity (zero to maximum) and the structure of the release also changes from mostly vertical to horizontal. This phase is often overlooked for three main reasons: (1) it is complex and transitional in nature, (2) it is relatively short lived in duration, and (3) it

is presumed to have little effect on the long term dynamics of the current. Following the acceleration phase, the current reaches a steady-state phase referred to as the slumping phase. During this phase, a planar (cylindrical) current advances with a constant (nearly constant) velocity and height (Gladstone 1998). At the end of the slumping phase, the current typically transitions to the inertial self-similar phase where the buoyancy driving force is balanced by the current's inertia. During this phase, the current starts to decelerate as a consequence of its diminishing front height. Finally, as the current's thickness continues to decrease, viscous and/or capillary forces become dominant, and the current evolves into the self-similar viscous/capillary phase.

Fixed volume releases have been extensively investigated over the last several decades (see e.g. Simpson 1982) generally through one of two canonical configurations, namely planar (Britter & Simpson 1978; Rottman & Simpson 1983) or axisymmetric (Didden & Maxworthy 1982, Huq 1996) geometry. In the planar release case, a flat rectangular gate initially separates a rectangular reservoir of fluid from an ambient of different, usually smaller density. Similarly, at the start of the axisymmetric three-dimensional release, the release is confined inside a hollow circular cylinder at the centre of a large tank containing the ambient fluid (Huppert 1982, Cantero *et al.* 2007b), or in an expanding reservoir of relatively small angle of expansion, typically 10-15° (Huppert & Simpson 1980).

By considering an idealized inviscid current and neglecting mixing at the interface, Benjamin (1968) derived his well-known Froude number expression  $u_N = Fr\sqrt{g'h_N}$  relating the front velocity  $u_N$  of a slumping steady-state gravity current to the front height  $h_N$  ( $g'$  is the reduced gravity). He showed that the Froude number  $Fr$  is

solely dependent on the relative depth of the “head” of the current with respect to the ambient. His idealized energy balance analysis restricted the maximum attainable front height in a confined geometry to half the total depth of the ambient fluid. However, as Benjamin recognized, the turbulent nature of gravity currents coupled with mixing along the interface of the current, necessitates the use of semi-empirical analysis to more accurately quantify the evolution of such complex flows.

Huppert & Simpson (1980) later conducted a large number of planar and axisymmetric fixed volume experiments to examine the slumping phase of gravity currents. They varied several parameters including the initial depth ratio (ratio of the height of the current to that of the ambient), the vertical aspect ratio (initial ratio of the height to the length or radius of the current), the initial volume of release, and the density ratio. They proposed that during the slumping phase, a planar (resp. axisymmetric) current’s evolution could be modeled as a series of two-dimensional rectangles (resp. concentric circular disks) with negligible entrainment (this is the basis for the box model analysis discussed later in the paper). The experiments further confirmed that the slumping motion of the current is controlled by the head and the authors proposed a correlation for the Froude number expression from their experimental data. Their semi-empirical Froude number expression, again, solely depends on the fractional depth of the current (Eq. 5-15).

Studies of gravity currents beyond the classical planar or axisymmetric framework have been rare to our knowledge, despite the fact that the majority of gravity currents in real situations originate from an arbitrary, usually non-axisymmetric

configuration. The underlying assumption is that the initial details of the release are soon forgotten after the release.

Recently, Zgheib *et al.* (2014) explored the slumping phase (short term) and inertial self-similar phase (longer term) behaviours of non-axisymmetric fixed-volume gravity currents. They demonstrated, through experiments and simulations, that gravity currents initiating from non-axisymmetric cross-sectional geometries do not become axisymmetric, nor do they retain their initial shape during the slumping and inertial phases of the current. In particular, the local speed of propagation of a material front generated by the release of a patch of arbitrary shape can vary significantly, thus leading to local “fast fronts” and “slow fronts” during all the observed phases of spreading. They explained the dynamics of non-circular gravity currents by observing that during the acceleration and early part of the slumping phases, the initial release appears to partition itself into local volumes along the front. The subsequent forward propagation of the front is dictated by these local volumes (in particular the local height of the front) along the direction locally normal to the front. Using this key observation, they developed a simple locally-dependent box model, referred to as the extended box model (EBM) that is based on a partitioning of the initial release and local front velocity, and showed that the EBM could predict with a reasonable degree of accuracy the dynamics of non-circular gravity currents, both temporally and spatially.

Following the work of Zgheib *et al.* (2014), the present paper aims at answering some remaining open questions regarding the dynamics of non-circular gravity currents. The shape of the propagating front of a planar or an axisymmetric current, by definition, remains self-similar. Furthermore, in the different regimes of propagation their speed

follows self-similar power-laws in time. In the case of a non-axisymmetric initial release, the shape of the propagating front substantially differs from the initial release and remains non-axisymmetric. A natural question that arises is, does the propagating front evolve towards a self-similar non-axisymmetric shape? If so, what is the relation between this self-similar shape of the spreading current and the shape of the initial release? The applicability of the extended box model is validated against two sets of direct numerical simulations and subsequently the extended box model is used to study the self-similar evolution of a wide range of initial releases of different aspect ratio.

Self-similar shape of the propagating front requires that the front velocity be self-similar as well. We also explore the local Froude number variation of the current along the circumference of the non-axisymmetric current and compare the simulation results with those from existing front Froude number relations. In addition, we use the results of the fully-resolved direct numerical simulations to (i) describe the local flow structure of non-axisymmetric gravity currents, and (ii) evaluate the validity of the assumptions used in the EBM.

In this work we also examine the robustness and the range of validity of the observed dependence of non-axisymmetric spreading on the shape of the initial release. Zgheib *et al.* (2014) reported the results for only Boussinesq saline currents spreading along the bottom boundary. Here we consider non-Boussinesq currents, lighter currents spreading on the top surface, particle-laden turbidity currents and demonstrate that the dependence of non-axisymmetric spreading on the shape of the initial release persists in all these cases. Only in case of low Reynolds number

( $Re \sim O(100)$ ) non-axisymmetric releases, viscous effects dominate and the current is observed to evolve to a circular shape.

This chapter is arranged as follows. The experimental and numerical setups are presented in § 5.2. The question of the self-similarity of the shape of non-axisymmetric high- $Re$  currents and the relevancy of the models of front Froude function are addressed in § 5.3. In § 5.4, we discuss the assumptions used in the extended box model and use the EBM to propose a scaling law for the prediction of the self-similar shape of non-cylindrical gravity currents. A qualitative investigation of other types of currents is presented in § 5.5. Finally, a summary and discussion of the present findings are given in § 5.6.

## **5.2 Experimental and Numerical Procedures**

### **5.2.1 Experimental Setup**

The experimental setup is shown in Figure 5-1. The experiments are carried out in a glass square tank ( $120\text{cm} \times 120\text{cm} \times 40\text{cm}$ ) at the centre of which we place a hollow cylinder of equivalent radius  $R_0$ , filled up to a height  $h_0$  with a fluid of different density than the ambient fluid of height  $H$ . Two different cross-sectional shapes are considered, namely a circular section (CS) for verification and comparison with previous results and a rounded rectangular section (RR) i.e. a rectangle where the two shorter edges are replaced by semi-circles. The initial aspect ratio  $\chi_0$  of the rounded-rectangle cylinder, here defined as the ratio of the longest to the shortest side, is  $\chi_0 = 3.8$ . Fluorescent dye is added to the fluid inside the cylinder. Black light tubes mounted on two sides of the tank illuminates the fluorescent dye inside a dark room allowing the current to be solely visible.

Unless stated otherwise, the ambient fluid is tap water of density  $\rho_a = 1000 \text{ kg/m}^3$  while the current consists of salty water of density  $\rho_c = 1100 \text{ kg/m}^3$ . The depth ratio  $h_0/H$  (initial height of the current to that of the ambient) for all the experiments was held at unity. The initial vertical aspect ratio  $\lambda = h_0/R_0$  (height/radius) was varied between 0.25 and 7. The radius  $R_0$  for the non-axisymmetric cross-sections is calculated from the surface area  $A$  via  $R_0 = \sqrt{A/\pi} \approx 4.6 \text{ cm}$ . The two geometries were chosen to have roughly the same cross sectional area, so that for a fixed initial height, the volume of release is constant whatever the initial cross-sectional shape. The tank and the cylinder are simultaneously filled. When the desired vertical aspect ratio is reached, the water in the tank is given sufficient time to reach a stagnant state. The hollow cylinder is then raised rapidly via a pulley system connected to a weight.

The front location and the current's height are measured using a mirror placed beneath the tank, which allows for a plan bottom view of the front evolution (Figure 5-2), while the side view of the current provides information about the height's evolution (Figure 5-5). The pixel resolution was about  $R_0/82$  (0.5mm) and  $h_0/44$  (2mm) for a  $\lambda = 2$ -release in the horizontal and vertical direction, respectively. The front location is obtained from the plan view images using the MATLAB® Graphics inbuilt function `Imread®`, where each pixel is assigned a value in the intensity range [0,255]. All values between 1 and 254 can be considered as different shades of grey (0 corresponding to the black color). The front is easily determined since here there is a significant jump (within a few pixels) in the intensity levels at the current-ambient interface. Note that the location of the front was found to be insensitive to the chosen cut-off value. As can be seen from the example in Figure 5-2, the location of the front is well extracted.

The local front location is then computed as follows: the local radial location of the front  $\bar{r}_N(\theta, t)$ , along the azimuthal  $\theta$ -direction is first calculated by averaging along a sector of angle  $2\alpha = \pi/36$  around the front location as

$$\bar{r}_N(\theta, t) = \frac{1}{2\alpha} \int_{\theta-\alpha}^{\theta+\alpha} r_N(\theta, t) d\theta, \quad (5-1)$$

where the  $\theta$ -coordinate's origin is taken along the  $x$ -direction and  $r_N(\theta, t)$  is the radial distance at time  $t$  between the centre of mass of the current and a point at the front of the current. We further use the symmetry of the flow, when applicable, by taking the average value of  $\bar{r}_N(\theta, t)$  along the symmetry directions. For instance, the “fast” front position in Figure 5-3 is computed as  $\bar{r}_F(t) = [\bar{r}_N(\theta = 0, t) + \bar{r}_N(\theta = \pi, t)]/2$  and similarly for the “slow” front position i.e.  $\bar{r}_S(t) = [\bar{r}_N(\theta = \pi/2, t) + \bar{r}_N(\theta = 3\pi/2, t)]/2$ .

### 5.2.2 Preliminary Verifications

As a preliminary verification we performed two sets of experiments, in order to check that the outer vertical walls of the tank did not affect the dynamics of the non-circular gravity currents. In the first set of experiments, we consider three rounded-rectangular releases under nominally identical conditions except that the initial orientation of the RR-cylinder relative to the tank walls is varied, in particular the angle between the initial longest side of the RR-cylinder and the tank wall is 0, 45 and 90° in the experiments denoted as Exp 5-2, 5-3 and 5-4 in Table 5-1, respectively. The temporal evolution of the slow and fast fronts is displayed in Figure 5-3. The dynamics of the fronts is observed to be similar in all cases. The slight difference between the three realizations is indicative of experimental measurement uncertainty, which is much smaller than the observed difference between the fast and slow fronts.

The second set of experiments consists of placing two vertical panels, each at an opposite end of the tank and having the same width and height as the tank at a distance of 10 cm (that is roughly  $2R_0$ ) from the tank walls normal to the  $x$ -axis. In that case, the size of the tank is shorter in one direction by about  $4R_0$ . We repeated the previous experiments of rounded-rectangular releases in this smaller tank and compared the temporal evolution of the front position and velocity. It was found that the dynamics of the current was not affected by the presence of the wall as long as the current's front was at a distance larger than  $2R_0$  from the lateral walls (not shown). The above tests allow us to conclude that the dynamics of the non-circular gravity currents shown in the present experiments is not influenced by the presence, shape or orientation of the walls of the tank.

As a final verification, we use simple estimates to show that both the slumping and the inertial self-similar regimes of propagation are covered in the present experiments and simulations. By matching the (nearly) constant velocity during the slumping phase with the inertial phase scaling of a circular current, the transition time from the slumping to the inertial phase can be estimated as (Cantero *et al.* 2007a)

$$t_{SI} = \left( \frac{\pi^{1/4}}{2} \xi_0 \right)^2 \frac{r_0 h_0^{1/2}}{F_{c,sl}^2}. \quad (5-2)$$

Hoult (1972) and Huppert & Simpson (1980) have proposed the following values of  $\xi_0 = 1.3$  and  $\xi_0 = 1.16$ , respectively. The constant  $F_{c,sl} \approx 0.3$  represents the mean front velocity during the slumping phase. For our axisymmetric release (Exp 5-1 and Sim 5-2), the transition time computed from (5-2) is  $t_{SI} \approx 4.2$  (resp. 3.3), for  $\xi_0 = 1.3$  (resp. 1.16).

These values are well below the characteristic duration of the experiments and simulations which is 14, approximately. As confirmed later, the gravity currents presented here undergo the acceleration phase, the slumping phase and eventually the inertial self-similar phase.

### 5.2.3 Numerical Procedure

In this paper, all the variables are dimensionless, choosing  $h_0$  as length scale,  $U = \sqrt{g'h_0}$  as velocity scale,  $h_0/U$  as time scale and  $\rho_a$  as density scale ( $g'$  is the reduced gravity defined as  $g' = g(\rho_c - \rho_a)/\rho_a$ ). We define  $x$  ( $y$ ) as the direction of the major (minor) axis when applicable, and  $z$  as the direction parallel to gravity.

The physical configuration of the simulations is identical to the experimental setup. We solve the concentration equation along with the incompressible Navier-Stokes equations. The system reads in dimensionless form

$$\nabla \cdot \mathbf{u} = 0, \quad (5-3)$$

$$\frac{D\mathbf{u}}{dt} = \rho \mathbf{e}^g - \nabla p + \frac{1}{Re} \nabla^2 \mathbf{u}, \quad (5-4)$$

$$\frac{\partial \rho}{\partial t} + \nabla \cdot (\rho \mathbf{u}) = \frac{1}{Sc Re} \nabla^2 \rho, \quad (5-5)$$

where  $\mathbf{u}$ ,  $p$ , and  $\rho$  are the local velocity, total pressure and density in the flow, respectively and  $\mathbf{e}^g$  is a unit vector pointing in the direction of gravity. Two dimensionless parameters have been introduced in (5-4) and (5-5) namely the Reynolds number and the Schmidt number defined as

$$Re = Uh_0/\nu, \quad Sc = \nu/\kappa. \quad (5-6)$$

Here  $\kappa$  is the molecular diffusivity and  $\nu$  is the kinematic viscosity of the fluid. Equations (5-3)-(5-5) are solved inside a rectangular box of size  $15 \times 15 \times 1$  with a spectral code

(Cantero *et al.* 2007a,b). Note that the experimental tank size was approximately  $12 \times 12$  in the  $x$ - $y$  plane for  $\lambda = 2$ . No-slip and free-slip boundary conditions are imposed for the velocity at the bottom and top walls, respectively, while periodic boundary conditions are imposed at the sidewalls. Zero normal gradient are imposed for the concentration at the bottom and top walls. Fourier expansions are used along the two horizontal periodic directions, and a Chebyshev expansion with Gauss-Lobatto quadrature points (Canuto *et al.* 1988) is used along the vertical non-periodic direction. The reader is referred to Cortese & Balachandar (1995) and Cantero *et al.* (2007b) for a detailed description of the numerical approach and for results obtained with the same code in axisymmetric configurations, respectively.

In the present work, we simulate the collapse of a non-axisymmetric patch of heavy fluid at  $Re = 8950$  with a grid resolution of  $880 \times 880 \times 179$  corresponding to 140 million degrees of freedom, approximately. The numerical resolution was selected to have between 4 and 6 decades of decay in the energy spectrum for all the variables and the time step was selected to produce a Courant number smaller than 0.5. In the simulations, the Schmidt number is set to unity. Note that this value is smaller than that of saline gravity current for which  $Sc \approx 700$ , but it has been shown that the dynamics of gravity currents is independent of the Schmidt number as long as the Reynolds number is large, which is the case here (Bonometti & Balachandar 2008).

### **5.3 High-Reynolds Number Boussinesq Density Currents**

In this section, we present results from experiments and fully-resolved simulations of density currents of non-axisymmetric initial shape, the parameters of

which being summarized in Table 5-1. In particular, a detailed description of the local flow structure in this type of flow as compared to a cylindrical release is given.

### **5.3.1 Self-Similarity of the Front Contour of Non-Circular / Non-Planar Gravity Currents**

The temporal evolution of the spreading of gravity currents with two different initial cross-sectional shapes is presented in Figures 5-4(a & b). The figure shows a plan-view of a composite image of the front evolution for each experiment at various instances in time. The cylindrical release is shown for comparison in frame (a). While the case of the circular release shows small undulations at the front due to the lobe and cleft instability (Simpson 1972, Härtel *et al.* 2000), the current retains its overall symmetry as it propagates outward. Conversely for the RR-current, as shown in Zgheib *et al.* (2014), the long-time circumferential shape is approximately an ellipse, but with switched major and minor axes as compared to the initial shape. Lobes and clefts are observed at the front even in this non-axisymmetric release. Note that the characteristic size of these lobes and clefts are an order of magnitude smaller than the length scale of the larger scale flow pattern.

It is noteworthy that the phrase “switching of the major and minor axes” is one that has been consistently used to describe the evolution of elliptic free jets (Quinn 1989; Gutmark & Grinstein 1999). As an elliptic jet propagates downstream, its shear layer along the minor axis plane grows at a faster rate compared to the shear layer along the major axis plane. This unequal growth rate results in a crossover point at a downstream location from the nozzle, where the jet temporarily attains a circular-like cross-section before its major and minor axis switch. Throughout this study, we will employ “switching of axes” for the RR case to denote that due to a relatively faster

propagation of the front along the minor axis ( $y$ -axis) compared to a relatively slower spreading along its major axis ( $x$ -axis) as shown in Figure 5-4, the major and minor axes will eventually switch making the initial minor axis of the RR geometry the major axis of the current at later stages of spreading.

In the case of planar and axisymmetric releases, it has been shown that provided the Reynolds number is large enough, the current enters a self-similar inertial regime in which the evolution of the front position scales as  $t^{2/3}$  and  $t^{1/2}$ , respectively (Hoult 1972; Huppert & Simpson 1980; Ungarish 2009). The corresponding front velocities in the inertial regime scale as  $t^{-1/3}$  and  $t^{-1/2}$  for the planar and the axisymmetric currents, respectively. Regarding non-axisymmetric releases, Zgheib *et al.* (2014) plotted in their Figure 5-4b the time evolution of the velocity of the fast and slow fronts of an initially rounded-rectangular release and observed that at the later times, it roughly follows  $t^{-1/2}$ . Here we verify that the self-similar behaviour is valid for the entire propagating front. Self-similar evolution of an axisymmetric current can be expressed as (provided the front remains convex in shape)

$$r_N(\theta, t) = R_N(t) f(\theta), \quad (5-7)$$

where  $f(\theta)$  is the self-similar shape of the front. It follows that the self-similar front velocity

$$u_N(\theta, t) = \frac{dR_N}{dt} f(\theta) = U_N(t) f(\theta), \quad (5-8)$$

and provided a constant Froude number applies (as will be the case for a current spreading in a deep ambient), the self-similar front height around the circumference of the current can be expressed as

$$h_N(\theta, t) = H_N(t) f(\theta) . \quad (5-9)$$

Furthermore, in the inertial and viscous self-similar regimes, the front velocity has been shown to follow a power law behaviour of the form (Fay 1969, Fannelop & Waldman 1971; Hoult 1972, Huppert & Simpson 1980, Rottman & Simpson 1983, Cantero et al, 2007)

$$U_N(t) \propto t^\alpha \quad (5-10)$$

where the power-law exponent takes the value  $-1/2$  in the inertial regime of axisymmetric spreading and  $-4/5$  or  $-7/8$  in the viscous regime. The corresponding power-law evolutions of the mean radius and height are given by

$$R_N(t) \propto t^{1+\alpha} \quad \text{and} \quad H_N(t) \propto t^{2\alpha} . \quad (5-11)$$

Based on an estimate of inertial-to viscous transition time (Cantero *et al.* 2007) we expect the dominant spreading of the rounded rectangle shown in Figure 4b to be in the inertial regime. To test whether the non-axisymmetric spreading of the RR release is indeed self-similar and predominantly in the inertial regime, in Figure 4c we replot the contours of the front in the scaled coordinates  $\eta = x t^{-1/2}$  and  $\zeta = y t^{-1/2}$ . It can be observed that the rounded-rectangle reaches a self-similar shape resembling an ellipse, with its major and minor axis different from those of the initial release.

In section 5.2.1, we defined the initial aspect ratio  $\chi_0$  of the release as the ratio of the longest side to the shortest side of the initial cross-section. Similarly, we define the self-similar aspect ratio  $\chi_\infty$  as the ratio of the longest to the shortest sides. In the present case of the rounded-rectangular release displayed in Figure 5-4c, we have  $\chi_0 = 3.8$  and  $\chi_\infty \approx 1.39$ , respectively. Note that in Figure 5-4c we have varied the value  $\alpha$  in the range  $-2/3 \leq \alpha \leq -1/2$  and verified that the value  $\alpha = -1/2$  gives the best

collapse in terms of self-similar shape<sup>3</sup>. Overall, Figure 5-4 confirms that initially non-circular gravity currents eventually reach a self-similar shape (in the inertial regime) which is non-axisymmetric. We shall see later that the present finding is supported by both direct numerical simulations and results from the extended box model.

### 5.3.2 Local Front Froude Number of Non-Circular / Non-Planar Gravity Currents

Table 5-1 presents the velocity and height ratios for various releases. The local fast and slow front velocities  $u_F$  and  $u_S$  are computed from  $\bar{r}_F(t)$  and  $\bar{r}_S(t)$  by differentiating in time. The maximum velocity ratio between the fastest front and the slowest front is in the range 2.2-2.6 in the RR-cases. This indicates that the local instantaneous fast front can be up to 2 to 3 times faster than the slowest portion of the front. This strong variation of local front velocity is confirmed by the measured mean velocity ratio which is about 1.9 to 2 for the RR-current. The mean velocity ratio in Table 5-1 is computed as follows

$$\overline{u_F/u_S} = \frac{1}{t_{max}} \int_{t=0}^{t_{max}} (u_F/u_S) dt \quad (5-12)$$

where, as indicated in Table 5-1,  $t_{max} = 12.6$  (resp. 6.5) for  $\lambda = 2$  (resp.  $\lambda = 4$ ).

We present in Figure 5-5a side view of the evolution of the current for the RR- and CS-cases. For the circular release, the height is observed to be roughly uniform at all stages of propagation. The RR-current shows clear variations in the current's thickness, in particular between the central region (corresponding to a spreading along the minor  $y$ -axis) and the edges (corresponding to a spreading along the major  $x$ -axis).

---

<sup>3</sup> This was also confirmed by a best fit for the slope in the log-log plots of time versus local fast and slow front positions. This analysis was done both for the experimental data and for the simulation results to be discussed below.

For instance, at  $t \geq 2.6$ , the current is already thicker at the midplane than at the edges (note that the height is almost uniform for the CS-current at the same dimensionless time). At  $t = 5.2$ , the height at the midplane is 3 to 4 times larger than at the edge. The height contrast along the front circumference decreases with time, as the absolute height is decreasing. The height ratio, however, is still larger than unity (about 2) at time  $t = 13$  as the current has crossed a distance of  $10R_0$ , approximately. Moreover, as can be seen from the  $x$ - $y$  plan-view images (Figure 5-2), the maximum height of the current is located close to the front, in the “head” of the gravity current. Therefore, it is reasonable to consider that the observed thickness in Figure 5-5 (especially along the minor axis) corresponds to the front height of the current as opposed to that of the interior body of the current which is significantly smaller, and hence hidden in the snapshots of Figure 5-5. The same RR-configuration was simulated, and in Figure 5-6a we present the current’s height evolution via iso-surfaces of density. In Figure 5-6b, we display the corresponding contours of the current height. Similar to the experimental findings, the heavy fluid is observed to aggregate along its periphery with a clear distinction in thickness of about a factor of two between the minor and major axes. It is in fact this height inhomogeneity which leads to local velocity variations.

The present simulation results enable us to compare the value of the local Froude number along the front and specifically at the slow and fast sections of the fronts. One may assess the relevancy of the various Froude functions reported in the literature with respect to the propagation of non-circular gravity currents. The simulations give access to local instantaneous front height  $h_N$  and velocity  $u_N$  information, and hence allow us to compute the Froude number as  $Fr = u_N / \sqrt{h_N}$ . In

order to evaluate the height  $h_N$  for the slow and fast fronts, first the local height of the current  $h$ , is defined as,

$$h(x, y) = \int_0^H \rho dz . \quad (5-13)$$

This local current height is then averaged over a wedge of  $5^\circ$  aligned along the  $x$  (slow front) and  $y$  (fast front) axes. The averaging being performed over a distance extending between the front of the current and the location of the maximum height in the head.

The instantaneous local Froude number  $Fr = u_N/\sqrt{h_N}$  of the slow and fast sections of the front of an initially rounded-rectangular release is plotted in Figure 5-7. The fast front- $Fr$  fluctuates in the range 0.9 to 1.1 for  $2 \leq t \leq 10$  and monotonically decreases to about 0.7 at later times (in the self-similar inertial regime). On the contrary, the slow front- $Fr$  is significantly lower at early times ( in the range 0.6 to 0.8 for  $2 \leq t \leq 10$ ) but seems to catch up with the fast front at later time times, i.e.  $Fr \approx 0.7$  for  $t > 10$ . The larger value of the fast front- $Fr$  as compared to that of the slow front during the early stage of spreading suggests that the increase in front velocity due to the mass redistribution inside the current is larger than the increase of height. Conversely, at late times (here  $t > 10$ ) the evolution of the front velocity and height is similar for both the fast and slow fronts as the value of the local Froude number is roughly similar. This is in line with the fact that the current has entered the self-similar inertial phase.

Numerical simulations can also be used to evaluate the other models of Froude functions. These models generally depend on the ratio  $a = h_N/H$  of the nose height of the current to that of the ambient. We consider in the following three models of Froude functions, namely the Benjamin (1968)'s front condition

$$Fr^B(a) = \sqrt{\frac{a(1-a)(2-a)}{(1+a)}}, \quad (5-14)$$

which is valid for  $a \leq 1/2$ , the Huppert & Simpson (1980)'s relation

$$Fr^{HS}(a) = \min(0.5a^{-1/3}, 1.19), \quad (5-15)$$

and the circulation based model of Borden & Meiburg (2013) which reads

$$Fr^{BM}(a) = \sqrt{2a}(1-a). \quad (5-16)$$

Benjamin's and BM's model give almost identical results and consistently under-predict the local Froude number by about 50%. Alternatively, the Huppert & Simpson's correlation is in reasonable agreement with the simulated fast front-Froude number, but over-estimates the slow front-Froude number by about 30% for the whole duration of spreading.

## 5.4 Extended Box Model Simulations

Zgheib *et al.* (2014) proposed an extension of the box model, initially developed by Huppert & Simpson (1980), capable of capturing the dynamics of non-axisymmetric gravity currents. Here we use this extended box model (EBM) to investigate the long-time inertial self-similar dynamics of non-axisymmetric currents.

### 5.4.1 Equations and Assumptions

The classical box model generally used for predicting the evolution of gravity currents (Huppert & Simpson 1980; Dade & Huppert 1995) has been shown to admirably reproduce the dynamics of axisymmetric and planar releases (see e.g. Ungarish & Zemach 2005). In the case of finite releases, the box model assumes the fluids to be immiscible with negligible entrainment with the ambient so that the mass

and volume of the current are conserved throughout the duration of spreading. Additionally, the height is taken to be uniform along the body of the current and the current is advanced outward normal to the front with a velocity proportional to the square root of the height. According to this model, the height intrinsically remains uniform along the circumference of the patch, so the speed of propagation is uniform along the current's front during all phases of spreading. Therefore, using the classical box model, an initially non-axisymmetric current inevitably becomes axisymmetric.

The extended box model proposed by Zgheib *et al.* (2014) is based on the partitioning of the initial release using inward directions normal to the front. An example of such partitioning is given in Figure 5-8b. Here, each segment of the front is now associated with a sub-volume of initial release. Once the various sub-volumes are obtained, the same procedure as in the classical box model is applied locally for each sub-volume, where the front is advanced outward normal to itself. More particularly in the EBM, the current is defined by the front position  $\{x_N(s, t), y_N(s, t)\}$ , height  $h_N(s, t)$ , the outward normal front velocity  $u_N(s, t)$  where  $s$  is the distance measured along the circumference of the front. An additional variable, namely the area per arc length  $\sigma(s, t)$  is also used in the model (Figure 5-8a). An integration of  $\sigma(s, t)$  over the entire arc length of the advancing front yield the total area covered by the planform of the advancing current. The EBM can be summarized by the following set of coupled equations (Zgheib *et al.* 2014),

$$u_N = Fr\sqrt{h_N} \quad ; \quad Fr = \min(0.5h_N^{-1/3}, 1.19) \quad (5-17)$$

$$\left\{ \frac{\partial x_N}{\partial t}, \frac{\partial y_N}{\partial t} \right\} = u_N \frac{\{ \partial y_N / \partial s, -\partial x_N / \partial s \}}{\sqrt{(\partial x_N / \partial s)^2 + (\partial y_N / \partial s)^2}}, \quad (5-18a)$$

$$\frac{\partial \sigma}{\partial t} = u_N, \quad (5-18b)$$

$$\frac{\partial \sigma h_N}{\partial t} = 0, \quad (5-19)$$

where  $Fr$  is the Froude number, which is here calculated from the Huppert & Simpson (1980)'s empirical relation<sup>4</sup>. All variables are dimensionless. Equations (5-17), (5-18) and (5-19) refer to the Froude front condition, kinematic relations and mass conservation, respectively. In Eq (5-18a), the current is restricted to normal outward spreading with velocity  $u_N$ . It will be shown below that this is a good approximation despite the non-uniform height distribution along the front, which might induce a tangential velocity component. The increase in the current's surface area is captured in (5-18b). This step is inexistent in the classical box model as the area increase can be directly inferred from the radius of the current.

Analytical solutions of (5-17)-(5-19) are not feasible in the case of arbitrary initial patches however, the system may be solved numerically. Details about the numerical procedure used for solving (5-17)-(5-19) and verification of spatial and temporal convergence are given in the Appendix.

#### 5.4.2 Examination of the Extended Box Model

The EBM involves various approximations which can be summarized as follows. (H1) The volume of initial release is partitioned with the help of inward propagating (normal to the front) geometric rays, and accordingly different sub-volumes are assigned to the different portions of the front. (H2) As the current propagates, the height

---

<sup>4</sup> Note that any other model of Froude number function could be used without loss of generality, provided this function is applicable for the whole range of height ratio of nose to ambient  $h_N/H$  considered here.

of the current is not taken to be a constant over the entire release. It varies along the front depending on the local speed of propagation. (H3) The velocity of propagation is taken to be normal to the front. Since there is variation in the height of the current along the front, it can be expected that there is some cross-flow (tangential velocity) induced by this variation in the current height. However, since the pressure gradient normal to the front is expected to far exceed the tangential gradient at the front, the current velocity is likely to be predominantly normal to the front. (H4) Finally we assume that even in the present case of non-axisymmetric propagation, the Huppert-Simpson front relation can be used to express the front velocity in terms of local front height. Here we examine these assumptions relative to the results of fully-resolved simulations.

Let us first examine the direction of fluid velocity at the front of the current. To focus on the velocity of the outward propagating current and eliminate the contribution from the inward propagating ambient, we define the depth-averaged velocity of the current as follows

$$\bar{u} = \frac{\int_0^H \rho u dz}{\int_0^H \rho dz} \quad ; \quad \bar{v} = \frac{\int_0^H \rho v dz}{\int_0^H \rho dz}. \quad (5-20)$$

Recall that  $\rho = 1$  in the current and  $\rho = 0$  in the ambient. From (5-20), one can extract the velocity along the front and compute the normal-to-the-front and tangential components of the front velocity  $u_n$  and  $u_\theta$  as plotted in Figure 5-9. The simulation results indicate that the normal velocity is an order of magnitude larger than the tangential component of velocity over the entire front of the current. Furthermore, the faster propagation of the current along the  $y$ -axis ( $\theta = \pi/2$ ) is clear. Integrating over the entire front, we find the average normal-to-the-front and tangential front velocities to be

about 0.37 (0.19) and 0.03 (0.03) at  $t = 1.5$  (7) respectively. Interestingly, the tangential velocity is mostly positive at  $t = 1.5$  (when the height is nearly uniform) indicating a slight cross-flow towards the fast front, while  $u_\theta$  is mostly negative at  $t = 7$  (when the height is much larger at the fast front), in line with the expectation that there may be some cross-flow induced by the hydrostatic pressure gradient stemming from the variation in the current height. Overall, this corroborates approximation H3. Secondly, approximation H2 can be readily verified thanks to Figure 5a and 6b which shows that the height of the current is not homogeneous along the front during spreading.

We also present in Figure 5-9 the normal-to-the-front velocity estimated by Huppert & Simpson (1980)'s front Froude number relation using both the head of the current's mean height and the maximum height taken from the simulation. At the early time  $t = 1.5$ , reasonable agreement is observed between the simulation results and the prediction however at  $t = 7$ , the Huppert & Simpson prediction is significantly larger by 45% than the simulation results. It is noteworthy that even though the simulated front velocity in the present case is consistently lower than the Huppert and Simpson prediction, the extended box model with Huppert and Simpson front velocity is capable of predicting the front motion reasonably well (Zgheib *et al.* 2014). This is not a contradiction: in the box model, the height of the current is under-predicted since the current is taken to be of uniform height. This under-prediction of the front height somewhat compensates the presently observed overestimation of the front velocity given by the Huppert and Simpson Froude number relation.

Two snapshots of the height distribution of the rounded-rectangular release are presented in Figure 5-9b together with streamlines (evaluated from the vertically-

averaged velocity defined in (5-20)). At early times, the streamlines resemble the inward propagating geometric rays shown in Figure 5-8b. At later times, the streamlines are preferentially normal to the front. This is consistent with the earlier observation that the velocity of the current is dominantly oriented along the normal direction. This also provides some support for approximation H1 that the initial partitioning of the release volume is dictated by the inward propagating normal to the front (geometric rays).

### 5.4.3 A Scaling Law for the Final Shape of Non-Circular Gravity Currents

In this section we use the extended box model to analyze the characteristic, self-similar development of a non-axisymmetric gravity current. As shown earlier by experiments, an initially non-circular gravity current eventually reaches an inertial self-similar shape which is non-axisymmetric. Figure 5-10a presents the evolution of the front obtained from an EBM simulation for an initially elliptical release. Here, the initial major and minor axes of the ellipse are approximately 0.90 and 0.24, respectively. These dimensions correspond to an initial horizontal aspect ratio of  $\chi_0 \approx 3.8$  and a vertical aspect ratio of  $\lambda \approx 2$ . We show 11 contours of the front in the  $(\eta = xt^{-1/2}, \zeta = yt^{-1/2})$ -plane from an initial time of  $t = 100$  to a final time of  $t = 200$  with a time increment of  $\Delta t = 10$ . Clearly, the current has reached a self-similar shape.

We performed some simulation campaigns with the EBM where the initial horizontal aspect  $\chi_0$  of a non-circular gravity currents was varied in the range  $1 \leq \chi_0 \leq 20$ . For each  $\chi_0$ -case, the self-similar aspect ratio  $\chi_\infty$  was measured. To be more explicit, we take the value of  $\chi_\infty$  at a sufficiently large time, here  $t = 200$ , so the self-similar regime was reached. Finally, simulations were performed for two initial non-circular shapes, namely elliptical and rounded-rectangular shapes. The results are

summarized in Figure 5-10b. For comparison, we also plotted the results obtained by the experiments and simulations of Table 1. All the data roughly follow a similar trend which can be modeled by the following simple scaling law,

$$\chi_\infty = 1 + \ln \chi_0^{1/3}. \quad (5-1)$$

In the case of a circular release, it can be shown that the temporal evolution of the front height  $h_N$ , radius  $r_N$  and normal-to-the-front velocity  $u_N$  in the inertial self-similar regime scale as  $t^{2\alpha}$ ,  $t^{-\alpha}$  and  $t^\alpha$  with  $\alpha = -1/2$  (see e.g. Ungarish 2009, p122). Figure 5-11 displays the azimuthal evolution of the front height, radius and normal-to-the-front velocity using the aforementioned scaling from Sim 5-1 ( $\chi_0 = 3.8$ ) and Sim 5-3 ( $\chi_0 = 8$ ). Here  $\theta$  is the angle measured counter-clockwise from the  $x$ -axis. We observe these quantities for both horizontal aspect ratios to reach a self-similar profile that resembles a sinusoidal curve with a period of  $\pi$ . For Sim 5-1 ( $\chi_0 = 3.8$ ), we plot the azimuthal dependence of radius, speed, and height from  $t = 3.15$  (red curve) to  $t = 17.15$  (blue curve) with a constant time increment of  $\Delta t = 1.75$ . The green curve at  $t = 8.4$  represents the time at which these quantities become roughly self-similar. Similarly for Sim 5-3 ( $\chi_0 = 8$ ), we plot the azimuthal evolution from  $t = 4$  (red curve) to  $t = 22$  (blue curve) with a constant time increment of  $\Delta t = 2$ . The green curve at  $t = 16$  represents the time beyond which these quantities become roughly self-similar. Beyond the self-similar phase, the height, speed, and radius are observed to attain a minimum value at  $\theta = 0, \pi$ , and  $2\pi$ , and a maximum value at  $\theta = \pi/2$  and  $3\pi/2$ . This self-similar shape is indicative of an elliptical like shape whose minor axis coincides with the  $\theta = 0$  line, which corresponds to the  $x$ -axis in the  $x$ - $y$  plane.

If we subtract the mean value from each curve at the final time  $t_f = 17.15$  for Sim 5-1 (resp.  $t_f = 22$  for Sim 5-3), then the scaled radius ( $r_N t_f^{-1/2}$ ), front speed ( $u_N t_f^{1/2}$ ), and front height ( $h_N t_f$ ) may be approximately described by a single sinusoidal function of the form

$$f(\theta) = -A \cos(2\theta + \theta_0). \quad (5-22)$$

Where  $A$  and  $\theta_0$  represent the amplitude and phase angle, respectively. The phase angle  $\theta_0$  is the angle the  $x$ -axis makes with the major axis of the rounded rectangle. In the present case,  $\theta_0 = 0$  since we choose the  $x$ -axis to coincide with the major axis of the RR. The amplitude  $A$  is obtained from the average RMS value of the three curves (radius, speed, and height), from which the mean value is subtracted. The amplitude is  $A \approx 0.22$  for Sim 1 and  $A \approx 0.32$  for Sim 3.

In Figure 5-12, we plot the azimuthal evolution at the end of each simulation for the scaled front ( $r_N t_f^{-1/2}$ ), speed ( $u_N t_f^{1/2}$ ), and height ( $h_N t_f$ ), for which the mean value of each curve has been subtracted. We plot the results from Sim 5-1 and Sim 5-3 and observe good agreement between the three curves and the sinusoidal function  $f(\theta)$  defined in Eq. (5-22). It follows that if you know the self-similar shape of the front, then you could roughly predict the front height (or front speed) of the current provided you have access to the front height (or front speed) at some azimuthal orientation.

## 5.5 Discussion

In this section, we present quantitative and qualitative results from additional experiments and simulations in which one parameter at a time was varied so that one may assess the robustness of the non-axisymmetric spreading of non-circular releases to a larger class of non-axisymmetric releases of material.

### 5.5.1 Varying Current-to-Ambient Density Ratio

We investigate in Figure 5-13a the case of a dam-break (water in air) flow of a heavy current of density ratio  $\rho_c/\rho_a = 10^3$ . At  $t = 74$  the initial major axis ( $x$ -coordinate) still remains the major axis of the spreading current, but by  $t = 147$  and later, the current spreads faster along the  $y$ -direction. This flipping of axes is similar to what has been observed by Zgheib *et al.* (2014) for the Boussinesq currents. Note that the global contour of the front is not as smooth as in the Boussinesq case (Figure 5-4b). At  $t = 147$  and 220 breakage of the front into smaller chunks can be observed. This is attributed to interactions between the front of the current and the bottom glass wall. At large density ratios, wall friction can significantly affect the front speed (Bonometti *et al.* 2008). The surface of the bottom wall in terms of degree of dryness and hence local variations of wall friction may have played a role in the experiment. In addition, capillary effects are likely to be significant at late times ( $t \geq 100$ ) since the front height is only a fraction of the initial height, of the order of the capillary length  $l_c = \sqrt{\sigma_{st}/\rho_c g}$ ,  $\sigma_{st}$  being the surface tension between the current and the ambient. In such a case, the dynamics of the contact line defining the current's front, may be influenced by the wettability properties of the wall (Yarin 2006).

### 5.5.2 Turbidity Current

Figure 5-13b presents the case of a turbidity current resulting from the release of a non-axisymmetric homogeneous mixture of polyurethane particles in water spreading in fresh water ambient. The polyurethane particles have a density of  $1050 \text{ kg/m}^3$  and a diameter ranging between  $280$  and  $320 \text{ }\mu\text{m}$ . The measured effective density of the mixture is  $\rho_c = 1007 \text{ kg/m}^3$  well in the Boussinesq range. The current exhibits the same

behaviour as in the case of Boussinesq saline currents developing fast and slow moving fronts. The fast front spread on average over 2 times as fast as the slow front so that by  $t = 8.2$ , the major and minor axes have switched. Note that similar to the dam-break flow in Figure 5-13a, the global contour of the front is less smooth than in the saline Boussinesq case. Here, the irregularity may be partly attributed to the initial inhomogeneity in the particle suspension in the RR-cylinder and partly to the sedimentation effects which start occurring before the release of the turbidity current.

### **5.5.3 Effect of Wall Friction**

The evolution of a light top Boussinesq gravity current is presented in Figure 5-13c. In this case the initial fluid within the rounded-rectangle cylinder is pure water while the ambient is saline water. The lighter current here spreads at the top and there is no friction along the surface of spreading (friction with air and dissipation due to surface waves are negligible). Clearly, the evolution is similar to that of the Boussinesq heavy current spreading along the bottom wall.

### **5.5.4 Influence of the Reynolds Number**

A viscous current is presented in Figure 5-13d, that is a dam-break honey-in-air current. Here, honey has a density of  $1400 \text{ kg/m}^3$  and a viscosity of  $67 \text{ kg/m.s}$ . To ensure a relatively long-term viscous spreading, the height ratio was increased to  $\lambda = 3$ , which results in a Reynolds number of  $Re = 126$ . When viscous forces prevail, as in such a low Reynolds number configuration, the transfer of momentum inside the current occurs at a much faster rate than in the high- $Re$  cases. The present dam-break low-Reynolds number non-axisymmetric release is therefore observed to become axisymmetric after having crossed a distance of about  $1H$ . Here, the source momentum

stemming from the pressure gradient at the front is quickly transferred by diffusion along the circumference, hence leading to rapid homogenization of the front height and velocity. As a consequence, the current's evolution quickly becomes axisymmetric and the current enters the viscous phase (and eventually the capillary phase). Overall, inspecting the present results suggest that the non-axisymmetric evolution is to be expected provided the Reynolds number is large, typically  $Re \geq O(10^4)$ .

### 5.5.5 Varying the Vertical and Horizontal Aspect Ratios

The dependence on the vertical aspect ratio is examined by doubling the vertical aspect ratio while maintaining the same density ratio. We present in Figure 5-14a the same configuration for two initial vertical aspect ratios  $\lambda = 2$  and 4. The fast and slow fronts are again observed to change the orientation of the initial major and minor axes of the release. Other experiments with smaller vertical aspect ratios of 0.25 and 0.5 were also conducted, and the same preferential direction of spreading and switching of major and minor axes was always observed. We may conclude that the switching of the initial major and minor axes is not sensitive to the vertical aspect ratio, at least in the range  $0.25 \leq \lambda \leq 4$ .

In Figure 5-14b, we investigate the effect of varying the initial horizontal aspect ratio  $\chi_0$  on the front dynamics. We present results from simulations 5-1 and 5-3 for the RR geometry for two values of  $\chi_0$ , namely  $\chi_0 = 3.8$  and  $\chi_0 = 8$ . In both configurations, the width of the RR is held constant. We observe some interesting features. The travelled distance along the major axis (slow front) for both configurations are identical for the entire duration of Sim 5-1 ( $\chi_0 = 8$ ). On the other hand, along the initial minor

axis, we observe a collapse between both curves up to a time of  $t \approx 5.5$ , beyond which the fast front of Sim 5-1 begins to slow down and deviate from the fast front of Sim 5-3.

The perfect agreement between Sim 5-1 and Sim 5-3 along the initial major axis implies that the slow front is not affected by increasing the initial length of the RR as it will not have access to it. Furthermore, this allows us to stipulate that any further increase in the length of the RR will not affect the travelled distance along the major axis. This is not the case however for the fast front, increasing the length of the RR results in farther propagation along the initial minor axis. Initially the front along the minor axis does not perceive the finite nature of the release, and advances as a planar (two-dimensional) current of lock-length equivalent to half the width of the RR. The time for which this planar-like behaviour endures, depends strongly on the initial length of the RR.

### **5.5.6 Possible Influence of the Initial Curvature and the Local Instantaneous Curvature**

It is important to consider if the non-axisymmetric spreading of the current is a consequence of the local initial or instantaneous curvature at the front. To investigate the effect of *local initial curvature*, we numerically compared the evolution of the rounded-rectangular release with that of a true rectangle of same cross-sectional area and aspect ratio (Figure 5-15). Indeed, one may wonder if the larger curvature at the rounded edges may be the reason for its local slower propagation, since it is known that, for the same initial volume of release, planar currents with no curvature spread faster than axisymmetric cylindrical currents as a result of the radially diverging geometry. In Figure 5-15, however, the dynamics of the current with flat sides (true rectangle) is similar to that of the current with rounded sides. Notwithstanding the

differences in the initial local curvature between the currents, the path of the inward propagating rays is relatively similar in both cases. Initial local curvature hence appears to be not important in the process of non-axisymmetric spreading as long as the “redistribution” of material is similar. Furthermore, two other observations from Figure 5-4b suggest that the phenomenon is not a consequence of *local instantaneous curvature*. First, the curvature at the front of the current in the  $x$ -direction is alternatively larger, equal and smaller than that in the  $y$ -direction at time  $t = 0, 3.5, \text{ and } 7$ , respectively. Nevertheless, the front velocity along the  $y$ -direction is consistently larger than that along the  $x$ -direction for all time (not shown), independent of the relative magnitude of local curvature. Secondly, if the front dynamics was dominantly controlled by the local instantaneous curvature, a current that is circular should remain circular. In Figure 5-4b it can be observed that at  $t = 3.5$ , the front is nearly circular, however at later times the current continues to spread faster along the  $y$ -direction and increasingly departs from the circular shape. This suggests that the local front velocity is, to leading order, a strong function of the local height and is not strongly affected by instantaneous local curvature of the front.

### **5.5.7 Vortical Structures of Non-Circular / Non-Planar Gravity Currents**

Shortly after release, the current intrudes into the ambient fluid forming a smooth front in which Kelvin-Helmholtz rolled up vortices separate the body from the head of the current. The signature of these vortices is visible in the density iso-surface plots of Figure 5-6. The head of the current is complex and includes vortical structures that are not fully observable in the density iso-surface plots, but are better identified in isosurface plots of the swirling strength  $\lambda_{ci}$  in Figure 5-16. The swirling strength is

defined as the absolute value of the imaginary portion of the complex eigenvalue of the velocity gradient tensor. It is commonly used for identifying regions of intense vorticity (Zhou *et al.* 1999; Chakraborty *et al.* 2005; Cantero *et al.* 2007b). The maximum, mean and rms values of  $\lambda_{ci}$  at  $t = 3.5, 7,$  and  $14$  is  $\{65, 0.020, 0.34\}, \{25, 0.024, 0.30\},$  and  $\{14, 0.015, 0.15\},$  respectively. The swirling strength is highest at the head of the fast front of the current, where the flow is dominated by hairpin vortices and inclined vortical structures.

Owing to the preferential direction of spreading, the vortex tubes at the slow front, i.e. parallel to the  $y$ -axis undergo stretching and twisting (Figure 5-16c) before they eventually break up into smaller structures (Figure 5-16e). In Figure 5-17, the spatial distribution of the vertically averaged swirling strength reveals that the swirling strength at the fast front is as large as twice that at the slow front. Iso-surfaces of  $\lambda_{ci}$  for a cylindrical release of equivalent volume are displayed in Figure 5-18. For the sake of comparison, the maximum, mean, and rms values of  $\lambda_{ci}$  at  $t = 3.5, 7,$  and  $14$  is  $\{47, 0.032, 0.5\}, \{39, 0.038, 0.41\},$  and  $\{12, 0.020, 0.17\},$  respectively. It is noteworthy that the mean value of  $\lambda_{ci}$  is consistently larger in the circular case than in the rounded-rectangle release. We conjecture that the observed higher intensity of the swirling strength is due to the fact that the initial axisymmetry of the circular release artificially increase the coherence of the vortex tubes since the local stretching field is likely to be more uniform in this case. In any case, the explanation of the present observation remains unclear at the present time.

## 5.6 Summary and Discussions

Following the recent findings of Zgheib *et al.* (2014), we have presented experimental and numerical results for finite-release gravity currents of non-axisymmetric shape. In the present work, we demonstrate that a non-circular gravity current eventually reaches a non-circular self-similar shape in the inertial regime. Thanks to extended box model simulations, we propose a simple scaling law which relates the self-similar horizontal aspect ratio to the horizontal initial aspect ratio of the release. This law is found to be in reasonable agreement with results from the present experiments and fully-resolved simulations. Further qualitative experiments suggest that the non-axisymmetric spreading of initially a non-circular release is independent of the density ratio, vertical aspect ratio, wall friction, and Reynolds number provided  $Re \geq O(10^4)$ , which is typical for these types of flows.

It is noteworthy that the switching of axes reported in Zgheib *et al.* (2014) is not unique to non-axisymmetric gravity currents. Non-circular jets, and elliptic jets in particular, have been shown to flip axes (see e.g. Gutmark & Grinstein 1999). In fact, similar to gravity currents, the jet's initial shape dictates the subsequent transient cross-sectional configurations at different downstream locations. Nonetheless, the mechanisms leading to the switching of axes are quite different. In the case of the elliptic jet, the faster growth rate of the shear-layer along the flattest side of the jet, say normal to the minor  $y$ -axis, leads to a faster entrainment and hence the downstream cross-section of the jet will switch axes. After the switch, the flatter side of the jet is now normal to the  $x$ -direction, and the situation is reversed. In some cases, elliptic jets may undergo several flipping of axes, as shown by Quinn (1989). In the case of gravity

currents, the switch of axes is a consequence of the azimuthally-varying current height, which leads to local fast and slow fronts along the circumference, and the present results suggest that the switch is permanent. Furthermore, the switching of axes in the case of non-circular jets has been related to the dynamics of the rolled-up vortices. Although strong vortices are present at the front in the case of gravity currents, their presence is not essential in the switching of axes. For instance the axes switching is predicted in the extended box model, which does not account for any vortex roll-up at the front of the current.

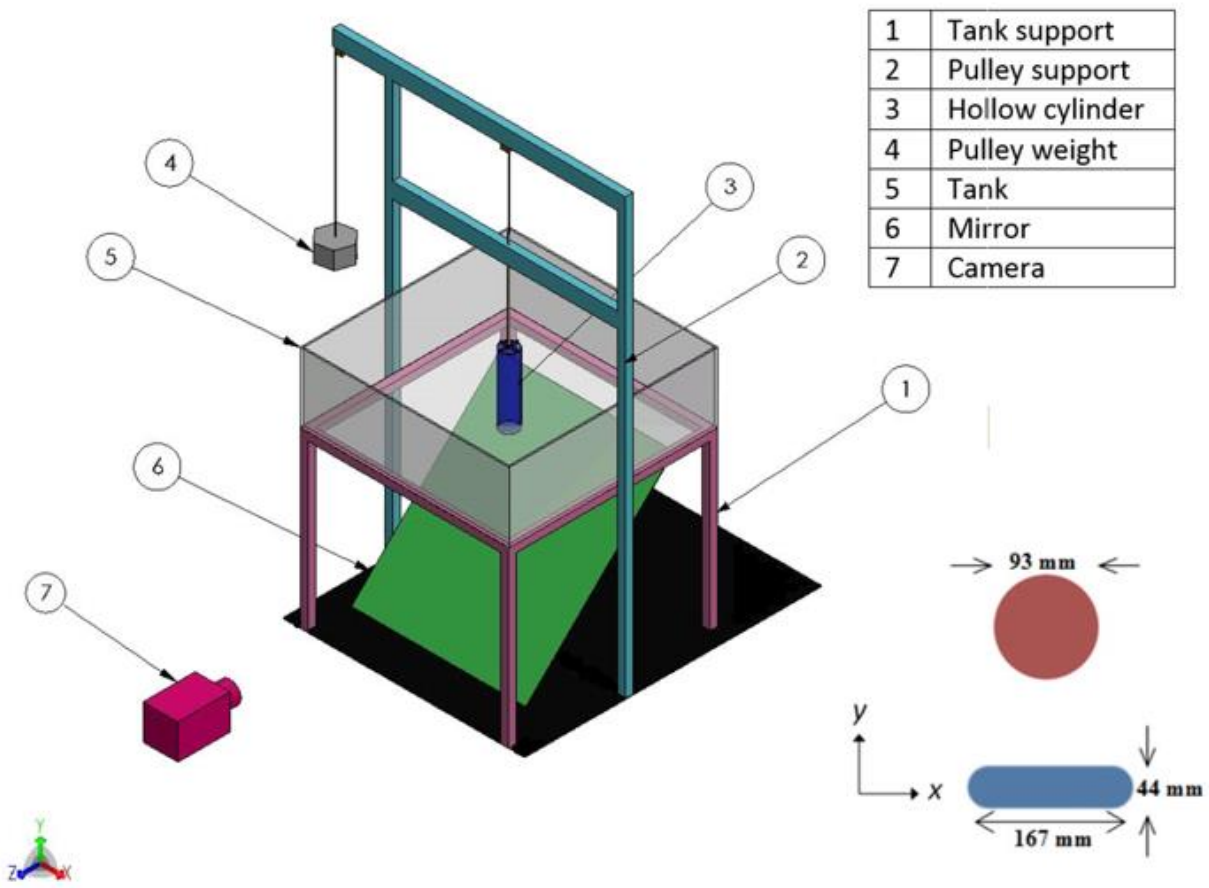


Figure 5-1. (Color online) Experimental setup. The experiments are carried out with two different cross-sectional geometries, namely a circular section (CS) and a rounded rectangle (RR). Both geometries have roughly the same cross sectional area, leading to an equivalent radius  $R_0$  of 4.6 and 4.7 cm for the CS- and RR-geometry, respectively,  $R_0$  being calculated from the surface area  $A$  as  $R_0 = \sqrt{A/\pi}$ . An inclined mirror is placed underneath the tank, so that the current's evolution is recorded both from the side and below. The square tank dimensions are  $120\text{cm} \times 120\text{cm} \times 40\text{cm}$ , corresponding to  $26R_0 \times 26R_0 \times 9R_0$  approximately. Gravity is pointing towards the  $-z$  direction.

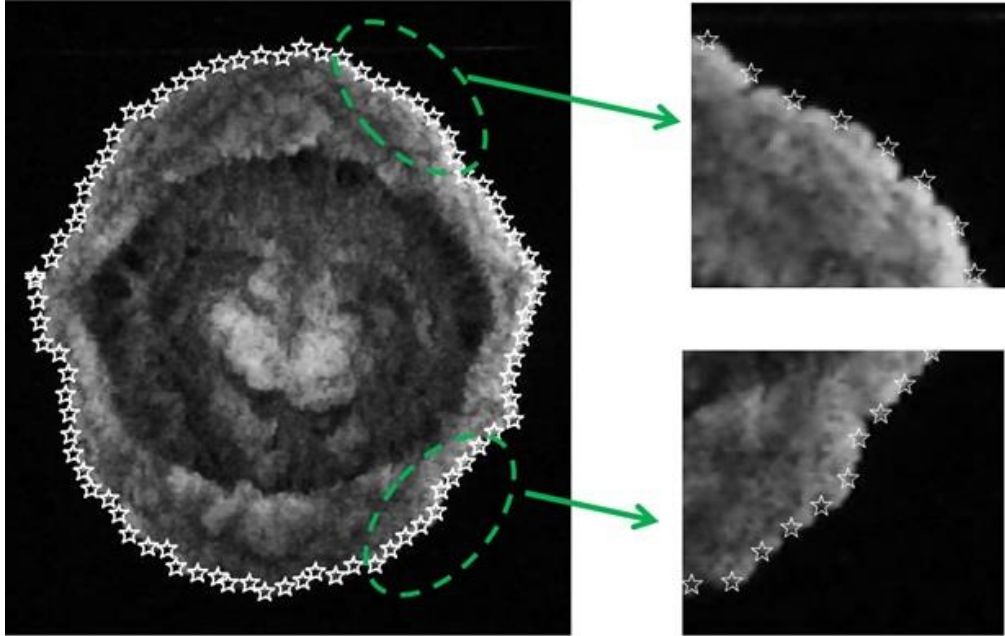


Figure 5-2. Example of front location detection from experiments. A plan view of the current (Exp 5-2 at  $t = 5.9$ ) is shown on the left along with the white star symbols corresponding to the extracted front location. A close up view on the right shows good agreement between the extracted and the actual front location.

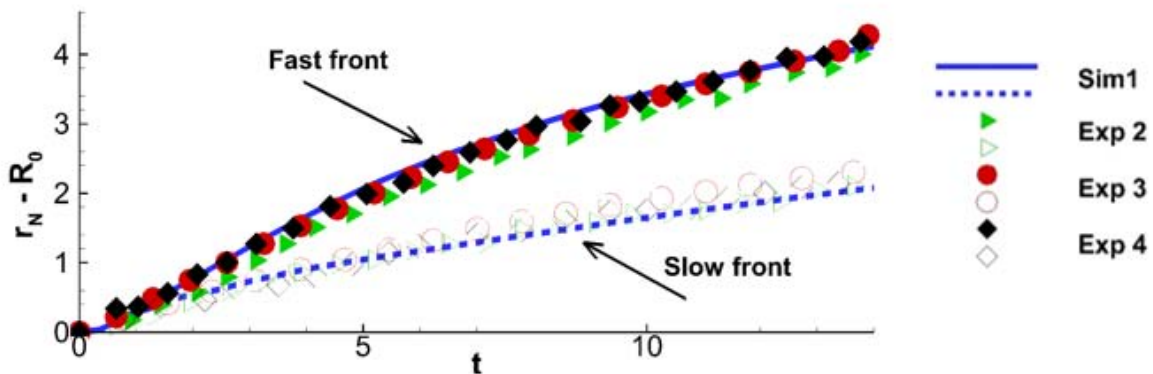


Figure 5-3. (Color online) Time evolution of the front position of the “slow” and “fast” fronts of RR-currents for various initial orientations of the rounded-rectangle cylinder relative to the tank walls. The angle between the initial longest side of the RR-cylinder and the tank wall is  $0^\circ$  (Exp 5-2),  $45^\circ$  (Exp 5-3) and  $90^\circ$  (Exp 5-4), respectively. The front location is averaged over a small sector of width  $2\alpha = \pi/36$ . Note that the tank walls are located at a minimum distance of  $13R_0$  from the centre of mass of the current, which corresponds to  $r_N - R_0 = 6$ , here (recall that the front position is scaled by  $h_0$  and that  $\lambda = h_0/R_0 = 2$ , here). For comparison, the results obtained with Sim 1, for which the “outer walls” are at a minimum distance of  $16R_0$ , is also plotted.

Table 5-1. Velocity ratio  $u_F/u_S$  and height ratio  $h_F/h_S$  between the fastest and slowest points of some gravity currents of initially arbitrary shape. The mean quantities are computed for  $0 \leq t \leq 22$  ( $\lambda = 1.4$ ),  $0 \leq t \leq 12.6$  ( $\lambda = 2$ ), and  $0 \leq t \leq 6.5$  ( $\lambda = 4$ ). CS, RR, and TR refer to the circle, rounded rectangle, and true rectangle, respectively (Figure 5-1).  $\lambda = h_0/R_0$  is the initial vertical aspect ratio.

Exp/Sim num	Initial shape	$h_0$ (m)	$\rho_c$ (Kg/m <sup>3</sup> )	$Re$	$\lambda$	$\rho_c/\rho_a$	$max(u_F/u_S)$	$\overline{u_F/u_S}$	$max(h_F/h_S)$	$\overline{h_F/h_S}$	comments
Exp 5-1	CS	0.092	1100	1100	2	1.1	1.02	0.99	-	-	saline current
Exp 5-2	RR	0.094	1100	1100	2	1.1	2.27	1.88	5.85	3.90	saline current
Exp 5-3	RR	0.094	1100	1100	2	1.1	2.24	1.96	-	-	saline current
Exp 5-4	RR	0.094	1100	1100	2	1.1	2.60	2.00	-	-	saline current
Exp 5-5	RR	0.188	1100	1100	4	1.1	2.17	1.77	-	-	saline current
Exp 5-6	RR	0.047	1000	1000	1	10 <sup>3</sup>	-	2.64*	-	-	dam-break flow
Exp 5-7	RR	0.094	1007 <sup>f</sup>	1400	2	1.007	-	2.46*	-	-	turbidity current
Exp 5-8	RR	0.047	1000	1100	1	0.93	-	2.56*	-	-	top current
Exp 5-9	RR	0.141	1400	1100	3	1400	-	1.10**	-	-	viscous current
Sim 5-1	RR	-	-	8.95×10 <sup>3</sup>	2	≈1	2.66	2.06	4.09	2.70	-
Sim 5-2	CS	-	-	8.95×10 <sup>3</sup>	2	≈1	1.00	1.00	1.00	1.00	-
Sim 5-3	RR	-	-	8.95×10 <sup>3</sup>	1.4	≈1	3.72	2.71	6.12	4.44	-
Sim 5-4	TR	-	-	8.95×10 <sup>3</sup>	2	≈1	2.60	1.98	3.95	2.66	-

\*mean quantities are computed for  $0 \leq t \leq t_f$ ,  $t_f$  corresponding to the maximum time shown in Figure 5-17.

\*\*mean velocity ratio computed for the post acceleration stage  $2200 \leq t \leq 33,500$ .

<sup>f</sup> see section 4.2 for the physical parameters of the particles and the mixture

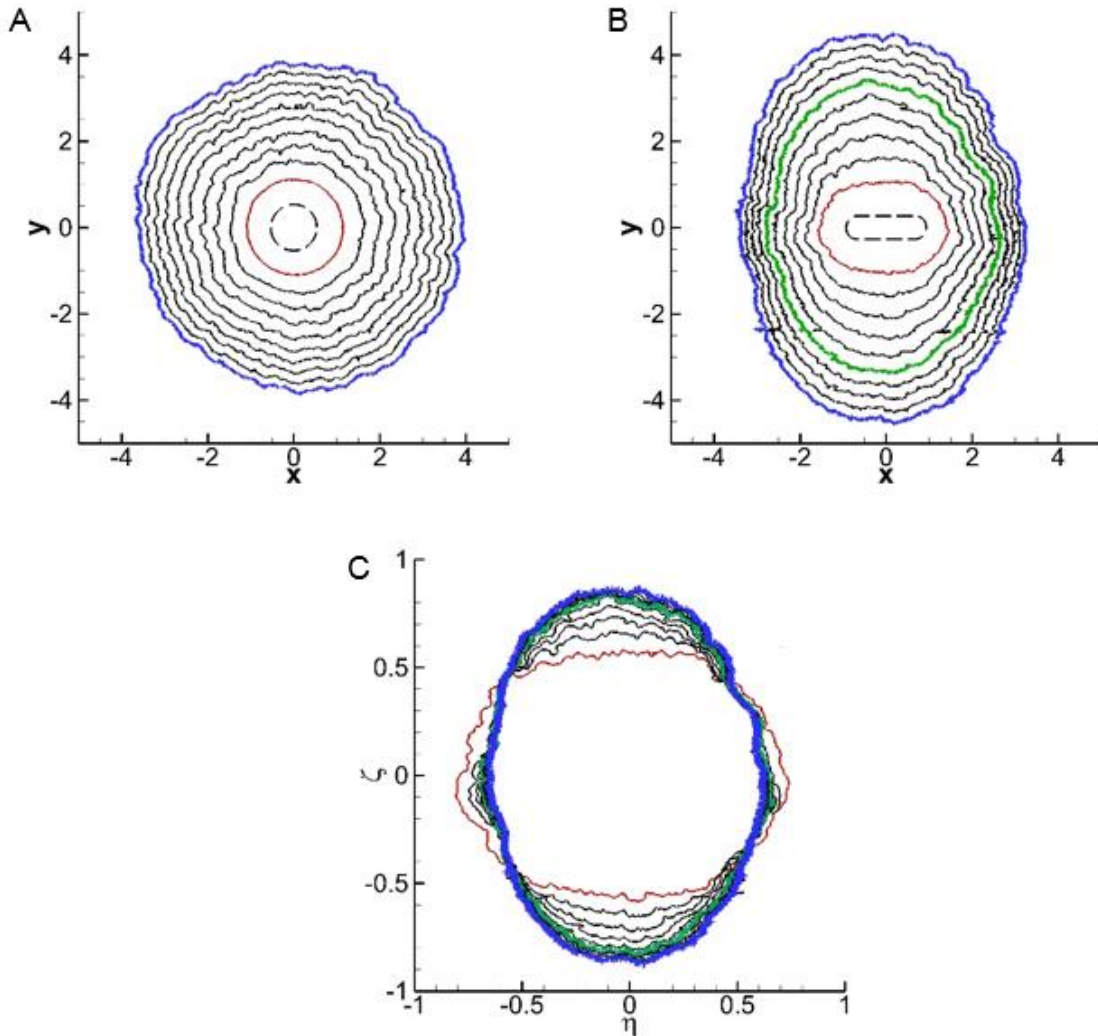


Figure 5-4. (Color online) Evolution of the front contours for A) a circular (Exp 5-1) and B) a rounded-rectangle release (Exp 5-2). Frame C) is similar to frame B) using the self-similar variables  $\eta = xt^{-1/2}$  and  $\zeta = yt^{-1/2}$  respectively. Note that here the variables are dimensionless so that in dimensional form the self-similar variables would become  $\eta = (g'h_0^3)^{-1/4}\tilde{x}\tilde{t}^{-1/2}$  and  $\zeta = (g'h_0^3)^{-1/4}\tilde{y}\tilde{t}^{-1/2}$ , respectively (where the tilde denotes a dimensional variable). The contours are plotted from  $t_0 = 2.1$  (red curve) to  $t_f = 13.8$  (blue curve) by steps of  $\Delta t = 1.3$ . Plotted in green is the curve corresponding the time  $t = 8.6$  for which the shape becomes roughly self-similar. It is noteworthy that at the time  $t_f$ , the currents have crossed a minimum distance of 7 to 8 initial equivalent radii, while the tank walls are located at  $x = y \approx \pm 6$  (axes are scaled by the initial height of the ambient  $H$ ). In frames A and B, the dashed line represents the initial location of the hollow cylinder.

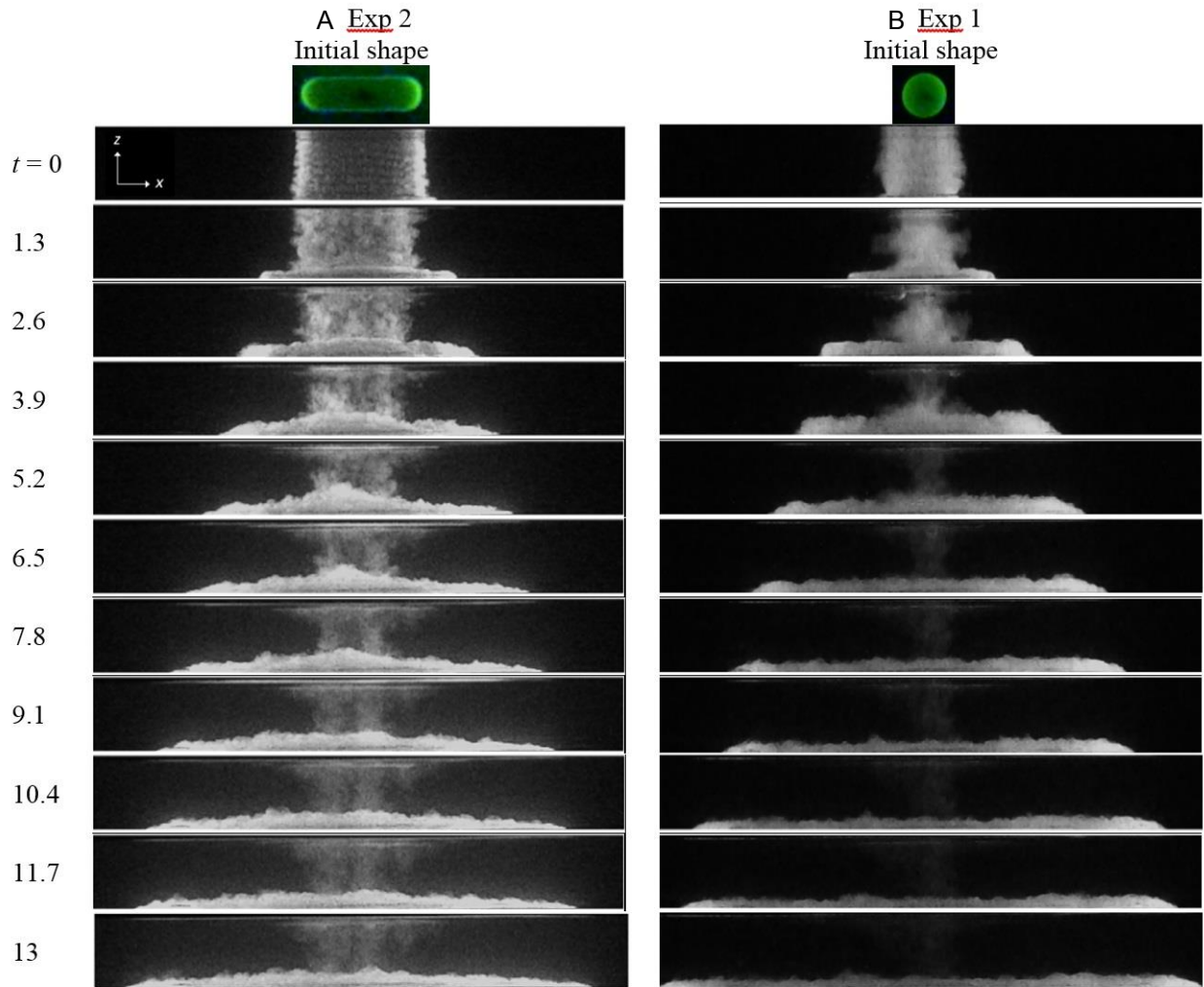


Figure 5-5. Side view of the A) rounded rectangle and B) circular gravity currents. Contrary to the RR-release, the current's thickness is roughly uniform for the circular release during spreading.

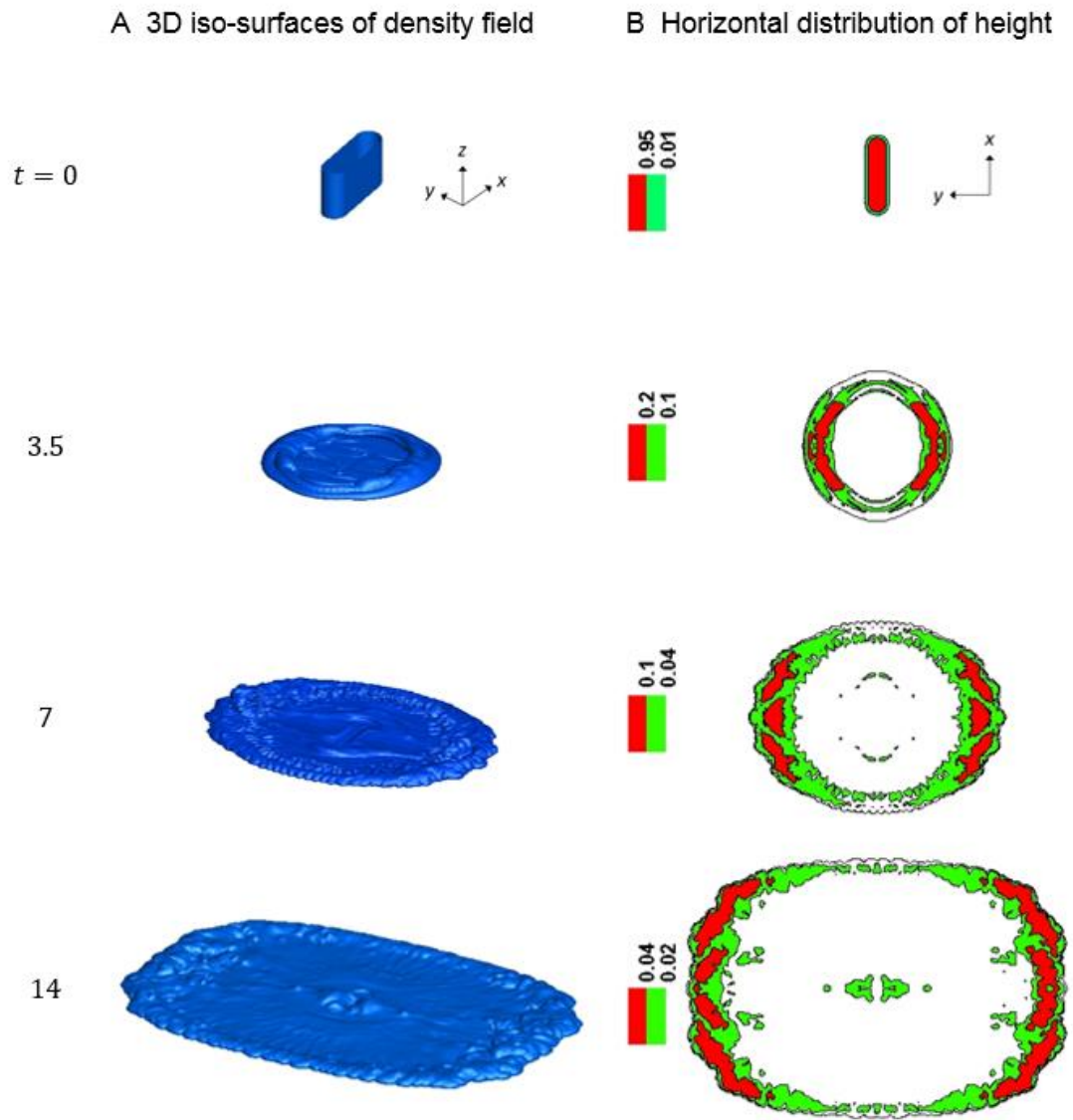


Figure 5-6. Height of the RR-gravity current (Sim 5-1). A) Iso-surfaces  $\rho = 10^{-2}$ , B) Distribution of the height along the horizontal plane. Note that the local height strongly varies along the circumference of the current, being maximum along the  $y$ -direction.

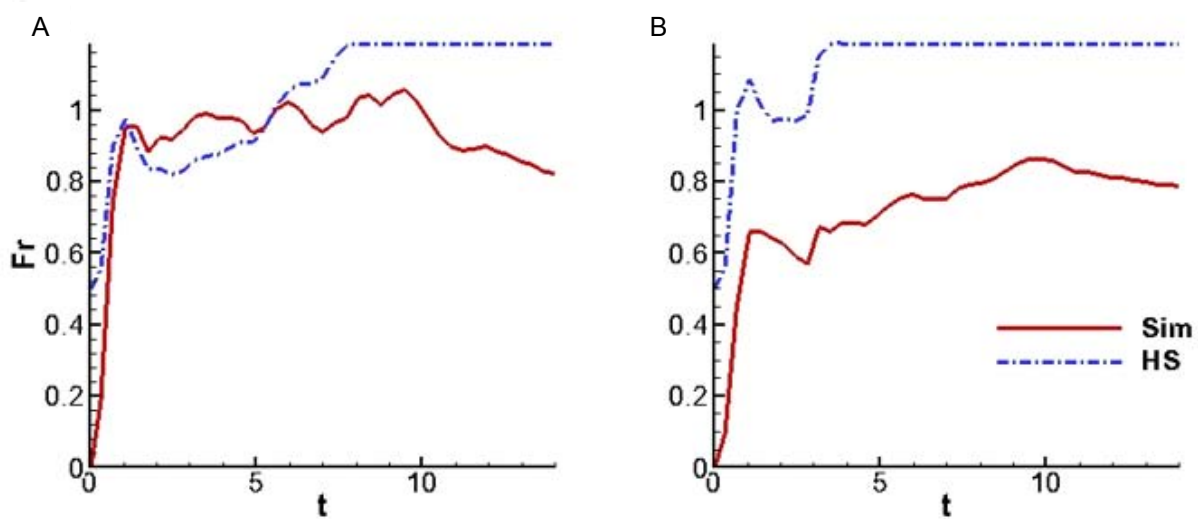


Figure 5-7. Time evolution of the local Froude number at A) the fast front and B) the slow front: (—),  $Fr = u_N/\sqrt{h_N}$ , Sim 5-1; (- · - · -),  $Fr^{HS}(a) = \min(a^{-1/3}, 1.19)$ ; (- - - -),  $Fr^B(a) = \sqrt{a(1-a)(2-a)/(1+a)}$ ; (— — —),  $Fr^{BM}(a) = \sqrt{2a(1-a)}$ . Here,  $a$  is defined as  $a = h_N/H$ .

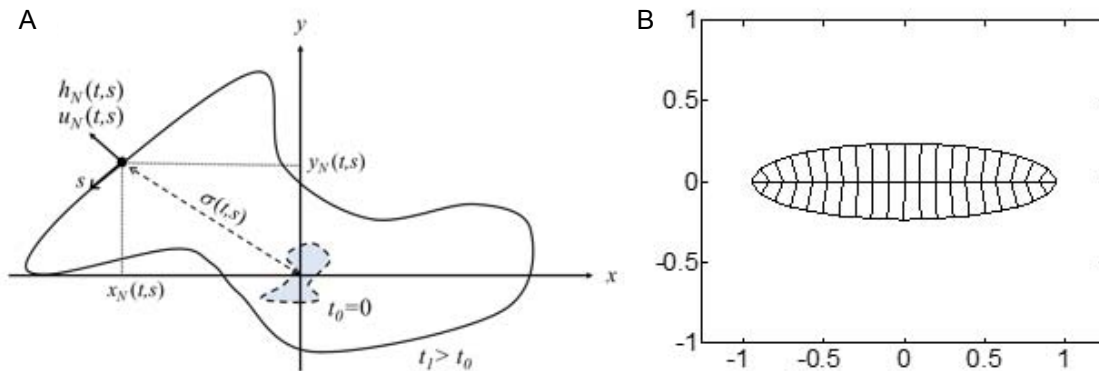


Figure 5-8. A), Notations used for the two-dimensional extended box model.  $\{x_N(s, t), y_N(s, t)\}$  denote the local position,  $h_N(s, t)$  the height,  $u_N(s, t)$  the outward normal velocity of the front and  $\sigma(s, t)$  the area per arc length. The independent variables  $s$  and  $t$  denote the curvilinear coordinate along the front and time, respectively. B), Example of initial partitioning of the initial elliptical body of a non-axisymmetric gravity current.

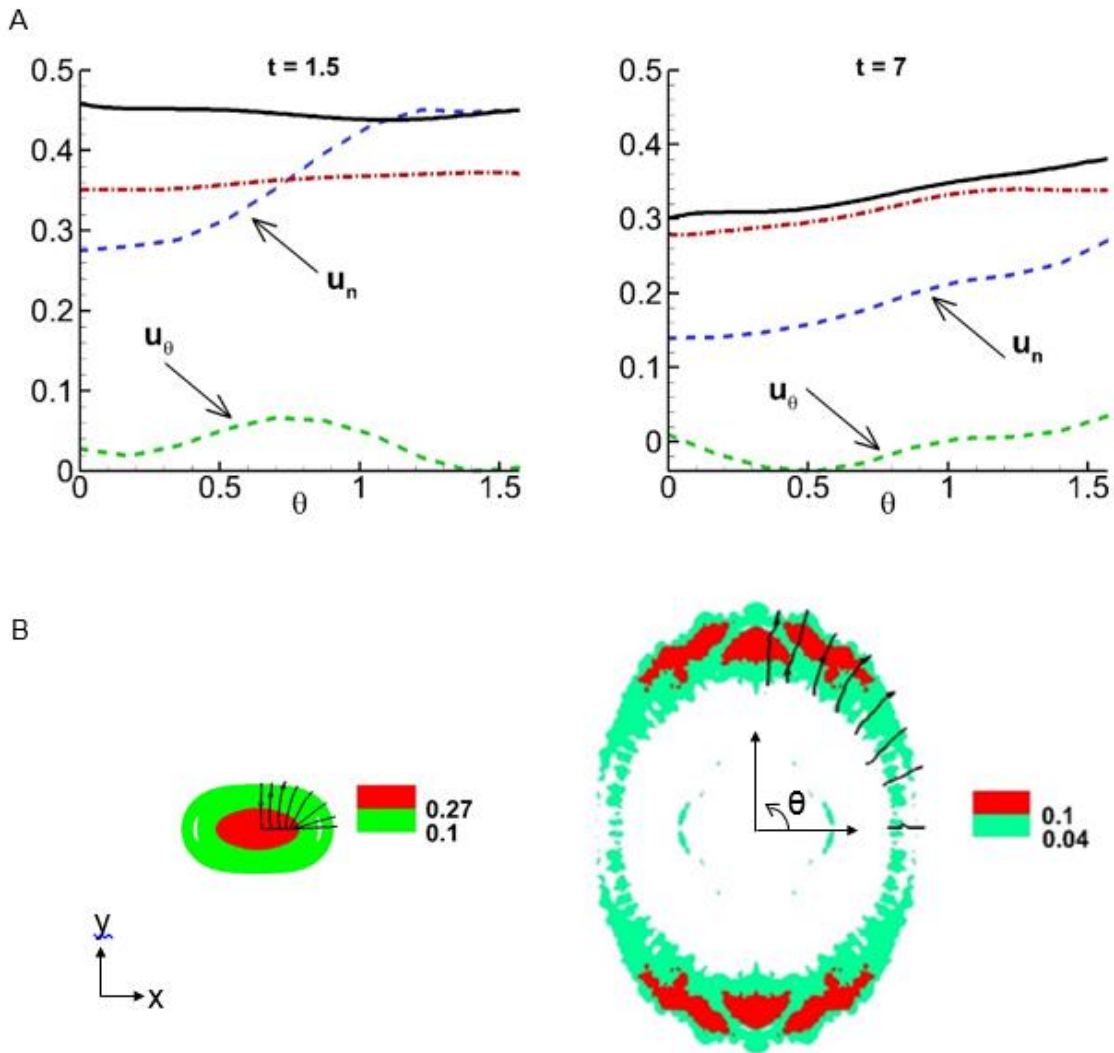


Figure 5-9. (Color online) A) Azimuthal evolution of the normal-to-the-front  $u_n$  and tangential component  $u_\theta$  of the front velocity of a rounded-rectangle gravity current at two different time instances (Sim 5-1). Also plotted is the velocity obtained via the Huppert & Simpson (1980)'s Froude function (Eq. 5-15) using the mean height (dash-dot red line) and the maximum height (solid black line) in the head of the current extracted from the fully-resolved simulation. B) Height distribution in the RR-current before and after the switch of axes at  $t = 1.5$  and  $t = 7$ , respectively. The streamlines of the vertically-averaged velocity field in the current are also plotted in the upper right corner. In frame A,  $\theta$  is measured counter clockwise from the  $x$ -axis.

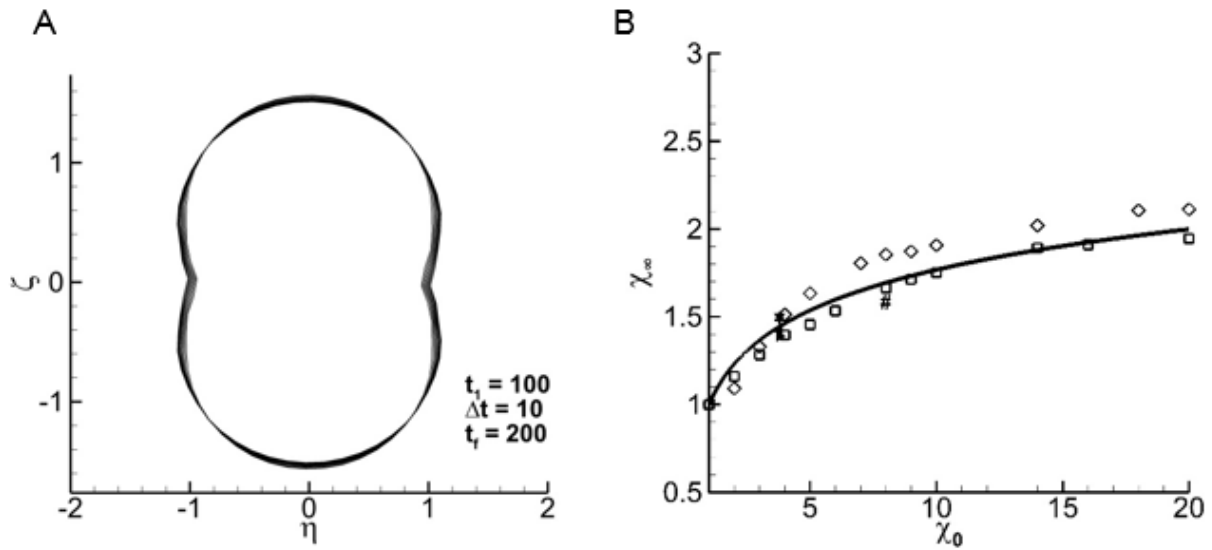


Figure 5-10. A) Evolution of the front contour of an initially elliptical release of horizontal initial aspect ratio  $\chi_0 = 3.8$  in the  $(\eta = xt^{-1/2}, \zeta = yt^{-1/2})$ -plane obtained from an EBM simulation. In (a), the contours are plotted from  $t_0 = 100$  to  $t_f = 200$  by steps of  $\Delta t = 10$ . B) Self-similar horizontal aspect ratio  $\chi_\infty$  of the front contour of non-axisymmetric gravity currents as a function of the horizontal initial aspect ratio  $\chi_0$ : ( $\blacktriangledown \blacktriangleleft \blacktriangleright$ ), experiments (5-2, 5-3, 5-4, respectively); ( $* \circ \# +$ ), fully-resolved simulations (5-1, 5-2, 5-3, 5-4 respectively); ( $\square \diamond$ ), EBM simulations with releases of initially elliptical and rounded-rectangle shape, respectively; (—), correlation  $\chi_\infty = 1 + \ln \chi_0^{1/3}$ .

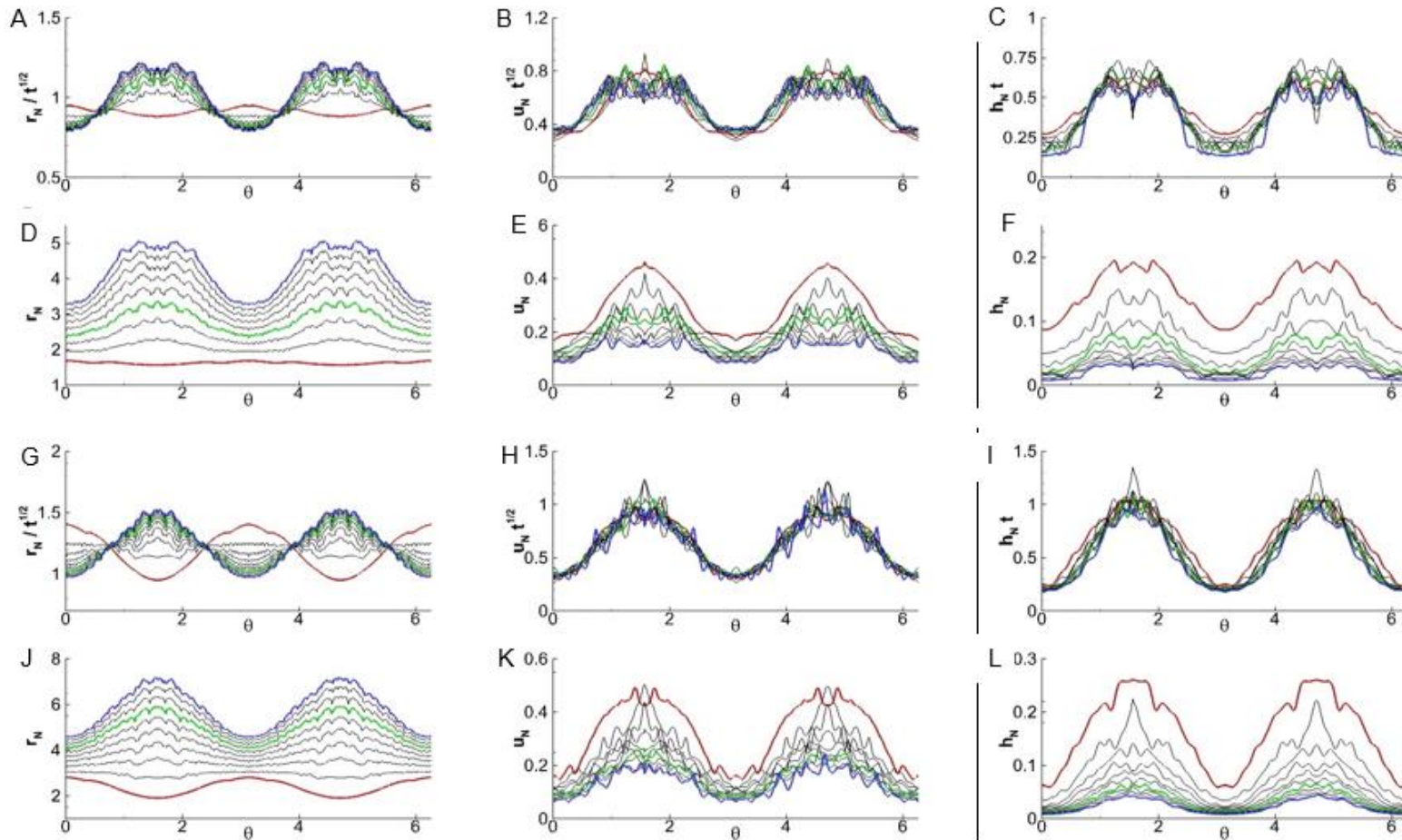


Figure 5-11. (Color online) Evolution for  $\chi_0 = 3.8$  (Sim 5-1) of the front contours (A & D), front speed (B & E), and mean front height (C & F). The contours are plotted from  $t_0 = 3.15$  (red curve) to  $t_f = 17.15$  (blue curve) by steps of  $\Delta t = 1.75$ . Plotted in green is the curve corresponding the time  $t = 8.4$  for which these quantities become roughly self-similar. Evolution for  $\chi_0 = 8$  (Sim 5-3) of the front contours (G & J), front speed (H & K), and mean front height (I & L). The contours are plotted from  $t_0 = 4$  (red curve) to  $t_f = 22$  (blue curve) by steps of  $\Delta t = 2$ . Plotted in green is the curve corresponding the time  $t = 16$  for which these quantities become roughly self-similar.

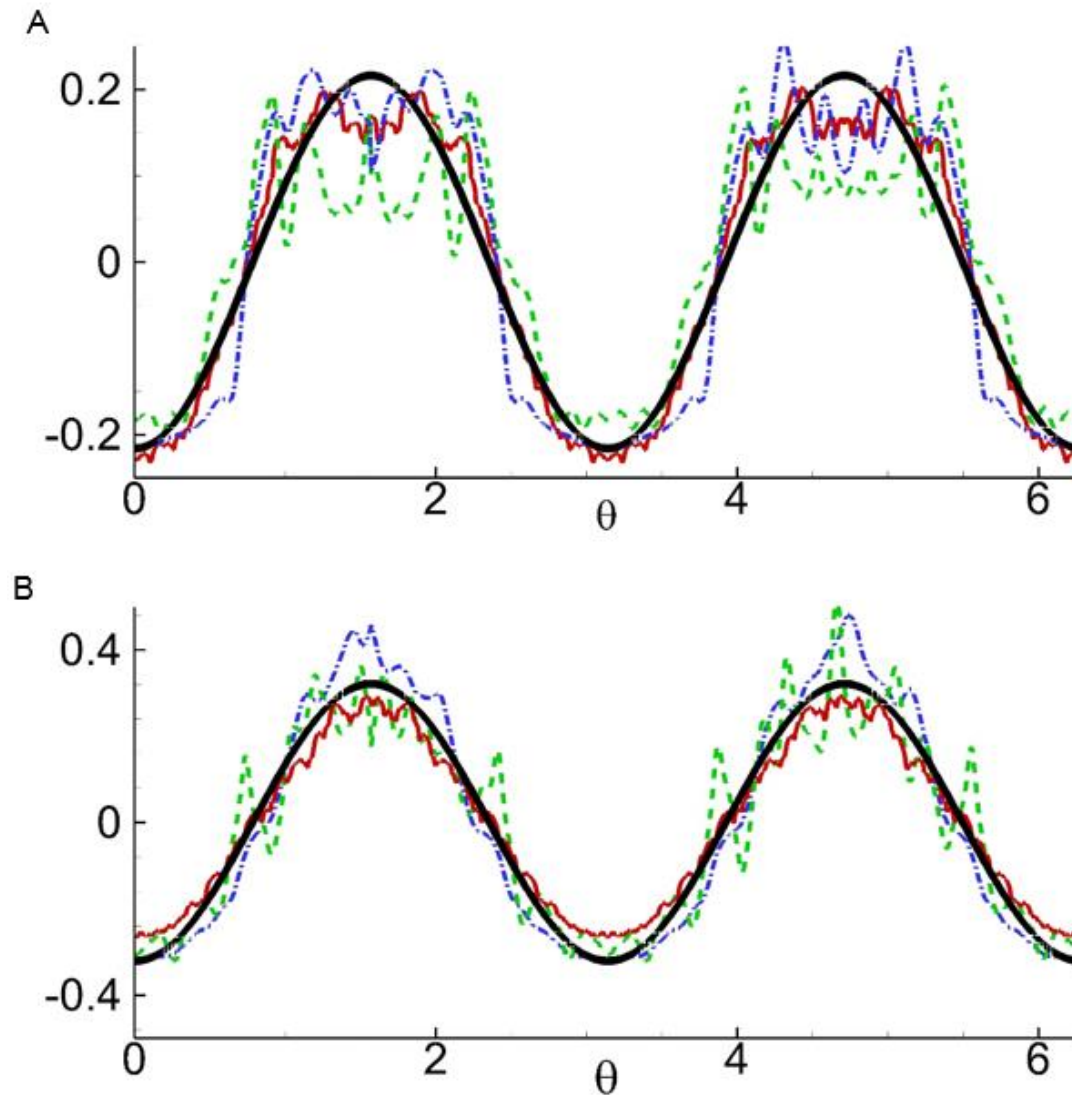


Figure 5-12. (Colour online) Azimuthal evolution at the final time of the scaled front location (red solid), speed (green dashed), and height (blue dash dot) from A) Sim 5-1 ( $\chi_0 = 3.8$ ) and B) Sim 5-3 ( $\chi_0 = 8$ ). The thick solid black line corresponds to  $f(\theta)$  from Eq. (5-22). The mean value is subtracted from each curve.

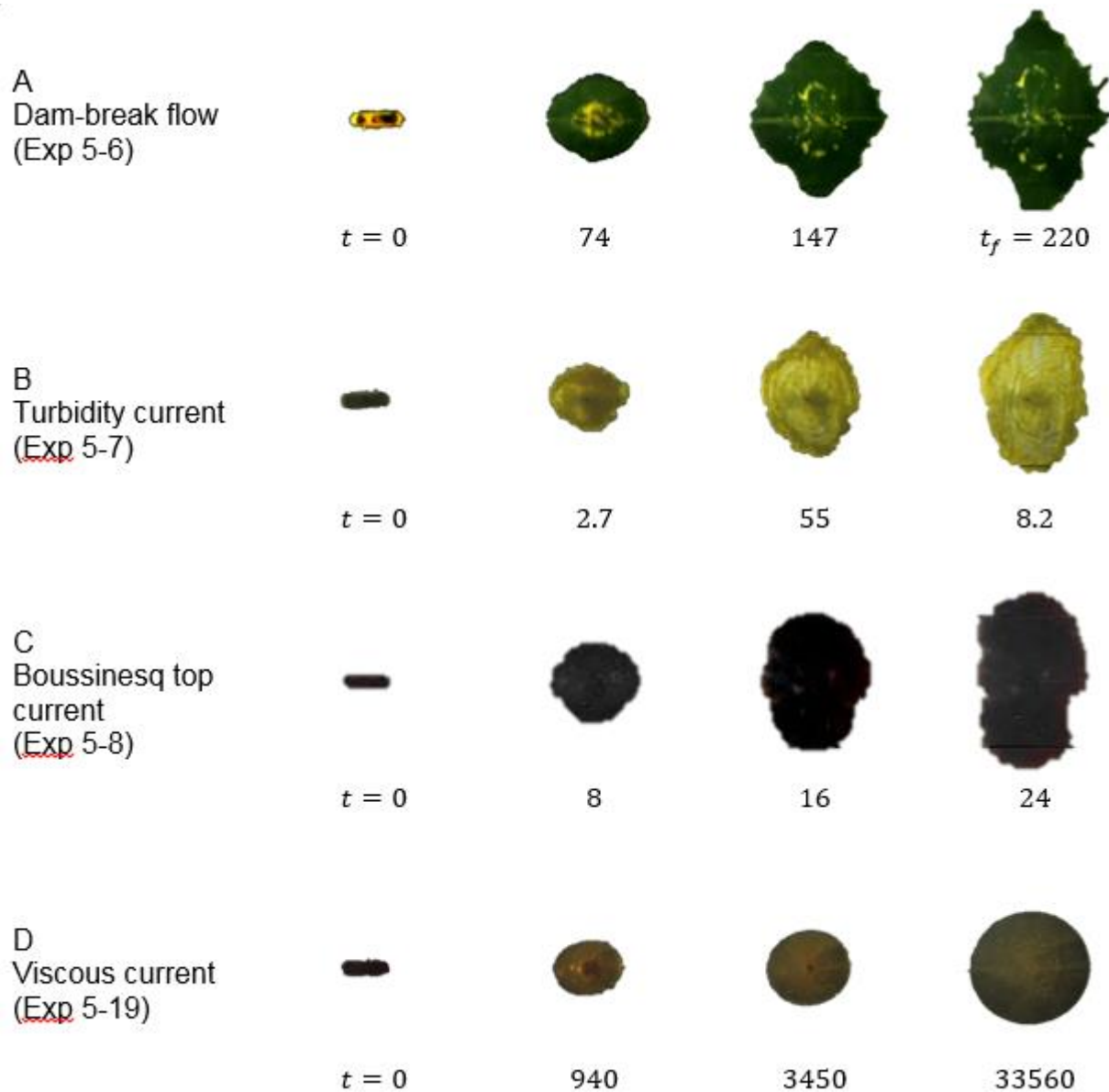


Figure 5-13. Experiments with the RR-initial geometry. A) dam-break flow (Exp 5-6); B) turbidity current (Exp 5-7); C) Boussinesq top current (Exp 5-8); D) viscous dam-break honey-in-air flow (Exp 5-9). Observe that the RR-viscous current does not switch axes, but rather becomes circular.  $t_f$  denotes the time up to which averaging is done in Table 5-1.

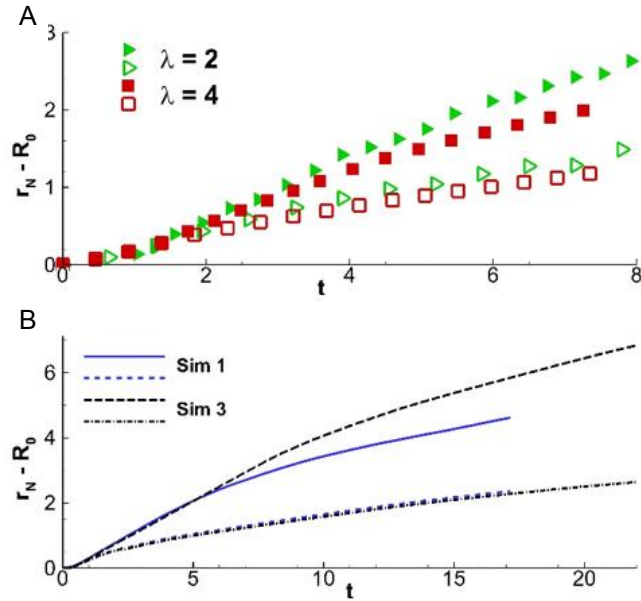


Figure 5-14. (Colour online) A) Time evolution of the fast front (solid symbols) and slow front (open symbols) of a RR release of initial vertical aspect ratio ( $\triangleright \blacktriangleright$ )  $\lambda = 2$ , Exp 5-2 and ( $\square \blacksquare$ )  $\lambda = 4$ , Exp 5-5. B) Time evolution of the fast and slow fronts of a RR release of initial horizontal aspect ratio (blue lines)  $\chi_0 = 3.8$ , Sim 5-1 and (black lines)  $\chi_0 = 8$ , Sim 5-3.

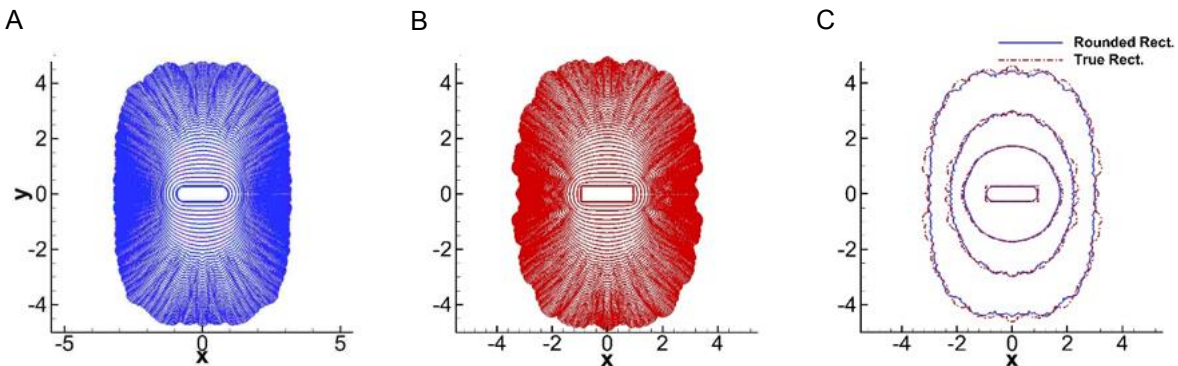


Figure 5-15. Effect of the local initial curvature. Composite picture of the front evolution obtained from simulations. Time separation between fronts is  $\Delta t = 0.35$  and the final run time is  $t = 16.1$  A) rounded rectangle (Sim 5-1); B) true rectangle (same physical parameters as Sim 5-1); C) comparison between the two geometries at  $t = 0, 3.5, 7,$  and  $14$ .

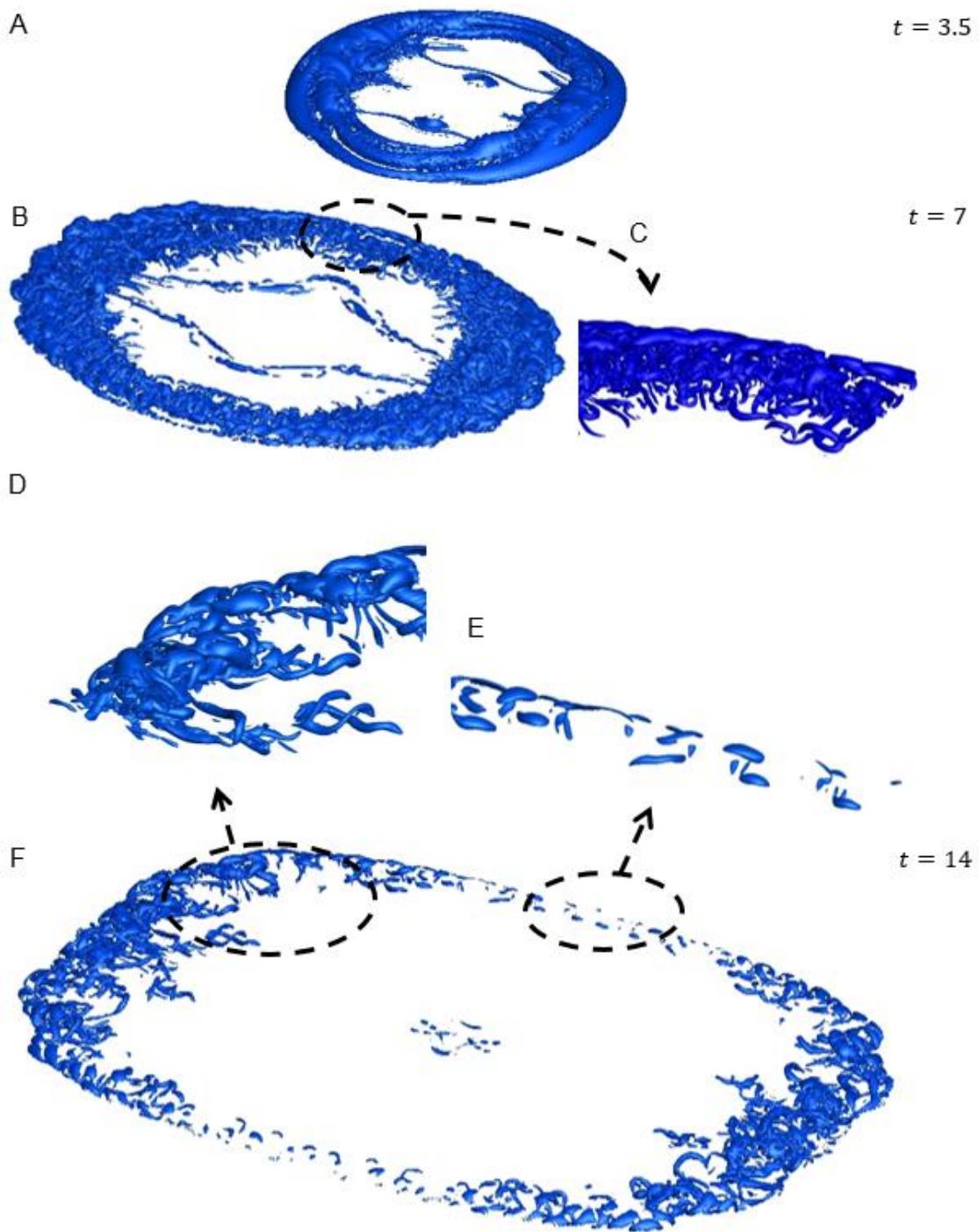


Figure 5-16. Isosurfaces of  $\lambda_{ci} = 2$  for the RR release (Sim 5-1) for  $t = 3.5, 7,$  and  $14$ . The vortical tubes are stretched and twisted before eventually breaking down into smaller structures.

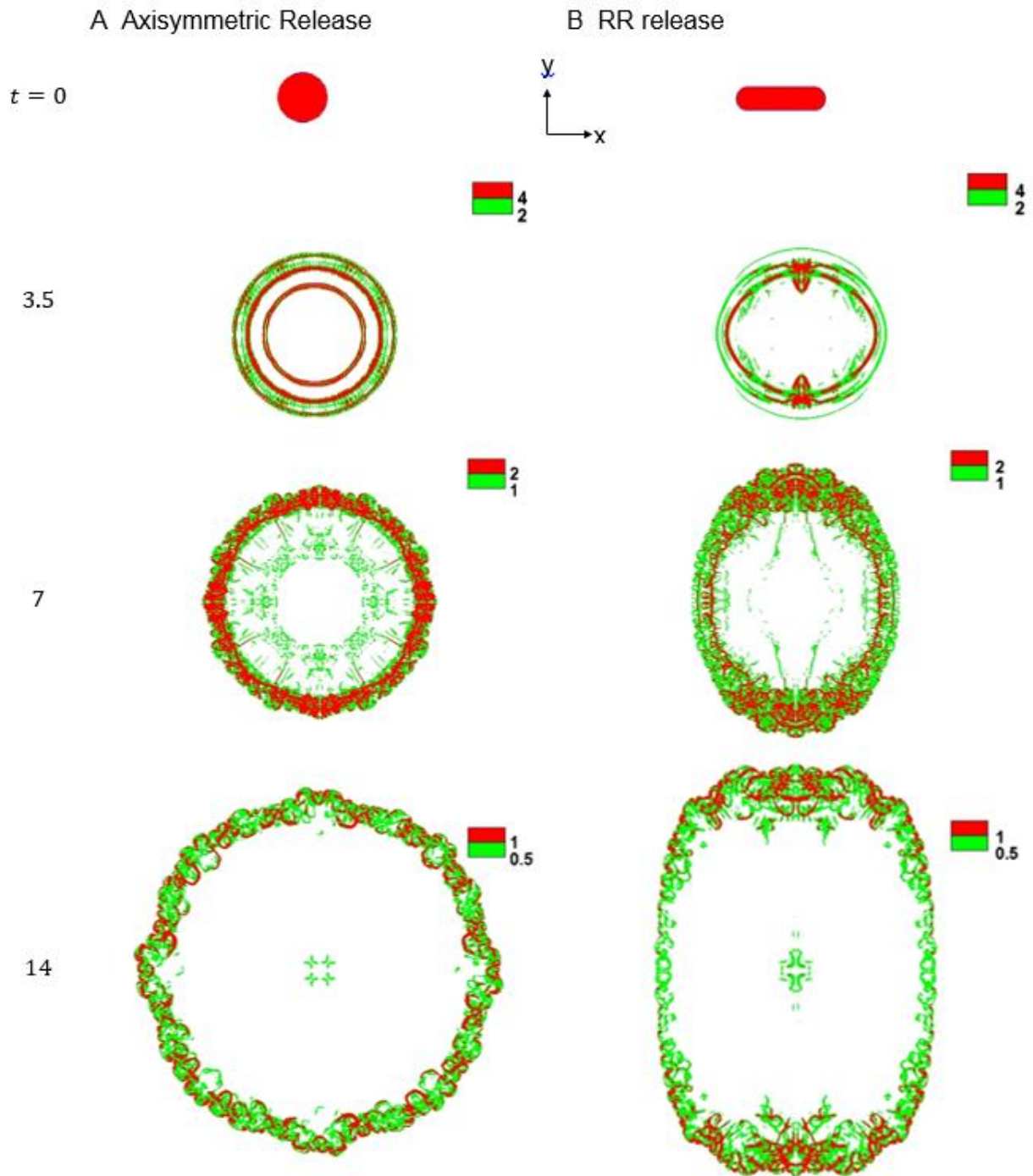


Figure 5-17. Vertically averaged  $\lambda_{ci}$  over the height of the current: A) axisymmetric release (Sim 5-2), B) RR release (Sim 5-1). The initial volume of the current is the same for both cases.

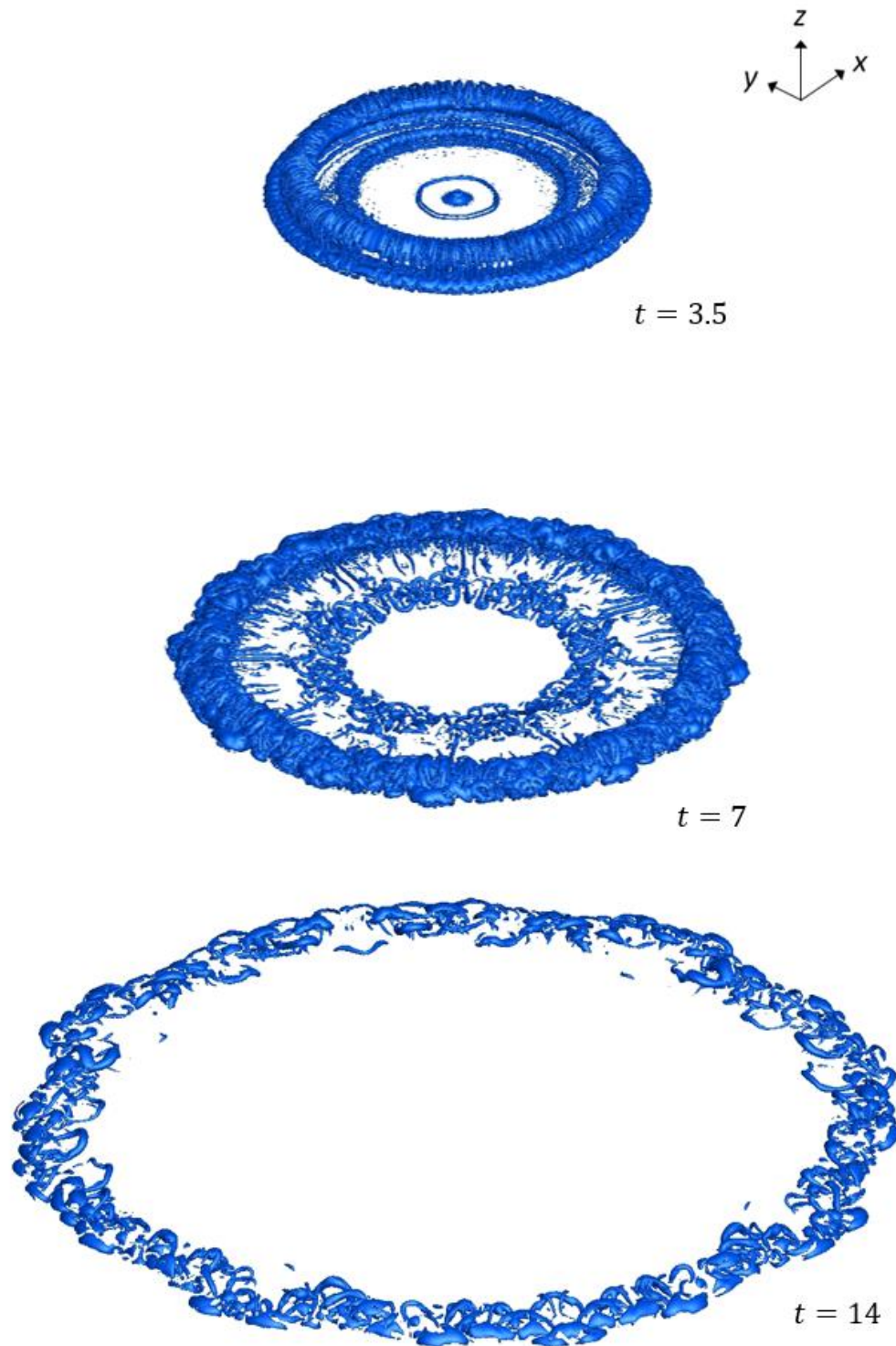


Figure 5-18. Isosurfaces of  $\lambda_{ci} = 2$  for the axisymmetric release (from Sim 5-2) for  $t = 3.5, 7, \text{ and } 14$ .

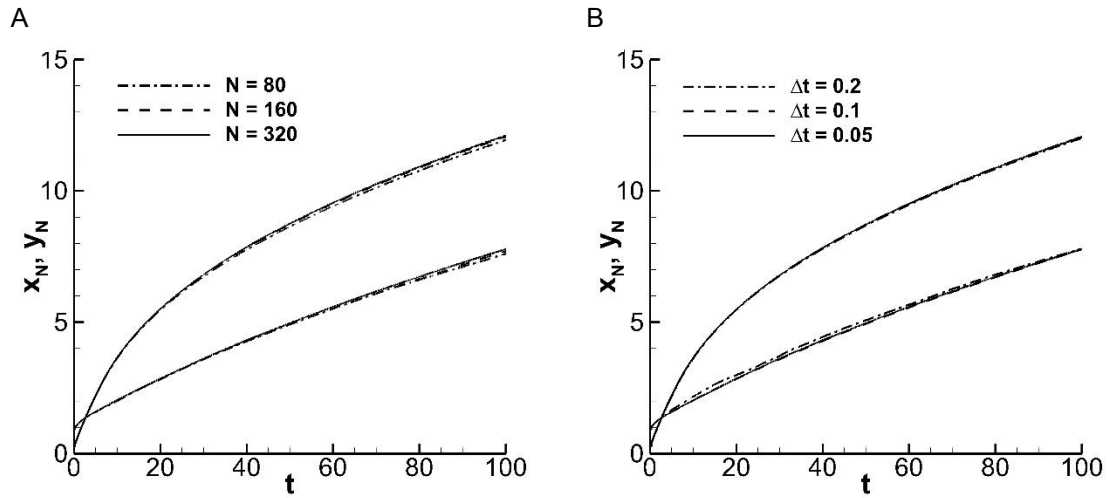


Figure 5-19. Spatial and temporal convergence for an initial elliptical release ( $\chi_0 = 3.8$ ) from the extended box model for A)  $\Delta t = 0.1$  B)  $N = 160$  points.

CHAPTER 6  
PROPAGATION & DEPOSITION OF NON-CIRCULAR FINITE RELEASE PARTICLE-  
LADEN CURRENTS

**6.1 Background**

When two fluids of different densities are brought into contact with one another (where the contact surface is parallel to the gravitational field), a hydrostatic pressure discontinuity forms along the interface and acts to set both fluids in motion. This type of fluid flow, denoted as a gravity current (Rottman & Simpson 1983; Hallworth *et al.* 2001) generally corresponds to the heavier of the two fluids intruding horizontally (normal to the gravitational field) into the lighter fluid. If we consider a laboratory setup in which both fluids are bounded by the impermeable walls of a finite domain (a tank for example), then the lighter fluid simultaneously moves to occupy the space abandoned by the heavier fluid. The initial density jump across the interface need not be large, in fact a density difference between both fluids of less than a percent is usually sufficient to generate a flow. The density difference can arise from a number of scenarios including temperature, concentration, or compositional disparities between the two fluids (Simpson 1982). Here, we are interested in flows in which the density difference originates from the suspension of relatively dense particles. These types of currents are known as particle-laden flows (Parker *et al.* 1986; Maxworthy 1999) and constitute a more complex subset of gravity currents. The added complexity comes from the fact that the density of the current strongly depends on the volume fraction of suspended particles which is spatially and temporally dependent since particles may (i) settle out and deposit on the floor, (ii) roll, slide, or saltate along the bottom wall, or (iii) be reentrained back into the current if the latter is energetic enough.

For the case of spherical particles, the speed at which particles settle out is often taken to be the terminal velocity of a free-falling single particle (Bonnecaze *et al.* 1993; Dade & Huppert 1995). The problems of bedload transport (Dufek & Bergantz 2007; Lee, Ha, & Balachandar 2012) and particle resuspension (Boegman & Ivey 2009) are essentially non-linear, with difficulties arising from the randomness of turbulent fluctuations and the complex topography of the bed.

Fixed volume, particle-laden flows are primarily investigated in one of two canonical configurations, namely a planar setting (Dade & Huppert 1995; Gladstone *et al.* 1998) and a circular axisymmetric setting (Bonnecaze *et al.* 1995; Ungarish & Huppert 1998; Gladstone & Woods 2000). These works were mostly experimental and theoretical. Problems such as bedload transport and particle resuspension are often difficult to measure experimentally and the use of alternative complementary approaches such as direct numerical simulations (DNS) is welcome. Here, we focus on three-dimensional flows where the release is neither planar nor axisymmetric. Those types of non-circular configurations have been recently studied in the context of saline density driven currents by Zgheib *et al.* 2014. They showed that the dynamics of a gravity current is influenced by the initial shape of the release up to times for which the current has entered a self-similar like regime. Our aim is to explore the case of particle-laden flows and in particular the azimuthal dependence of the initial non-circular shape on the velocity and extent of the current as well as the depositional pattern.

Direct numerical simulations of finite-release particle-laden flows have been performed for planar currents (Necker *et al.* 2002; Blanchette *et al.* 2005), however to the knowledge of the authors, no DNS studies for cylindrical releases have yet been

reported. DNS allows exploring the local near wall dynamics, specifically the bed shear stress and the near-wall velocity, both of which are critical parameters in the problems of bedload transport and particle resuspension. In addition, one can investigate the correlation relative to the larger scale vortical structures.

In this chapter, we perform a series of experiments of finite-volume, Boussinesq, particle-laden and density-driven (scalar) flows. Cylinders with two different cross sections are considered: a circle and a rounded rectangle (RR). For each experiment, we monitor the temporal evolution of the front as well as the final deposition profile of particles, both of which being highly dependent on the initial shape of release, as shown later. We vary several parameters, namely the settling velocity, the initial height aspect ratio of the release and the initial particle volume fraction, and analyze their influence on the current dynamics (front temporal evolution and deposition profile).

Companion direct numerical simulations are performed in which the setup is identical to that of the experiments. In our simulations, we do not account for particle resuspension or bedload transport. These assumptions will be discussed through the analysis of the spatial and temporal development of the wall shear stress and the near-wall fluctuating vertical velocity component inside the particle-laden flow.

Our chapter is structured as follows. In §6.2, we discuss the setup, procedure and results of the experiments. In particular, we investigate the effects of the various parameters on the front velocity and deposition profiles. Direct numerical simulations are described in §6.3, and compared to experimental results. In particular, the simplifications regarding bedload transport and particle resuspension are discussed in §6.3.4 and §6.3.5, respectively. Conclusions are drawn in §6.4

## 6.2 Experiments of Finite-Release Non-Circular Particle-Laden Currents

### 6.2.1 Experimental Setup

A particle-laden solution is confined within a hollow cylinder placed at the centre of a transparent glass square tank. The tank cross section is  $\tilde{L}_x \times \tilde{L}_y = 120 \times 120$  cm, and its walls are  $\tilde{L}_z = 40$  cm high (Figure 6-1). We consider two cross-sectional shapes for the hollow cylinder of height  $\tilde{h}_0$  and equivalent radius  $\tilde{R}_0$  the dimensions of which are given in Figure 6-2. The initial mixture, confined within the cylinder, is prepared by suspending polystyrene particles of density  $\tilde{\rho}_p = 1050$  kg/m<sup>3</sup>, volume fraction  $\phi_0$  and diameter  $\tilde{d}_p \approx 300 \pm 20$   $\mu$ m in tap water (here tilde denotes a dimensional quantity).

Initially, a fixed quantity of particles of mass  $\tilde{m}_p$  is poured into the hollow cylinder, and both the tank and the cylinder are slowly filled with tap water ( $\tilde{\rho}_a = 998$  kg/m<sup>3</sup>). Once the desired level ( $\tilde{h}_0$ ) is reached, the water is given time to arrive at a stagnant state. As a precaution against the clustering of particles, a few drops of non-agglomerating solution are added to the mixture in addition to an infrared fluorescent dye for visualization purposes. To bring the particles into suspension, two approaches were considered. In the first approach, a metallic net attached to a shape-fitted rigid structure that conforms to the inner perimeter of the hollow cylinder is used. The rigid structure is manually oscillated up and down within the hollow cylinder via two vertical rods that are connected to the structure at opposite ends. In the second approach, a brush of dimensions  $4 \times 1$  cm connected at its end with a rigid metallic rod sweeps the bottom floor inside the cylinder. The latter of the two approaches was found to be more effective at suspending the particles and was adopted for all the experiments shown herein.

### 6.2.2 Procedure

When the particles are fully suspended, the brush is retracted, and the hollow cylinder is swiftly lifted via a pulley system (Figure 6-1). To allow for a plan view of the current, a mirror at a  $45^\circ$  inclination is placed below the bottom transparent surface of the tank. A camera points towards the centre of the mirror at a distance of 6 m. The experiments are carried out in a dark room with black light illuminating the fluorescent dye injected into the mixture. Neon black light tubes are mounted on the four sides of the tank with close proximity to the bottom surface where the turbidity current spreads.

Two sets of data are extracted: the temporal front evolution of the current, as well as the final thickness of the deposit, once the current arrives at a standstill. To capture the location of the front, high resolution ( $2160 \times 2560$  pixels) 16-bit grayscale images are recorded every 20 ms. The front can be readily discerned since there is an order of magnitude jump between intensity levels in just a few pixels at the current-ambient interface. The height of the deposited particles is measured at the end of each experiment with a non-intrusive technique through laser reflection, the basic principle of which is triangulation. The probe has two main optical elements. The first is a light emitting diode, which projects a visible laser beam on the surface of the targeted element (in this case the deposit) whose elevation needs to be measured. A part of the incident beam is reflected from the surface of the deposit and impacts an ultra-sensitive optical sensor at an angle dependent on the distance between the diode and the surface. Before any experiments, calibration is performed, i.e. the elevation of the light emitting diode from the bottom surface of the tank is measured. Hence, once the distance between the diode and the targeted surface is measured, the height of the

deposit can be straightforwardly obtained. The laser has a measuring range of 2 mm with a resolution of 0.5  $\mu\text{m}$  and a spot diameter of 0.1 mm. The measurements are continuous with a frequency of 5 kHz . The 2 mm measuring range begins at a distance of 23 mm from the laser.

A mounted 2-axes motorized system is used to guide the laser over the bottom surface of the deposit. The system covers a range of 800  $\times$  800 mm, and depending on the area of the final deposit, the height of the particle deposit is measured every 25 or 50 mm. Since the height of the deposit at the centre of the release can exceed the aforementioned 2 mm measuring range, a micrometre was attached to the laser (inset of Figure 6-1) to allow for controlled vertical displacements.

To account for slight possible inclination in the tank supporting structure or possible minute height variations caused by the bending of the motorized axis (due to its own weight) as the laser sweeps over the bottom surface, dry measurements of the tank “topography” were computed by displacing a metallic plate of known thickness at various locations in the tank and recording the elevation measured by the laser. These values are then taken into account to correct the final thickness of the deposit.

Since the laser cannot be immersed in water, and because of the close proximity required between the laser and the deposit, the tank is slowly emptied at the end of each experiment and the deposit is allowed to dry overnight before any measurements are undertaken. The thickness is recorded at multiple height levels of the laser apparatus to ensure that the surface of the deposit always lies in the 2 mm measuring range of the laser.

## 6.2.3 Results

### 6.2.3.1 Evolution in the horizontal (x,y)-plane

Various experiments were carried out in order to assess the dependence of the dynamics on the initial volume fraction  $\phi_0$ , initial height aspect ratio  $\lambda$  and settling velocity  $\tilde{V}_s$ . Here, the initial volume fraction  $\phi_0$  is the ratio of the volume occupied by the particles to the total volume of the mixture at the time of release and  $\lambda$  is defined as the initial height  $\tilde{h}_0$  of the mixture inside the cylinder divided by the equivalent radius  $\tilde{R}_0$  of the cylinder ( $\lambda = \tilde{h}_0/\tilde{R}_0$ ). Unless stated otherwise, all variables are scaled by the following characteristic length, velocity, and time, respectively, viz

$$\tilde{L} = \tilde{h}_0, \quad \tilde{U} = \sqrt{\tilde{g} \frac{\tilde{\rho}_{c0} - \tilde{\rho}_a}{\tilde{\rho}_a} \tilde{h}_0}, \quad \tilde{T} = \frac{\tilde{L}}{\tilde{U}}, \quad (6-1)$$

where  $\tilde{g}$  is the gravitational acceleration and  $\tilde{\rho}_{c0}$  ( $\tilde{\rho}_a$ ) is the initial equivalent density of the mixture (ambient fluid). In practice, the initial density of the mixture is computed as  $\tilde{\rho}_{c0} = \phi_0 \tilde{\rho}_p + (1 - \phi_0) \tilde{\rho}_a$  where  $\tilde{\rho}_p$  is the density of the particles.

A list of the experiments is shown in Table 6-1. Note that the shape refers to the cross-sectional outline of the hollow cylinder, with RR denoting the rounded rectangular cylinder and C signifying a circular cylinder. Both geometries were chosen to have similar cross sectional areas so that for a fixed initial height, the volume of the release for the rounded rectangle or the circular cylinder is the same. We follow Cantero *et al.* (2008a) by defining the settling velocity ( $V_s$ ) of the particles as

$$\tilde{V}_s = \tilde{\tau}(1 - \beta)\tilde{g} \quad (6-2)$$

where

$$\tilde{\tau} = \frac{\tilde{d}_p^2(\hat{\rho} + 1/2)}{18\tilde{\nu}(1 + 0.15Re_p^{0.687})} \quad \text{and} \quad \beta = \frac{3}{2\hat{\rho} + 1} \quad (6-3)$$

with  $\hat{\rho} = \tilde{\rho}_p/\tilde{\rho}_a$  denoting the ratio of the particle density to the fluid density,  $Re_p = \frac{\tilde{v}_s \tilde{d}_p}{\tilde{\nu}}$  representing the particle Reynolds number, and  $\tilde{\nu}$  the kinematic viscosity of the interstitial fluid (water). Finally, the Reynolds number is defined as

$$Re = \frac{\tilde{h}_0 \tilde{U}}{\tilde{\nu}}. \quad (6-4)$$

We firstly explore the effect of the initial shape of the release on the temporal evolution of the front of a particle-laden current. Here, we investigate the finite-release of monodisperse, particle-laden currents for a non-planar, non-axisymmetric geometry. Let us consider for example the rounded-rectangular release shown in Figure 6-3B. Note that for comparison, we present the case of a circular release in Figure 6-3A. Initially, the longest side of the rounded rectangle is parallel to the  $y$ -axis, and once released, the front advances in all directions. The current is seen to attain a roughly circular cross-section at  $t = 10$ . However, at later stages of spreading ( $t > 10$ ), a difference between the spreading distances along the  $x$  and  $y$ -axes is observed. Clearly, the spreading is faster along the  $x$ -axis of the release. This preferred spreading direction is observed to persist until the current comes to rest at  $t \approx 70$  (not shown). Note that from  $t = 40$  to  $t \approx 70$ , the current advances at such a slower rate that its final layout is almost identical to that at  $t = 40$ .

As for the rounded-rectangular cross-section, we define two specific axes, denoted as minor and major axes, which initially correspond to the direction of shorter and longer sides, respectively. In the present work, they are initially parallel to the  $x$ - and  $y$ -axes, respectively. In the following, we refer to the switching of axes when the

current's major axis rotates by 90 degrees (with respect to the centre of the release in the  $x$ - $y$  plane) from the time it is released to the time when it arrives at a complete standstill. For the rectangular release displayed in Figure 6-3B, the current is observed to switch axes (snapshots at  $t = 0$  and  $t = 40$ ). Note that this switching of axes for this initial shape of release has been previously reported in the case of homogeneous saline currents (Zgheib *et al.* 2015a).

We plot in Figure 6-4 the mean front location at select instances for saline and particulate currents pertaining to experiments 6-3, 6-4, 6-7, and 6-8. Here, the front position which is plotted in the  $(x \geq 0, y \geq 0)$ -domain has been averaged in space using symmetry along the  $x$ - and  $y$ -axes, respectively. To be more explicit, we exploit the 4-fold symmetry in the  $x$ - $y$  plane by first mapping all points along the front onto the first quadrant  $(x \geq 0, y \geq 0)$ . In practice, a point on the front of coordinates  $(x, y)$  will get the new coordinates  $(|x|, |y|)$  that belong to the first quadrant. We then convert the Cartesian coordinates  $(|x|, |y|)$  to polar coordinates  $(r, \theta)$ , with  $r$  being the radial distance from the origin to the point and  $\theta$  the angle made with respect to the  $x$ -axis. Subsequently, we average all the  $r$  values at each equally spaced  $\theta$  by steps of  $\pi/180$ .

Bonnecaze *et al.* (1995) and Necker *et al.* (2002) have shown that for finite-volume axisymmetric and planar releases, homogeneous and particulate currents advance at similar speeds until enough particles have settled and particle-laden fronts begin to progressively slow down and deviate from scalar driven fronts. For the circular release (Figure 6-4A), we observe that the time of separation occurs after  $t \approx 10$ . Interestingly, for the rounded-rectangular release (Figure 6-4B), the time from which deviation between saline and particulate fronts is observed, is azimuthally dependent.

Until  $t = 5$ , both currents advance at the same rate. At  $t = 10$ , the particulate front overtakes the saline front along the  $x$ -axis, with the fronts progressively reuniting as we get closer to the  $y$ -axis. At later times ( $t = 20$ ), the particle-laden front matches the saline front along the  $x$ -axis. Finally, at  $t = 40$ , the difference between the fronts grows, with a larger discrepancy along the  $y$ -axis.

We plot in Figure 6-5 the contour plots of the mean deposition thickness  $\bar{h}_d$  of the current displayed in Figure 6-3. Here,  $\bar{h}_d$  has been obtained by averaging the local deposition thickness over the four quadrants as

$$\bar{h}_d(x \geq 0, y \geq 0) = \frac{1}{4}(h_d(x, y) + h_d(-x, y) + h_d(x, -y) + h_d(-x, -y)). \quad (6-5)$$

The deposit of the circular release remains axisymmetric with regular spacing between contour levels indicating a uniform steady decline in the amount of deposit along the radial direction. Alternatively, for the rounded rectangular release, the contour lines spatially evolve from an initial rectangular-like outline conforming to the initial shape of the release to another rectangular-like outline, the longest side being aligned with the  $x$ -axis. In addition, the spacing between the contours is no longer uniform as in the circular case. For example, the distance between the contour  $\bar{h}_d = 4 \times 10^{-2}$  and  $\bar{h}_d = 2.5 \times 10^{-2}$  is 4 times larger along the  $x$ -axis as compared to the  $y$ -axis. Overall, Figure 6-5 shows that the final layout of the deposition profile is influenced by the initial shape of the release.

### 6.2.3.2 Evolution along the $x$ - and $y$ -axes

The dynamics and deposition of a finite-volume release of particle-laden currents is here shown to depend on the initial shape of the release. For the RR-geometry considered here, we identify two specific directions along which the variability in front

position and amount of sedimentation is the most contrasted, namely the so-called minor and major axes oriented along the  $x$ -axis and  $y$ -axis, respectively.

For the RR-geometry, the initial major (resp. minor) axis corresponds to the slowest (resp. fastest) direction of spreading along which the current covers the smallest (resp. largest) distance. The time evolution of the front position along the minor  $x$ - and major  $y$ -axis of the RR-turbidity and the RR-saline currents is presented in Figure 6-6. The vertical dashed line indicates the time  $t_c$  beyond which the fronts continually deviate from one another as a result of particle sedimentation. Here,  $t_c$  is computed as the time from which

$$r_s > r_p \quad \text{and} \quad d(r_s - r_p)/dt > 0.02, \quad (6-6)$$

where  $r_s$  and  $r_p$  are the distances between the centre and the front of the saline and particulate currents, respectively. The time  $t_c$  is observed to be non-uniform along the front, but rather azimuthally dependent. The deviation between the saline-driven and particle-driven fronts is observed to first occur along the major axis  $t_c \approx 9$ . Along the minor axis, the fronts advance at the same rate for a longer time  $t_c \approx 18$ . Figure 6-6 shows that both saline and particulate currents exhibit a preferential spreading direction, which leads to the switching of major and minor axes.

In Figure 6-7, we present the mean deposition thickness  $\bar{h}_d$  of the final deposit along the  $x$ - and  $y$ -axes. The deposition thickness along the major axis sharply drops beyond  $r = 1$ . Along the minor axis, however, the variation in thickness is slower and the current has deposited particles over a distance of 10 times the corresponding lock length. Figures 6-6 and 6-7 indicate that the radial position of the front at time  $t_c$  is close to the location where the deposition thickness becomes negligible, say less than a

percent. This may suggest that the change in the dynamics between the turbidity current and the saline current at  $t \approx t_c$  is due to the fact that most of the particles have sedimented and hence for  $t > t_c$  the concentration of particles in the turbidity current is much smaller than  $\phi_0$ , these particles being transported as a suspension.

### 6.2.3.3 Influence of the settling velocity

While the effect of varying the settling velocity (via particle diameter) has been investigated in the past for circular turbidity currents (Bonnecaze *et al.* 1995), we here explore the configuration of non-circular geometries in Figure 6-8. In this section, we will mainly consider Exp 6-3 ( $V_s = 0.029$ ), 6-4 ( $V_s = 0$ ), and 6-5 ( $V_s = 0.11$ ). Note that Exp 6-4 is a saline current but here, it is regarded as a limiting case of a particle-laden current with zero settling velocity, while the particles diameter in Exp 6-5 are about twice as large as those in Exp 6-3. Note that the initial density of the current in these experiments is identical, and hence the currents are likely to advance at the same velocity at early times, as confirmed in Figure 6-8 showing the temporal evolution of the front position. Here, the effect of settling velocity is first perceived along the initial major axis, for which the front dynamics deviate from one experiment to the other at a much earlier time ( $t \approx 3$ ). In the case  $V_s = 0.11$ , the current ceases to advance along the major axis at  $t \approx 5$ , while along the initial minor axis, the deviation occurs at  $t \approx 6$ . It is important to note that switching of axes is observed for all the cases considered in Figure 6-8. As for the deposition pattern, we observe that the larger  $V_s$ , the smaller the extent and hence the larger the thickness at the centre (not shown). For instance,  $\bar{h}_d \approx 6 \times 10^{-2}$  ( $9 \times 10^{-2}$ ) at the centre of the pattern for  $V_s = 0.029$  ( $0.11$ ). This is in line with

the results of Figure 6-8 showing that the distance of propagation is smaller as  $V_s$  is increased, due to the stronger sedimentation process.

#### **6.2.3.4 Influence of the settling velocity**

In this section, we consider the effect of the initial volume fraction  $\phi_0$  by comparing the results of Exp 6-3 to those of Exp 6-6 for which  $\phi_0 = 0.27$  and  $0.13$ , respectively. Figure 6-9 shows the time evolution of the front position along the  $x$ - and  $y$ -axis in both cases. We observe that with a smaller initial particle volume fraction, the extent of the front along the specific axes is smaller as well, however the switching of axes is still identifiable. The smaller spreading distance in Exp 6-6, which is a result of the lower initial volume fraction, is observed to vary azimuthally since the propagation distance ( $r_N - r_N(t = 0)$ ) is shorter by 50% along the major axis and by 20% along the minor axis, as compared to the propagation distance in Exp 6-3. The deposition profile of the  $\phi_0 = 0.27$ -current is somewhat similar to that of the  $\phi_0 = 0.13$ -current, as shown in Figure 6-10. A close inspection of the deposition patterns in both cases (Figure 6-5B and 6-10A) indicates that the extent of the deposit is slightly smaller in the case of the current of smaller initial volume fraction, as a result of the initial reduced gravity, and hence smaller front speed.

#### **6.2.3.4 Influence of the initial height aspect ratio**

In order to investigate the influence of the initial height aspect ratio  $\lambda$ , we carried out three experiments where the geometry, volume fraction, and particle diameter were held constant. Three values of  $\lambda$  were chosen:  $= 0.5$ ,  $1$  and  $2$  (corresponding to experiments 6-10, 6-3 and 6-1, respectively). In Figure 6-11, we compare the time evolution of the front position along the  $x$ - and  $y$ -axes. Note that for clarity, we choose a

fixed length scale of  $\tilde{h}_0 = 4.65$  cm pertaining to Exp 6-3. This is equivalent to plot  $r_N \lambda$  as a function of  $t\sqrt{\lambda}$ . For comparison we plotted in insert  $r_N$  as a function of  $t$ . As the initial height aspect ratio is increased, the extent of the current is increased, as expected. For all  $\lambda$ , the current's dynamics is non-axisymmetric and we observe a switching of axes, the long-time length-to-width ratio remaining uniform with a value of 1.9, approximately.

The final mean deposition thickness along the minor and major axes is shown in Figure 6-12. Firstly, as  $\lambda$  is increased, the thickness of the deposit at the centre of the release is observed to decrease (recall that we adopt a single length scale for all three experiments). Secondly, the slope of the deposition profile is lower (along both specific axes) as  $\lambda$  is increased. This indicates a stronger transport of the particles inside high- $\lambda$  currents, which is in line with the fact that here the Reynolds number of the currents is larger at high  $\lambda$  (Table 6-1), and hence the propagation is faster (in the range of Reynolds numbers considered here).

#### 6.2.3.4 Influence of the lateral boundaries

In order to assess the influence of the tank boundaries on the dynamics of the currents, we performed an extra-experiment (Exp 6-2) where we placed 2 vertical panels (each at an opposite end of the tank) having the same width and height as the tank at a distance of 10 cm from the tank walls normal to the  $x$ -axis. With the panels in place, the new dimensions of the tank become  $\tilde{L}_x \times \tilde{L}_y \times \tilde{L}_z = (100 \times 120 \times 40)$  cm. In Figure 6-13, we present the temporal evolution of the front position and velocity and the final mean deposition thickness along the minor  $x$ -axis. The results indicate that the position of the boundaries does not hinder the advancement of the current or its deposition profile. Furthermore, from the inset of Figure 6-13A, the front velocity is

observed to drop down to 10 times its maximum value as the front advances beyond  $t = 30$ . Here,  $u_N$  is calculated through backward differencing from a high order polynomial curve fit of the front position. The large reduction in speed as the current approaches the boundaries is the primary reason for the marginal effect of the lateral boundaries on the current dynamics and particle deposition.

### 6.3 Simulations of Finite-Release Non-Circular Particle-Laden Currents

#### 6.3.1 Equations and Numerical Setup

The particle-laden mixture is here treated as a continuum and a two-fluid formulation is adopted. We follow Cantero *et. al* (2008b) by implementing an Eulerian-Eulerian model of the two-phase flow equations. The model involves mass and momentum conservation equations for the continuum fluid phase, an algebraic equation for the particle phase momentum, where the particle velocity is taken to be equal to the local fluid velocity and an imposed settling velocity derived from the Stokes drag force on the particles and a transport equation for the dimensionless particle phase concentration  $\rho$ . The dimensionless system of equations reads

$$\nabla \cdot \mathbf{u} = 0 \quad (6-7)$$

$$\frac{D\mathbf{u}}{dt} = \rho \mathbf{e}^g - \nabla p + \frac{1}{Re} \nabla^2 \mathbf{u} \quad (6-8)$$

$$\mathbf{u}_p = \mathbf{u} + V_s \mathbf{e}^g \quad (6-9)$$

$$\frac{\partial \rho}{\partial t} + \nabla \cdot (\rho \mathbf{u}_p) = \frac{1}{Sc Re} \nabla^2 \rho. \quad (6-10)$$

We denote by  $\mathbf{u}_p$  and  $\mathbf{u}$  the velocities of the particle and continuum fluid phases, respectively. The settling velocity  $V_s$  is determined from the Stokes drag force on spherical particles with small particle Reynolds number as defined in (6-2).  $\mathbf{e}^g$  is a unit vector pointing in the direction of gravity. Here, we employ the Boussinesq

approximation assuming that small density differences between the particle-laden solution and the ambient play a role only in the buoyancy term (first term in the R.H.S of 6-8). Unless stated otherwise, all the parameters are dimensionless. The length, velocity and time scales are identical to those defined in (6-11). The density and total pressure are made dimensionless as follows (recall that tilde denotes a dimensional quantity)

$$\rho = \frac{\tilde{\rho} - \tilde{\rho}_a}{\tilde{\rho}_{c0} - \tilde{\rho}_a} ; \quad p = \frac{\tilde{p}}{\tilde{\rho}_a \tilde{U}^2}. \quad (6-11)$$

The Schmidt number introduced in (6-10) is defined as

$$Sc = \tilde{\nu} / \tilde{\kappa} . \quad (6-12)$$

where  $\tilde{\kappa}$  represents the molecular diffusivity of the continuum fluid phase.

The numerical setup depicted in Figure 6-14 is identical to that of the experiments. The simulations are carried out inside a rectangular computational domain of dimensions  $L_x \times L_y \times L_z$  using a spectral code which has been extensively validated (Cortese & Balachandar 1995; Cantero *et al.* 2007). Periodic boundary conditions are imposed along the horizontal  $x$ - and  $y$ -directions. No-slip and free-slip conditions are imposed for the velocity of the continuous phase along the bottom ( $z = 0$ ) and top ( $z = 1$ ) walls, respectively. Mixed and Neumann boundary conditions are imposed for the concentration of the particle phase at the bottom and top walls, which translate into zero particle resuspension and zero particle net flux, respectively, *viz*

$$\left( \frac{1}{Sc Re} \frac{\partial \rho}{\partial z} - V_s \rho \right)_{z=0} = 0; \quad \left( \frac{\partial \rho}{\partial z} \right)_{z=1} = 0. \quad (6-13)$$

We present results from the simulations listed in Table 6-2. Note that simulation 6-1 (circular release) corresponds to Exp 6-10 while simulations 6-2 and 6-3 (rounded-

rectangular release) correspond to Exp 6-1. The Reynolds number of all the simulations was set at  $Re = 8430$ , which is lower than that of the experiments ( $Re = 10520$ ). The Reynolds number and grid resolution were chosen to achieve a range between 4 and 6 decades of decay in the energy spectrum for all variables. The reason about having two simulations for a single experiment is to assess a possible effect of turbulence initially present in the real system due to (i) initial stirring performed inside the hollow cylinder in order to create a homogeneous suspension before releasing the current and (ii) the shear at the walls of the hollow cylinder which is generated during lift off. On the one hand, the release mechanism may generate some large-scale vorticity and velocity fluctuations in the current at the time of release. In Sim 6-2, the current is “ideally” placed in contact with the ambient fluid at the start of the simulation, i.e. no perturbation is artificially added. Since it is difficult to impose some large-scale, organized initial perturbation on the velocity field, the perturbation field in the experiments being unknown, we add a small random perturbation to the density field in Sim 6-3, in order to crudely approximate the possible presence of initial perturbation in the system.

### 6.3.1 Front Evolution

As a first verification, we compare in Figure 6-15 the time evolution of the front position for the circular case. As for the simulation, the front is taken as the location where the height of the current drops below a critical value  $\varepsilon$ . The height of the current is calculated by vertically integrating the concentration field between the bottom and top boundaries of the domain as

$$h = \int_0^1 \rho dz . \quad (6-14)$$

Here, we choose  $\varepsilon = 10^{-4}$ . Note that the location of the front is not sensitive to the value of  $\varepsilon$  in the range  $10^{-5} < \varepsilon < 10^{-3}$ . The simulation captures well the dynamics of the cylindrical particle-laden current both qualitatively and quantitatively, as indicated by the azimuthally averaged front position presented in Figure 6-15C, which is in good agreement with experimental data.

In Figure 6-16, we present the time evolution of a collapsing initially rounded-rectangular turbidity current, obtained from experiment and simulation. As for the simulation, two cases are shown (Sim 6-2 and 6-3) the difference being that an initial random perturbation of the density field was imposed in the latter (refer to §6.3.1 for a discussion). Both simulations are in good agreement with experimental data at early times, namely  $t \leq 14$  (Figure 6-16D). During this stage, the front contours are roughly similar in the simulations. Note that in Figure 6-16D, we track the front along the major and minor axes of the RR-current. The front along these axes was calculated by averaging the radial distances (along the positive and negative axes) bounded by a circular wedge centred along each axis with a half-wedge angle of 2.5 degrees. For  $t > 14$  (resp.  $t > 24$ ), the computed front of the Sim 6-2 (resp. Sim 6-3)-current begins to gradually deviate from the experimental one, with the front from the Sim 6-3-current providing a better match (than the Sim 6-2-current) to that observed in the experiments. The difference in the computed front location from the Sim 6-2 and Sim 6-3-current indicates that the initial perturbation does influence, even though slightly, the dynamics of the simulated currents. As observed in Figure 6-16C, the initial perturbation increases the three-dimensionality of the flow and results in a slower moving averaged front.

The fact that the computed current for which an initially perturbed density field was applied spreads slower than the unperturbed one may be interpreted as follows. Let us consider the front velocity of the gravity current to be given by the Huppert-Simpson (HS) relation (Huppert & Simpson, 1980)

$$\tilde{v}_N = Fr \sqrt{\tilde{g}_r \tilde{\eta}_N}. \quad (6-15)$$

where  $\tilde{v}_N$ ,  $\tilde{\eta}_N$ ,  $\tilde{g}_r$ , and  $Fr$  represent the front velocity, front height, reduced gravity, and the HS Froude number, respectively. During the late stages of the release, the ratio of the current height to ambient height is small, and the Froude number may be considered as a constant  $Fr = 1.19$ . Moreover, assuming the reduced gravity  $\tilde{g}_r$  to be constant and expressing the circumferential variation of current height  $\tilde{\eta}_N$  as the sum of a mean  $\bar{\eta}$  and fluctuating contribution  $\eta'$ , we can write

$$\tilde{v}_N = Fr \sqrt{\tilde{g}_r (\bar{\eta} + \eta')}. \quad (6-16)$$

In (6-16), we have assumed that the HS relation is applicable at every point along the front of the current. Using Taylor series expansion and applying the averaging operator to (6-16), we can approximate the mean front velocity as

$$\bar{v}_N = Fr \sqrt{\tilde{g}_r \bar{\eta}} \left( 1 - \frac{1}{8} \frac{\overline{\eta'^2}}{\bar{\eta}^2} \right). \quad (6-17)$$

Recall that the overbar denotes the azimuthal averaging operator. Note that  $Fr \sqrt{\tilde{g}_r \bar{\eta}}$  would be the front velocity if the current was of uniform height. (6-17) indicates that the larger the ratio of height fluctuations to mean height, the smaller the mean velocity. During the early stages of the release, the mean height of the current is large and therefore the fluctuations do not significantly affect the front velocity, however as the

mean front height diminishes,  $\overline{\eta'^2}/\overline{\eta}^2$  increases and leads to a slower moving front as observed in Figure 6-16D.

Another possible reason for the discrepancy between simulations and experiments is that in the simulations, we consider truly monodisperse particles of uniform density by imposing a unique settling velocity. In the experiments however, the size distribution of particles is not exactly monodisperse. This polydispersity of particles may affect the settling velocity leading to further variations in the volume fraction of particles inside the current, and consequently modify the reduced gravity and mean front velocity. It is also likely that the particles are not uniformly distributed within the hollow cylinder and some stratification may have occurred before the release, despite our best efforts to have a uniform distribution.

### 6.3.3 Particle Deposition

Iso-contours of the local deposition thickness  $h_d$  of a circular and non-circular turbidity current are plotted in Figure 6-17. Clearly, the deposited pattern strongly depends on the shape of release. The cylindrical release exhibits a roughly circular sedimentation profile (Figure 6-17A and C) while that of the RR-release is of rectangular shape, the longer side being along the x-axis (contrary to the initial orientation of the rounded rectangle), the extent of the deposit being well captured in the simulations (Figure 6-17D). Note that in the experiments, the deposit is thickest at the centre of the domain and decreases as one moves radially outwards, whereas in the simulations, a second local maximum is observed at  $r \approx 1.3$  for the circular release and at  $1.5 \leq r \leq 2$  for the RR-one, the specific location being azimuthally dependent. The possible reason for this discrepancy is discussed later.

The mean final deposition thickness  $\bar{h}_d$  obtained from the experiment is compared with simulation results in Figure 6-17E and f for the circular and RR-release, respectively. As for the circular release, the numerical deposition thickness is overpredicted (underpredicted) close to the centre (at intermediate radial distances  $1.8 < r < 2.8$ ) and is in good agreement with experiment at larger  $r > 3$ . Recall that a local peak at  $r \approx 1.3$  is visible in the numerical deposition thickness as opposed to the experimental one. For the RR release, a roughly similar trend is observed, however comparison is more difficult since the final thickness is not azimuthally averaged as in the circular case.

In order to understand the presence of the second local maximum of deposition thickness in the simulation, we present in Figure 6-18 the space-time diagram of the azimuthally averaged height  $\bar{h}$  and mass deposition rate of particles per unit area  $\bar{m}_d$  of the cylindrical release. Here,  $\bar{h}$  and  $\bar{m}_d$  are computed as

$$\begin{aligned}\bar{h}(r, t) &= \frac{1}{2\pi} \int_0^{2\pi} h(r, \theta, t) d\theta \\ \bar{m}_d(r, t) &= \frac{V_s}{2\pi} \int_0^{2\pi} \rho(r, \theta, z = 0, t) d\theta.\end{aligned}\tag{6-18}$$

We observe in Figure 6-18A that at  $t \approx 3.5$ , a bare region for which the height of the current is negligible, appears at  $r \approx 0.6$ . This region widens as the current spreads radially outwards. At  $t \approx 4.5$ , the extent of the bare region is at a maximum. The existence of such a bare region leads to an adverse hydrostatic pressure gradient, which slows the trailing edge behind the moving front and eventually reverses flow direction radially inward. This flow reversal seems to be correlated to the location of the second maximum of deposition as observed from the comparison of  $\bar{h}$  and the mass

deposition rate of particles in Figure 6-18A and B, respectively. A similar flow reversal is observed for the RR release (not shown) and is likely to be responsible for the second maximum in the deposition profiles.

### 6.3.4 Possible Contribution of Bedload Transport

The discrepancy between the experimental and numerical deposition profiles may be due to either the redistribution of particles as a result of local bedload transport or possible near-wall particle resuspension. Recall that bedload transport is not accounted for in the present simulations. However, if the flow is energetic and the near-wall shear stress exceeds a critical value, particles may roll or slide over the bed or even be reentrained back into the current. Since the pioneering work of Shields (1936), it is widely accepted that for a near-bed Reynolds number  $Re_*$  there exists a critical shear stress  $\tilde{\tau}_{cr}$  above which particles are set in motion (these quantities are defined in 6-19). The value of the critical shear stress depends on several parameters including the particle and fluid densities, the particle diameter as well as the kinematic viscosity of the fluid. For the present experimental conditions, we estimate the critical shear stress to be  $\tilde{\tau}_{cr} \approx 0.016 \text{ N/m}^2$  and the corresponding near-bed critical Reynolds number  $Re_* \approx 1.2$ , using

$$\tilde{\tau}_{cr} = (\tilde{\rho}_p - \tilde{\rho}_a) \tilde{g} \tilde{d}_p \theta_{cr}; \quad Re_* = \frac{\sqrt{\tilde{\tau}_{cr} / \tilde{\rho}_a} \tilde{d}_p}{\tilde{\nu}} \quad (6-19)$$

where  $\theta_{cr}$  is the so-called critical Shields parameter which depends on  $Re_*$  and is here estimated as  $\theta_{cr} \approx 0.1$  using the Shields (1936)'s diagram.

In order to assess the possible contribution of bedload transport, we plot in Figure 6-19A-B the space-time diagram of the azimuthally averaged vertical gradient  $\overline{du_r/dz}$  of the radial velocity at the bottom wall for the circular release. Note that a value

of the critical shear stress  $\tilde{\tau}_{cr} \approx 0.016 \text{ N/m}^2$  corresponds to  $|\overline{du_r/dz}| \approx 13$ . A positive (resp. negative) velocity gradient above this value is likely to indicate outward (resp. inward) bedload transport. In Figure 6-19, only the regions of  $|\overline{du_r/dz}| > 13$  are mapped. The wall shear stress is observed to be predominantly positive and above the threshold in a significant region of the space-time diagram (Figure 6-19A). According to this criterion, possible outward bedload transport is likely to be present. Note that some small regions of significantly negative wall shear stress are also visible, for instance at  $(r \approx 1, t \approx 2.5)$  as seen in Figure 6-19B. Interestingly, such a region is observed to be at the vicinity of a region of significantly positive wall shear stress located at  $(r \approx 0.5, t \approx 2.5)$  approximately. This may lead to bedload transport in such a way that particles accumulate at some specific radial location. This is in line with the observation of a second local maximum of the mean deposition thickness of the circular release, the location of which being at  $r \approx 1.3$  (Figure 6-17E).

As for the RR-release, the mean quantities  $\overline{du/dz}$  and  $\overline{dv/dz}$  corresponding to the vertical velocity gradient at the bottom wall along the minor  $x$ - and major  $y$ -axis are plotted in Figure 6-19C-F. The overbar here denotes the following averaging

$$\begin{aligned}\overline{du/dz}(x, 0, 0, t) &= \frac{1}{2}[du/dz(x, 0, 0, t) - du/dz(-x, 0, 0, t)] \\ \overline{dv/dz}(0, y, 0, t) &= \frac{1}{2}[dv/dz(0, y, 0, t) - dv/dz(0, -y, 0, t)]\end{aligned}\tag{6-21}$$

where  $u$  and  $v$  are the velocity components in the  $x$ - and  $y$ -directions, respectively. Again a significant (resp. small) region of highly positive (resp. negative) wall shear stress is observed, suggesting the possible contribution of bedload transport to be significant. Note that in this non-circular release, the wall shear stress is different between the  $x$ - and  $y$ -directions, both in terms of distribution and intensity. This is in line

with the highly non-axisymmetric spatial distribution of the mean deposition thickness observed in Figure 6-17B and D.

Figure 6-20 presents the radial distribution of  $\overline{du_r/dz}$  at two time instances  $t = 2$  and  $t = 2.5$ , respectively, in the case of the circular release. Three regimes are defined depending on the specific value of  $\overline{du_r/dz}$ , namely a region of no-bedload transport ( $-13 \leq \overline{du_r/dz} \leq 13$ ), possible outward transport  $\overline{du_r/dz} > 13$  and possible inward transport  $\overline{du_r/dz} < -13$ . Strong fluctuations of the bottom shear stress are observed. For instance at the time  $t = 2.5$ ,  $\overline{du_r/dz} \approx 220$  at  $r \approx 0.6$  while  $\overline{du_r/dz} \approx -150$  at  $r \approx 0.75$ . In addition, the local wall shear stress appears to be highly time-dependent, since the aforementioned fluctuation is not visible at time  $t = 2$  for instance.

Iso-contours of the current's concentration and zones of high vorticity are plotted in Figure 6-21 for the same time instances as in Figure 6-20. Here, regions of high vorticity are obtained from contours of the swirling strength  $\lambda_{ci}$  which is defined as the absolute value of the imaginary part of the complex eigenvalue of the velocity gradient tensor (Zhou *et. al.* 1999; Chakraborty *et. al.* 2005). Considering Figure 6-20 together with Figure 6-21, one may observe that the positive and negative peaks of  $\overline{du_r/dz}$  are strongly correlated with the regions of high vorticity. In particular, the peak of positive (resp. negative) shear stress is found to correspond to the presence of a counter-clockwise (resp. clockwise) rotating vortex tube that is generated close to the bottom wall. For example, at  $t = 2$ , the negative peak observed at  $r \approx 1.1$  in Figure 6-20 corresponds to the clockwise rotating vortex tube denoted as  $V_{1a}$  in Figure 6-21A and located at ( $r \approx 1.1, z \approx 0.05$ ).

### 6.3.5 Possible Contribution of Particle Resuspension

In this section, we aim at assessing the possible effect of particle resuspension on the dynamics and deposition of a particle-laden current. In general, resuspension occurs when the bottom shear stress is large enough to dislodge the particle from the bed and the near wall vertical velocity exceeds the particle settling velocity. In Figure 6-21, we plot the radial distribution of the vertical velocity component  $w$  at two distances from the bottom wall, namely  $z = 4d_p$  and  $2d_p$ , respectively. For comparison, the criterion  $w = V_s$  is also plotted. Recall that all the variables in Figure 6-21 are azimuthally averaged. At  $t = 2$ , one can see at a distance of  $z = 2d_p$  from the wall that the vertical velocity never reaches the threshold value  $w = V_s$ , while for  $z = 4d_p$  the region for which  $w > V_s$  is marginal. Similarly, at  $t = 2.5$  only few  $w > V_s$  regions are observed. Overall, the results of Figure 6-21 support the assumption done in the simulations that the possible contribution of resuspension is small and hence can be neglected.

### 6.3.5 Vortex Dynamics

As mentioned earlier, the high values of the bottom shear stress and local vertical velocity  $w$  are observed in regions of near-wall vortex tubes. For instance, the vortex tubes  $V_{1a}$  and  $V_{1b}$  depicted in Figure 6-21 exhibit a clockwise rotation and hence act to push fluid vertically upward (resp. downward) in the region just behind (resp. in front of) the centre of the vortex core. This is in line with the positive and negative values of  $w$  in the vicinity of  $V_{1a}$  and  $V_{1b}$ . One can also observe the presence of two counter rotating vortices, namely  $V_{3b}$  (counter-clockwise rotating) and  $V_4$  (clockwise

rotating) inside the body of the current (see e.g. Figure 6-21B) leading to local oscillations in the amplitude of  $w$ .

Unlike the bottom shear stress, which remains above the critical value  $|\overline{du_r/dz}| > 13$  over a wide portion of the current's length, the amplitude of the vertical velocity component  $w$  is above the critical condition  $w > 0.02$  only in some narrow regions of the current. Again, these regions correspond to the presence of intense near-wall vortex structures which move radially outwards at a velocity which is close to that of the current's front. These vortex tubes may grow in size and intensity ( $V_{1a}$  vs.  $V_{1b}$ ), move closer to the bottom wall ( $V_{3a}$  vs.  $V_{3b}$ ) or away from the bottom wall ( $V_{1a}$  vs.  $V_{1b}$ ). Interestingly, as the counter-clockwise rotating vortex  $V_{3b}$  approaches the bottom wall, it locally accelerates the flow near the surface. This local acceleration coupled with the no-slip boundary condition at the bottom wall results in the formation of a clockwise rotating tube  $V_4$ .

## 6.4 Conclusion

We have presented results from experiments and simulations of circular and non-circular finite-volume Boussinesq density currents, including particle-laden and density-driven (scalar) flows. The initial shape of the release was shown to significantly influence the propagation and deposition of the particle, with a substantial azimuthal dependence for non-circular releases. In particular, the measurements of the time evolution of the front and spatial distribution of the final deposition thickness indicate that for a rounded-rectangular release, the current advances the fastest (resp. slowest), extends the farthest (resp. shortest) and deposits the most (resp. least) amount of particles along its initial shortest (resp. longest) side.

Various parameters such as the settling velocity, height aspect ratio and initial volume fraction of particles in the mixture were varied in order to assess their influence on the dynamics and deposition of non-circular releases and confirm the robustness of the abovementioned dynamics with respect to these parameters.

Fully-resolved simulations were performed in order to complement the experiments and provide insight about local processes involved in the deposition of the particles in circular and non-circular releases, in particular bedload transport and particle resuspension. Firstly, the front speed and deposition pattern compares favourably with experiments, however slight differences are observed. The thickness at the centre of the deposit is smaller in the experiments than in the simulations, and some local extrema in the deposition profile are observed in the simulations contrary to experiments where the measured thickness monotonically decreases as one moves radially outwards.

The spatial and temporal evolution of the near-wall vertical velocity inside the current was considered and suggests that particle resuspension only marginally occurs in the present problem. In particular, the vertical component of the near-wall velocity rarely exceeds the settling velocity, and when this occurs it is limited to a small portion of the domain only, supporting the assumption done in the simulations that the contribution of resuspension can be neglected.

A detailed inspection of the spatial and temporal evolution of the wall shear stress inside the current reveals that bedload transport is likely to influence the deposition of particles. More specifically, the wall shear stress is found to be significant (as compared to a critical threshold) over a wide portion of the current's body and for

significant times. This effect however is not taken into account in the simulations and may need to be included to confirm if it is responsible for the observed discrepancy between experiments and simulations. Overall, the regions of largest near-wall vertical velocity and wall shear stress were observed to correspond to the location of vortices. This confirms that the local structure of the flow inside non-circular particle-laden flows may have a significant influence on the transport and deposition of particles.

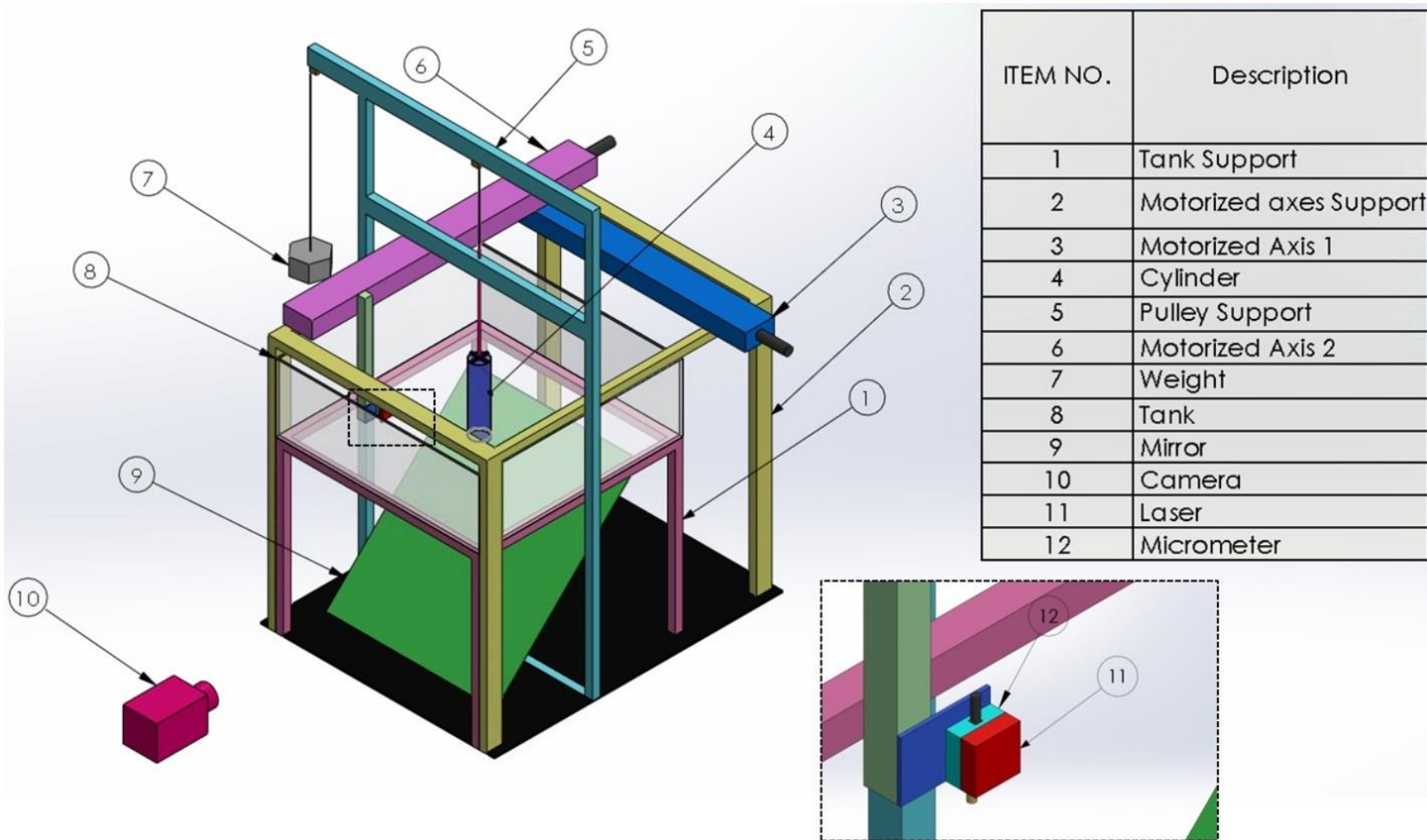


Figure 6-1. Isometric view of the experimental setup. Inset: close-up view of the apparatus used to measure the deposit height. Note that for clarity, the tank and the motorized axes support have been removed from the picture in the inset.

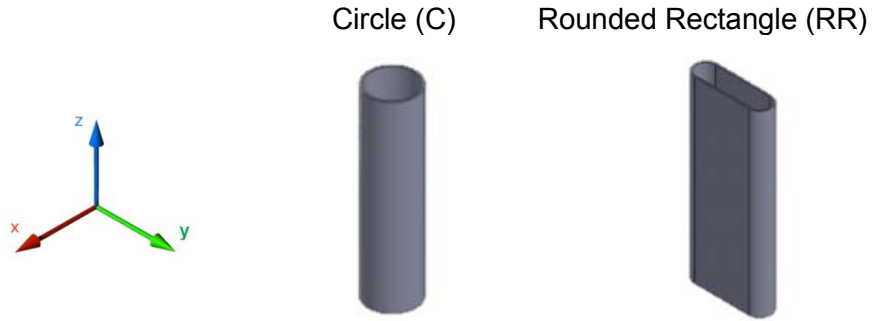


Figure 6-2. Shape of the hollow cylinders used in the experiments. The height and equivalent radius of each cylinder are 400 mm and 46 mm, respectively. The size of the longest (shortest) side of the RR cylinder is 167 (44) mm. Note that the horizontal cross-section area is similar for both cylinders.

Table 6-1: List of experiments. RR, rounded-rectangle; C, circle;  $Re$ , Reynolds number defined in (6-4);  $\lambda = \tilde{h}_0/\tilde{R}_0$ , initial height aspect ratio with  $\tilde{h}_0$  being the initial height of the mixture inside the cylinder and  $\tilde{R}_0$  the equivalent radius of the cylinder;  $\tilde{\rho}_{c0}$  ( $\text{kg}/\text{m}^3$ ), initial density of the mixture;  $\tilde{m}_p$  (g), initial mass of particles;  $\phi_0$ , initial volume fraction;  $\tilde{d}_p$  ( $\mu\text{m}$ ), mean particle diameter;  $V_s$ , dimensionless settling velocity. The symbol  $\Upsilon$  indicates that the experiment was done in a tank with narrower lateral boundaries. The symbol \* indicates that the experiment is for a saline current.

Experiment	Shape	$Re$	$\lambda$	$\tilde{\rho}_{c0}$	$\tilde{m}_p$	$\phi_0$	$\tilde{d}_p$	$V_s$
6-1	RR	10520	2	1012	180	0.27	$300 \pm 20$	0.020
6-2	RR $\Upsilon$	10520	2	1012	180	0.27	$300 \pm 20$	0.020
6-3	RR	3720	1	1012	90	0.27	$300 \pm 20$	0.029
6-4	RR*	3720	1	1012	0	-	-	-
6-5	RR	3720	1	1012	90	0.27	$670 \pm 40$	0.11
6-6	RR	2630	1	1005	45	0.13	$300 \pm 20$	0.04
6-7	C	3720	1	1012	90	0.27	$300 \pm 20$	0.029
6-8	C*	3720	1	1012	0	-	-	-
6-9	RR	1315	0.5	1012	45	0.27	$300 \pm 20$	0.04
6-10	C	10520	2	1012	180	0.27	$300 \pm 20$	0.020

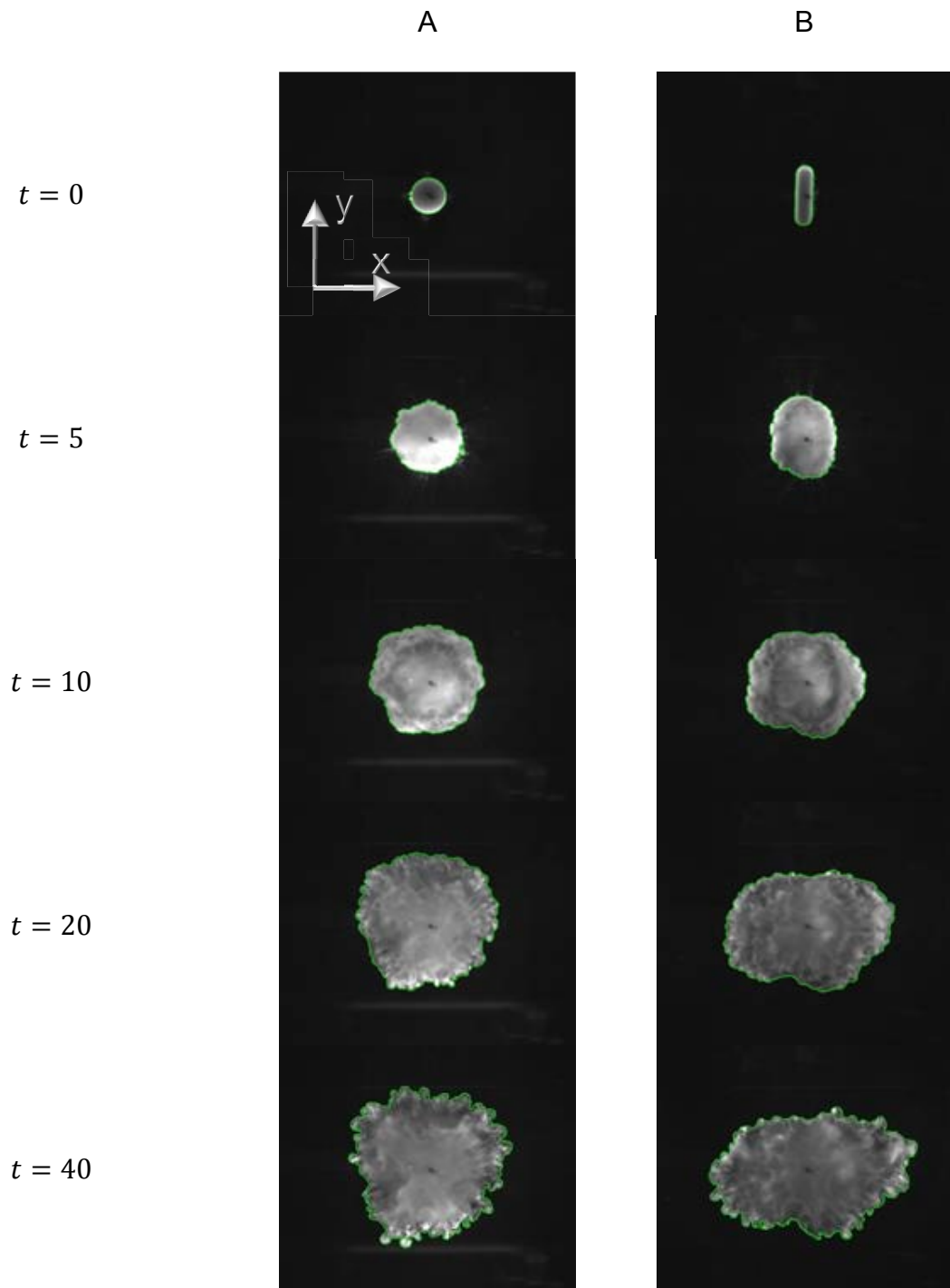


Figure 6-3. Top view of the collapse of a turbidity current of initial A) circular cross-section (Exp 6-7) and B) non-circular cross-section (Exp 6-3). The detected front is plotted in green contour..

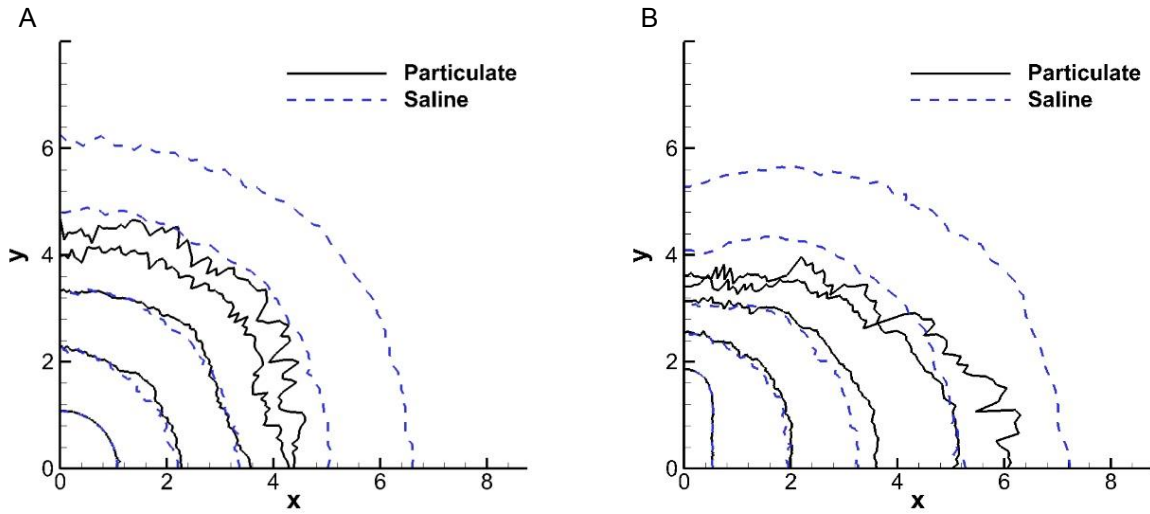


Figure 6-4. Time evolution of the mean front location of a particulate (solid line) and saline (dashed line) current of initial A) circular cross-section (Exp 6-7 and 6-8) and B) rounded-rectangle cross-section (Exp 6-3 and 6-4). The fronts are shown at  $t = 0, 5, 10, 20,$  and  $40$ .

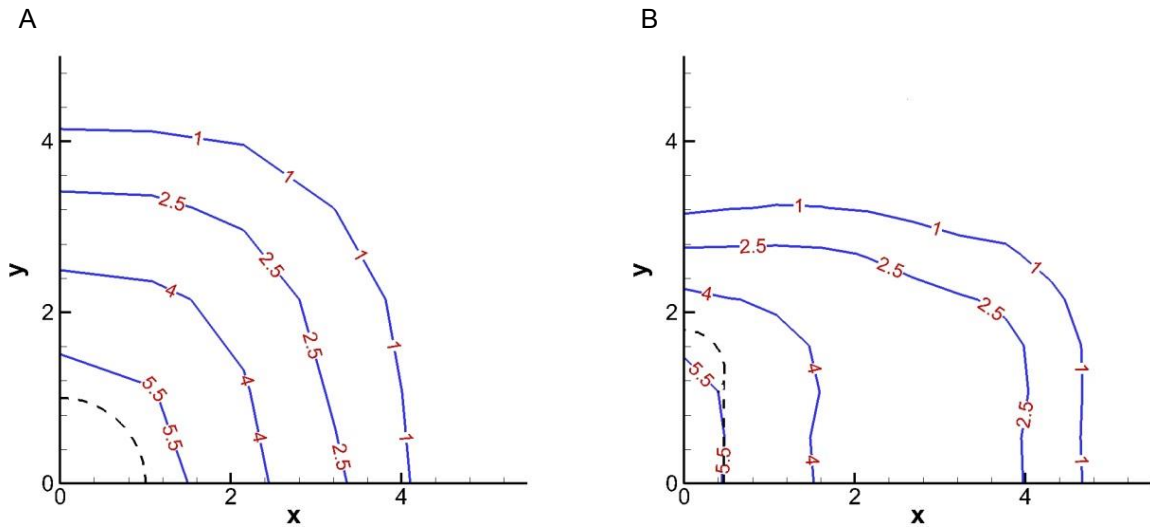


Figure 6-5. Iso-contours of the dimensionless mean deposition thickness  $\bar{h}_d$  of a turbidity current of initial A) circular cross-section (Exp 6-7) and B) non-circular cross-section (Exp 6-3). The dashed lines represent the boundaries of the hollow cylinders. Values of  $\bar{h}_d$  are given in percent.

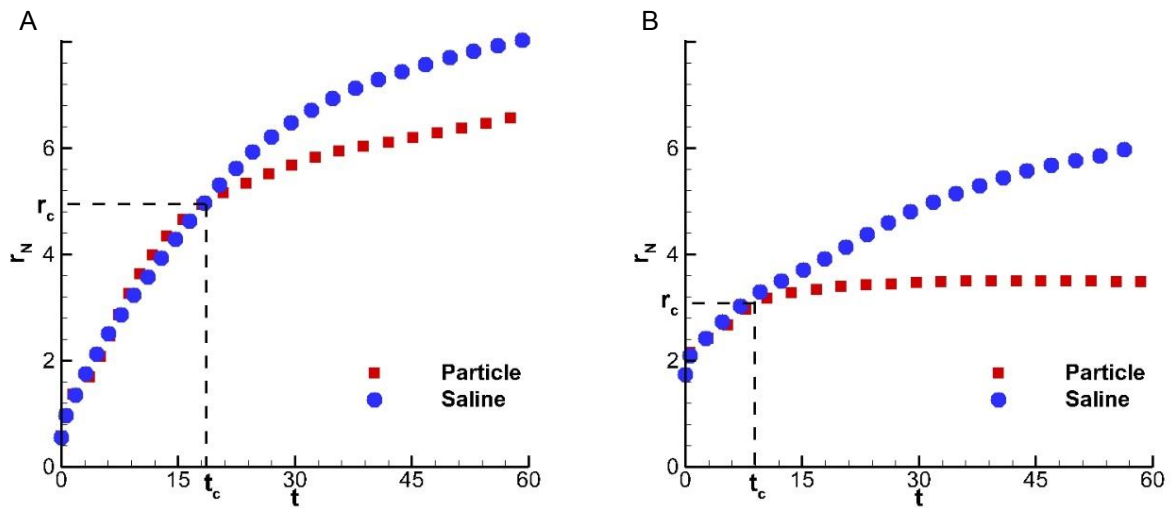


Figure 6-6. Front position  $r_N$  versus time for the RR-turbidity current (Exp 6-3, squares) and the RR-saline current (Exp 6-4, circles) along A) the minor x-axis and B) the major y-axis. The vertical (horizontal) dashed line corresponds to the critical time  $t_c$  (location  $r_c$ ) beyond which the saline front progressively deviates from the particle-laden front.

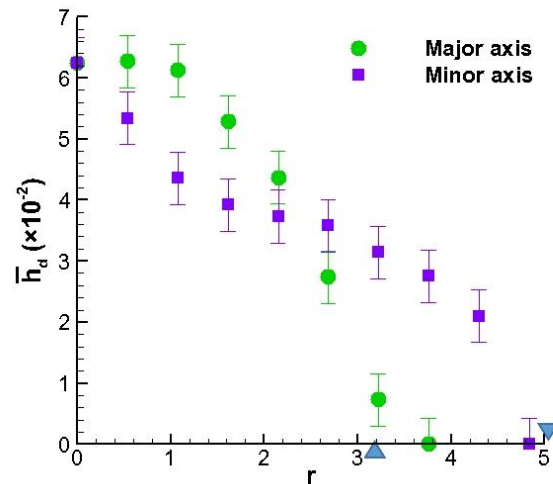


Figure 6-7. Mean final deposition thickness  $\bar{h}_d$  versus radial distance along the minor x-axis (squares) and major y-axis (circles) for the RR-turbidity current (Exp 6-3). The bars correspond to the measurement error. The upward (downward) triangles indicate the location of the critical radius of the front  $r_c$  along the minor (major) axis (Figure 6-5 for details).

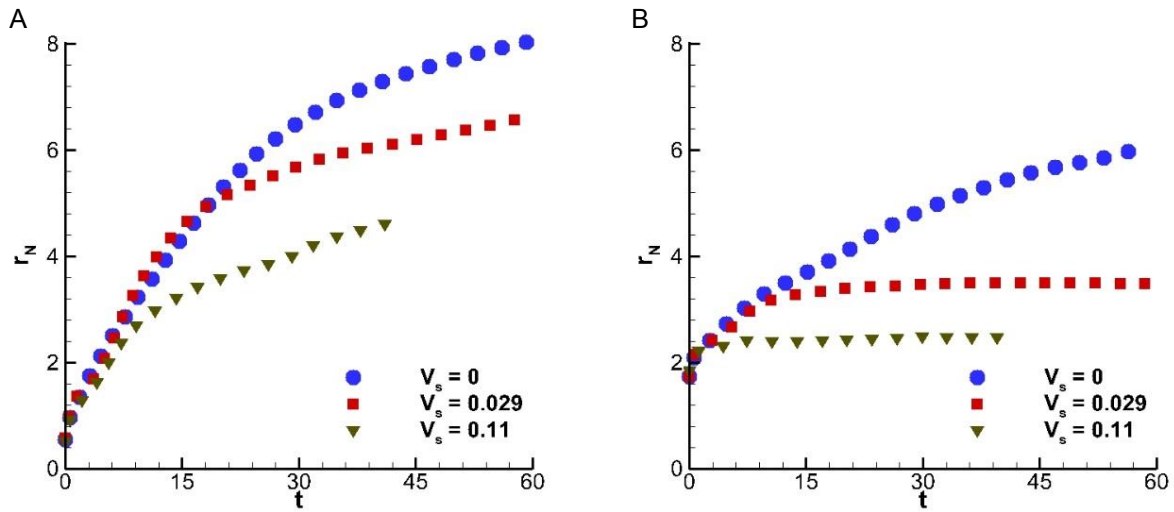


Figure 6-8. Front position versus time for currents of various settling velocity  $V_s$  along A) the minor x-axis and B) the major y-axis: ●,  $V_s=0$  (Exp 6-4); ■,  $V_s=0.029$  (Exp 6-3); ▼,  $V_s=0.11$  (Exp 6-5).

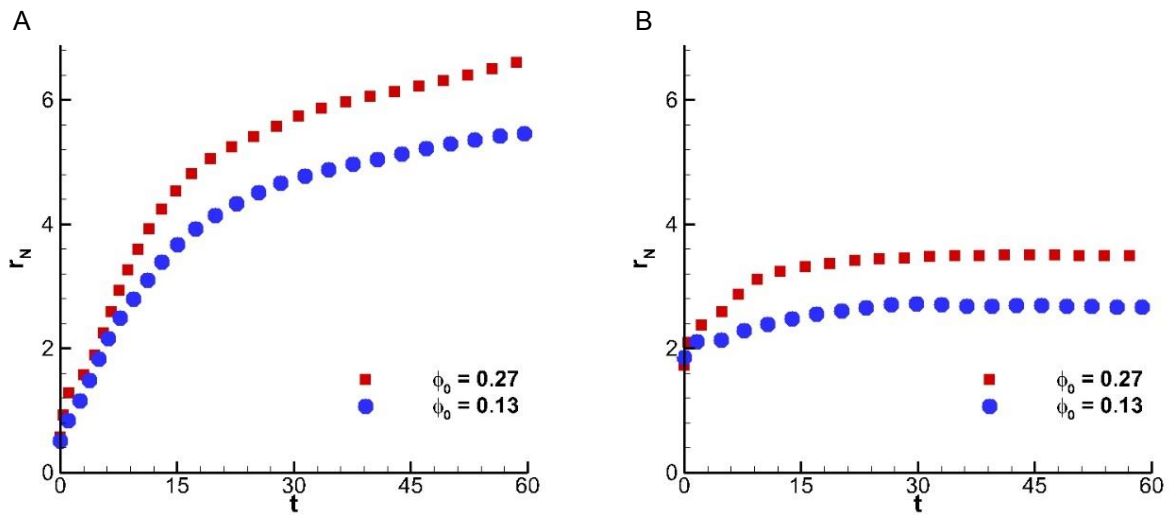


Figure 6-9. Front position versus time for various initial volume fraction  $\phi_0$  along A) the minor x-axis and B) the major y-axis: ●,  $\phi_0 = 0.13$  (Exp 6-6); ■,  $\phi_0 = 0.27$  (Exp 6-4).

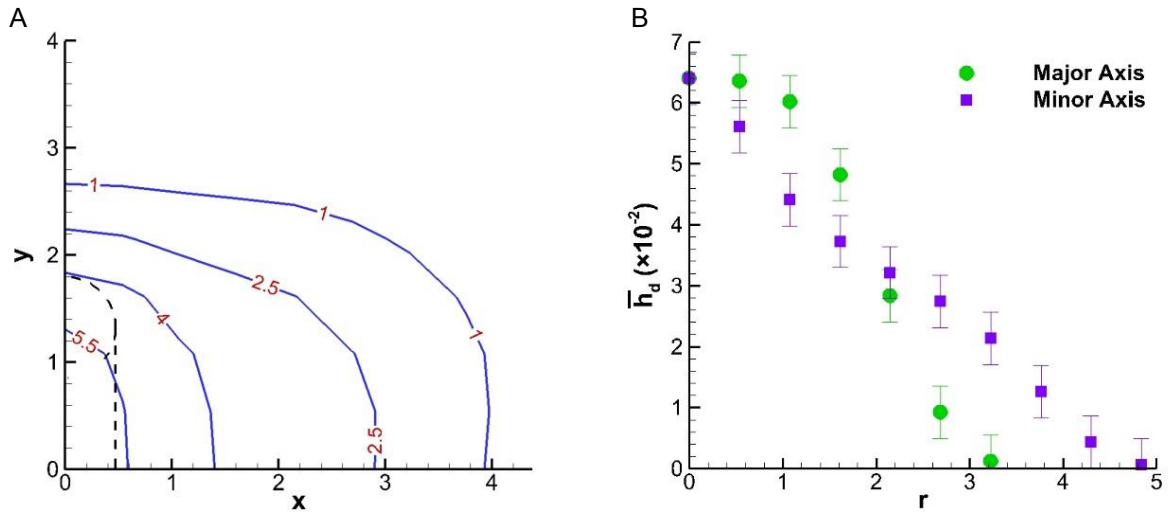


Figure 6-10. A) Iso-contours of the mean deposition thickness  $\bar{h}_d$  of the  $\phi_0 = 0.13$  - turbidity current (Exp 6-6). The dashed line represents the boundaries of the hollow cylinder. Values of  $\bar{h}_d$  are given in percent. B) Corresponding mean final deposition thickness versus radial distance along the major  $y$ -axis (circles) and minor  $x$ -axis (squares). The bars correspond to the measurement error.

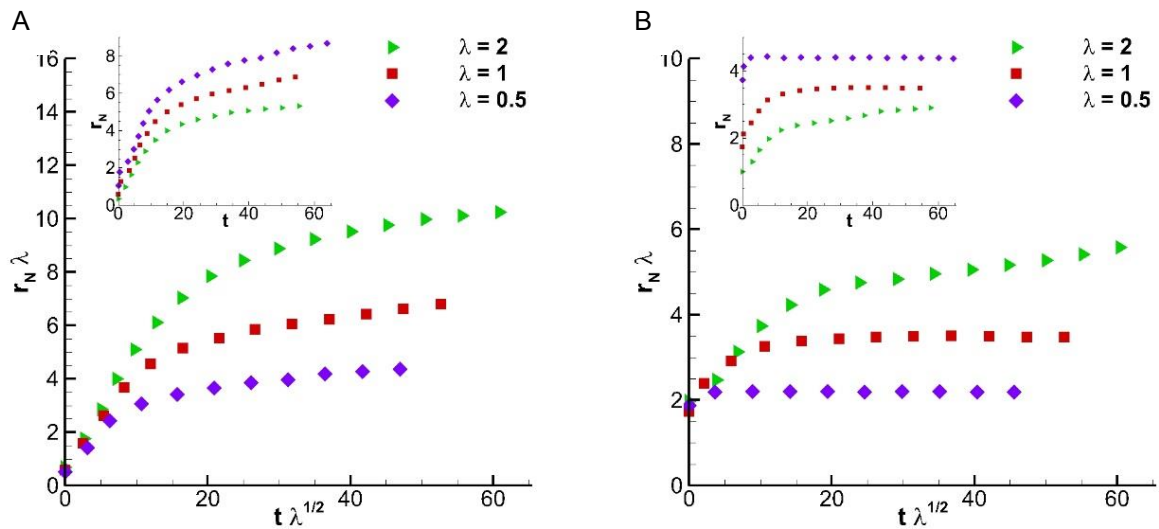


Figure 6-11. Front position versus time for currents of various initial height aspect ratio  $\lambda$  along A) the minor  $x$ -axis and B) the major  $y$ -axis:  $\blacklozenge$ ,  $\lambda=0.5$  (Exp 6-10);  $\blacksquare$ ,  $\lambda=1$  (Exp 6-3);  $\blacktriangleright$ ,  $\lambda=2$  (Exp 6-1).

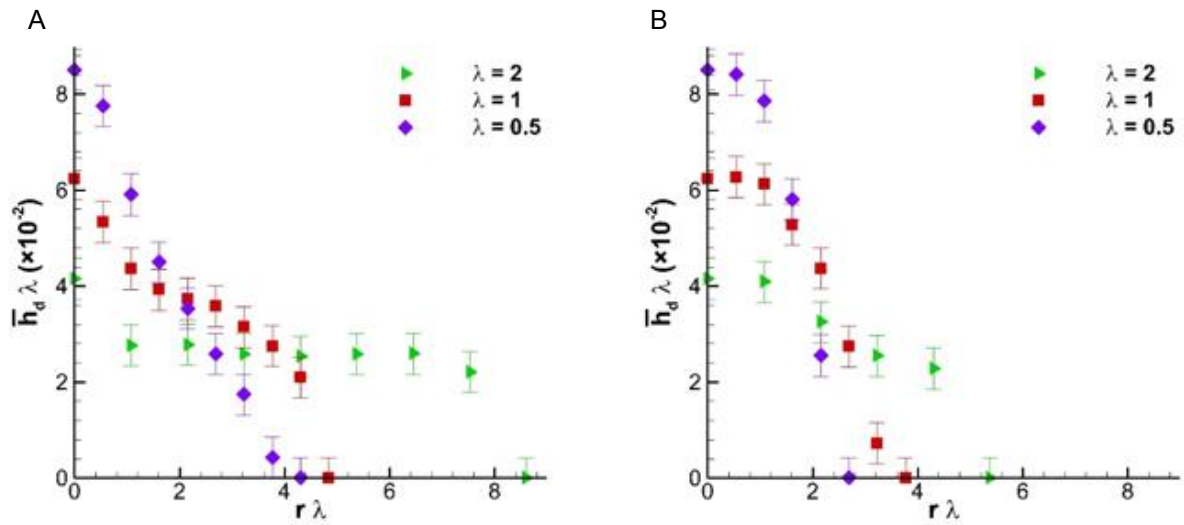


Figure 6-12. Mean final deposition thickness  $\bar{h}_d$  versus radial distance for various initial height aspect ratio  $\lambda$  along A) the minor x-axis and B) the major y-axis:  $\blacklozenge$ ,  $\lambda=0.5$  (Exp 6-10);  $\blacksquare$ ,  $\lambda=1$  (Exp 6-3);  $\blacktriangleright$ ,  $\lambda=2$  (Exp 6-1). The bars correspond to the measurement error.

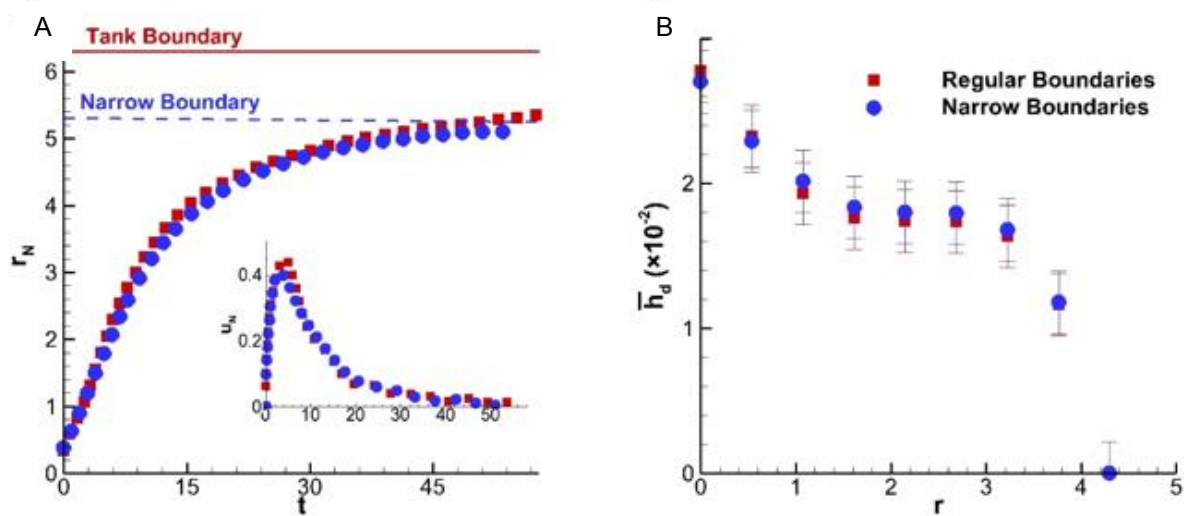


Figure 6-13. A) Front position versus time for Exp 6-1 (squares) and Exp 6-2 (circles) along the minor x-axis. The solid and dashed lines represent the location of the tank lateral wall in Exp 6-1 and 6-2, respectively. Inset: time evolution of the front velocity. B) Corresponding mean final deposition thickness  $\bar{h}_d$ .

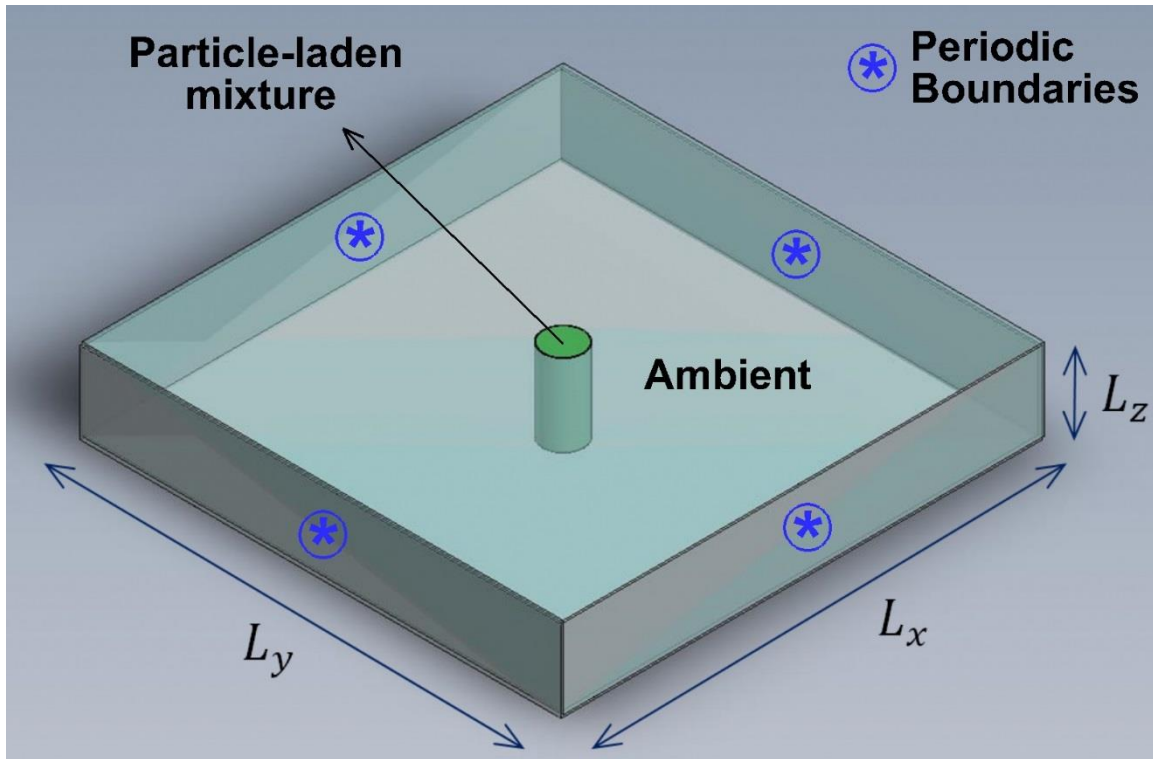


Figure 6-14. Numerical setup.

Table 6-2. List of simulations. RR, rounded-rectangle; C, circle;  $Re$ , Reynolds number defined in (6-4);  $\lambda = \tilde{h}_0/\tilde{R}_0$ , initial height aspect ratio with  $\tilde{h}_0$  being the initial height of the mixture inside the cylinder and  $\tilde{R}_0$  the equivalent radius of the cylinder;  $V_s$ , dimensionless settling velocity;  $L_x, L_y, L_z$ , dimensions of the computational domain (gravity is along the z-direction);  $N_x, N_y, N_z$ , Grid resolution. The symbol \* indicates cases where the initial concentration field is randomly perturbed.

Sim no.	Shape	$Re$	$\lambda$	$V_s$	Domain size	
					$L_x \times L_y \times L_z$	Grid Resolution $N_x \times N_y \times N_z$
6-1	C	8430	2	0.020	$12 \times 12 \times 1$	$640 \times 640 \times 159$
6-2	RR	8430	2	0.020	$10 \times 15 \times 1$	$534 \times 800 \times 159$
6-3	RR*	8430	2	0.020	$10 \times 15 \times 1$	$534 \times 800 \times 159$

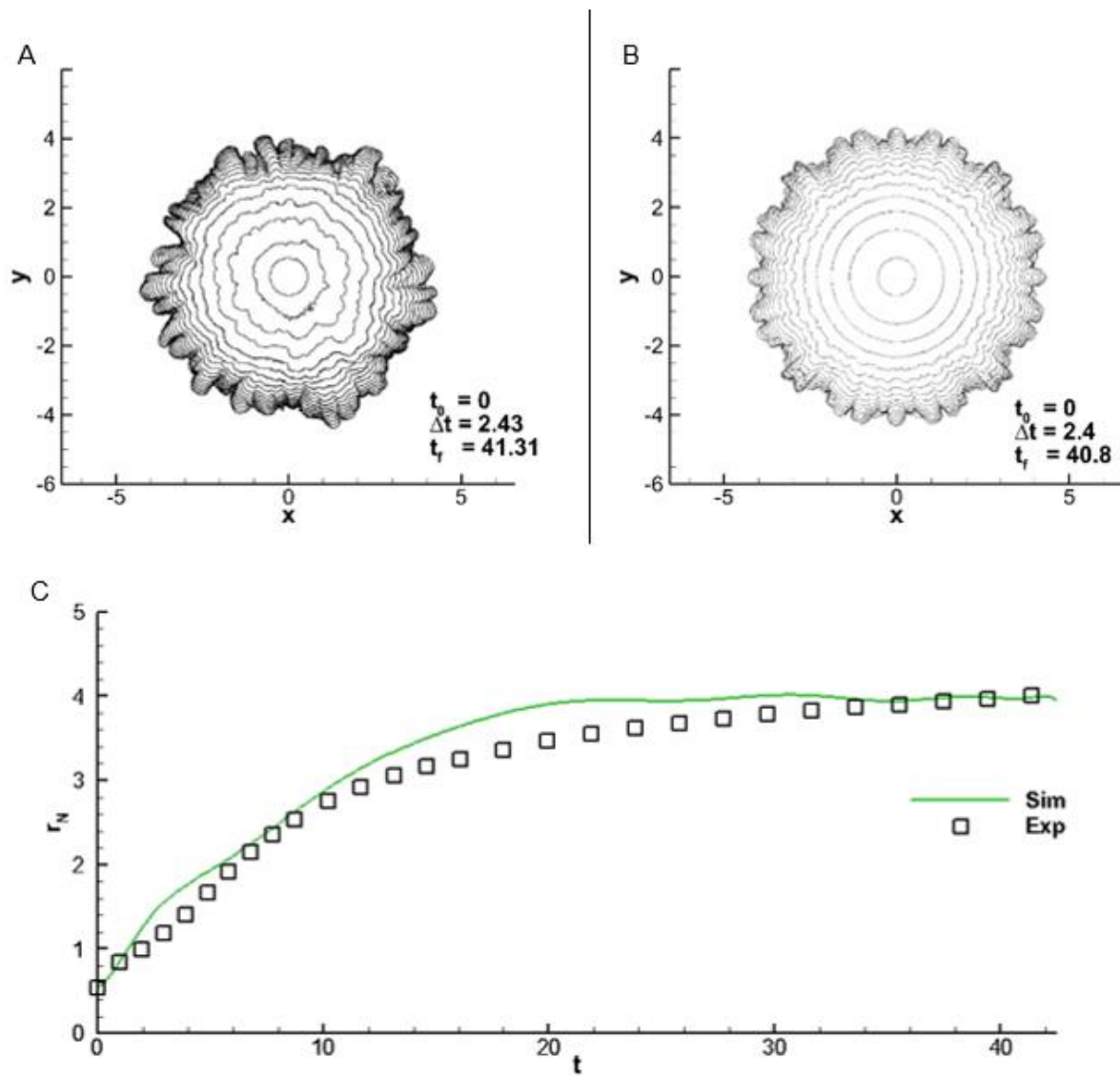


Figure 6-15. Temporal evolution of the front of a circular turbidity current: A) Exp 6-10; B) Sim 6-1. The contours are plotted from  $t = t_0$  to  $t = t_f$  by steps of  $\Delta t$ . C) Azimuthally averaged radial location of the front versus time for Exp 6-10 (symbols) and Sim 6-1 (solid line).

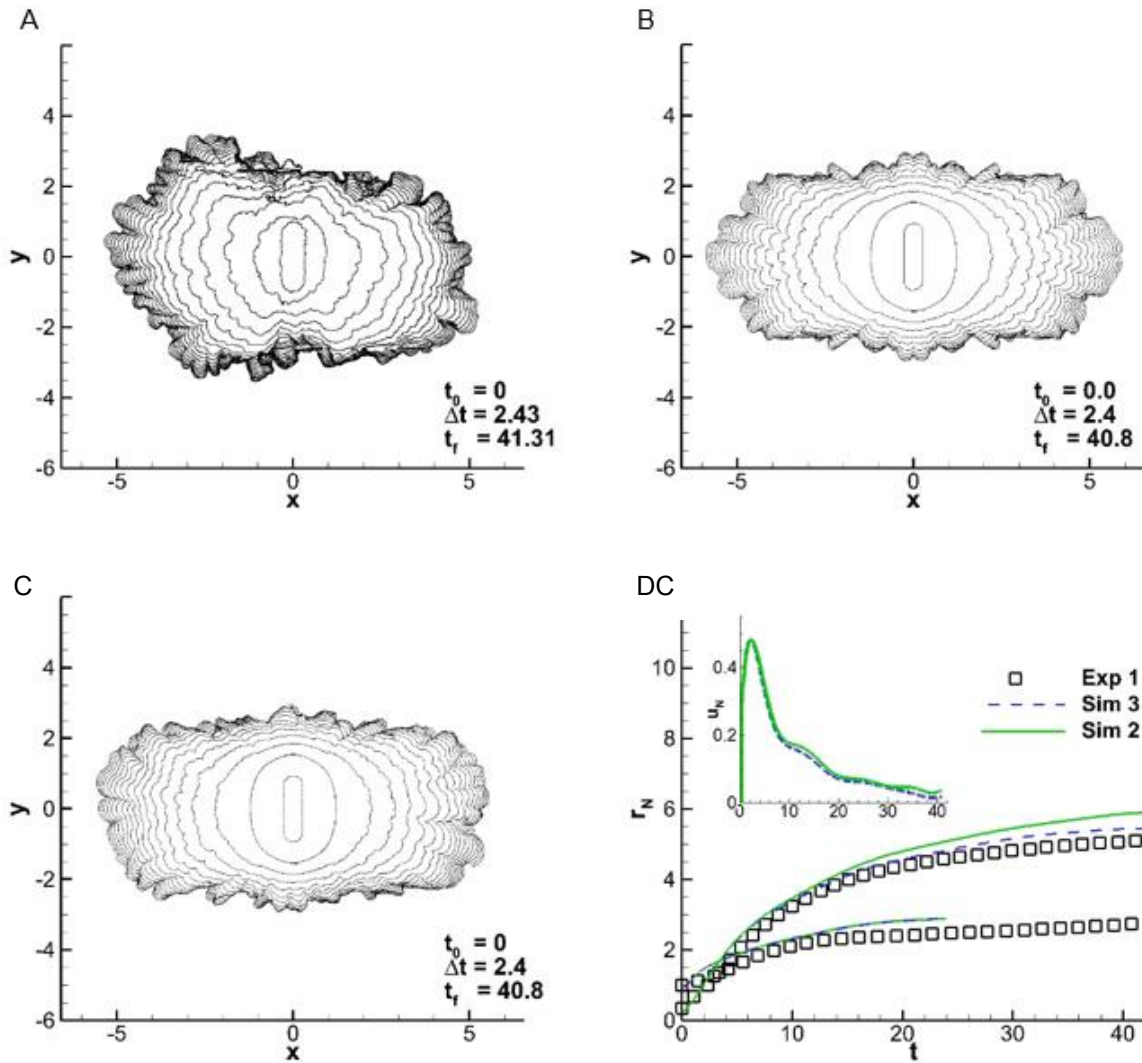


Figure 6-16. Temporal evolution of the front of an initially rounded-rectangular turbidity current: A) Exp 6-1; B) Sim 6-2; C) Sim 6-3. The contours are plotted from  $t = t_0$  to  $t = t_f$  by steps of  $\Delta t$ . D) Azimuthally averaged radial location of the front versus time for Exp 6-1 (symbols), Sim 6-2 (solid line) and Sim 6-3 (dashed line). For  $t > 24$ , the current's thickness along the major axis for Sim 6-2 and Sim 6-3 drops below the critical value  $\varepsilon = 10^{-4}$ . Inset: Front velocity along the minor axis for Sim 6-2 (solid line) and Sim 6-3 (dashed line).

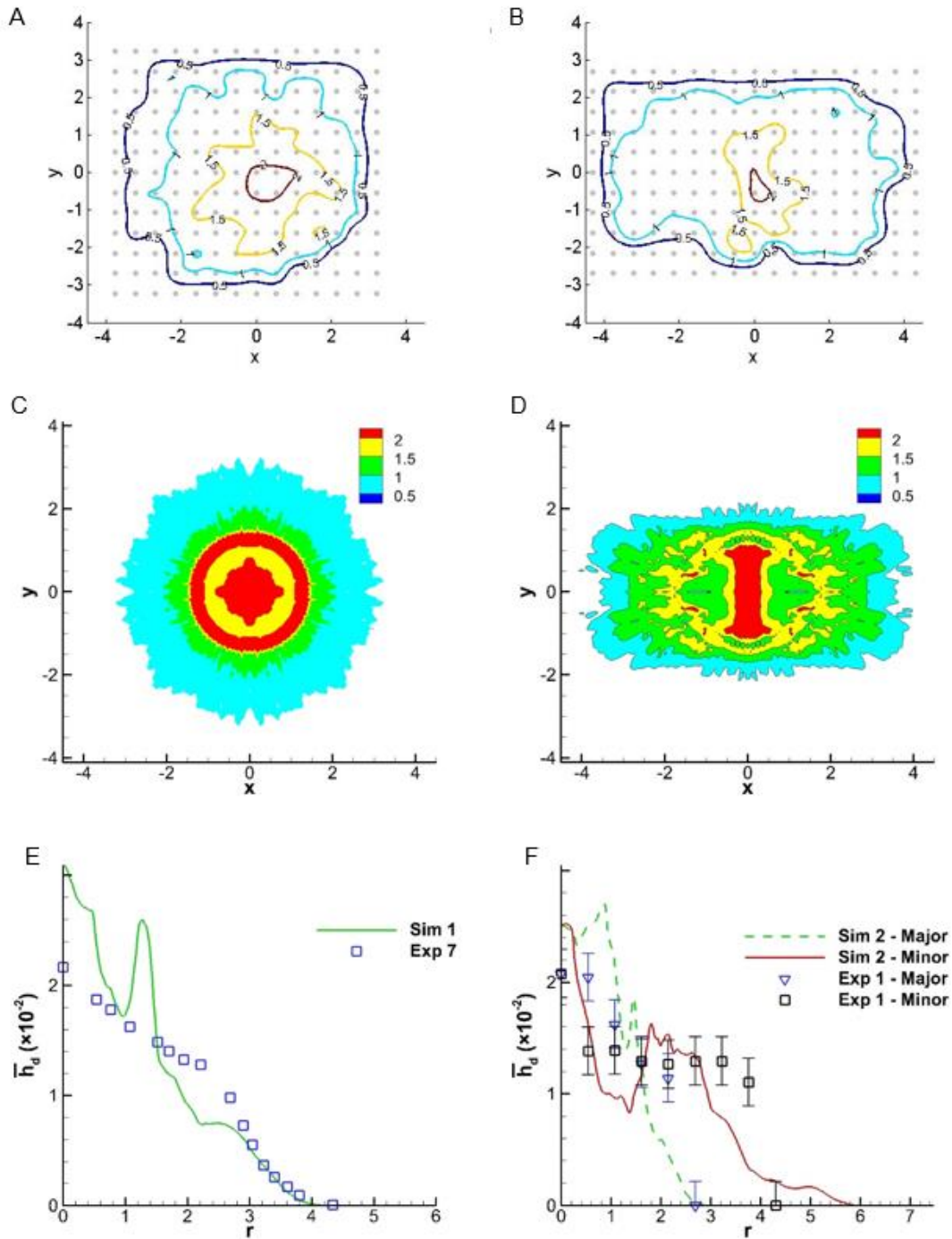


Figure 6-17. Contours of the dimensionless thickness of the deposit multiplied by 100 for A) Exp 6-10, B) Exp 6-1, C) Sim 6-1, and D) Sim 6-2. The circular marks in the background of A and B indicate the locations at which measurements were recorded. E) Azimuthally averaged deposition profile versus radial location (multiplied by 100) from Exp 6-10 (symbols) and Sim 6-1 (line). F) Dimensionless thickness of the deposit (multiplied by 100) along the major and minor axes from Exp 6-1 (symbols) and Sim 6-2 (lines).

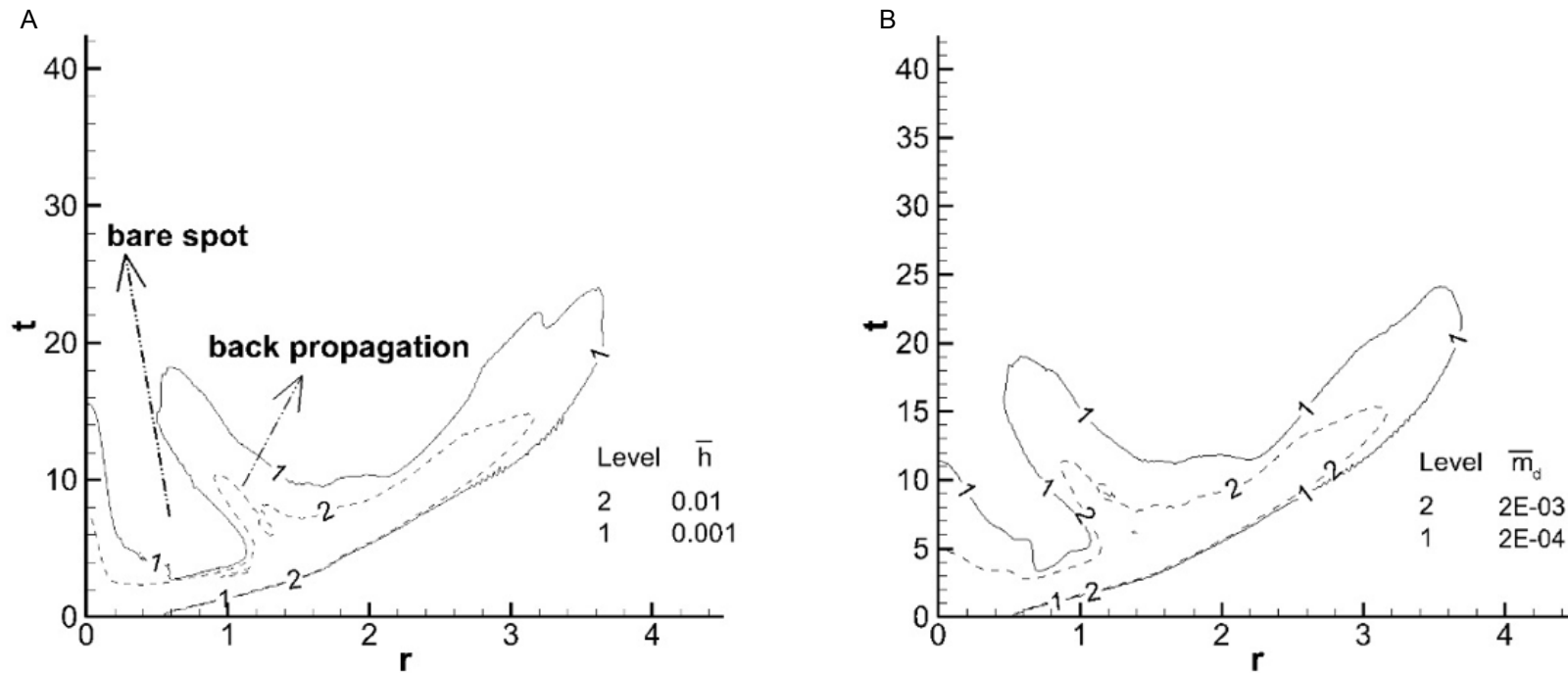


Figure 6-18. A) Contours in space and time of the azimuthally averaged height of the current for Sim 6-1. Flow reversal is observed around  $r = 1.2$  and  $t = 4.5$ . B) Contours in space and time of the azimuthally averaged, instantaneous mass deposition rate of particles per unit area for Sim 6-1.

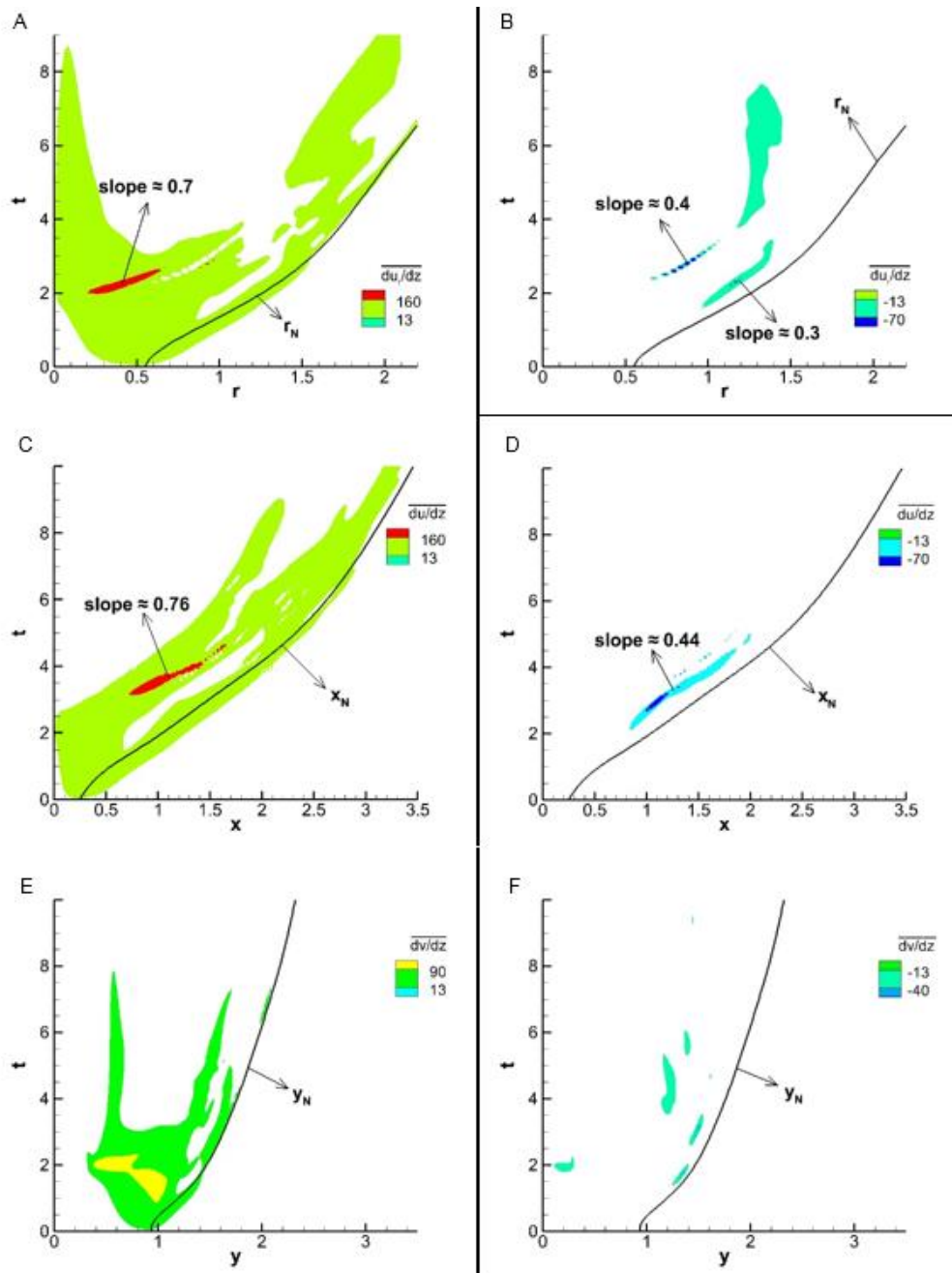


Figure 6-19. Contours in time and space of the azimuthally averaged, vertical gradient of the radial component of velocity for Sim 6-1: A) positive contours and B) negative contours. Contours in time and space of the vertical velocity gradient along the minor ( $x$ ) axis of the RR for Sim 2: C) positive contours and D) negative contours. Contours in time and space of the vertical velocity gradient along the major ( $y$ ) axis of the RR for Sim 6-2: E) positive contours and F) negative contours. The slope of peak values is calculated as change in distance divided by change in time. The solid black line in each figure corresponds to the front location (Figures 6-15C and 6-16D).

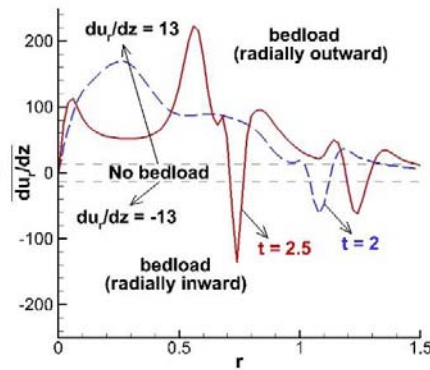


Figure 6-20. Snapshots of  $\overline{du_r/dz}$  from Sim 6-1 at  $t = 2$  (dashed line) and  $t = 2.5$  (solid line). The thin dashed horizontal lines corresponding to  $\overline{du_r/dz} = \pm 13$  separate three regions: (i) No bedload transport ( $|\overline{du_r/dz}| \leq 13$ ), (ii) potential for radially outward bedload transport ( $\overline{du_r/dz} > 13$ ), (iii) potential for radially inward bedload transport ( $\overline{du_r/dz} < -13$ ).

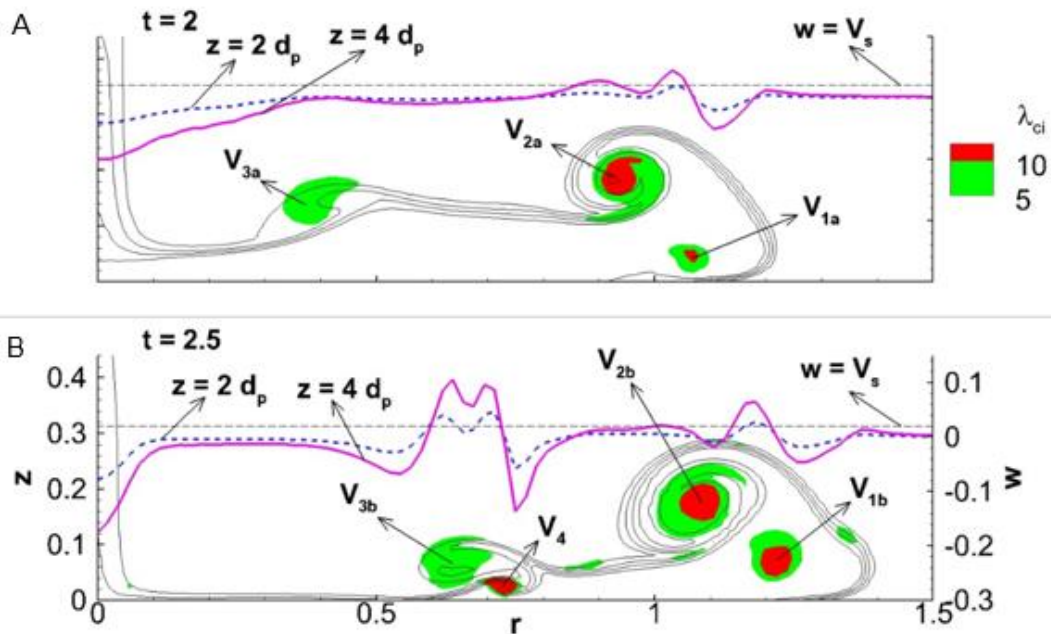


Figure 6-21. A) Snapshot of the current from Sim 6-1 at  $t = 2$ . The thin solid lines represent contours of density and mark the location of the current in the  $r$ - $z$  plane (all quantities in the figure are azimuthally averaged). Regions of high vorticity are denoted by the vortex tubes:  $V_{1a}$ ,  $V_{2a}$ , and  $V_{3a}$ . The thick solid (resp. dashed) line describes the radial variations in the vertical velocity component  $w$  at a distance of  $z = 4d_p$  (resp.  $z = 2d_p$ ) from the bottom wall (in dimensionless terms,  $d_p = 3.2 \times 10^{-3}$ ). Finally, the thin horizontal dashed line corresponds to a critical value of  $w = V_s$  above which, particles could lift off and be reentrained by the current. B) Same as A at  $t = 2.5$ .

## CHAPTER 7 INVESTIGATION OF FINITE RELEASE GRAVITY CURRENT ON A UNIFORM SLOPE

### 7.1 Background

Gravity currents occur when fluids of different density are brought together. They are relevant in many engineering applications such as the dispersion of hazardous gas cloud or the spillage heavy chemicals from marine vehicles. Gravity currents are also the chief mechanism responsible for backdraft, when oxygen is suddenly introduced to a fire trapped in an enclosure and is a real threat to firefighters (Fleischmann & McGrattan 1999). Most of the studies on gravity current tend to assume that they travel on a flat horizontal surface.

Laboratory experiments (Huppert & Simpson 1980, Marino *et al.* 2005) and numerical simulations (Cantero *et al.* 2007a, Blanchette *et al.*, 2005, Dai 2013) of finite release gravity currents in canonical setups (axisymmetric and planar releases on horizontal boundaries) reveal that a gravity current transitions through four main stages. A single, short lived, initial acceleration phase at the end of which the current attains its maximum velocity. A slumping phase succeeds the acceleration phase, it is characterized with a roughly uniform front height and a front speed that is constant or nearly constant. Following the slumping phase, the current transitions into the self-similar inertial phase where the front velocity decreases as a power law (Cantero *et al.* 2007b). Finally, viscous forces become important and a second self-similar regime is observed, termed the viscous phase. Here again the current's front velocity decays as a power law, however at a faster rate than in the inertial phase (Cantero *et al.* 2007b). For certain conditions, the current may not transition through an inertial self-similar phase. Cantero *et al.* (2006) reported that the existence of the inertial phase only occurs at

higher initial Reynolds number. For lower Reynolds number, the gravity current goes directly from the slumping to the viscous phase.

There are various types of gravity currents. The planar setup may be thought of as a two-dimensional release since the current is confined to move along a specified direction, whereas for the circular release, the current would spread radially outwards (in all directions) but remain axisymmetric because of the initial circular nature of the release.

Gravity current travelling on a horizontal surface is not the norm either in nature or in engineering practice. It is more common to find gravity currents travelling down a slope. In such situations, the dynamics of the current is altered as buoyancy and the sloping bottom break the axisymmetry. This changes the physical dynamics of the gravity currents. The formation and evolution of gravity current under such a condition is not well understood. Thus far, most studies have assumed that the gravity current on a sloping bottom to be planar (Dai 2013), i.e. the properties and structure of the gravity current is homogeneous in the spanwise direction. The current is said to be "two-dimensional". Britter & Linden (1980) performed experimental study of such a current and showed that entrainment effects are significant and the head of the gravity current increases in size as it travels down the slope. It was also reported that the front velocity normalized by cube root of the gravity flux is constant and appears to be independent of slope angle. Beghin *et al.* (1981) performed similar experiments and used flow visualization images to conclude that the shape of the current head is well approximated by a half-ellipse. More recently, researchers have conducted numerical simulations of gravity current. Using data from direct numerical simulations, Dai (2012) assessed the

validity of thermal theory to predict the properties of the gravity current head. More details of the dynamics of the gravity current has also been reported in Dai (2013).

For gravity currents released in a sloping rectangular channel, the large-scale motion of the flow remain two dimensional and the conclusions from the above mentioned studies would hold. However, for an axisymmetric initial release, the presence of the slope changes both the spanwise and streamwise dynamics of the gravity current and makes the large-scale flow fully three-dimensional. Studies of three-dimensional currents propagating down a uniform slope are relatively scarce, although this configuration is of more practical relevance as in powder snow avalanches and turbidity currents driven by submarine mud slides. Theoretical investigations have been conducted by Webber *et al.* (1993) who predicted that the gravity current will assume a self-similar circular wedge shape. Tickle (1996) expanded on the study by Webber *et al.* (1993) to include the effects of entrainment. Ross *et al.* (2002) carried out experiments and showed that contrary to the prediction of Webber *et al.* (1993), the gravity current takes on a shape that is more akin to a triangular wedge.

In the present investigation, we report data from fully-resolved three-dimensional direct numerical simulation of circular, finite release, Boussinesq gravity currents propagating down a uniform incline. Our data shows that in most cases, the gravity current evolve to a shape that is more similar to a triangular wedge. The physical mechanisms leading to the formation of this triangular shape and the entrainment properties of such a structure will be presented.

Unlike planar (two-dimensional) currents that are always unidirectional (do not admit a mean spanwise component of velocity), or axisymmetric currents that are ever

diverging, circular releases on sloping boundaries may exhibit nearly unidirectional, diverging, or even converging phases of spreading. Of specific interest is the converging phase of spreading, which leads to local peaks in buoyancy that translate into a second acceleration phase. The details of the second acceleration phase and the redistribution of material leading to its development will be discussed.

These finite release gravity currents are invariably dominated by the head, where most of the mixing and hence the entrainment of ambient fluid occurs. We present a simple method for defining the head and calculate the various properties of the head (volume, mass, shape, entrainment, ...). We find the entrainment coefficient to be nearly independent of the slope, which is inline with previous experimental results.

## **7.2 Theory and Laboratory Experiments**

The problem of a bottom flowing gravity current on a uniform slope has been investigated in the past. Webber *et al.* (1993) considered the motion of a heavy cloud released on an inclined smooth wall. He found that the two-dimensional shallow water equations admit an analytic solution consisting of a shallow wedge descending at a uniform velocity (Figure 7-1). In his model, the current advances as a coherent structure with a constant width to length ratio of  $\pi$  and a height that increases linearly from zero at the current's back end to its maximum value at the front of the current. At the current/ambient interface, the Froude condition was applied, and the shape was chosen such that the current does not spread in the lateral direction. The wedge does not entrain any ambient fluid, and therefore retains its shape as it descends. Webber's analytic solution neglects internal circulation within the current and assumes the top surface to remain flat.

Ross *et al.* (2002) conducted multiple experiments for Boussinesq (small current-to-ambient density ratio) bottom spreading gravity currents at slopes ranging from 5 to 20 degrees. Their experiments consisted of releasing a finite volume of heavy salty water inside a rectangular tank filled with relatively less dense tap water. The initial density of the current remained below  $1.03 \text{ g cm}^{-3}$  (only a few percent larger than that of the ambient tap water), and therefore their experiments may be classified as Boussinesq. In their experiments, they observe the gravity current to take on a shape that is more akin to a triangular wedge, where the majority of the heavy fluid accumulated at the front of the current. Towards the interior and back portions of the current, they observe a very thin layer of heavy fluid to form. Their experiments did not agree with the self-similar circular shallow wedge predicted by Webber *et al.* (1993).

### 7.3 Direct Numerical Simulations of Circular Gravity Currents on an Incline

#### 7.3.1 Numerical Model

We performed a number of simulations for which a slanted circular cylinder is released on a sloping boundary. We solve the conservation of mass and momentum equations as well as the transport equation for the density field inside a rectangular computational domain shown in Figure 7-2. The non-dimensional system of equations reads

$$\nabla \cdot \mathbf{u} = 0, \quad (7-1)$$

$$\frac{D\mathbf{u}}{dt} = \rho \mathbf{e}^g - \nabla p + \frac{1}{Re} \nabla^2 \mathbf{u}, \quad (7-2)$$

$$\frac{\partial \rho}{\partial t} + \nabla \cdot (\rho \mathbf{u}) = \frac{1}{Sc Re} \nabla^2 \rho. \quad (7-3)$$

Here,  $\mathbf{u}$ ,  $\rho$ ,  $p$ , and  $\nabla \cdot (\rho \mathbf{u})$  represent the divergence free velocity field, density, and pressure, respectively. The density  $\rho$  is rendered non-dimensional as follows

$$\rho = \frac{\rho^* - \rho_a^*}{\rho_{c0}^* - \rho_a^*}. \quad (7-4)$$

The asterisk denotes a dimensional quantity, all other quantities are to be taken as non-dimensional. The variables  $\rho^*$ ,  $\rho_a^*$ , and  $\rho_{c0}^*$  represent the local, ambient, and initial heavy fluid densities, respectively. Therefore, the value of  $\rho$  remains bounded between 0 and 1. The dimensionless pressure is given by

$$p = \frac{p^*}{\rho_a^*(U^*)^2}, \quad (7-5)$$

where  $p^*$  and  $U^*$  denote the local dimensional pressure and velocity scale, respectively.  $e^g$  is a unit vector pointing in the direction of gravity and the Schmidt,  $Sc$ , and Reynolds number,  $Re$ , are defined as

$$Sc = \frac{\nu^*}{\kappa^*}, \quad Re = \frac{\Lambda^* U^*}{\nu^*}, \quad (7-6)$$

where  $\nu^*$  and  $\kappa^*$  represent the kinematic viscosity and molecular diffusivity of the current. We follow Ross et al. by defining the length scale  $\Lambda^*$ , the velocity scale  $U^*$ , and the time scale  $T^*$  as

$$\Lambda^* = (V_0^*)^{1/3}, \quad U^* = \sqrt{g^* \frac{\rho_{c0}^* - \rho_a^*}{\rho_a^*} \Lambda^*}, \quad T^* = \frac{\Lambda^*}{U^*}, \quad (7-7)$$

where  $V_0^*$  is the initial volume of heavy fluid in the slanted cylinder, and  $g^*$  denotes the gravitational acceleration.

We implement the Boussinesq approximation of small density difference between the current and the ambient in that the density only appears in the buoyancy term of the momentum equation (first terms in the right hand side of Eq. 7-2). Equations 7-1 – 7-3 are solved using a spectral code (Cortese and Balachandar 1995, Cantero *et al.* 2007). In the wall normal,  $z$ -direction, no slip boundary condition is used for the velocity field at

the bottom wall and a free slip boundary condition is used at the top wall. Periodic boundary conditions are used for all variables in the streamwise,  $x$ , and spanwise,  $y$ , directions. This implies that a periodic array of gravity currents is being simulated. Care must be taken to ensure that these currents do not interact as we are interested in the development of an isolated gravity current. The length of the domain in the spanwise direction is chosen to ascertain that there is uninterrupted development of the gravity current. As for the density field, zero gradient conditions are enforced at the top and bottom boundaries.

Details of the numerical simulation are described in Table 7-1. The grid resolution was chosen to achieve between 4 to 6 decades of decay in the energy spectra for all variables. It is consistent with the requirement that the grid spacing must be of the order of  $O(ReSc)^{-1/2}$  (Birman *et al.* 2005, Hartel *et al.* 2000). The value of the Schmidt number is taken as unity for all simulations because of its weak influence on the flow (Bonometti and Balachandar 2008). The time step is chosen such that the Courant number remains below 0.5. We impose a small random disturbance to the initial density field to stimulate a faster transition to turbulence.

### **7.3.2 Initial Condition**

The heavy fluid is initially confined inside a truncated circular cylindrical segment of radius  $r_0 \cos \theta$  and mean height  $h_0$  as shown in Figure 7-3. Here, the angle  $\theta$  represents the inclination of the bottom plane with respect to the horizontal along the  $x$ -axis (there is no inclination along the  $y$ -axis). The radius and height are measured along the horizontal (normal to the direction of gravity) and vertical (parallel to the direction of gravity) directions, respectively. The shape of the cylinder conforms to that utilized in

the experiments of Ross *et al.* (2002). From the digitized images of Figure 5 in their manuscript, we observe that the lock radius along the inclined plane is held fixed at a non-dimensional value of  $r_0 = 0.6$ . In their experiments, the initial volume of the heavy fluid is taken as length scale. Consequently, we adopt the same length scale in our simulations and vary the mean height  $h_0$  such that the initial volume of the circular cylindrical segment  $V_0 = \pi(r_0 \cos \theta)^2 h_0$  is equal to 1, i.e.

$$h_0 = \frac{1}{\pi(r_0 \cos \theta)^2}. \quad (7-8)$$

#### 7.4 Structure

In Figure 7-4, we show multiple semi-transparent iso-surfaces of density ranging from  $0.01 \leq \rho \leq 0.5$ . Recall that a non-dimensional density value of  $\rho = 1$  (resp.  $\rho = 0$ ) corresponds to the current (resp. ambient) density at time of release. The effect of the slope on the gravity current is not immediately perceived. The influence of the slope becomes apparent after some finite time, specifically when the depth of the current becomes comparable to that of the slope (Ross *et al.* 2002). Because of the circular nature of the release, we observe the current to initially spread in an axisymmetric manner.

Shortly after release ( $t = 3$ ), the majority of the heavy fluid accumulates in an outer ring, with a thin layer of fluid residing in the interior of the ring. During those early stages, the current's front is smooth and nearly two-dimensional.

At  $t = 6$ , the effect of the inclined boundary is apparent. For the shallower slopes ( $\theta = 5^\circ$  and  $\theta = 10^\circ$ ), the current maintains its circular-like outline, whereas for the steeper slopes ( $\theta = 15^\circ$  and  $\theta = 20^\circ$ ), the current has developed into a boomerang-like structure that progressively thickens (the height of the current increases) as we move

closer to the front of the current near the symmetry plane ( $y = 0$ ). The thicker current at the downstream end is also due in part to the shape of the release. Recall that we are releasing a slanted circular cylinder, and therefore as the inclination of the bottom wall increases, the amount of heavy fluid downstream of the center of the cylinder increases as well (with respect to the amount of heavy fluid upstream of the center). The dark red color at the front (downstream end) of the current for  $\theta = 10^\circ, 15^\circ$  and  $20^\circ$  indicates a relatively denser region compared to its surroundings. We observe multiple undulations at the front of the current, these are the lobe and cleft instability pattern (Simpson 1982). These undulations are generally observed whenever heavy fluid decelerates into a lighter ambient, coupled with the presence of the no-slip boundary condition at the bottom wall (Cantero et al. 2007; Hartel et al. 2000; Simpson 1972). A pattern of rolled up Kelvin-Helmholtz vortices is also observed to develop around  $t = 6$ . These Kelvin-Helmholtz vortices along with lobe and cleft instability help to increase the three-dimensionality of the current.

At  $t = 10$ , we identify some key differences in the structure of the current for the different slopes. For  $\theta = 5^\circ$ , the current retains its circular shape, however as the inclination of the bottom wall steepens, the current is seen to gradually transition to a sharper V-like structure. The angle  $\gamma$  at the vertex of the V-shape is observed to decrease at steeper slopes from  $\gamma \approx 150^\circ$  at  $\theta = 5^\circ$  to  $\gamma \approx 80^\circ$  at  $\theta = 20^\circ$ . Here  $\gamma$  is crudely estimated as the vertex angle between the dashed black lines (Figure 7-4 at  $t = 10$ ). The current remains thickest along the centerline ( $y = 0$  plane) towards its downstream end, with the height and consequently the buoyancy progressively

decreasing as we move upstream until it vanishes at the rear end of the current. In the central region, we continue to observe only a thin film of heavy fluid.

For  $t \geq 20$  bare regions begin to appear behind the front of the gravity current surrounding a thin patch of heavy fluid. These bare regions create an adverse pressure gradient that act to slow down the advancing current. In fact, on a flat bottom these bare regions will result in a reverse flow (Zgheib *et al.* 2015). For the shallow slopes of  $\theta = 5^\circ$ , the current is still observed to have a circular-like front. The V-like structure for  $\theta = 10^\circ$  is still discernable (especially for  $t = 20$ ), however more heavy fluid seems to aggregate closer to the downstream end of the current. For the steeper slopes the shape of the current becomes more complex, especially for the  $\theta = 20^\circ$  case departure from the V-shape can be observed.

The structure of the current that we observe in the simulations resembles that in the experiments of Ross *et al.* (2002). They observe the majority of the heavy fluid to aggregate near the front. For the  $\theta = 15^\circ$  case, they report the same V-shape structure that we detect ( $t = 10$  in the simulations). Both simulations and experiments do not agree with the shallow water model of Webber *et al.* (1993).

In the shallow water model, any internal variations in the current's velocity are neglected. By assuming a constant velocity (independent of space and time), the height of the current becomes solely a function of the streamwise coordinate ( $h = h(x)$ ), increasing linearly with  $x$  at a rate of the slope ( $\tan\theta$ ). This linear increase results in a circular wedge-like structure for the current with a flat top surface. From what we observe in the experiments of Ross *et al.* (2002) and the present simulations, the current does not form a wedge like structure. The center of the current is always

occupied by a thin layer of fluid, and the top surface is observed to be more complex than the predicted flat shape in the shallow water model. The assumption of a constant velocity for the current is not warranted. In fact, the internal circulation within the current appears to be important (Figure 7-5). Furthermore, if internal circulation is taken into account, then the velocity in the current is no longer a constant, and the circular wedge-like structure would no longer be valid.

Figure 7-5 depicts the vortical structure in the current's interior for the various slopes  $\theta = (5^\circ, 10^\circ, 15^\circ, 20^\circ)$  at a single instance  $t = 10$ . The current's surface is visualized through a semi-transparent iso-surface of density  $\rho = 0.05$ . The vortical structures correspond to iso-surfaces of the swirling strength  $\lambda_{ci} = (3.5, 3.5, 4.5, 5)$  for  $\theta = (5^\circ, 10^\circ, 15^\circ, 20^\circ)$ , respectively. The swirling strength  $\lambda_{ci}$  represents regions of high vorticity. It is defined as the absolute value of the imaginary part of the complex eigenvalue of the velocity gradient tensor (Zhou *et al.* 1999; Chakraborty *et al.* 2005). A multitude of hairpin vortices are seen to be aligned along the front of the current. This network of hairpin vortices is responsible for the complex three-dimensional shape observed in Figure 7-4. Furthermore, these vortical structures reveal the importance of internal circulation within the current.

### 7.5 Front Velocity

We first define the current-ambient interface as the position where the vertically integrated height of the current  $\bar{h}(x, y, t)$  exceeds a small threshold value  $\epsilon$ . The front position  $\tilde{x}_N(y, t)$  is then taken as the maximum streamwise location of the detected interface. The height of the current  $\bar{h}$  is defined as

$$\bar{h}(x, y, t) = \int_0^{L_z} \rho(x, y, z, t) dz . \quad (7-9)$$

The small threshold value  $\epsilon$  is taken to be  $\epsilon = 10^{-3}$ . The front location is not however sensitive to the chosen value of  $\epsilon$  in the range  $[10^{-4}, 10^{-2}]$ . To obtain the temporal evolution of the mean front position  $x_N(t)$ , we average the front location  $\tilde{x}_N(y, t)$  over a segment of width  $\sigma = 0.15$  centered at the symmetry plane ( $y = 0$ ).

$$x_N(t) = \int_{-\sigma}^{\sigma} \tilde{x}_N(y, t) dy . \quad (7-10)$$

The front position,  $x_N(t)$  is not sensitive to the chosen value of  $\sigma$  in the range  $[0.05, 0.25]$ . The dependence on  $\epsilon$  and  $\sigma$  is shown in Figures 7-6 and 7-7.

The temporal evolution of the front from the present simulations is compared to previous experiments by Ross et al. (2002). In their experiments, they release a volume of relatively dense saline water into less dense tap water. Their experiments were carried out in a tank of rectangular cross section with dimensions  $2\text{m} \times 2.5\text{m}$  (width $\times$ height) and an elevation of  $0.85\text{m}$ . The bottom surface of the tank could be adjusted to give a range of slopes between  $5^\circ$  and  $20^\circ$ . A circular slanted cylinder initially contains the salty water mixture, whose density  $\rho_{c0}^*$  never exceeded the tap water density ( $\rho_a^*$ ) by more than 3%. The small density difference in the experiments justifies the use of the Boussinesq model. The initial reduced gravity of the experiments was  $g_0^* \approx 25\text{cm/s}^2$ , and the initial volume of the salty mixture was  $V_0^* \approx 1800\text{cm}^3$ . The above parameters indicate that the Reynolds number of their experiments was  $Re \approx 2 \times 10^4$ .

The temporal evolution of the front from the present simulations are compared to the experimental results of Ross et al. (2002) in Figure 7-8. The solid line in each of the

4 figures represents the simulation data, and symbols represent the experimental data obtained from the digitized images of the front position versus time from Ross *et al.* (2002). Multiple experiments were carried out for each slope, however these only differed slightly (in terms of initial volume and concentration of the saline solution) from one another. The variable  $x_0$  corresponds to the initial location of the front [ $x_0 = x_N(t = 0)$ ], and the difference  $(x_N - x_0)$  represents the streamwise distance travelled by the current. We observe very good agreement between our simulations and the published experimental data.

The front velocity is obtained by differentiating the front location with respect to time using a central (3 point stencil) finite difference scheme. Figure 7-9 shows the temporal evolution of the front velocity  $u_N(t)$  for the four slopes ( $5^\circ$ ,  $10^\circ$ ,  $15^\circ$ , and  $20^\circ$ ). The small circles represents the front velocity of the simulations as obtained from a central finite difference scheme. The solid line is a cubic 3<sup>rd</sup> order smoothing spline shown here to help guide the eyes. The dashed line is obtained from differentiating a 12<sup>th</sup> order polynomial curve fit (using least squares) to the temporal evolution of the front position  $x_N(t)$ . The other symbols correspond to experimental data of Ross *et al.* (2002). These sets of data are not directly obtained from Ross *et al.* (since they do not explicitly report the front velocity in their manuscript), but from differentiating the front location obtained from the digitized images of the temporal evolution of the front. It should be noted however, that Ross *et al.* (2002) do calculate the front velocity as it is needed to derive other quantities such as the Froude number. They state that the front speed is calculated by curve fitting a polynomial (using least squares method) to the front location as a function of time,  $x_N(t)$ , and then take the first derivative of the curve fit to

obtain the front speed,  $u_N(t)$ . We can see however, from Figure 7-9, that the front speed  $u_N(t)$  is not very sensitive to the method by which it is calculated. Using a 3-point central finite difference scheme on the front position  $x_N(t)$  or taking the first derivative of a curve fitted polynomial to the front position does not qualitatively alter  $u_N(t)$ , provided a high order polynomial curve fit is used. The location and amplitude of the second acceleration, might however be affected by the method used for steeper slopes ( $\theta = 20^\circ$ ). For the remainder of the chapter, we will adopt the front velocity obtained from the central finite difference scheme.

Figure 7-9 reveals some very interesting dynamics that have not been reported for finite release gravity currents on a sloping boundary. Unlike axisymmetric gravity currents that spread on horizontal flat surfaces, these downhill spreading, initially circular finite-release Boussinesq currents are seen to undergo a second acceleration phase immediately following the first acceleration phase. At the end of the first acceleration phase (denoted in Figure 7-9 by the first upward facing triangle on the time-axis), the current attains, for the majority of the slopes (excluding  $\theta = 20^\circ$ ), its maximum velocity. The current then decelerates to a local minimum (denoted by the downward facing triangle on the time-axis). Interestingly enough, at the end of the first acceleration phase, the current redistributes itself and undergoes a second acceleration phase to propel the front velocity to a local maximum value (denoted by the second upward facing triangle on the time-axis). The rate at which the front velocity transitions from its local minimum to the second acceleration is observed to increase with increasing slopes. Furthermore, the time it takes the current to undergo such a

transition (distance between the downward and second upward facing triangle) is seen to decrease on steeper slopes.

Beyond the second acceleration phase, the front velocity from the simulations and that obtained from differentiating the digitized images of Ross *et al.* (2002) experiments are in good agreement for the majority of the experiments. However, we do not clearly observe a second acceleration in their experiments. This could be due to the lower temporal resolution of the digitized data, having less than one data point per non-dimensional time unit.

The second acceleration phase is in itself interesting from a fluid mechanics point of view, but it also has a long term effect on the current. The second acceleration phase significantly raises the front velocity in a relatively short period of time (especially at steeper slopes), which allows the current's speed to asymptote to a larger value at later times. This could have implications in problems such as snow avalanches, where neglecting the second acceleration phase could underpredict the velocity, extent, erosive power, as well as the destructive capabilities of the avalanche.

The presence of the second acceleration phase indicates a rearrangement or redistribution of the heavy material within the current to increase the buoyancy at the downstream end of the current near the centerline ( $y = 0$  plane). Unlike planar, two-dimensional gravity currents (which are unidirectional whether advancing on a sloping or horizontal boundary), or cylindrical, axisymmetric currents on horizontal boundaries which are ever-diverging (as they continually expand radially outwards), circular currents on sloping boundaries will initially advance in a diverging manner (similar to the spreading on horizontal boundaries) and later seem to reorient themselves in such a

way to converge towards the centerline (during a finite time span). This convergence of material towards the centerline is the primary cause for the second acceleration phase. This mechanism will be explored in more detail in the next sections.

## 7.6 Mass Redistribution

### 7.6.1 Spanwise and Streamwise Average

In order to better understand how the material within the current redistributes itself at the various stages of spreading, we investigate the spanwise and streamwise averages of the vertically integrated density field of the current  $\bar{h}(x, y, t)$  defined previously in Eq. 7-9. We denote by  $\bar{h}_x(y, t)$  and  $\bar{h}_y(x, t)$  the streamwise and spanwise averages of  $\bar{h}(x, y, t)$ , respectively.

$$\begin{aligned}\bar{h}_x(y, t) &= \frac{1}{L_x} \int_0^{L_x} \bar{h}(x, y, t) dx \\ \bar{h}_y(x, t) &= \frac{1}{L_y} \int_{-L_y/2}^{L_y/2} \bar{h}(x, y, t) dy\end{aligned}\tag{7-11}$$

These quantities are shown in Figure 7-10 for the different slopes at various time instances. Firstly, from  $\bar{h}_x(y, t)$ , we observe the current to retain its symmetry about the centerline plane ( $y = 0$ ).

At  $t = 3$ , the spanwise mass distribution, ( $\bar{h}_x$ ) is very similar for all slopes. We notice the mass to be uniformly distributed in the central region ( $-1 \leq y \leq 1$ ) with a symmetric peak at  $y = \pm 1.5$  before a sharp decline to a zero value. Furthermore, from the streamwise mass distribution, we observe two non-symmetric peaks at the downstream and upstream ends of the current. The asymmetry in the peaks is primarily a consequence of the sloping boundary. For the larger slopes ( $\theta = 15^\circ$  and  $\theta = 20^\circ$ ), the asymmetry between the downstream and upstream edges of the current is amplified

with a larger portion of heavy material aggregating closer to the downstream side of the current.

At  $t = 6$ , we detect a mass buildup near the centerline ( $y = 0$ ) for  $\bar{h}_x$ . The mass buildup is intensified for larger slopes becoming easily identifiable at  $\theta = 15^\circ$  and  $\theta = 20^\circ$ . Furthermore, with respect to the spanwise average, we observe the heavy material to continue to aggregate near the downstream end of the current ( $\bar{h}_y$  plots) for all slopes. The mass buildup and the preferential accumulation of heavy material at the downstream end of the current increase the buoyancy in the foremost centerline region of the current and subsequently result in the aforementioned second acceleration phase in the front velocity. The time for which the mass buildup is perceived ( $3 \lesssim t \lesssim 6$ ) is inline with the initiation of the second acceleration phase (Figure 7-9).

At later times ( $t > 10$ ), the majority of heavy fluid continues to reside close to the centerline ( $y = 0$ ), decreasing slowly as we move outwards in the spanwise direction. The extent of the current in the spanwise direction is also seen to decrease with increasing slope, while the relative amount of heavy fluid near the centerline (with respect to the total amount of heavy fluid within the current) is observed to increase with steeper slopes.

### 7.6.2 Instantaneous Velocity Field

The density weighted, vertically averaged streamwise and spanwise components of velocity provide a good indication of the instantaneous redistribution of the heavy fluid. The components of the instantaneous vector field shown in Figure 7-11 are defined as

$$\text{streamwise component: } \bar{u}_\rho(x, y, t) = \frac{1}{L_z} \int_0^{L_z} \rho u \, dz \quad (7-12)$$

$$\text{spanwise component: } \bar{v}_\rho(x, y, t) = \frac{1}{L_z} \int_0^{L_z} \rho v \, dz$$

where  $u(x, y, z, t)$  and  $v(x, y, z, t)$  are the streamwise and spanwise components of the three-dimensional velocity field  $\mathbf{u}(x, y, z, t)$ , respectively. The vector field overlays iso-contours of the vertically averaged height  $\bar{h}(x, y, t)$ . For each of the 4 slopes, a reference vector of 0.5 magnitude is shown in the upper left corner for  $t = 3$  ( $\theta = 5^\circ$  and  $10^\circ$ ) or  $t = 2$  ( $\theta = 15^\circ$  and  $20^\circ$ ). The vector length scale is the same for all instances belonging to the same slope, however it changes from one slope to another for the purpose of clarity (note how the reference vector length for  $\theta = 5^\circ$  is greater than that of the other slopes).

For the shallowest slope ( $\theta = 5^\circ$ ), it is more difficult to observe the converging of heavy fluid towards the centerline ( $y = 0$ ) as it is quite weak. It is only at  $t = 6$  that we notice some of the vectors in the front most region of the current to point in the direction of the centerline. This small rushing of heavy fluid towards the center conforms with the slow rate of increase of the front velocity during the second acceleration phase (Figure 7-9)

For  $\theta = 10^\circ$ , the current is initially in a diverging state ( $t = 3$ ), moving away from or parallel to the centerline, but not towards it. At  $t = 4$ , the heavy fluid begins to redistribute itself within the current as some of the heavy material is seen to progress towards the centerline. This mass buildup around the center is observed at later instances (up to  $t = 8$ ) with various degrees of intensity. Recall from Figure 7-9, that the second acceleration for  $\theta = 10^\circ$  initiated at around  $t = 5$ , shortly after the heavy fluid is observed to converge towards the centerline.

For the steeper slopes ( $\theta = 15^\circ$  and  $20^\circ$ ), the rushing of heavy fluid towards the  $y = 0$  plane is more intense and occurs over a shorter period of time compared to the shallower slopes ( $\theta = 5^\circ$  and  $10^\circ$ ). At  $t = 4$  and  $t = 5$ , just around the time that the second acceleration begins to take effect (downward facing arrow in Figure 7-9), we observe a strong surge of heavy fluid streaming towards the symmetry plane ( $y = 0$ ). Shortly thereafter, at  $t \geq 6$ , the current reorients itself to flow in the streamwise  $x$ -direction.

The short period of time during which the current converges towards the centerline, and the elevated intensity of the mass buildup during this period conforms to the faster rate (with respect to the shallower slopes) at which the front velocity, during the second acceleration phase, transitions from its minimum to its maximum value (Figure 7-9).

### 7.7 Internal Circulation and Froude Number

The streamwise and spanwise average plots (Figure 7-10), and the instantaneous density weighted, vertically averaged velocity field (Figure 7-11) reconfirm the importance of internal circulation within the gravity current. Recall that internal circulation was neglected in the shallow water model of Webber *et al.* (1993).

Figure 7-12 shows the temporal evolution of  $|\bar{w}|_{\text{Max}}$ , the maximum magnitude of the Favre average of the vertical component of the velocity,  $w$ . It is defined as

$$\bar{w} = \frac{\int_0^{L_z} \rho w dz}{\int_0^{L_z} \rho dz} \quad ; \quad |\bar{w}|_{\text{Max}} = \max[\text{abs}(\bar{w})] \quad (7-13)$$

$\bar{w}$  provides a measure of internal circulation.  $|\bar{w}|_{\text{Max}}$  is related to the big vortex roll-up at the front and to the hairpin structures seen in Figure 7-5.

The value of  $|\bar{w}|_{\text{Max}}$ , throughout the entire simulation, is comparable to the value of the front velocity  $u_N$  (Figure 7-9) for the respective bottom wall inclination  $\theta$ .  $|\bar{w}|_{\text{Max}}$  is largest during early times where the current transitions through the first and second acceleration phases. During those acceleration phases, the current's structure changes significantly. Beyond the second acceleration phase, the magnitude of  $|\bar{w}|_{\text{Max}}$  is seen to steadily decline, remaining however of the same order as the front velocity  $u_N$ .

The Froude number of a gravity current relates the front speed  $u_N$  to the nose height  $h_N$ . Here, we calculate the Froude number by using the maximum height  $\bar{h}_{\text{Max}}$ , defined as the maximum value of  $\bar{h}(x, y, t)$  in the domain. The Froude number is defined as

$$Fr = \frac{u_N}{(\bar{h}_{\text{Max}})^{1/2}} \quad (7-14)$$

Figure 7-13 shows the temporal evolution of the Froude number for the 4 different slopes. For each slope, we plot  $\xi(t)$  and  $\eta(t)$ , the streamwise and spanwise coordinates of the position of the maximum height  $\bar{h}_{\text{Max}}$ , respectively. The red circular hollow symbols represent the Froude number as calculated from Eq. 7-14, and the solid black line is a 3<sup>rd</sup> order cubic spline smoothing of the red hollow symbols to help guide the eyes. The blue triangular symbols are from the experimental data of Ross *et al.* (2002). For all the slopes, we observe  $\bar{h}_{\text{Max}}$  to be located slightly behind the front of the current at close proximity to the centerline ( $y = 0$ ). The vertical dashed line in the Froude number plots marks the time for which the current attains its maximum velocity at the end of the second acceleration phase (upward facing triangle in Figure 7-9). Our simulations are in good agreement with the experimental data of Ross *et al.* (2002) for all 4 slopes. Beyond the second acceleration phase, we observe the Froude number to

attain a nearly constant value, which appears to increase with steeper slopes. Figure 7-14 shows the dependence of the mean Froude number  $\overline{Fr}$  on bottom inclination  $\theta$ , beyond the second acceleration phase. The mean Froude number is defined as

$$\overline{Fr} = \frac{1}{t_f - t_s} \int_{t_s}^{t_f} Fr(t) dt \quad (7-15)$$

where  $t_s$  and  $t_f$  represent the non-dimensional times that mark the end of the second acceleration phase and the end of the simulations ( $t = 30$ ), respectively. The mean Froude number is seen to increase with increasing slopes from a value of 0.8 to 1.2 at  $\theta = 5^\circ$  to  $20^\circ$ , respectively.

### 7.8 Head and Entrainment

Gravity currents from finite releases are known to take the shape of a slug with an elevated head and a relatively thin trailing body (Cantero et al. 2007, Dai 2012). These finite release currents are invariably dominated by the head, which are generally more turbulent and energetic compared to the trailing body. Most studies consider entrainment of ambient fluid into the current to occur mostly in the head (Ross et al 2002, Beghin et al. 1981, Maxworthy 2010). The definition of what constitutes the head of a gravity current is somewhat ambiguous as there is no clear mathematical expression for defining the shape of the head. In the case of planar (resp. axisymmetric) currents, the shape of the head is inferred from the width (resp. azimuthally) and depth-averaged density field of the current. For these canonical geometries, it is relatively easy to identify the head of the current (Dai 2013).

### 7.8.1 Defining the Head of the Gravity Current

The present configuration is neither planar nor-axisymmetric, and defining the head of the current is more challenging than for canonical setups. In essence, a robust method should provide a three-dimensional indicator function  $I(x, y, z, t)$  defined as

$$\begin{aligned} I(x, y, z, t) &= 1 && \text{in the head of the current} \\ I(x, y, z, t) &= 0 && \text{elsewhere} \end{aligned} \tag{7-16}$$

In the present study, we propose a simple method by which we define the indicator function  $I$ . The method consists of 2 steps. First we determine the shape of the current by choosing a threshold iso-surface of density ( $\rho = \rho_{th}$ ). The height of the current  $h(x, y, z, t)$  at every point simply becomes the vertical distance from the bottom wall to this iso-surface. Second we define the head of the current as the location where the height  $h$  exceeds a threshold value  $h_{th}$ . Table 7-2 shows the different combinations of  $\rho_{th}$  and  $h_{th}$  considered in this study. Three values of  $\rho_{th}$  were examined,  $\rho_{th} = 10^{-2}$ ,  $5 \times 10^{-3}$ , and  $3 \times 10^{-3}$ . For each of the iso-surface values, we considered three height thresholds  $h_{th} = 0.3, 0.25$ , and  $0.2$ . Out of the 9 possible combinations, we chose case  $1a$  (Table 7-2) which corresponds to  $\rho_{th} = 10^{-2}$  and  $h_{th} = 0.3$ .

A wall normal view of the head, obtained using the threshold  $1a$  is depicted in Figure 7-15. For each bottom inclination  $\theta$ , we show the evolution of the head at 6 select instances, namely  $t = 3, 5, 7, 10, 15$ , and  $20$ . The red, green, and cyan colors represent thresholds  $1a, 1b$ , and  $1c$ , respectively. Employing the parameters from threshold  $1a$  (red color), we observe the shape of the head to conform to the three-dimensional structure of the current in Figure 7-4. The different shapes the head attains (circular, boomerang, V-shape, ...) as it evolves in time are well captured. Moreover, the thin

layer of fluid in Figure 7-4 does not fall under the chosen threshold criterion and is therefore excluded from the head. The total buoyancy in the domain is conserved, but the shape of the head continues to grow with time due to entrainment of ambient fluid.

## 7.8.2 Properties of the Head

Once the head is defined, its properties (volume, mass, position of the center of mass, etc.) and other derived quantities (time rate of change of volume, time rate of change of mass, speed of the center of mass) may be easily extracted. Table 7-3 lists the various properties and derived quantities pertaining to the head.

### 7.8.2.1 Geometric Properties and Total Buoyancy

Figure 7-16 depicts the temporal evolution of volume  $V$ , mass  $M$ , wall-normal projected area  $A$ , mean height of the head  $\tilde{h}$ , and the time rates of change ( $V'$  and  $M'$ ) of the volume of mass, respectively. The extracted quantities are shown as lines, and the first order derived quantities (involving time rates of change) are shown as symbols for clarity. The evolution of the aforementioned quantities is shown for a time range spanning the beginning ( $t = 0$ ) to the end of each simulation ( $t = 30$ ). However, we should keep in mind that these quantities are representative of the head, and therefore they are only meaningful after the head has formed. Because the head needs a finite time to develop (around 2 time units in the present case), we only need to monitor and investigate these quantities in a time range from  $t = 2$  onwards.

The volume of the head continues to increase with time due to entrainment of ambient fluid. The mean time rate of change ( $\bar{V}'$ ) is observed to increase with the slope from a value of  $\bar{V}' \approx 0.1$  at ( $\theta = 5^\circ$ ) to  $\bar{V}' \approx 0.55$  at ( $\theta = 20^\circ$ ). Here  $\bar{V}'$  represents the average time rate of change from  $t = 10$  to  $t = 30$ . The area  $A$  is seen to increase at

roughly the same rate as the volume, whereas the mean height of the head,  $\tilde{h}$ , is observed to first increase linearly between  $t = 2$  and  $t = 4$ , and then quickly asymptote to a constant value. The rate at which the mean height increases and the value to which it asymptotes are observed to depend on the slope (the rate being faster and the value of the asymptote being larger for steeper slopes). The volume is therefore growing more as a result of spanwise expansion and increase in plan area of the head, and less because of the head increasing in mean height. This is inline with previously published results on downhill spreading planar gravity currents (Dai 2013). Dai (2013) observed the length and height of the head to initially increase at a rate which depended on the slope angle. He then observed the length to continue to increase at a much larger rate than the height. As for the mass in the head, it asymptotes to a constant value beyond  $t \approx 10$ . The mass in the head (beyond  $t \approx 10$ ) makes up about one fourth of the initial released mass for  $\theta = 5^\circ$ , and around 50 to 60% of the initial mass for the steeper slopes,  $\theta = 10^\circ$ ,  $15^\circ$ , and  $20^\circ$ .

Figure 7-17 shows the length ( $L$ ), width ( $W$ ), their ratio ( $L/W$ ), and its time rate of change  $(L/W)'$  in the head of the current. We observe both the length and the width to continue to increase with time, however their ratio ( $L/W$ ) asymptotes to a constant value, which depends on the slope angle,  $\theta$  (being larger for larger slopes). Beyond  $t \approx 15$ , the time rate of change of  $(L/W)$  is small ( $(L/W)' < 0.05$ ), and the current attains a self-similar form. This is inline with the three-dimensional structure of the current shown in Figure 7-4, where similar profiles are detected for  $t = 20$  and  $t = 30$ .

### 7.8.2.2 Comparisons with Thermal Theory and Experiments

In the present section we test some of the properties of the head of the gravity current against those adopted for thermal theory developed for free axisymmetric vertical thermals. Turner (1973) shows that the extreme horizontal radius of a thermal and the speed of the cap of the thermal to vary as

$$\begin{aligned}\hat{r} &\propto t^{1/2} \\ \hat{w} &\propto t^{-1/2}\end{aligned}\tag{7-17}$$

In our notation (Table 7-3), the extreme horizontal radius  $\hat{r}$  would represent the maximum height ( $H$ ) or the maximum width ( $W$ ) of the head, and the speed of the cap of the thermal ( $\hat{w}$ ) is synonymous to the speed of the center of mass ( $u_{CM}$ ).

Figure 7-18 shows the log-log plots of the temporal evolution of  $u_{CM}$ ,  $H$ , and  $W$  for slopes  $\theta = 5^\circ$ ,  $10^\circ$ ,  $15^\circ$ , and  $20^\circ$ . A blown up view for  $t > 10$  is shown on the right side of each figure. The solid black lines correspond to  $t^{-1/2}$  ( $u_{CM}$ ),  $0.22 t^{1/2}$  ( $H$ ), and  $2 t^{1/2}$  ( $W$ ). The relationships in Eq. 7-17 are observed to be satisfied. Even though  $H$  and  $W$  both increase as the square root of time, the width is observed to increase at an order of magnitude faster rate.

The quantity  $C$  (Table 7-3), which has the form of a Froude number is shown in Figure 7-19. The value of  $C$  in our simulations remains constant beyond  $t \approx 10$ , and its mean value,  $\bar{C}$  (beyond  $t = 10$ ), is shown to depend on the inclination angle  $\theta$ . It increases from  $\bar{C} \approx 0.6$  at  $\theta = 5^\circ$  to  $\bar{C} \approx 0.9$  at  $\theta = 20^\circ$ . A constant value of  $C$  is usually observed in experiments (Turner 1973), however reported values may differ significantly from one experiment to the other. For vertical spreading thermals, a mean value of  $C = 1.2$  is reported (Turner 1973). It is tempting to conjecture that the increase in  $\bar{C}$  observed

in the simulation could continue to larger values as  $\theta \rightarrow 90^\circ$ . However, it should be noted that rising thermals are axisymmetric, when the sloping plane offers only a plane of symmetry.

The entrainment of ambient fluid occurs primarily in the head of the gravity current (Beghin *et al.* 1981, Ross *et al.* 2002). It is the region where most of the heavy fluid accumulates and the majority of mixing occurs since the elevated head is much more energetic than the thin trailing body. The entrainment coefficient  $\alpha$  (defined in Table 7-3) is shown in Figure 7-20 at the various slopes ( $\theta = 5^\circ, 10^\circ, 15^\circ$ , and  $20^\circ$ ). Beyond the second accelerations phase, the value of  $\alpha$  does not appear to be significantly influenced by the slope (similar observations were reported by Ross *et al.* 2002). Average values ( $\bar{\alpha}$ ) beyond  $t = 10$  compare well with previous experiments and theoretical models, where the entrainment coefficient is found to be of order 0.1 (Ross *et al.* 2002, Beghin *et al.* 1981, Turner 1973). The square symbols in Figure 7-20 are from the experiments of Beghin *et al.* (1981) in which he investigates the release of a planar current on a sloping boundary. The plus symbols are from the integral model of Ross *et al.* (2002).

### 7.9 Reynolds Number Dependence

Another set of simulations with a lower  $Re$  (Table 7-1) was carried out to investigate the effect of the Reynolds number on the front position, velocity, and entrainment.

From Figure 7-21, we observe the effect of the Reynolds number on the front position to be most significant at small slopes. Its influence on the front position is seen

to decrease at steeper slopes as the gap between the computed fronts at the  $Re = 5000$  and  $Re = 1000$ -cases becomes tighter.

### 7.10 Conclusion

We performed highly resolved numerical simulations to investigate the dynamics of a circular finite release on a sloping boundary. Two values of the Reynolds number ( $Re = 5000$  and  $Re = 1000$ ) were considered with four different slopes ( $\theta = 5^\circ, 10^\circ, 15^\circ$ , and  $20^\circ$ ). The shape of the release was chosen to conform to previous experiments of Ross *et al.* (2002). In their experiment, they observe the current to take on a shape that is more akin to a triangular wedge contrary to the self-similar circular shallow wedge predicted using shallow water equations (Webber *et al.* 1993). In our simulations, we observe the current to develop into a shape that resembles that of the experiments of Ross *et al.* (2002).

We presented the three-dimensional structure of the current for the various slopes at different instances in time. The heavy fluid was seen to aggregate near the front of the current with a thin layer of heavy material occupying the interior portion of the wedge. For the shallow slope of  $\theta = 5^\circ$ , the current's front resembled a circular arc. As the slope steepened, the current redistributed itself to form a triangular, V-like structure.

The current's front position from our simulations compared very well with the experimental data of Ross *et al.* (2002). They did not however explicitly plot the temporal evolution of the front speed. To compare the front speed obtained from our simulations to their experiments, we differentiated the digitized data pertaining to the front position in their manuscript.

The front velocity revealed some surprising results. Planar gravity currents (on horizontal and sloping boundaries), and axisymmetric currents (on horizontal boundaries) undergo a single acceleration phase immediately after release. The front speed in our simulations, however was seen to transition through two acceleration phases. This peculiar behavior warranted more investigation.

The presence of the second acceleration phase indicates a rearrangement or redistribution of the heavy material within the current to increase the buoyancy at the downstream end of the current near the centerline ( $y = 0$  plane). Unlike planar, two-dimensional gravity currents (which are unidirectional whether advancing on a sloping or horizontal boundary), or cylindrical, axisymmetric currents on horizontal boundaries which are ever-diverging (as they continually expand radially outwards), circular currents on sloping boundaries will initially advance in a diverging manner (similar to the spreading on horizontal boundaries) and later seem to reorient themselves in such a way to converge towards the centerline (during a finite time span). This convergence of material towards the centerline is the primary cause for the second acceleration phase.

We first explored the distribution of heavy material within the domain by averaging the vertically integrated density in the spanwise and streamwise directions. These averages revealed a buildup of heavy fluid along the centerline, close to the downstream end of the current. The time at which the mass buildup was detected was in line with the initiation of the second acceleration phase.

We then computed the density weighted, vertically averaged streamwise and spanwise components of velocity. The vector plots revealed a rushing of heavy material (near the downstream end of the current) towards the centerline. The time at which this

converging flow (towards the centerline) occurred was consistent with the mass buildup observed in the spanwise and streamwise averages of the integrated vertical density as well as the initiation of the second acceleration phase in the front velocity plots.

Beyond the second acceleration phase, the front velocity from the simulations and that obtained from differentiating the digitized images of Ross *et al.* (2002) experiments are in good agreement for the majority of the experiments. However, we do not clearly observe the second acceleration to occur in their experiments. This could be due to the lower temporal resolution of the digitized data, having less than one data point per non-dimensional time unit.

The Froude number was calculated using the maximum height in the current (which is located along the centerline, close to the downstream end of the current). The Froude number compared well with the experiments of Ross *et al.* (2002) and was seen to quickly reach a constant value beyond the second acceleration phase. That value was seen to increase with steeper slopes.

We presented a simple method for detecting the head of the gravity current and used it to extract the various properties pertaining to the head (volume, mass, shape, growth rates, etc.). The volume of the head was observed to continue to increase as a result of entrainment of ambient fluid. The mass in the head however, beyond the second acceleration phase, remained constant making up around half of the initial released mass (for the steeper slopes). The shape of the current was observed to reach a self-similar shape, with the width to length ratio approaching a constant value at about  $t = 15$ .

Thermal theory pertaining to free axisymmetric vertical thermals suggests the speed of the center of mass and the horizontal extreme coordinate of the thermal cap to evolve (beyond the self-similar phase) as the inverse of the square root, and the square root of time, respectively. These relations were found to be satisfied in the present simulations. The constant  $C$ , which takes the form of a Froude number, was seen to reach a constant value, as suggested by the thermal theory. The value was observed to increase with larger slopes, but remained below the mean value of  $C = 1.2$ , reported in Turner (1973). Turner (1973), however states that there could be large variations in angle of spread between experiments.

The entrainment coefficient was calculated and compared well to previous experiments and theoretical models. It was found to be of the order of 0.1 and to depend very little on the slope.

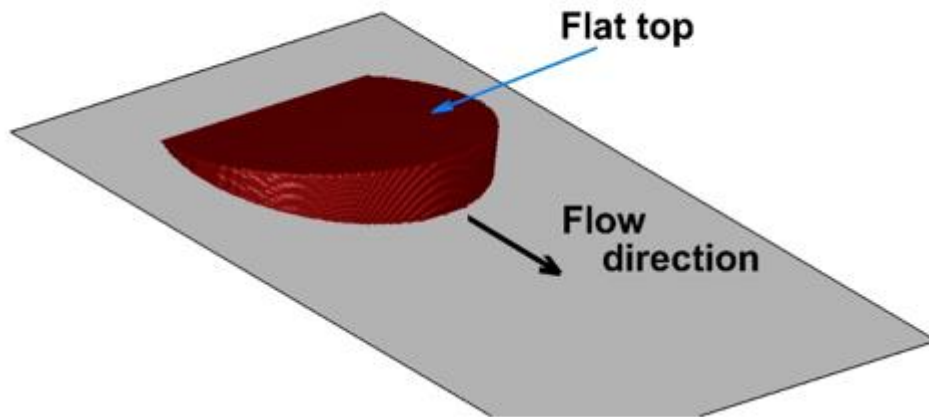


Figure 7-1. Schematic of the shallow water model of Webber *et al.* (1993).

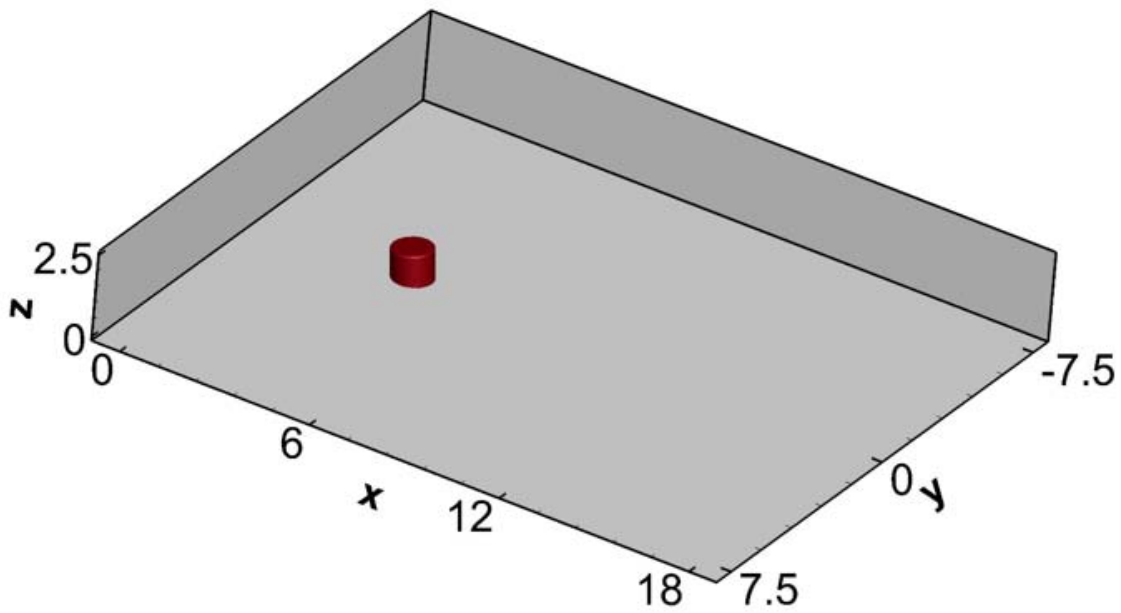


Figure 7-2. Schematic of the rectangular numerical domain.

Table 7-1. List of simulations. The bottom inclination is denoted by  $\theta$ , and  $Re$  represents the Reynolds number. The domain size is the same for all simulations with the grid resolution being larger for the larger Reynolds number.

Simulation number	$\theta$	$Re$	Domain size ( $L_x \times L_y \times L_z$ )	Grid resolution ( $N_x \times N_y \times N_z$ )
7-1	5°	5000	(18 × 15 × 2.5)	(700 × 600 × 201)
7-2	10°	5000	(18 × 15 × 2.5)	(700 × 600 × 201)
7-3	15°	5000	(18 × 15 × 2.5)	(700 × 600 × 201)
7-4	20°	5000	(18 × 15 × 2.5)	(700 × 600 × 201)
7-5	5°	1000	(18 × 15 × 2.5)	(488 × 366 × 101)
7-6	10°	1000	(18 × 15 × 2.5)	(488 × 366 × 101)
7-7	15°	1000	(18 × 15 × 2.5)	(488 × 366 × 101)
7-8	20°	1000	(18 × 15 × 2.5)	(488 × 366 × 101)

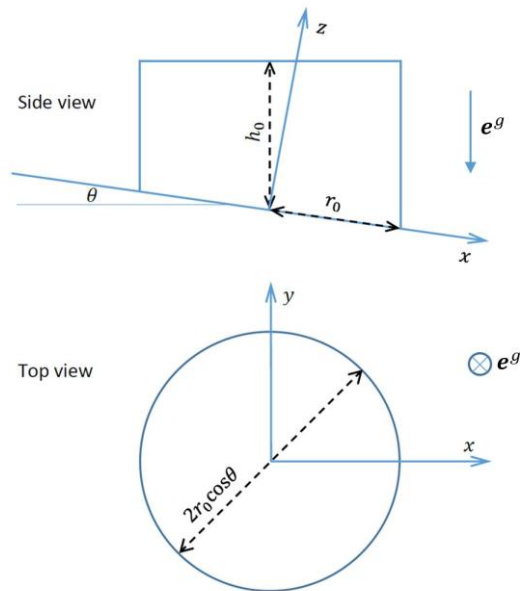
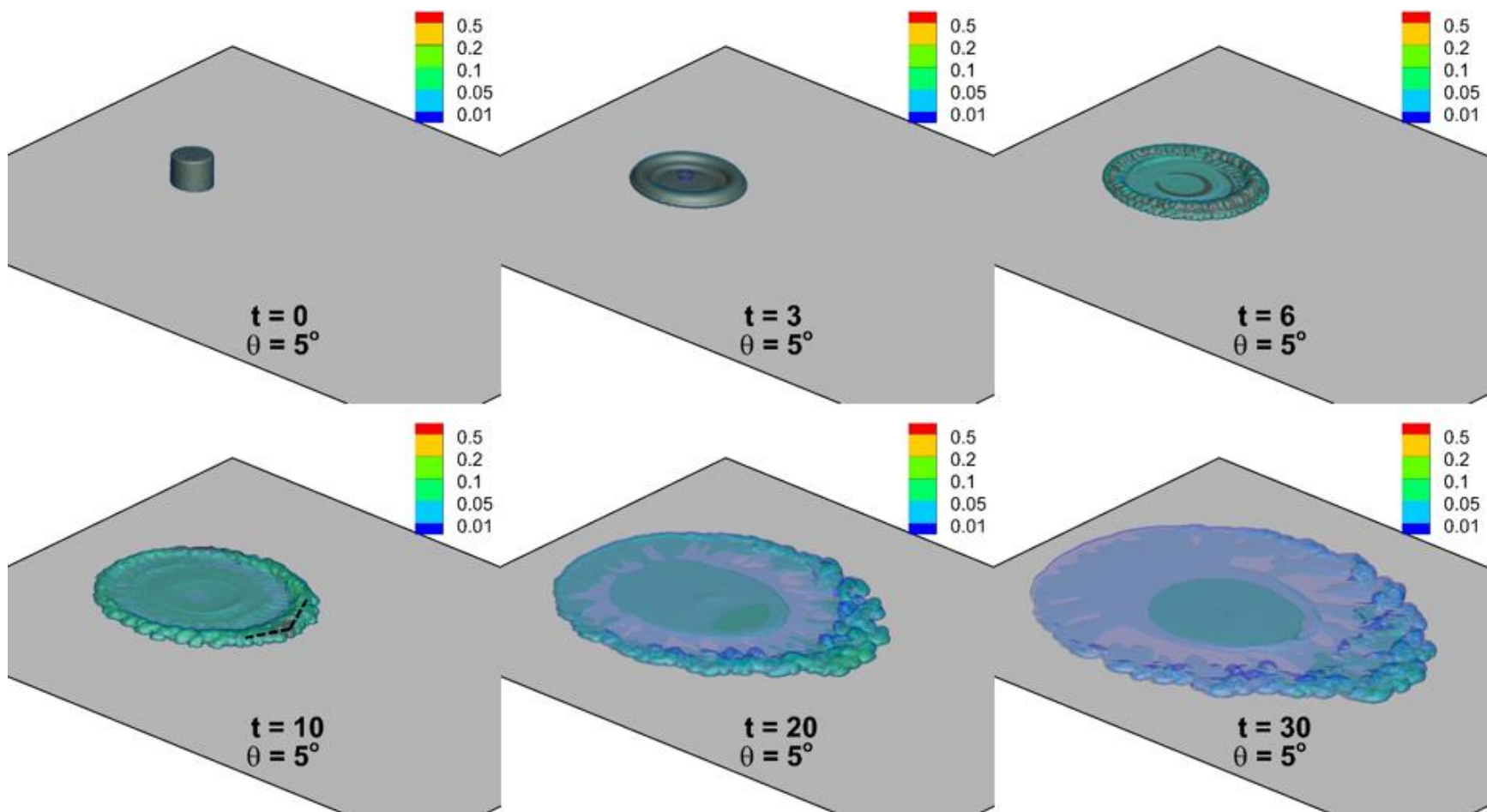
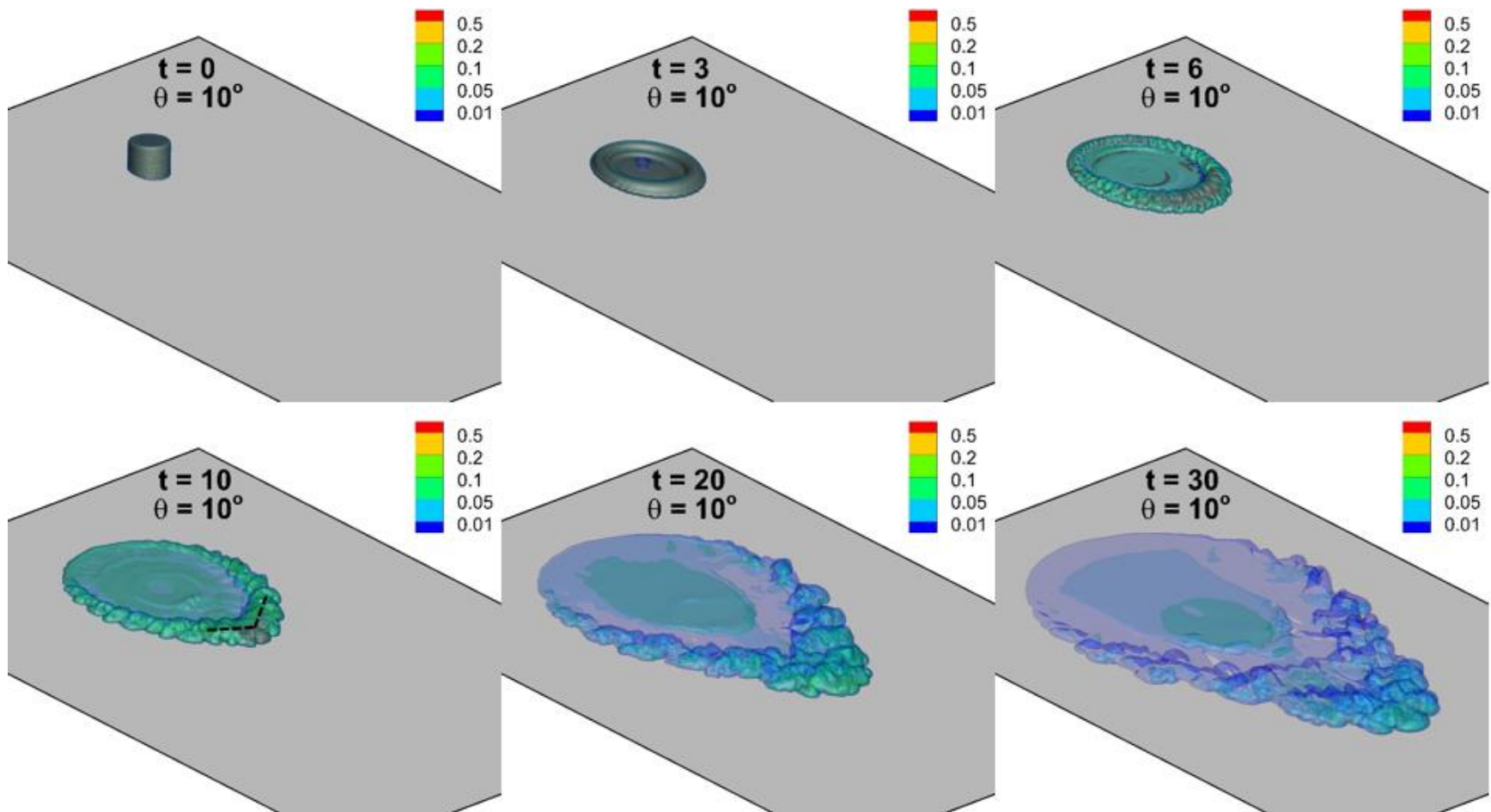
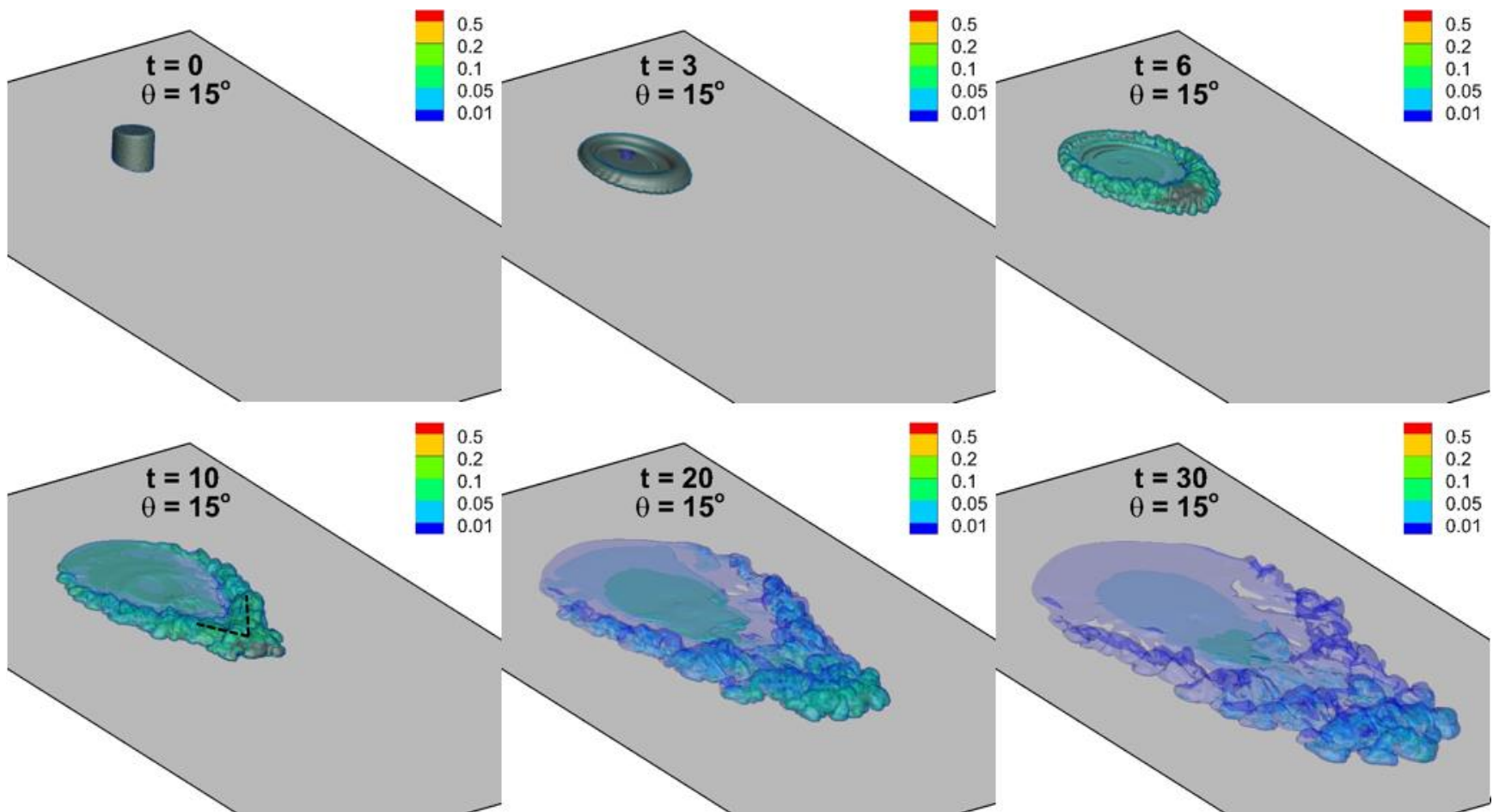


Figure 7-3. Side view and top view of the initial shape of the slanted cylinder containing the heavy fluid.







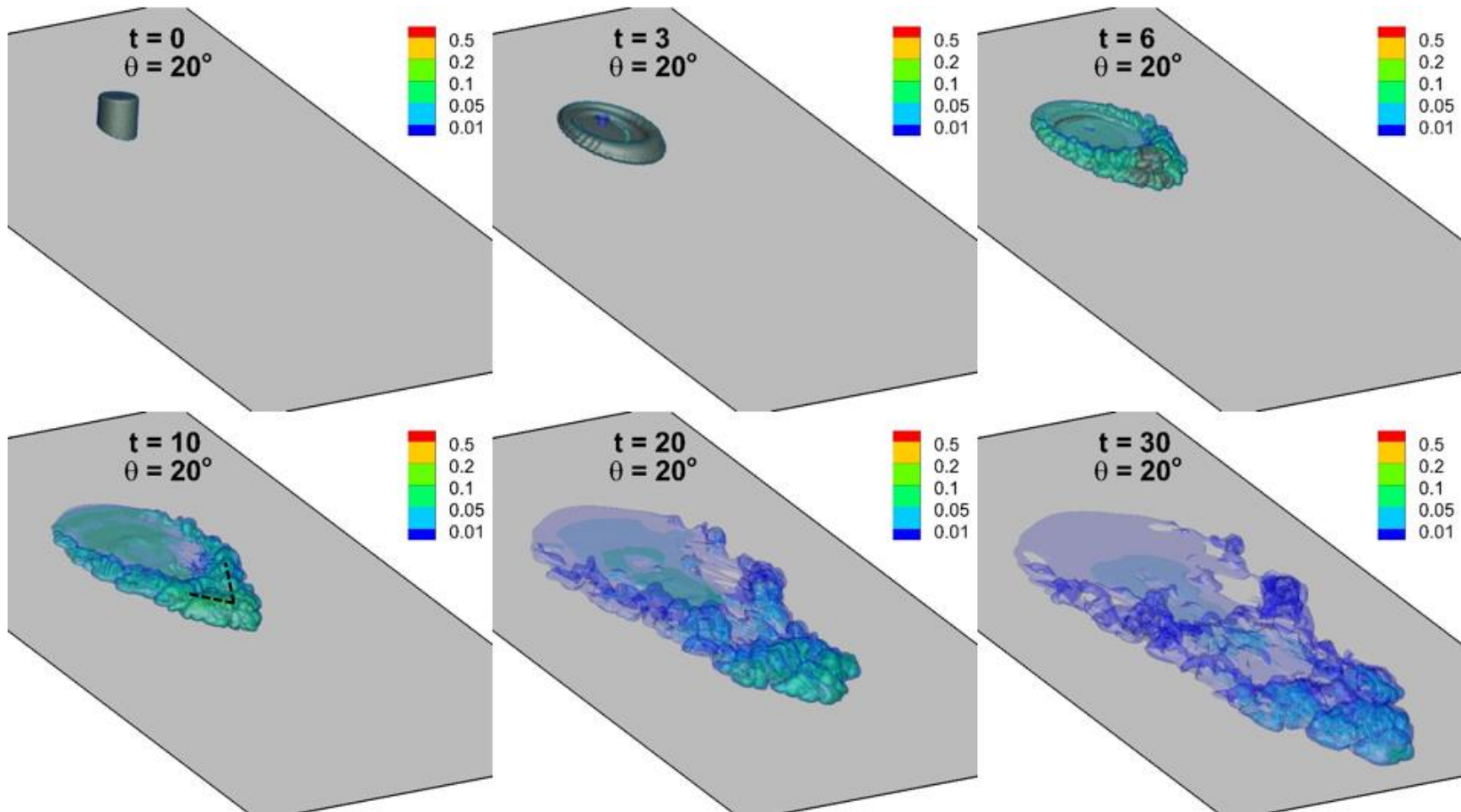


Figure 7-4. Snapshots of the current at various times ( $t = 0, 3, 6, 10, 20, 30$ ) for various slopes  $\theta = (5^\circ, 10^\circ, 15^\circ, 20^\circ)$ . The current is visualized with multiple semi-transparent iso-surfaces of density with a value of  $\rho = (0.01, 0.05, 0.1, 0.2, 0.5)$ .

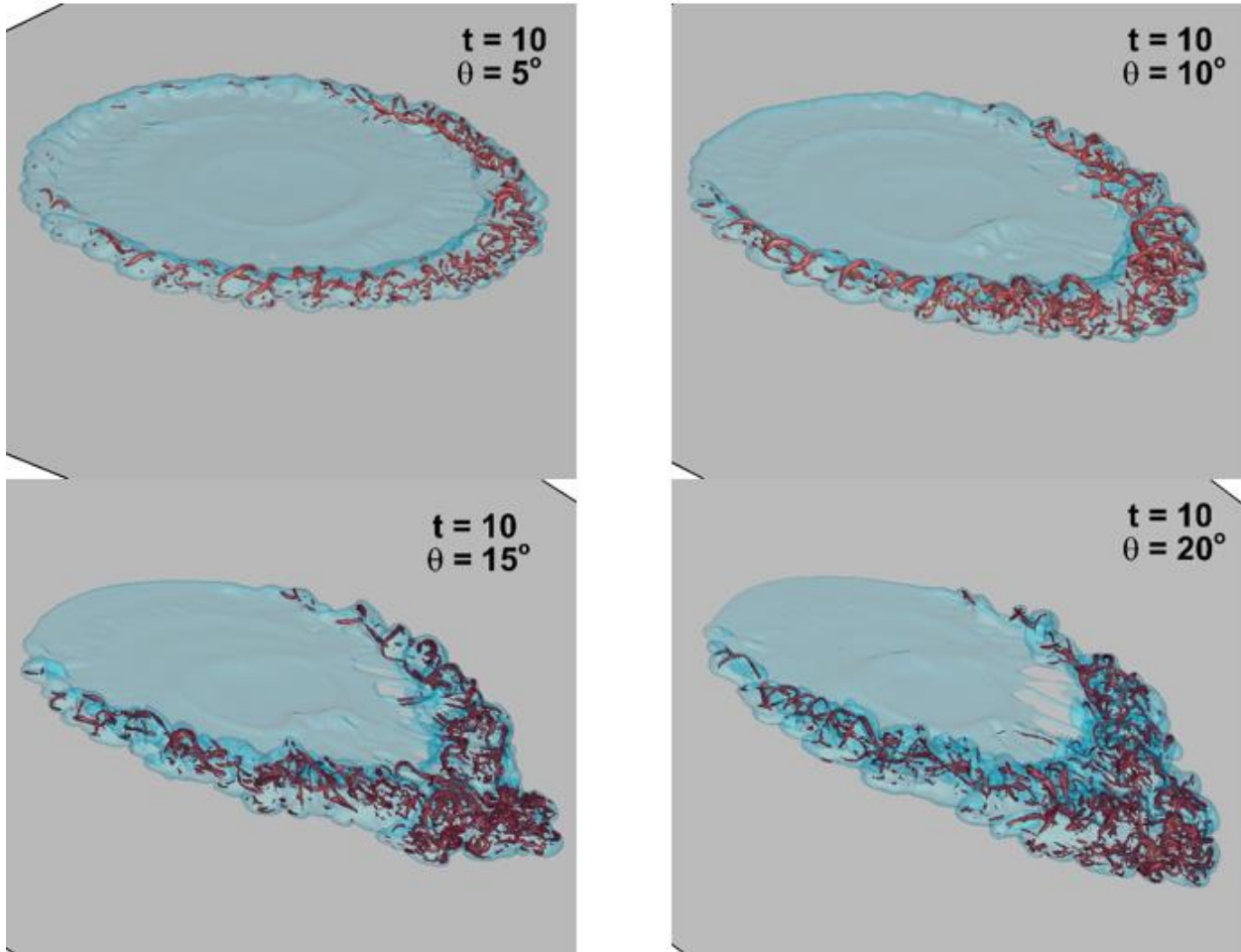


Figure 7-5. Snapshots of the current at  $t = 10$  for various slopes  $\theta = (5^\circ, 10^\circ, 15^\circ, 20^\circ)$ . The current is visualized with a semi-transparent iso-surfaces of density with a value of  $\rho = 0.05$ . The vortical structures in the interior of the current correspond to iso-surfaces of the swirling strength  $\lambda_{ci} = (3.5, 3.5, 4.5, 5)$  for  $\theta = (5^\circ, 10^\circ, 15^\circ, 20^\circ)$ , respectively.

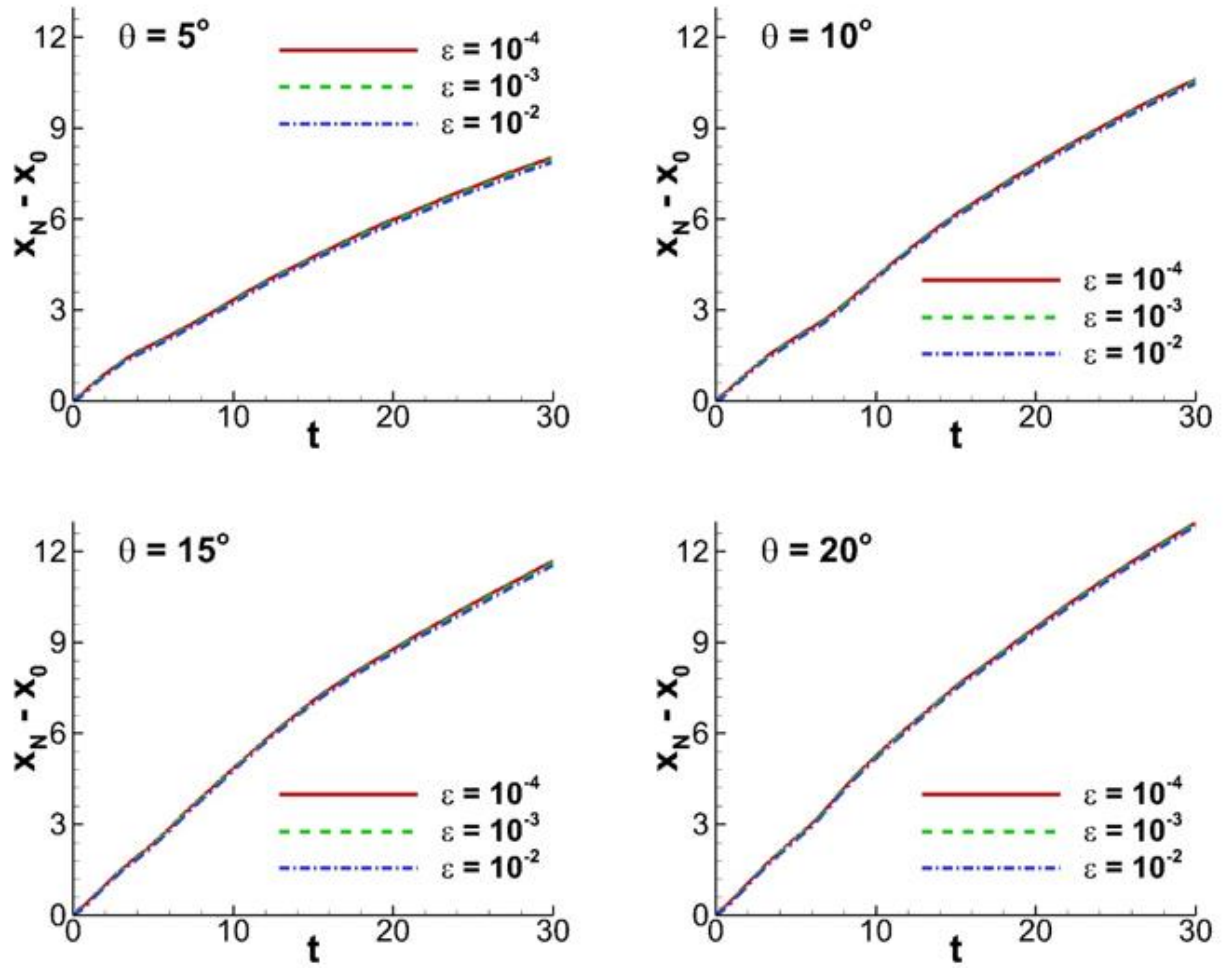


Figure 7-6. Sensitivity of the calculated front position to the small threshold value  $\epsilon$  for a fixed  $\sigma = 0.15$ .

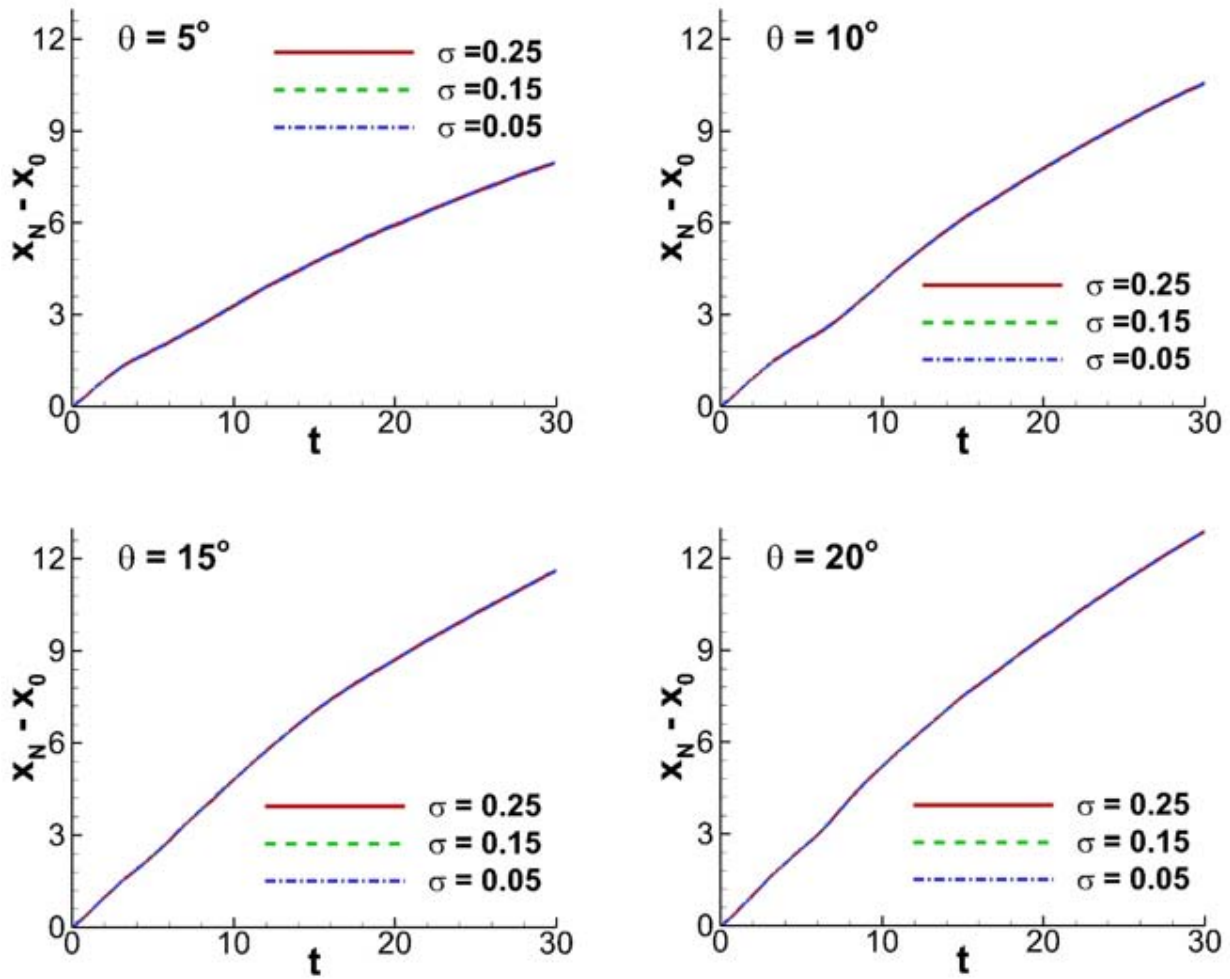


Figure 7-7. Sensitivity of the calculated front position to the segment length  $\sigma$  for a fixed  $\epsilon = 10^{-3}$ .

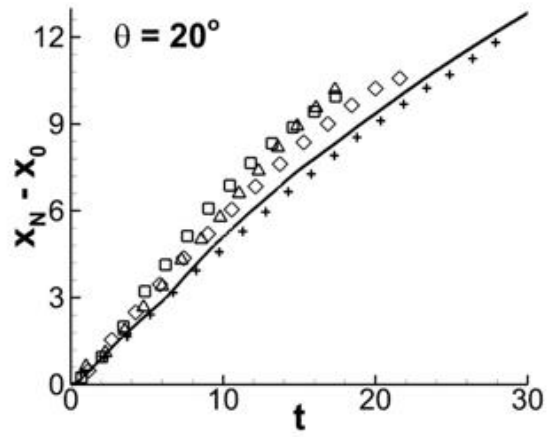
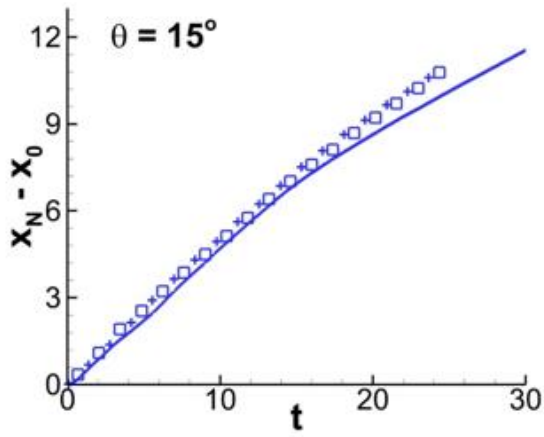
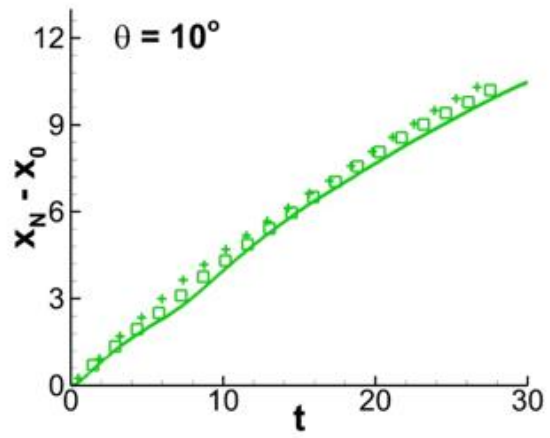
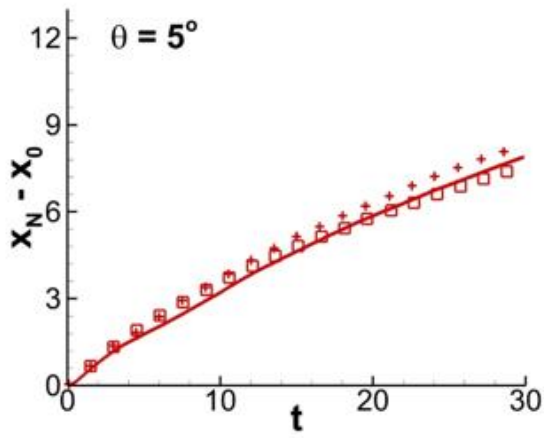


Figure 7-8. Front position as a function of time. The solid line is from the present simulations, and the symbols are from the experiments of Ross *et al.* (2002).

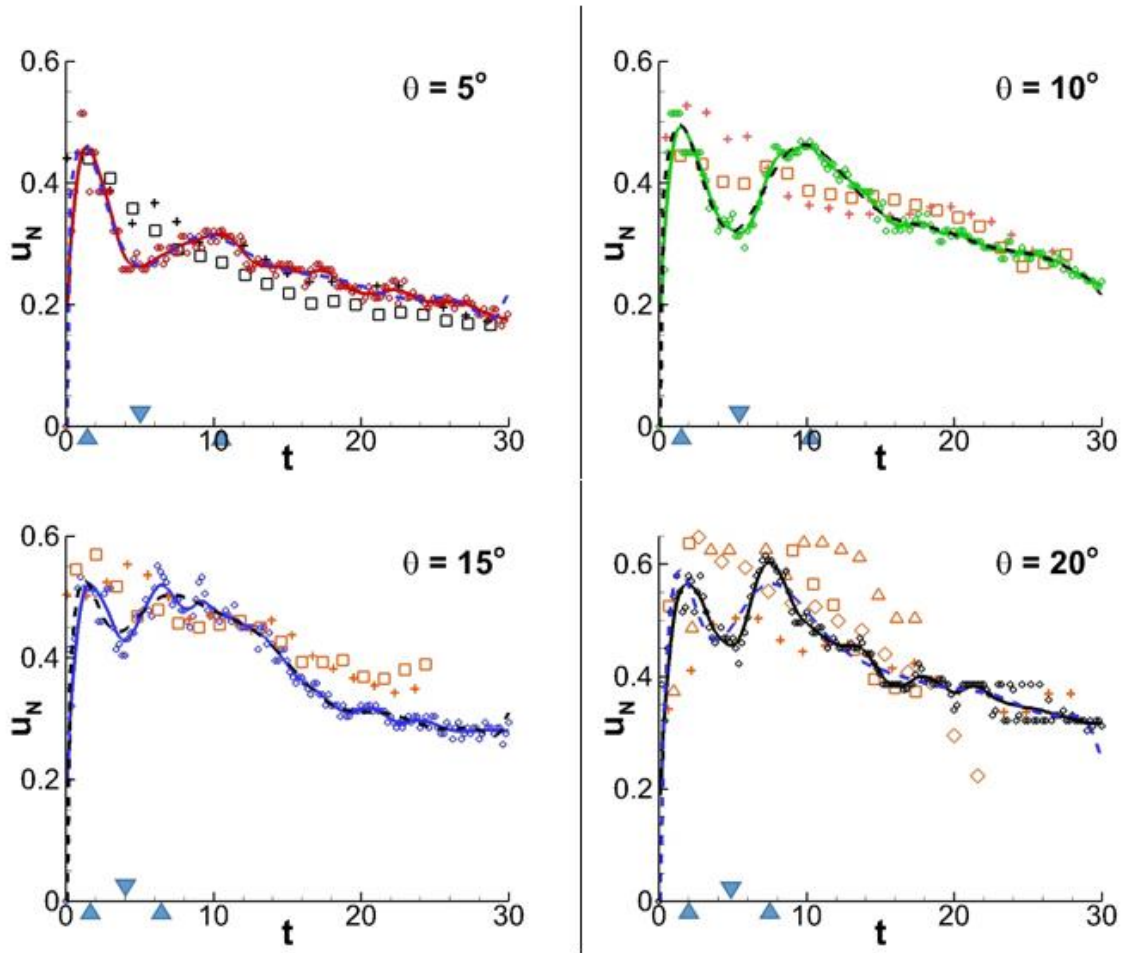
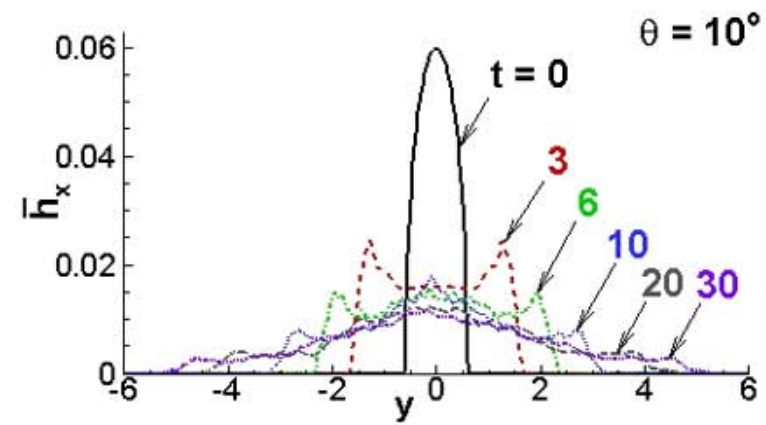
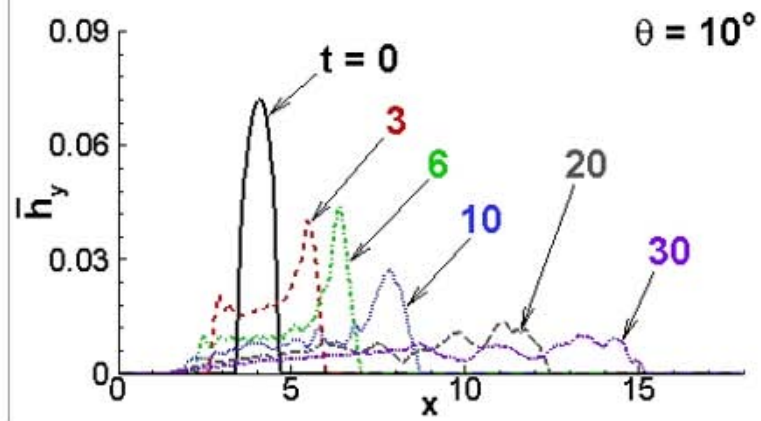
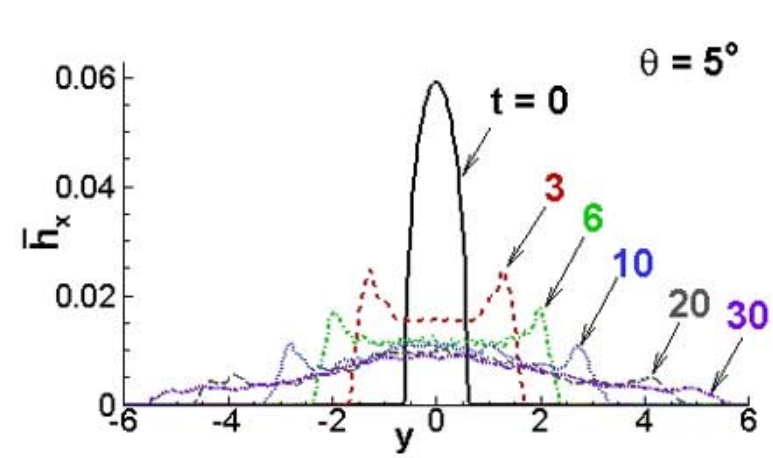
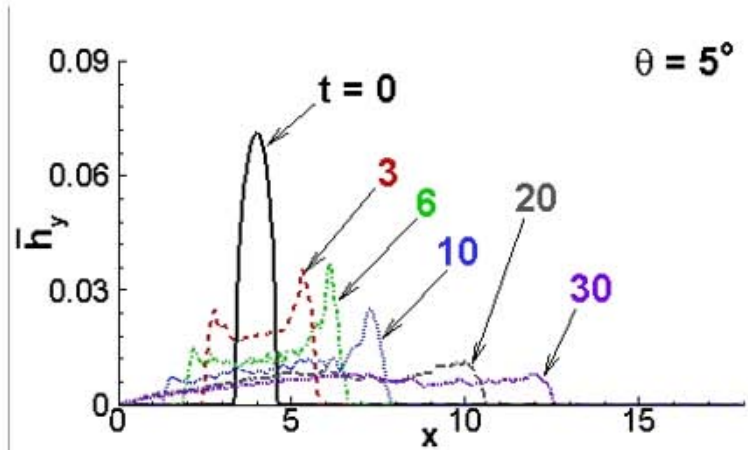


Figure 7-9. Front speed as a function of time. The small circles are the simulation data obtained using the finite difference. The solid line is a cubic 3<sup>rd</sup> order smoothing spline shown to help guide the eyes. The dashed line is the derivative of a 12<sup>th</sup> order polynomial curve fit to the front position  $x_N(t)$ . The large symbols are from the experiments of Ross *et al.* (2002) obtained by differentiating the data extracted from the digitized front position plots (Figure 5 in their manuscript).



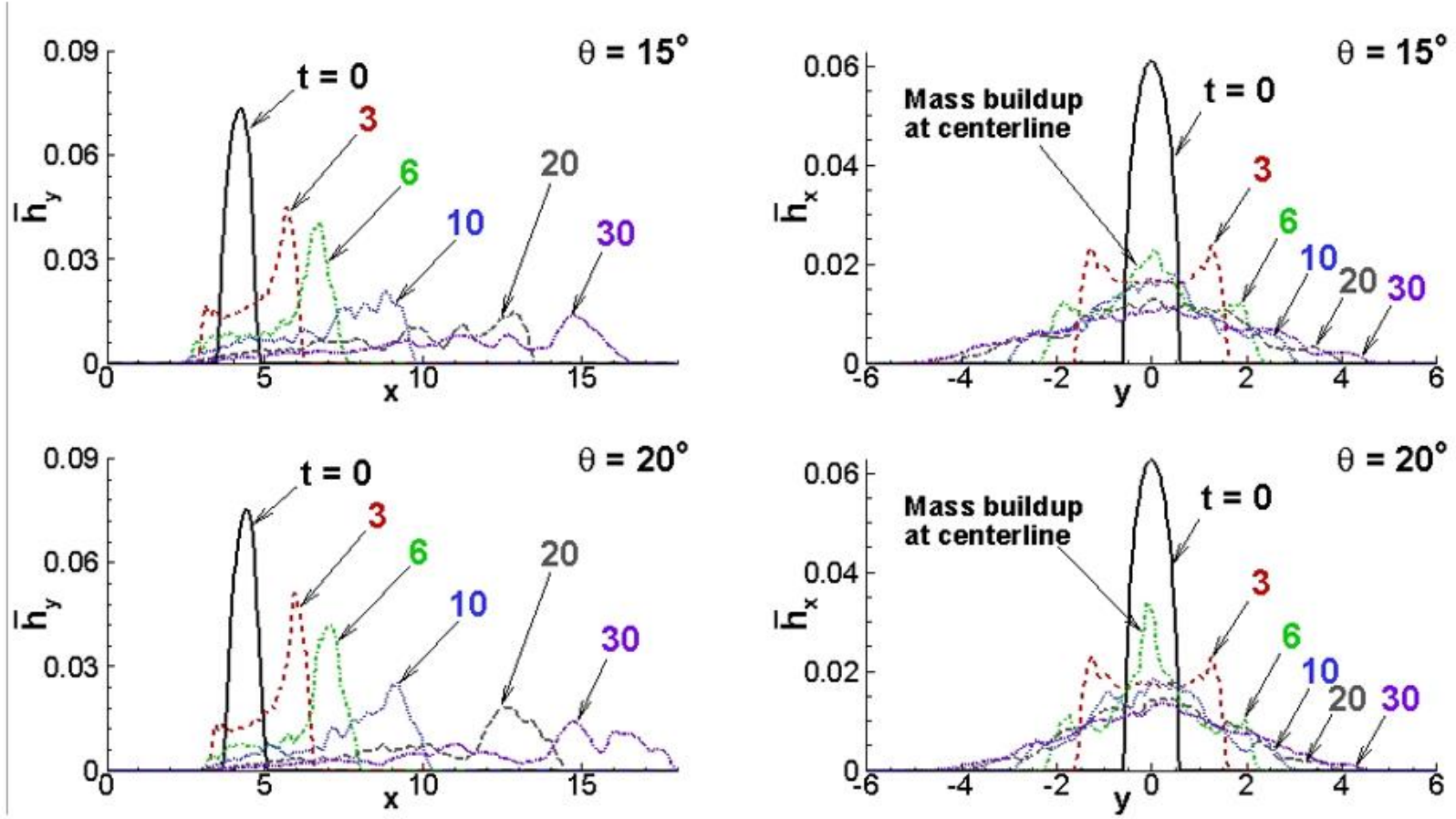
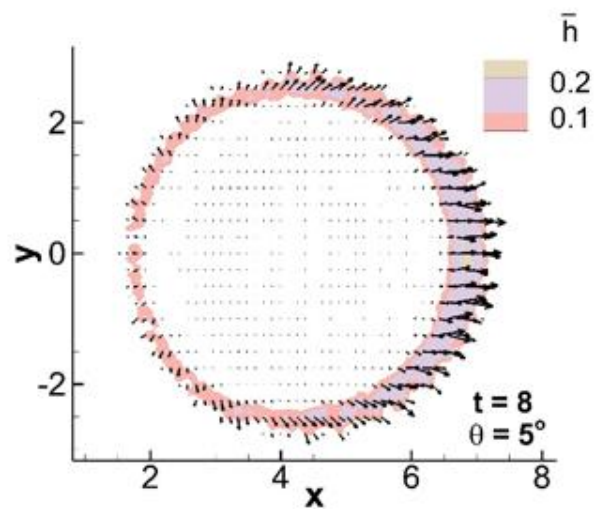
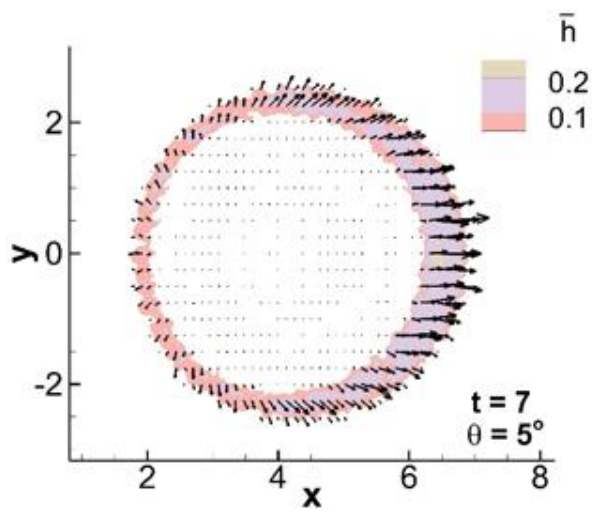
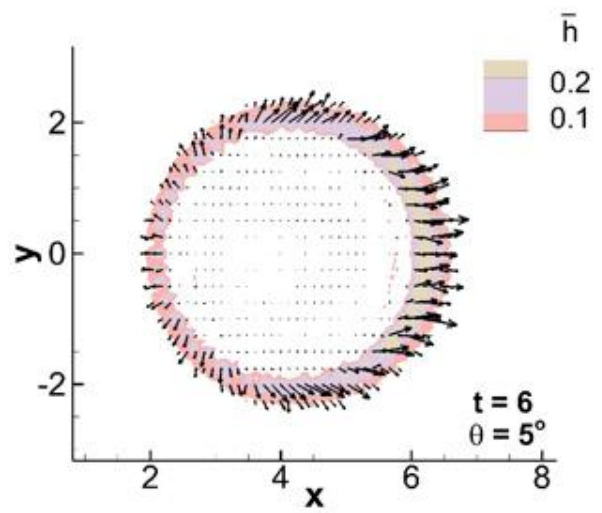
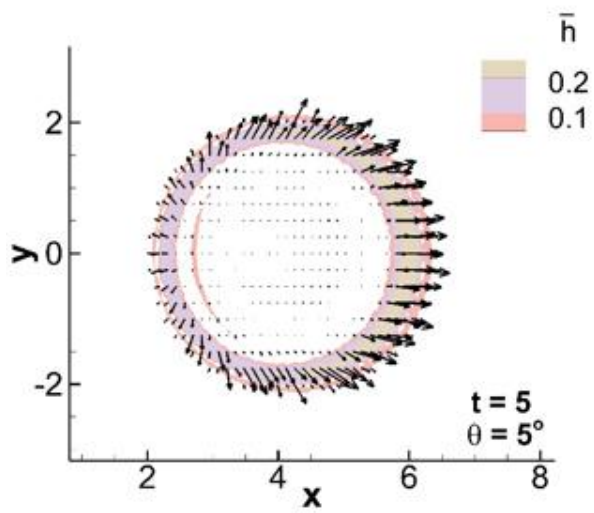
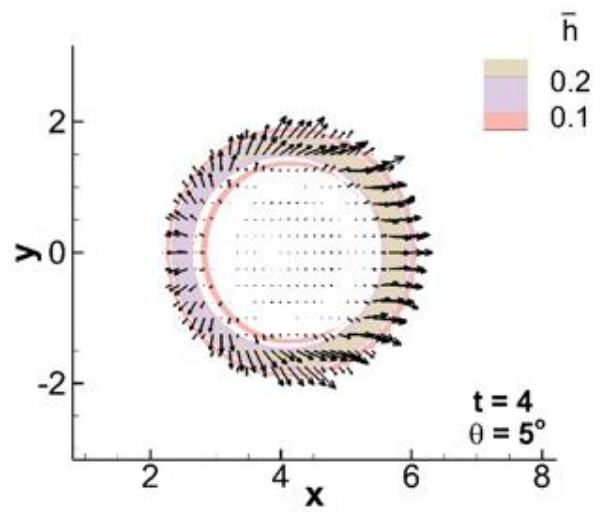
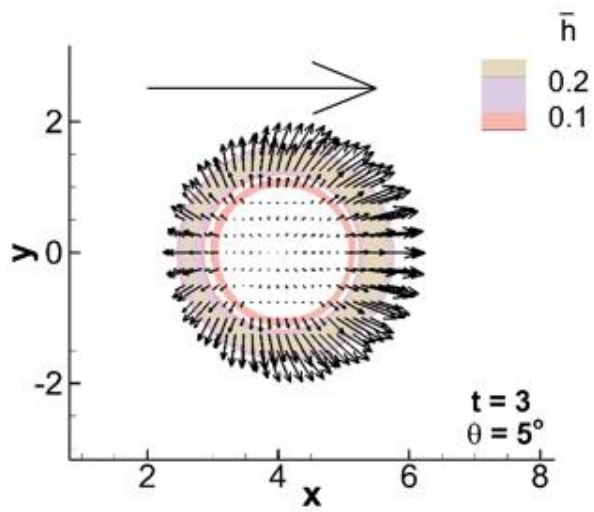
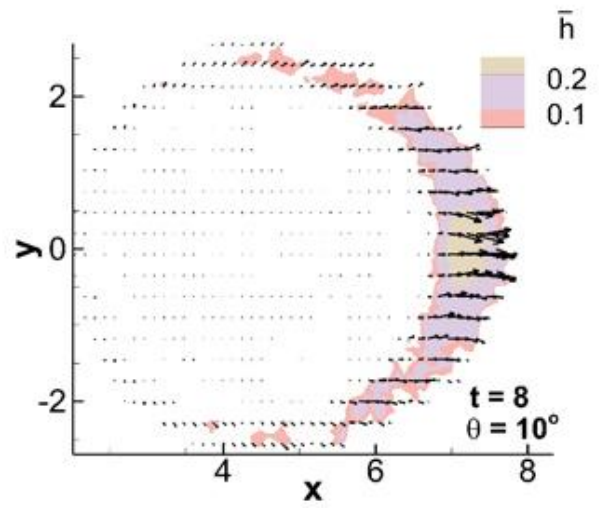
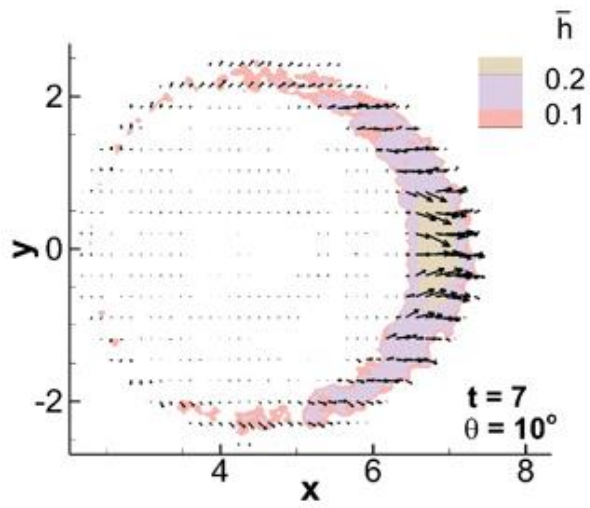
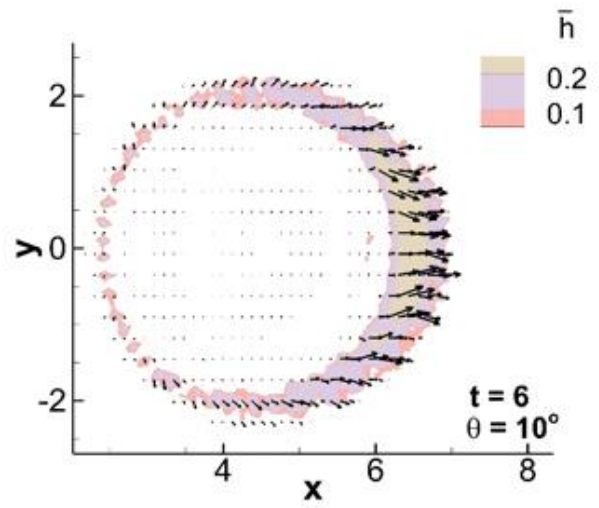
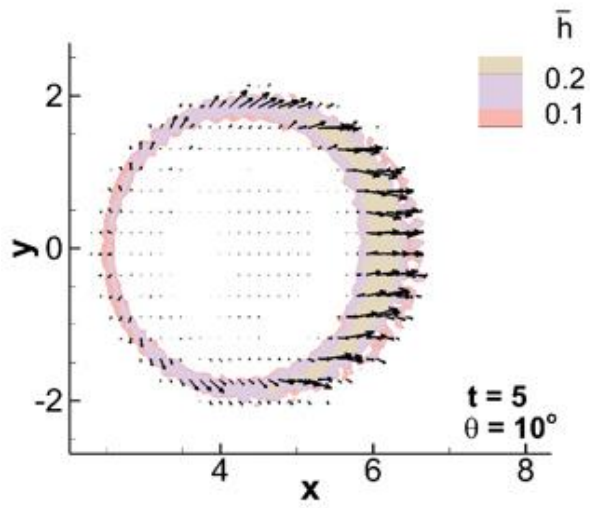
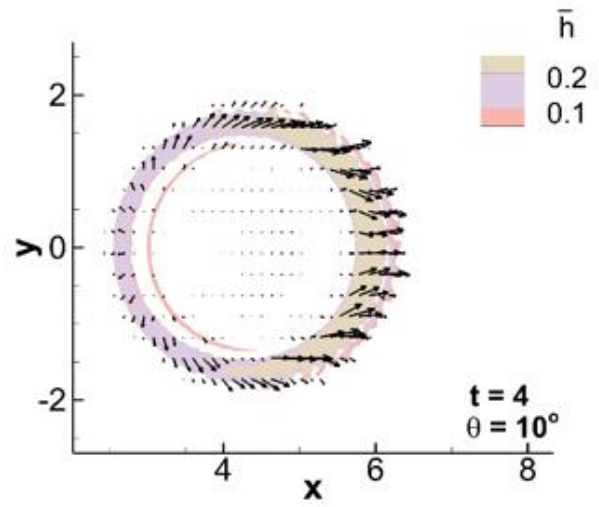
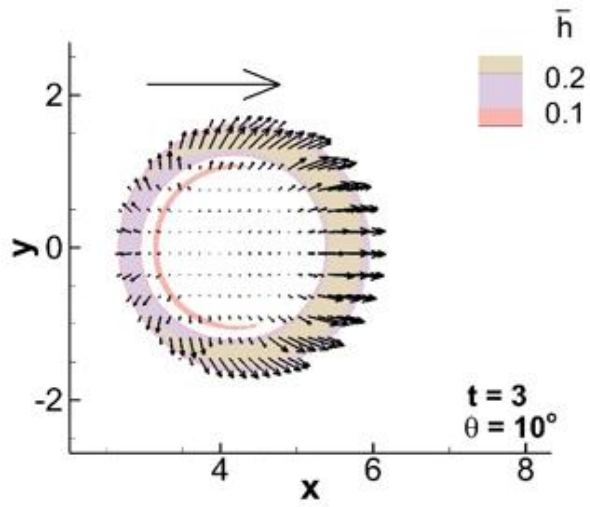
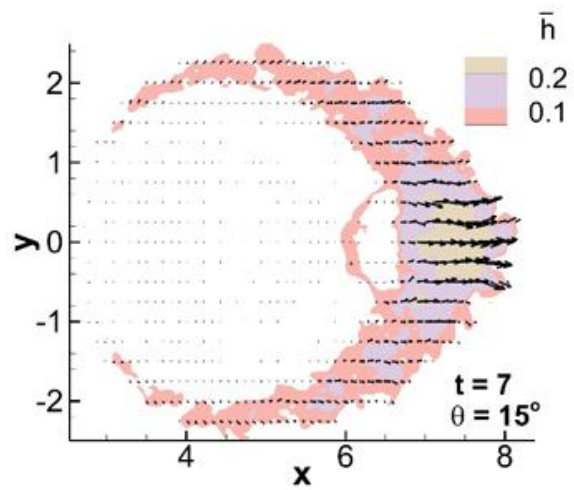
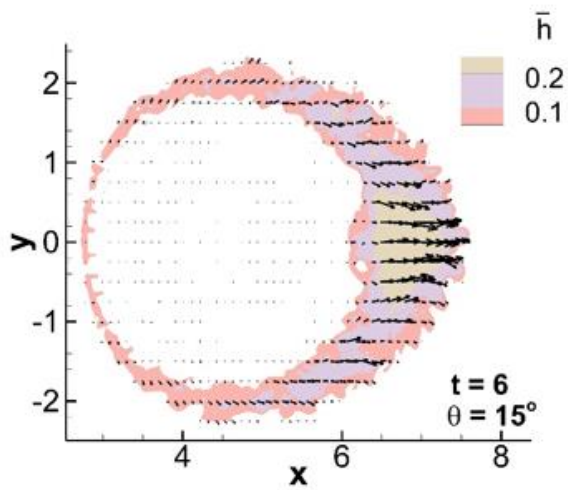
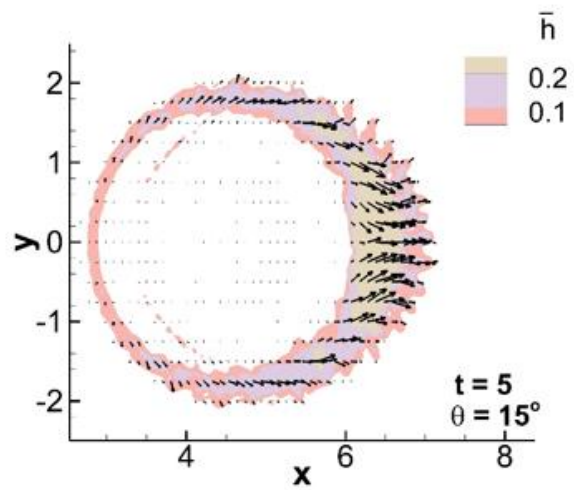
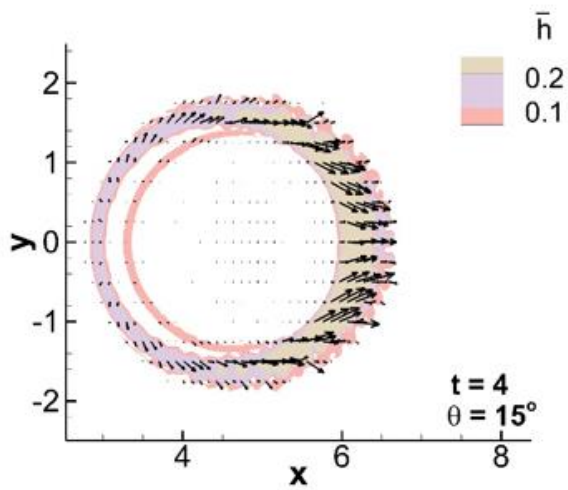
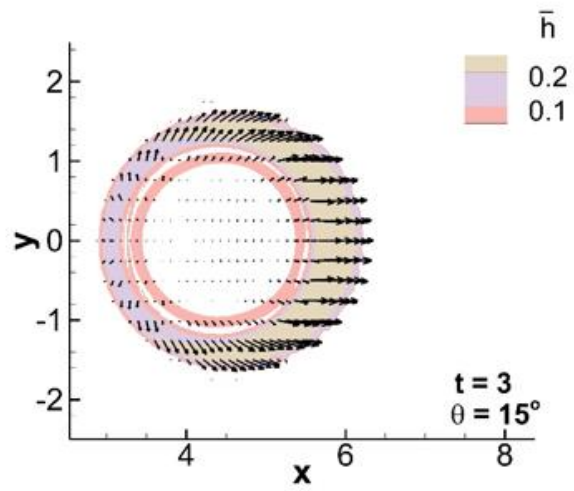
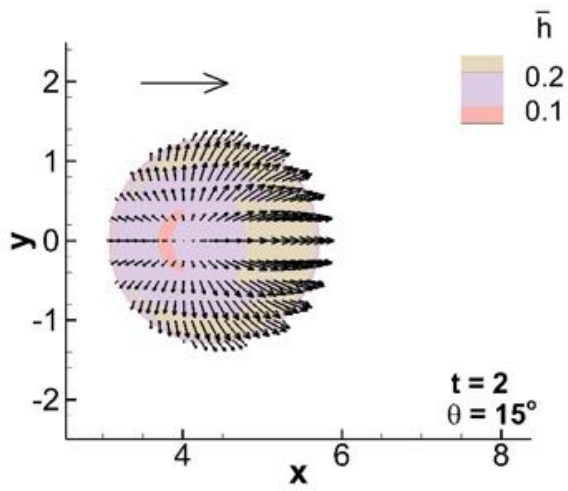


Figure 7-10. Streamwise ( $\bar{h}_x$ ) and spanwise ( $\bar{h}_y$ ) averages of the mean height ( $\bar{h}$ ) at  $t = 0, 3, 6, 10, 20, 30$  for  $\theta = 5^\circ, 10^\circ, 15^\circ, 20^\circ$ .  $\bar{h}_x$  reveals a mass buildup near the centerline.







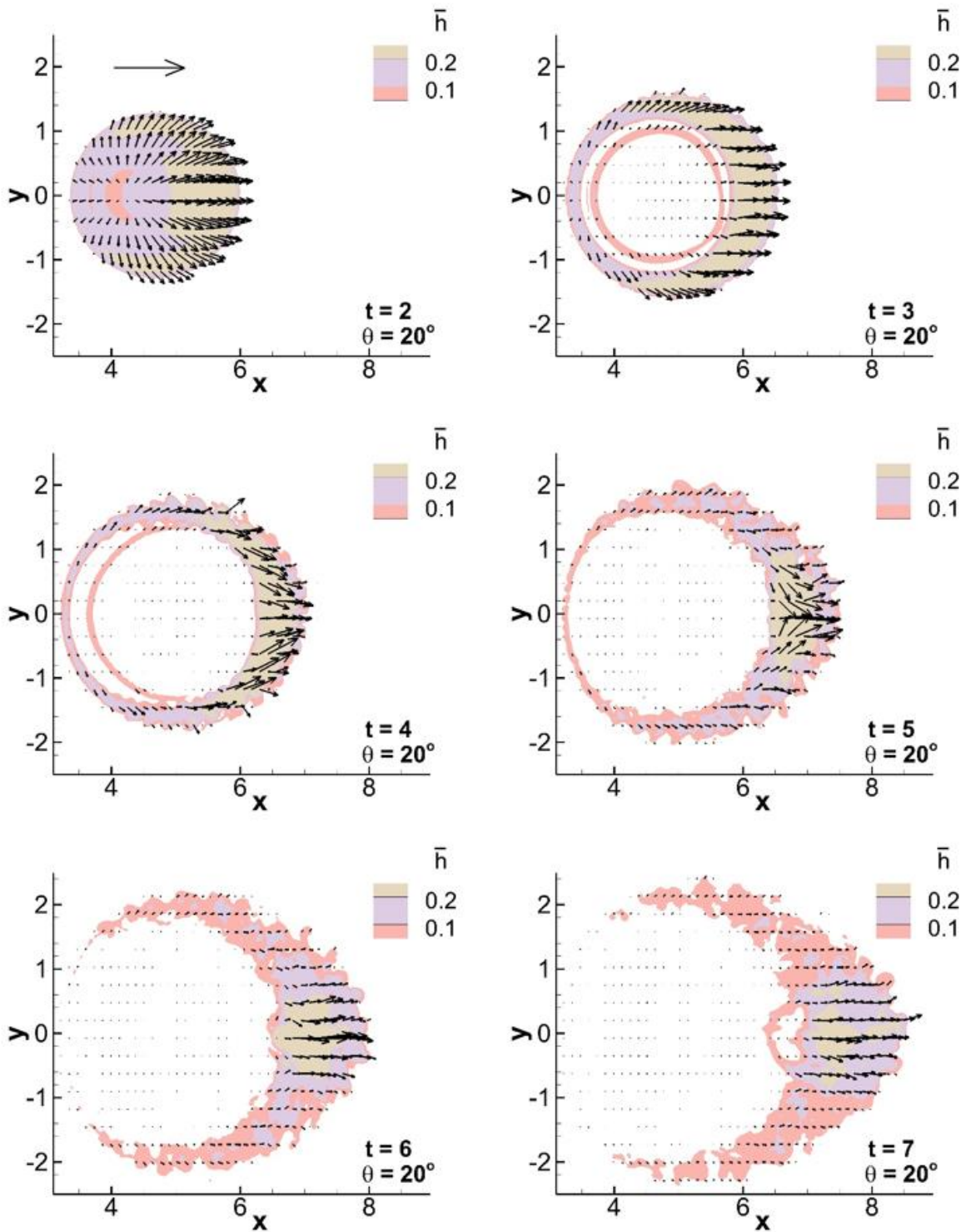


Figure 7-11. Instantaneous vector field derived from the density weighted, vertically averaged streamwise and spanwise components of velocity. The vector field overlays iso-contours of the vertically integrated current height  $\bar{h}$ .

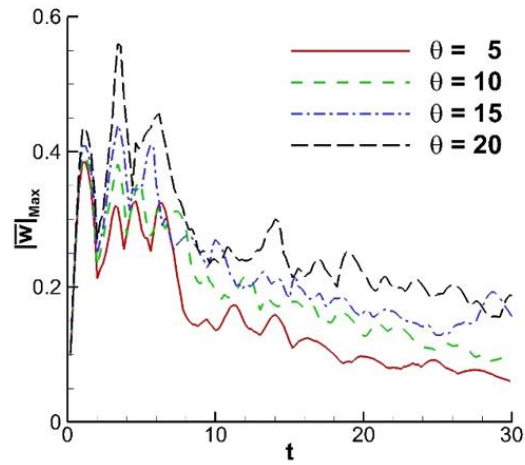


Figure 7-12. Temporal evolution of the maximum magnitude of the Favre average of the vertical component of the velocity.

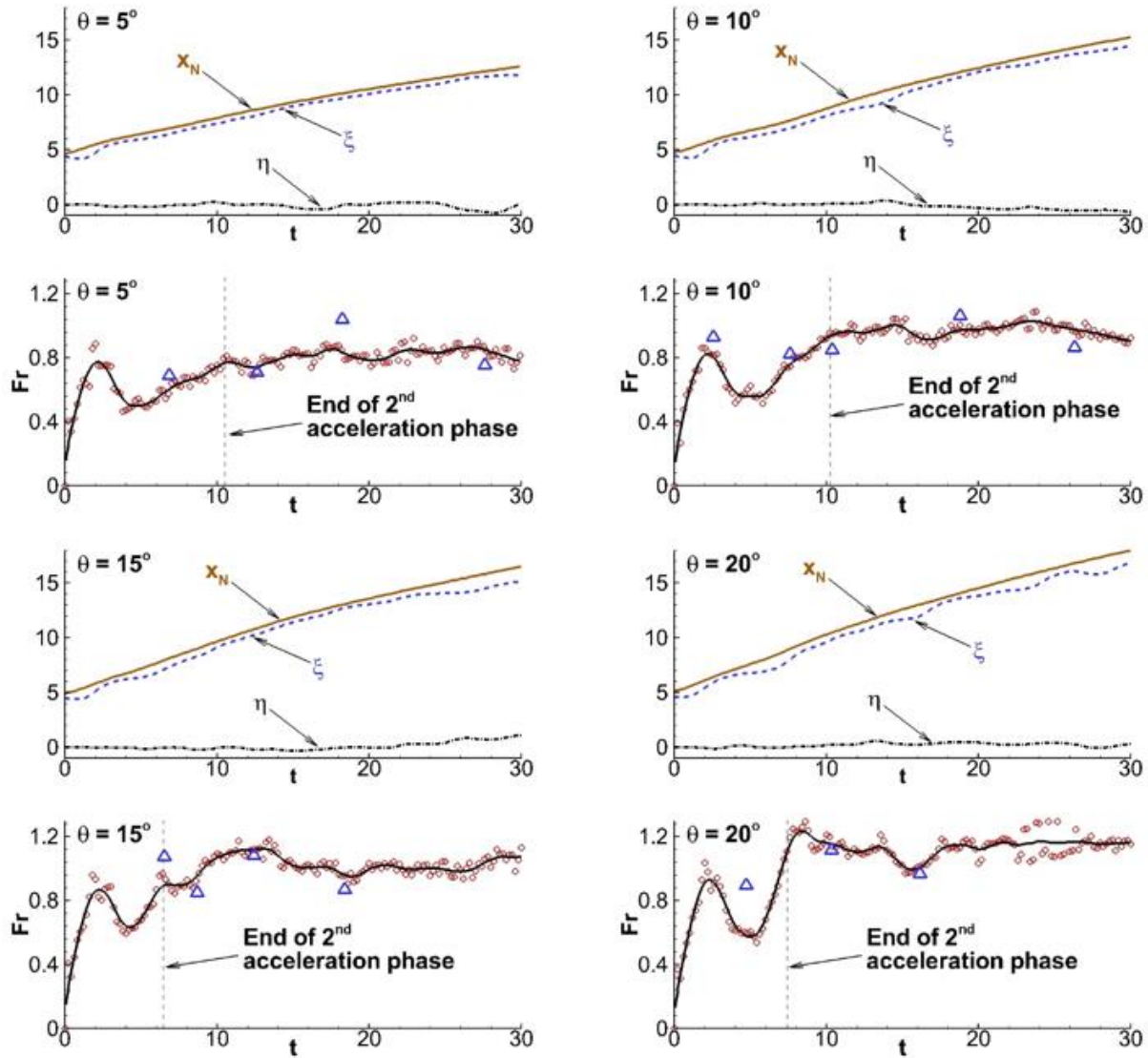


Figure 7-13. Temporal evolution of the Froude number: The circles correspond to the present simulation data. The solid black line is a 3<sup>rd</sup> order smoothing spline to help guide the eyes. The triangles correspond to experimental data from Ross *et al.* (2002). The vertical dashed line marks the end of the second acceleration phase. The front position is denoted by  $x_N$ .  $\xi(t)$  and  $\eta(t)$  represent the streamwise and spanwise coordinates of the position of the maximum height  $\bar{h}_{\text{Max}}$  (used for calculating the Froude number), respectively

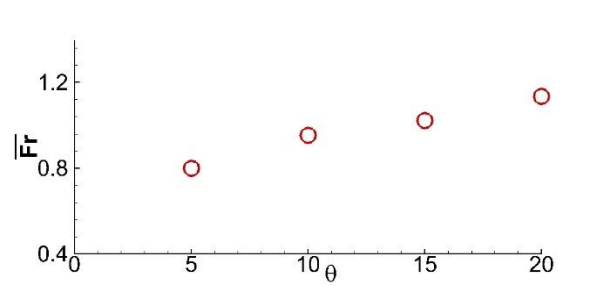
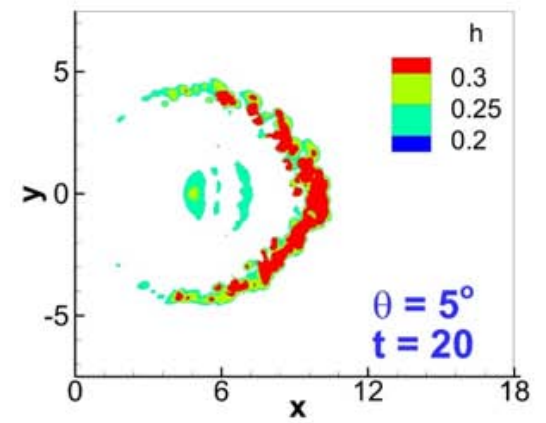
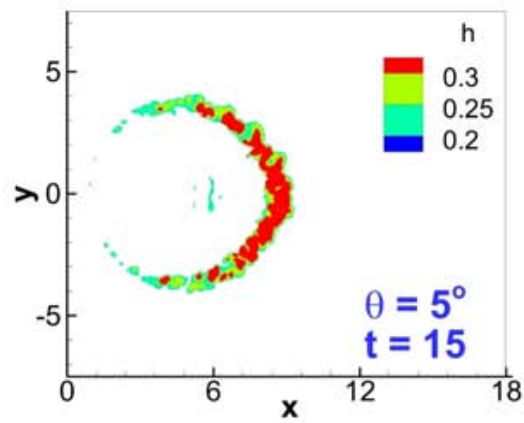
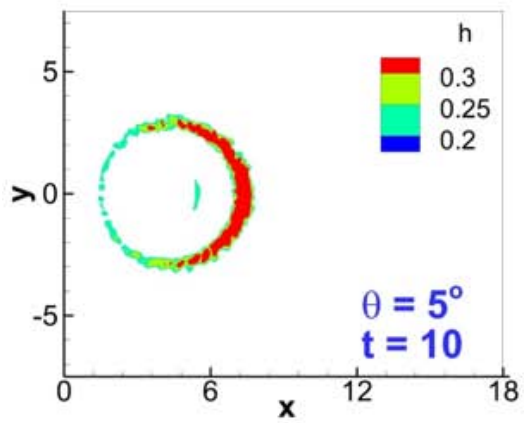
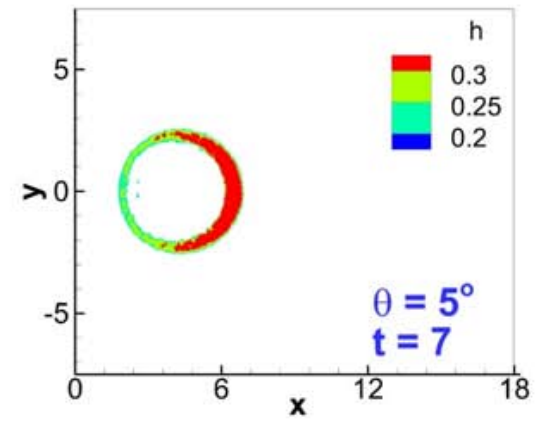
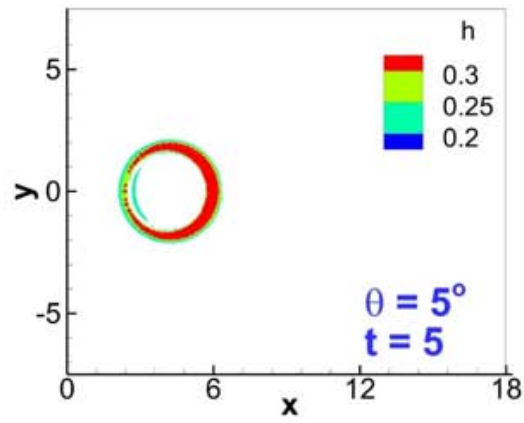
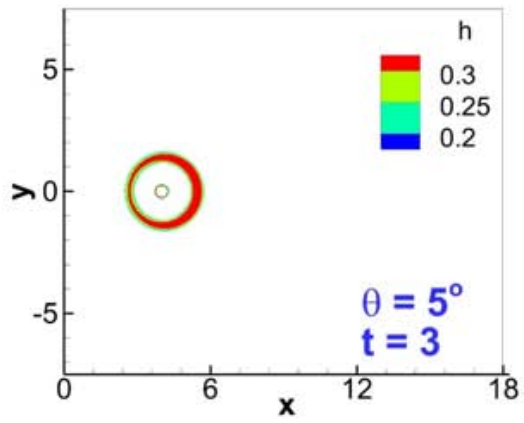
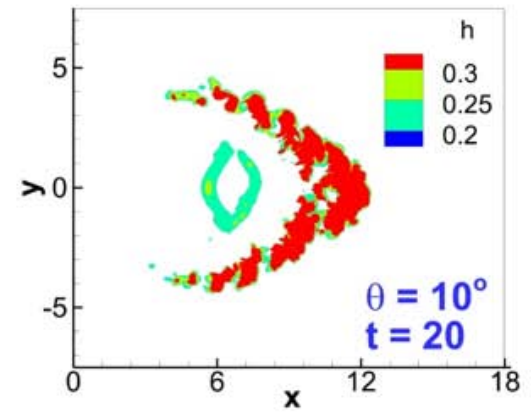
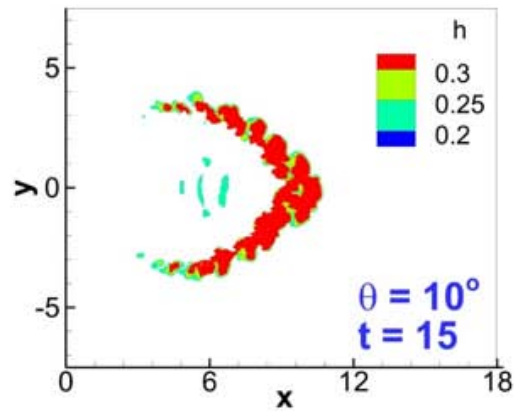
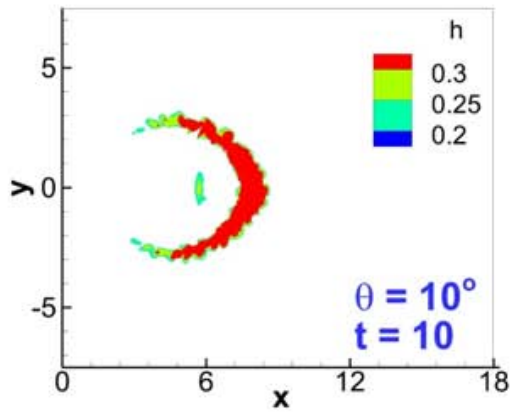
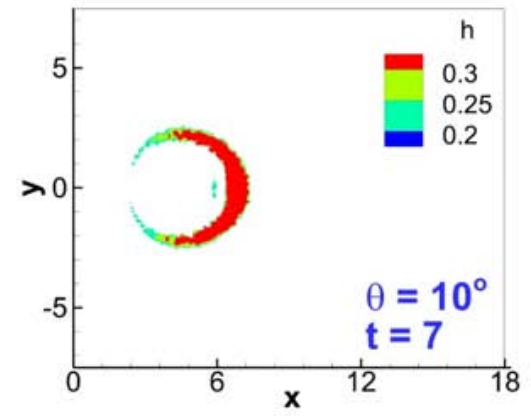
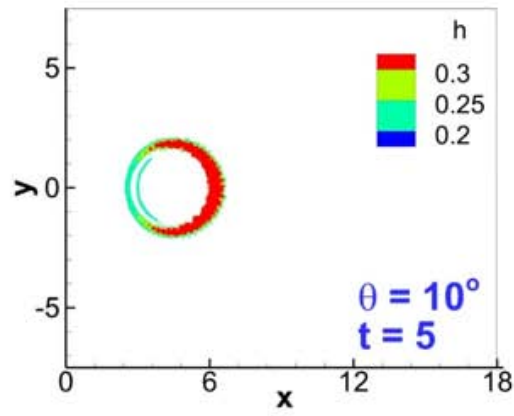
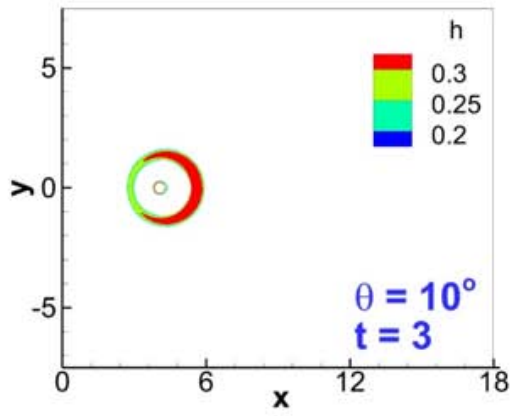


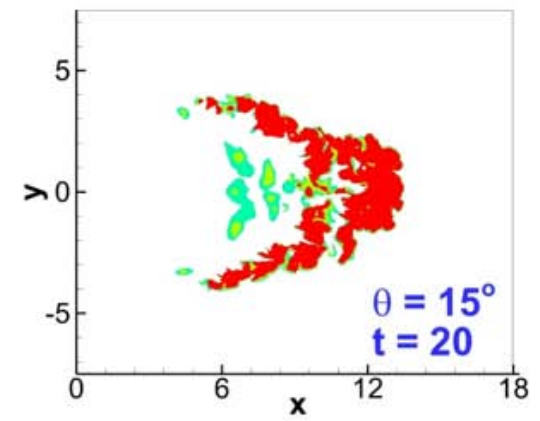
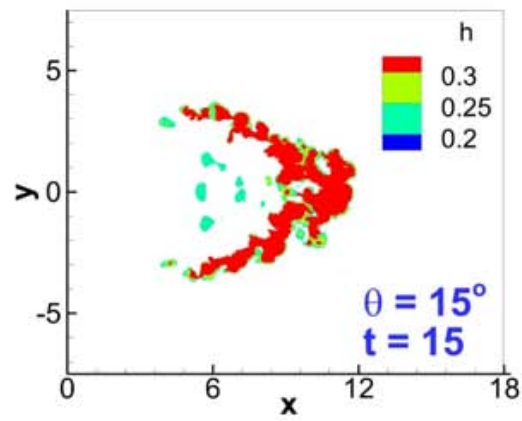
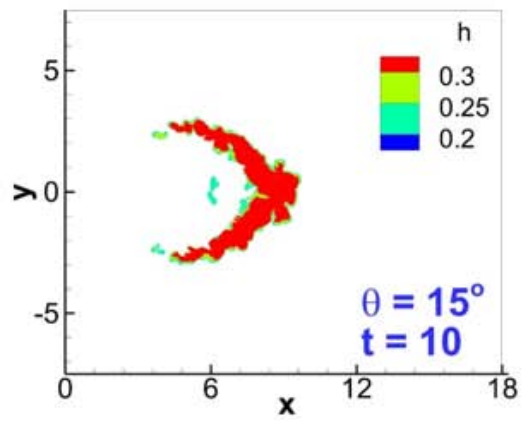
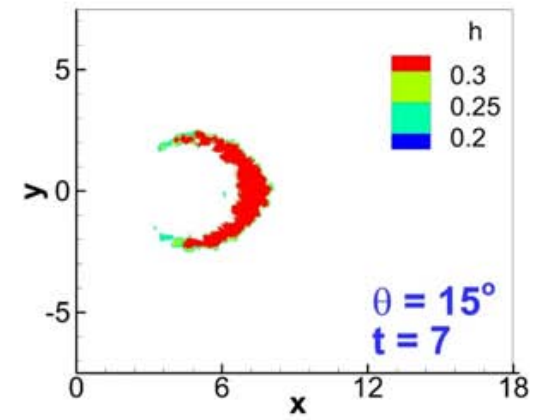
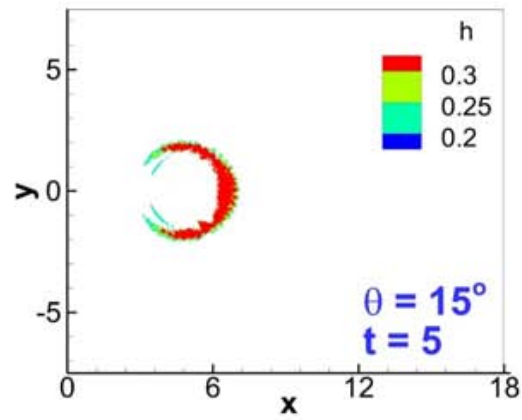
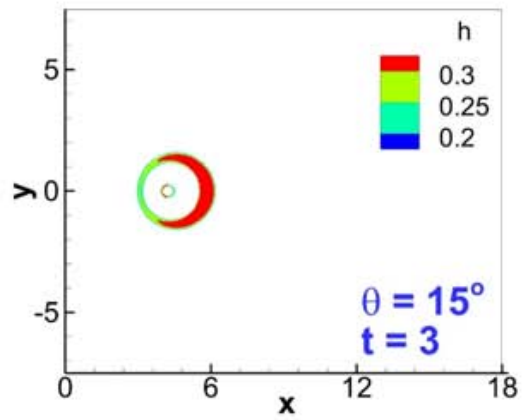
Figure 7-14. Mean Froude number as a function of bottom inclination. The Froude number is observed to increase linearly with bottom slope.

Table 7-2. Parameters used for defining the head.

Case number	$\rho_{th}$	$h_{th}$
1a	$1 \times 10^{-2}$	0.30
1b	$1 \times 10^{-2}$	0.25
1c	$1 \times 10^{-2}$	0.20
2a	$5 \times 10^{-3}$	0.30
2b	$5 \times 10^{-3}$	0.25
2c	$5 \times 10^{-3}$	0.20
3a	$3 \times 10^{-3}$	0.30
3b	$3 \times 10^{-3}$	0.25
3c	$3 \times 10^{-3}$	0.20







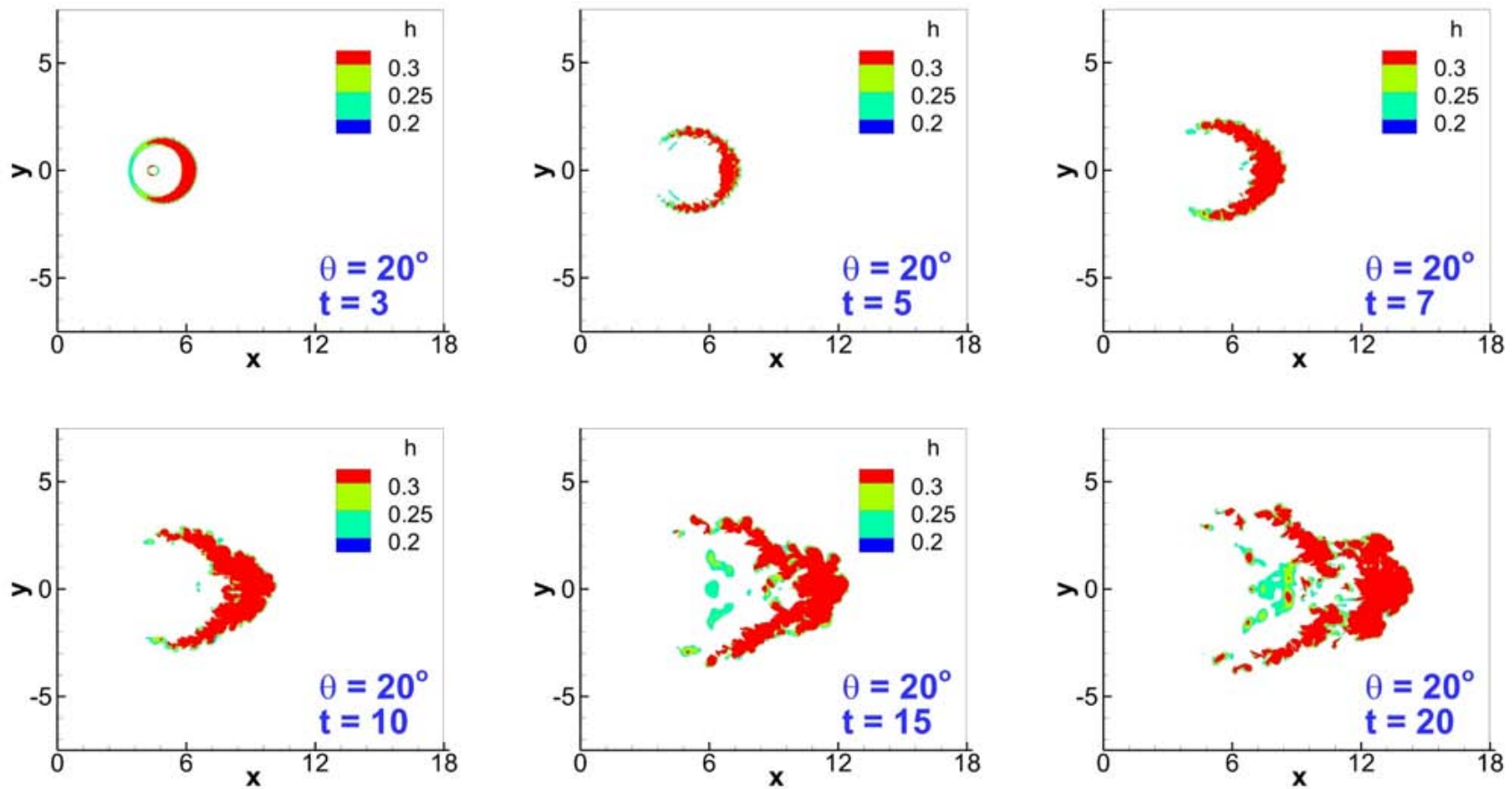


Figure 7-15. Wall-normal view of the shape of the head as defined by Eq. 7-16 for the parameters of case 1 (Table 7-2). The red color corresponds to the adopted parameters of case 1a.

Table 7-3. Parameters and derived quantities pertaining to the head of the gravity current.

Symbol	Quantity it represents	Definition
$V$	Volume	$V = \int_{-L_y/2}^{L_y/2} \int_0^{L_x} h I \, dx dy$
$M$	Mass	$M = \int_0^{L_z} \int_{-L_y/2}^{L_y/2} \int_0^{L_x} \rho I \, dx dy dz$
$x_{CM}$	Streamwise position of the center of mass	$x_{CM} = \frac{1}{M} \int_0^{L_z} \int_{-L_y/2}^{L_y/2} \int_0^{L_x} \rho x I \, dx dy dz$
$A$	Wall normal projected area	$A = \int_{-L_y/2}^{L_y/2} \int_0^{L_x} I \, dx dy$
$H$	Maximum height	$H = \max(Ih)$
$L$	Streamwise length	$L = \max(Ix) - \min(Ix)$
$W$	Spanwise width	$W = \max(Iy) - \min(Iy)$
$\tilde{h}$	Mean height	$\tilde{h} = V/A$
$V'$	Time rate of change of volume	$V' = dV/dt$
$M'$	Time rate of change of mass	$M' = dM/dt$
$u_{CM}$	Speed of the center of mass	$u_{CM} = d(x_{CM})/dt$
$\alpha$	Entrainment coefficient	$\alpha = \frac{V'}{A u_{CM}}$
$(L/W)'$	Time rate of change of length to width ratio	$(L/W)' = \frac{d(L/W)}{dt}$
$C$	Constant with the form of a Froude number	$C = \frac{u_{CM}}{\sqrt{\tilde{h}_{Max}}}$

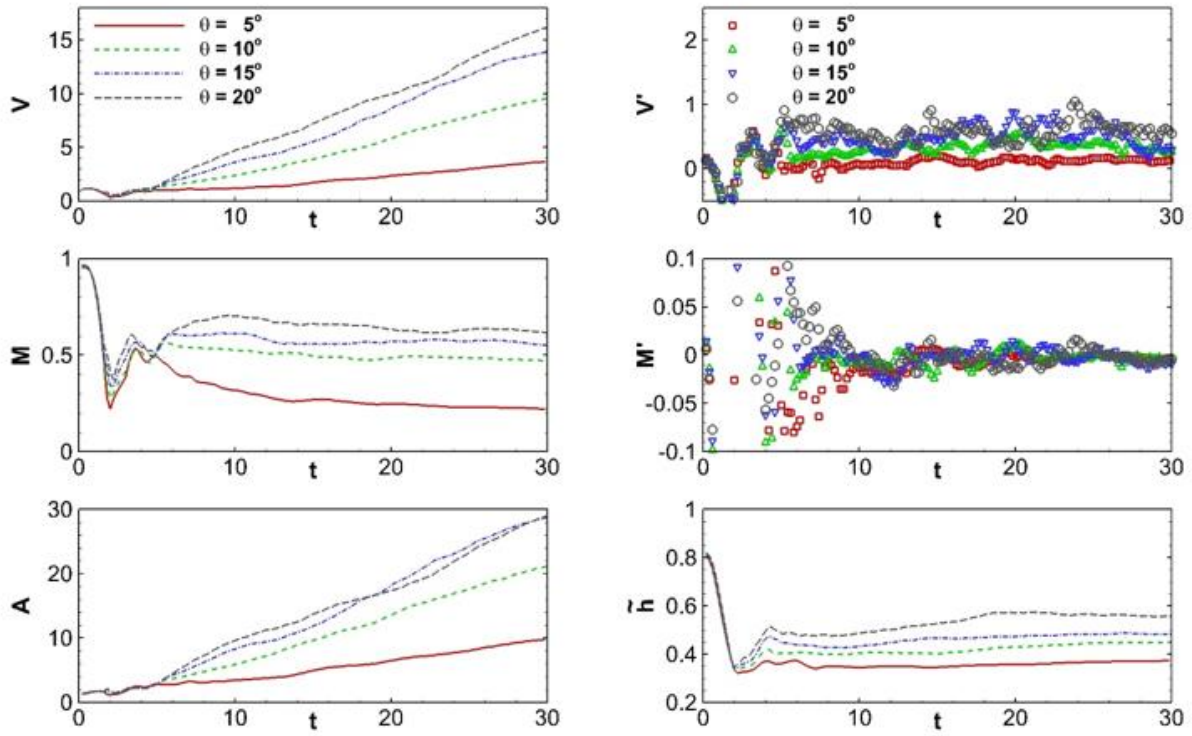


Figure 7-16. Temporal evolution of the volume  $V$ , mass  $M$ , wall-normal projected area  $A$ , mean height of the head  $\tilde{h}$ , and the time rates of change  $V'$  and  $M'$  of the volume and mass, respectively.

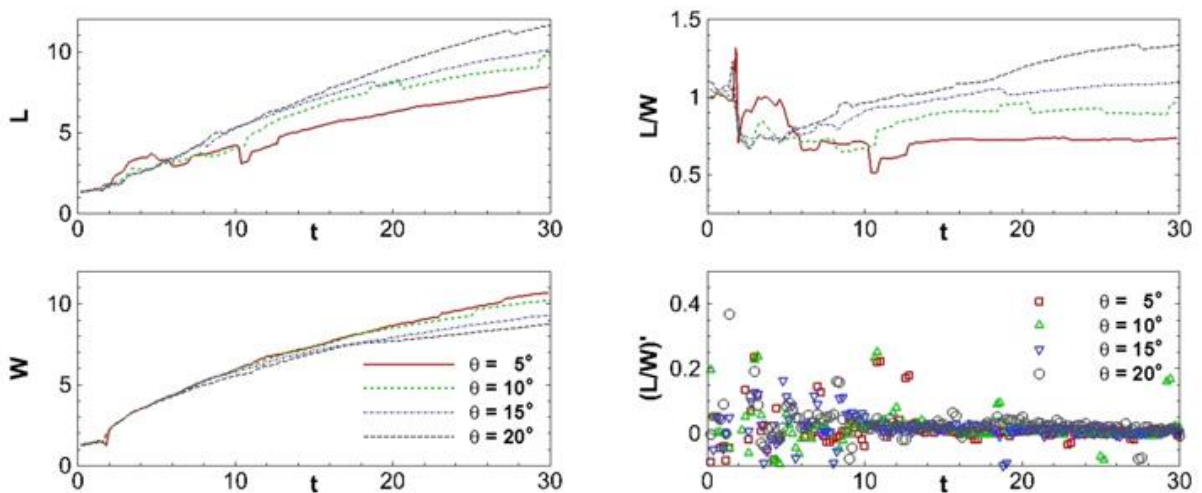


Figure 7-17. Length ( $L$ ), width ( $W$ ), length to width ratio ( $L/W$ ), and the time rate of change of the length to width ratio  $(L/W)'$  as function of time for  $\theta = 5^\circ, 10^\circ, 15^\circ, 20^\circ$ .

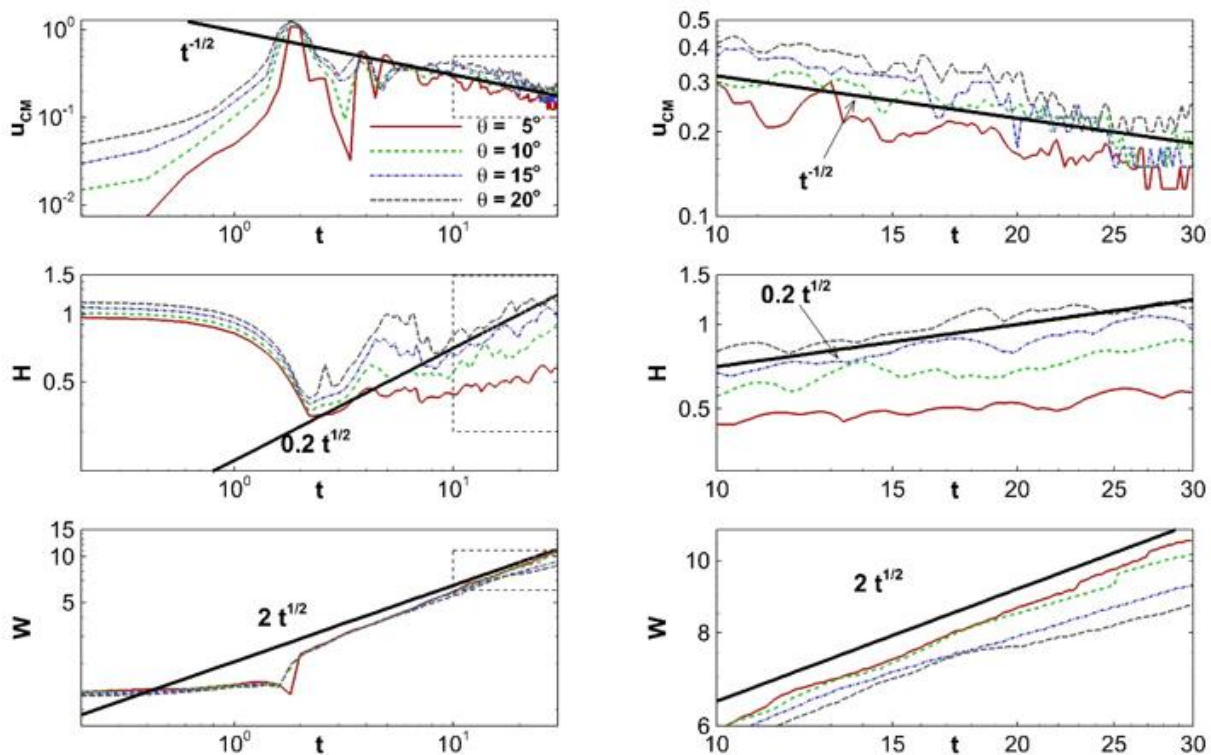


Figure 7-18. Log log plots of the speed of the center of mass ( $u_{CM}$ ), maximum height ( $H$ ), and maximum width ( $W$ ) in the head as function of time for  $\theta = 5^\circ, 10^\circ, 15^\circ, 20^\circ$ . A blown up view, corresponding to the dashed rectangle is shown on the right hand side.

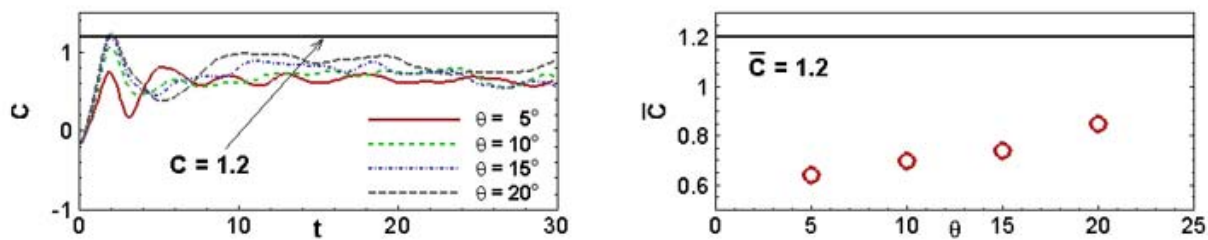


Figure 7-19. (Left)  $C$  as a function of time. (Right) mean value of  $C$  as a function of bottom slope  $\theta$ .

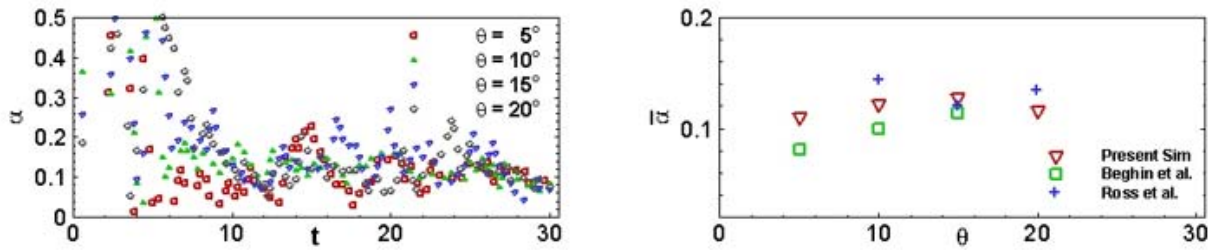


Figure 7-20. (Left) Temporal evolution of the entrainment coefficient  $\alpha$ . (Right) Mean value of  $\alpha$  beyond  $t = 10$  as a function of bottom slope  $\theta$ .

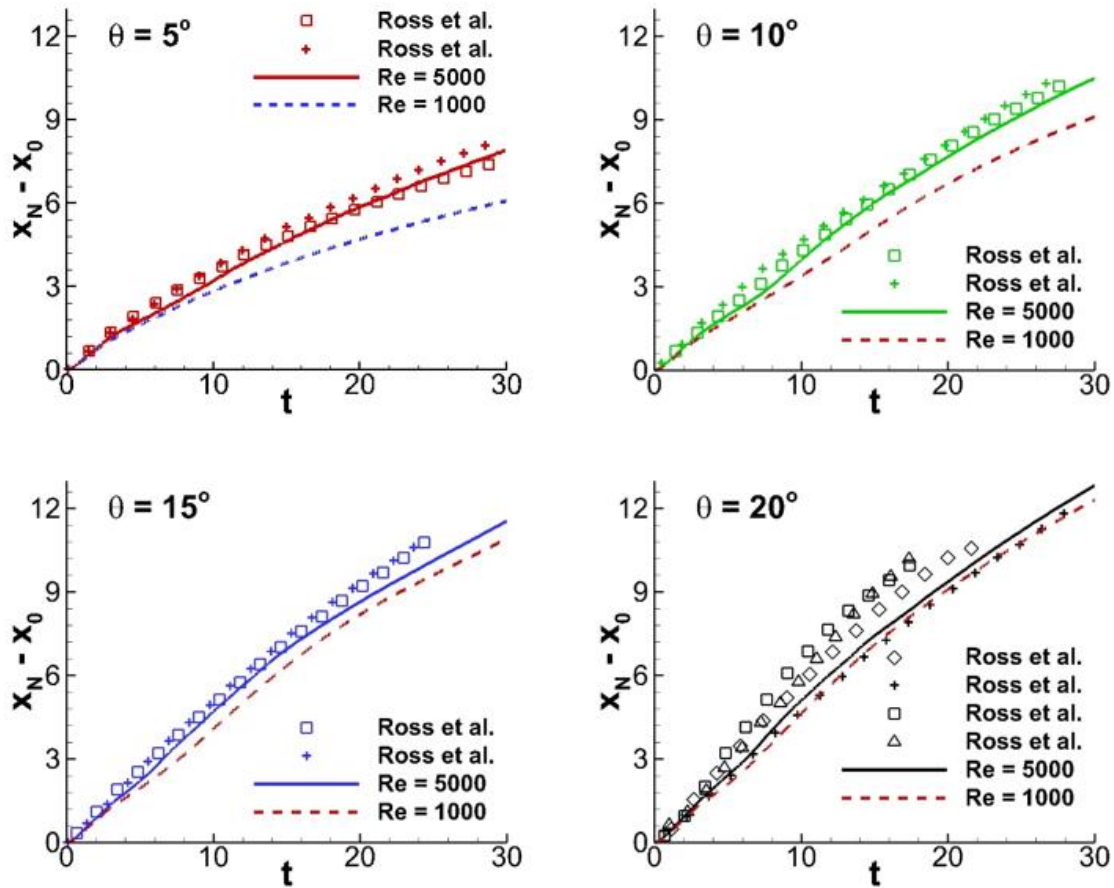


Figure 7-21. Front position as a function of time for different slopes. The influence of the Reynolds number on the front position is significant for shallow slopes and becomes less important at higher slopes.

## CHAPTER 8 CONCLUSIONS AND FUTURE WORK

We have addressed a simple, yet fundamental question in fluid dynamics: when a fluid is suddenly discharged into an ambient environment of different density, does the shape of the release affect the dynamics of the flow? The answer is yes, and the dependence on the initial shape may be very significant. To that end, we have conducted numerous experiments (covering a wide range of parameters), performed direct numerical simulations (DNS), and proposed a simple model to capture the essential dynamics of the flow.

It turns out that in those types of finite releases, the shape of the release greatly influences the subsequent spreading of the current. We observe that, provided the Reynolds number is large ( $Re > O(10^3)$ ), a non-circular release can have substantial azimuthal variations in terms of propagation speed, thickness (or height), maximum extent, and amount of deposition (in case of particle-laden flows). For certain geometries, we may identify principal directions along which the discrepancy in the abovementioned quantities (speed, thickness, ...) is highest. In the case of the rectangular releases, these principal directions represent the major and minor axes of the rectangular cross-section.

The difference in velocities along these principal directions is large to the extent that, for a plan view, the current front (beyond the self-similar inertial phase of spreading) resembles an ellipse whose major and minor axes are aligned with the minor and major axes of the initial rectangular cross-section, respectively. In some cases, the velocity along the initial minor axis was twice that along the initial major axis for extended periods of time. Moreover, for the case of particle-laden currents from

rectangular releases, the extent and amount of deposition (in addition to the front velocity) differed greatly along the principal axes.

The dependence of these fixed volume releases on the initial shape means that one could, by solely changing the shape (while maintaining the same volume) of release, “guide” the current to flow in certain directions and control, to some extent, the amount of deposition in each direction.

Details on the experiments, simulations, and the proposed theoretical model are discussed in Chapter 2. The experiments covered a wide range of parameters including Boussinesq and highly non-Boussinesq bottom currents, light surface flows, viscous (low Reynolds number) currents, and particle-laden flows. Various initial shapes were considered including axisymmetric and non-axisymmetric cross sections. The DNS on the other hand tailored exclusively to Boussinesq bottom currents (both scalar and particle-laden). We also provided further details on the proposed extended box model. The governing equations are derived and then discretized to be solved numerically.

In Chapter 3, we investigated Boussinesq scalar (conservative) currents both experimentally and numerically (direct numerical simulations). The shape of the release was found to greatly affect the spreading distance and front velocities as well as the thickness of the current. Azimuthal variations differed by as much as a factor of 2 along the principal directions of the release. A simple theoretical model was proposed, which was able to correctly capture the preferential spreading direction resulting from non-circular releases.

Direct numerical simulations (DNS) for axisymmetric particle-laden currents were explored in Chapter 4. The study aimed at understanding the early stages of fixed

volume releases. A set of coherent, large-scale vortex tubes were observed to advance at close proximity to the bottom surface. Unlike vertically averaged numerical models, the DNS allows us to explore these three-dimensional vortical structures which play an important role in the near-wall dynamics, especially in terms of erosion and resuspension of particles.

A wide range of experiments are reported in Chapter 5. The experiments considered different types of gravity currents (Boussinesq and highly non-Boussinesq, surface, viscous, and particle-laden flows). Here, the main objective was to test the dependency of the initial shape for a wide variety of conditions. We found the flow to be strongly dependent on the initial shape, provided the Reynolds number remains large ( $Re > O(10^3)$ ). Some of the main assumptions behind the extended box model are examined and validated using DNS.

In Chapter 6, we remain in the context of Boussinesq bottom flows, however for monodisperse particle-laden currents. We monitor two quantities in the experiments, these are the location of the front and the final thickness of the deposit. Various parameters were varied to assess the dependence on the settling velocity, particle volume fraction, and initial height aspect ratio. Corresponding direct numerical simulations (DNS) were performed. The front location from the DNS compared favorably with experiments, however there were some noticeable differences in the thickness of the deposit. Those differences were attributed to a lack of bedload transport mechanism in the simulations.

We performed highly resolved numerical simulations in Chapter 7 to investigate the dynamics of a circular slanted cylinder released on a sloping boundary. The front

position from our simulations compared favorably with the experiments of Ross *et al.* (2002). The front velocity revealed some surprising features. Planar gravity currents (on horizontal and sloping boundaries), and axisymmetric currents (on horizontal boundaries) undergo a single acceleration phase immediately after release. The front speed in our simulations, however was seen to transition through two acceleration phases. This peculiar behavior was attributed to a mass buildup of heavy material near the front of the current around the centerline. We presented a simple method for detecting the head of the gravity current and used it to extract the various properties pertaining to the head (volume, mass, shape, growth rates, etc.). Thermal theory pertaining to free axisymmetric vertical thermals suggests the speed of the center of mass and the horizontal extreme coordinate of the thermal cap evolve (beyond the self-similar phase) as  $t^{-1/2}$ , and  $t^{1/2}$ , respectively. These relations were found to be satisfied in the present simulations. The entrainment coefficient was calculated and compared well to previous experiments and theoretical models. It was found to be of the order of 0.1 and to depend very little on the slope.

There are other situations where the manner in which particle-laden material is discharged into an ambient environment could affect how the current develops and where the particles eventually rain out. One such example is dredging. Dredging consists of releasing a volume of particles or turbid mixture at the surface of a body of water. The density of particles or that of the turbid mixture is larger than water, and therefore after release, the mixture descends as a coherent body vertically downwards. Under certain conditions, a gravity current might form after the dynamic collapse of the current with the bottom surface. The dynamics of the current could be influenced by the

initial shape of the release, and hence the particles may not deposit as intended. In some applications, there is a desire for accurate placement of particles at the bottom surface, either for environmental safety considerations (toxic material), or for financial considerations where the released material is relatively expensive or hard to come by. Gaining a better understanding of how the shape of the release affects the final deposition profile of the sediments would be helpful for these types of situations where accurate placement of sediment is essential.

Following the studies conducted for this thesis, there are a number of complementary projects that we would like to explore in the future. (1) The first project is to develop a shallow water code for Boussinesq currents that can handle non-canonical initial conditions. The shallow water equations are a very popular tool in the field of gravity currents, it is worthwhile to investigate how well they could capture the dynamics of non-circular releases. (2) The second project is to extend the EBM model to incorporate particle-laden flows. The EBM, is a quick predictive tool that has been quite effective in exploring the non-uniform behavior of non-circular density currents. (3) Our current Navier-Stokes solver (Spectral code used in Chapters 3-7) does not account for redistribution of sediments on the bottom wall (due to bedload transport). We are currently working on incorporating the effects of bedload transport. This is a one-way coupling problem between the flow and the deposited sediments through the shear stress at the bottom surface. Including the effects of bedload transport could offer significant improvement in capturing the final deposition profile for particle-laden currents. (4) Finally, we are interested in performing experiments on finite release gravity currents on uniform slopes. DNS results in Chapter 7 have revealed some very

interesting dynamics in which front velocity of the current is seen to undergo 2 acceleration phases. It is worthwhile to verify these results with a new set of experiments.

## APPENDIX NUMERICAL DETAILS OF THE EXTENDED BOX MODEL

We discretize equations (5-17)-(5-19) into a set of equidistant Lagrangian points and use an eighth-order central finite difference scheme for the spatial derivatives. A third order Runge-Kutta low storage scheme is used for time integration. Each time step consists of two stages. The first is an intermediate stage where the governing equations (5-17)-(5-19) are integrated. At the end of this stage, because of the azimuthal variations, the Lagrangian points are no longer equidistant. Each sub-volume associated with a Lagrangian point is then assumed to be homogeneously distributed (along the front) between its two adjacent midpoints.

The second stage involves remapping the non-equidistant Lagrangian points to render them equidistant along the front. This step is necessary, especially in the case of concave corners, as in the plus-shape configuration presented in figure 7 of Zgheib *et al.* (2014) for instance, as Lagrangian points may cross each other causing the front to fold on itself. This problem is classically encountered in Lagrangian techniques such as Front Tracking approaches (Unverdi & Tryggvason 1992). Once the points are remapped, new midpoints are calculated and the sub-volumes of the release associated with each new Lagrangian point is computed. Then a step of redistributing the sub-volumes per unit arc length ( $\sigma h_N$ ) is performed, and this step preserves the total volume of the release.  $u_N$  and  $h_N$  are interpolated at the new equi-spaced Lagrangian points.

An example of spatial and temporal convergence of the present method is shown in Figure 5-19 for the RR configuration. In Figure 5-19a, the time step for integration of equations (5-17)-(5-19) was fixed at  $\Delta t = 0.1$ . Initially the front was discretized with 80 Lagrangian points. The number of points was then doubled and the criterion for

convergence was met when the mean of the absolute value of the difference in the front location (for the fast and slow fronts) between two successive cases, denoted  $\epsilon$ , fell below 1%,  $\epsilon$  being defined as,

$$\epsilon = \frac{1}{100} \int_0^{100} \frac{|r_N^I(t) - r_N^{II}(t)|}{r_N^I(t)} dt \quad (\text{A-12})$$

Here  $r_N^I(t)$  is the front location for a specific spatial resolution, and  $r_N^{II}(t)$  is the front location for twice the spatial resolution. The criterion for convergence was tested and met along the fast and slow fronts separately. In Figure 5-19b, the spatial resolution was set at 160 Lagrangian points, for which three different time steps differing by a factor of two were used. It can be seen that the present method is robust even for a moderately low number of Lagrangian points and moderately large time steps, leading to insignificant computational time as compared to Navier-Stokes simulations.

## LIST OF REFERENCES

- Allen, J. R. L. 1982 *Sedimentary Structures: their Character and Physical Basis*. Elsevier.
- Bagnold, R. A. 1941. *The physics of blown sand and desert dunes*. Methuen.
- Beghin, P., Hopfinger, E. J., & Britter, R. E. 1981. Gravitational convection from instantaneous sources on inclined boundaries. *J. Fluid Mech.* **107**, 407–422.
- Benjamin, T.B. 1968. Density currents and related phenomena. *J. Fluid Mech.* **31**, 209-248.
- Birman V., Martin J.E., & Meiburg E. 2005. The non-Boussinesq lock-exchange problem. Part 2. High-resolution simulations. *J. Fluid Mech.* **537**, 125–44.
- Blanchette, F., Strauss, M., Meiburg, E., Kneller, B., Glinsky, M. 2005. High-resolution numerical simulations of resuspending gravity currents: condition for self-sustainment. *J. Geophys. Res.* **110**, c12022.
- Boegman, L., & Ivey, G. N. 2009. Flow separation and resuspension beneath shoaling nonlinear internal waves. *Journal of Geophysical Research: Oceans*, **114**(C2), 1978-2012.
- Bonnecaze, R. T., Hallworth, M. A., Huppert H. E., & Lister, J. R. 1995 Axisymmetric particle-driven gravity currents. *J. Fluid Mech* **294**, 93-122.
- Bonnecaze, R. T., Huppert H. E., & Lister, J. R. 1993 Particle-driven gravity currents. *J. Fluid Mech* **250**, 339-369.
- Bonometti T. & Balachandar S. 2008 Effect of Schmidt number on the structure and propagation of density currents. *Theor. Comput. Fluid Dyn.* **22**, 341-361.
- Bonometti T. & Balachandar S. 2008. Effect of Schmidt number on the structure and propagation of density currents. *Theor. Comput. Fluid Dyn.* **22**, 341-361.
- Bonometti, T., Balachandar, S. & Magnaudet, J. 2008. Wall effects in non-Boussinesq density currents. *J. Fluid Mech.* **616**, 445-475.
- Borden, Z. & Meiburg, E. 2013. Circulation based models for Boussinesq gravity currents. *Phys. Fluids* **25**, 101301.
- Brady, J. F. & Acrivos, A. 1981 Steady flow in a channel or tube with an accelerating surface velocity. An exact solution to the Navier-Stokes equations with reverse flow. *J. Fluid Mech.* **112**, 127-150.
- Britter R.E. 1989. Atmospheric dispersion of dense gases. *Annu. Rev. Fluid Mech.* **21**, 317-344.

- Britter, R. E. & Linden, P. F. 1980. The motion of the front of a gravity current travelling down an incline. *J. Fluid Mech.* **99**, 531–543.
- Britter, R. E., & Simpson, J. E. 1978. Experiments on the dynamics of a gravity current head. *J. Fluid Mech.* **88**, 223-240. Cantero, M. I., Balachandar, S. & Garcia, M. H. 2007b. High-resolution simulations of cylindrical density currents. *J. Fluid Mech.* **590**, 437-469.
- Cantero, M., Balachandar, S. & Garcia, M. 2007b High-resolution simulations of cylindrical density currents. *J. Fluid Mech.* **590**, 437-469.
- Cantero, M. I., Balachandar, S. & Garcia, M. H. 2008a. An Eulerian–Eulerian model for gravity currents driven by inertial particles. *Intl J. Multiphase Flow* **34**, 484–501.
- Cantero M., Balachandar S., García M. & Bock D. 2008b. Turbulent structures in planar gravity currents and their influence on the flow dynamics. *J. Geophys. Res. - Oceans*, **113**, C08018.
- Cantero, M. I., García, M. H., & Balachandar, S. 2008c. Effect of particle inertia on the dynamics of depositional particulate density currents. *Computers & Geosciences*, **34**(10), 1307-1318.
- Cantero, M., Lee, J. R., Balachandar, S. & Garcia, M. 2007a. On the front velocity of gravity currents. *J. Fluid Mech.* **586**, 1–39.
- Canuto, C., Hussaini, M., Quarteroni, A. & Zang, T. 1988. Spectral Methods in Fluid Dynamics. Springer.
- Chakraborty, P., Balachandar, S. & Adrian, R. 2005. On the relationships between local vortex identification schemes. *J. Fluid Mech.* **535**, 189–214.
- Choi, S.-U., Garcia, M., 1995. Modeling of one-dimensional turbidity currents with a dissipative-Galerkin finite element method. *J. Hydra. Res.* **33** (5), 623–648.
- Cortese, T. & Balachandar, S. 1995. High performance spectral simulation of turbulent flows in massively parallel machines with distributed memory. *Intl J. Supercomputer Applic* **9**, 187–204.
- Dade W. & Huppert H. 1995. A box model for non-entraining suspension-driven gravity surges on horizontal surfaces, *Sedimentology* **42**, 453–471.
- Dai, A. 2013. Experiments on gravity currents propagating on different bottom slopes. *J. Fluid Mech.* **731**, 117-141.
- Dai, A., Ozdemir, C. E., Cantero, M. I., & Balachandar, S. 2012. Gravity Currents from Instantaneous Sources Down a Slope. *J. Hydraulic Eng.* **138**, 237–246.

- Didden, N., & Maxworthy, T. 1982. Viscous spreading of plane and axisymmetric gravity currents. *J. Fluid Mech.* **121**, 27-42.
- Doyle J. & Carlson J.M. 2000. Power laws, highly optimized tolerance, and generalized source coding. *Phys. Rev. Lett.* **84**, 5656.
- Dufek, J., & Bergantz, G. W. 2007. Suspended load and bed-load transport of particle-laden gravity currents: the role of particle–bed interaction. *Theoretical and Computational Fluid Dynamics*, **21**(2), 119-145.
- Etienne J., Hopfinger E.J., & Saramito P. 2005. Numerical simulations of high density ratio lock-exchange flows. *Phys Fluids*. **17** 036601.
- Faillietaz J., Louchet F. & Grasso J.R. 2004. Two-threshold model for scaling laws of noninteracting snow avalanches. *Phys. Rev. Lett.* **93**, 208001.
- Fleischmann, C. M., & McGrattan, K. B. 1999. Numerical and experimental gravity currents related to backdrafts. *Fire Safety Journal* **33**, 21-34.
- Francis, P. 1993 *Volcanoes. A planetary perspective*, Francis, P. Clarendon Press, Oxford (UK)
- Garcia, M., Parker, G. 1993. Experiments on the entrainment of sediment into suspension by a dense bottom current. *J. Geophys. Res.* **98** (C3), 4793–4807.
- Gladstone, C., Phillips, J. C., & Sparks, R. S. J. 1998. Experiments on bidisperse, constant-volume gravity currents: propagation and sediment deposition. *Sedimentology*, **45**, 833-844.
- Gladstone, C., & Woods, A. 2000. On the application of box models to particle-driven gravity currents. *J. Fluid Mech.* **416**, 187-195.
- Gröbelbauer H.P. Fanneløp T.K. & Britter R.E. 1993. The propagation of intrusion fronts of high density ratio. *J. Fluid Mech.* **250**, 669-687.
- Grundy, R. E., & Rottman, J. W. 1986. Self-similar solutions of the shallow-water equations representing gravity currents with variable inflow. *J. Fluid Mech.* **169**, 337-351.
- Gutmark, E. J. & Grinstein, F. F. 1999. Flow control with noncircular jets. *Ann. Rev. Fluid Mech.* **31**, 239-272.
- Hacker, J., Linden, P. F., & Dalziel, S. B. 1996. Mixing in lock-release gravity currents. *Dyn. of Atmospheres and Oceans* **24**, 183-195.
- Hall F.F., Neff W.D. & Frazier T.V. 1976. Wind shear observations in thunderstorm density currents. *Nature* **264**, 408-411.

- Hallworth, M., & Huppert, H. 1998. Abrupt transitions in high-concentration, particle-driven gravity currents. *Phys. Fluids*, **10**, 1083-1087.
- Hallworth, M. A., Huppert, H. E., Phillips, J. C., & Sparks, R. S. J. 1996. Entrainment into two-dimensional and axisymmetric turbulent gravity currents. *J. Fluid Mech.* **308**, 289-312.
- Hallworth M.A., Huppert H.E. & Ungarish M. 2001. Axisymmetric gravity currents in a rotating system: experimental and numerical investigations. *J. Fluid Mech.* **447**, 1-29.
- Härtel, C., Fredrik C., & Mattias T. 2000. Analysis and direct numerical simulation of the flow at a gravity-current head. Part 2. The lobe-and-cleft instability. *J. Fluid Mech.* **418**, 213-229.
- Hogg, A., Hallworth, M., & Huppert, H. 2005. On gravity currents driven by constant fluxes of saline and particle-laden fluid in the presence of a uniform flow. *J. Fluid Mech.* **539**, 349-385.
- Hopfinger E.J. 1983. Snow avalanche motion and related phenomena. *Annu. Rev. Fluid Mech.* **15**, 47-76.
- Hoult D.P. 1972. Oil spreading in the sea. *Annu. Rev. Fluid Mech.* **4**, 341-368.
- Huppert, H. E. 1982. Propagation of two-dimensional and axisymmetric viscous gravity currents over a rigid horizontal surface. *J. Fluid Mech.* **121**, 43-58.
- Huppert H.E. 2006. Gravity currents: a personal perspective. *J. Fluid Mech.* **554**, 299-322.
- Huppert, H. E. & Simpson, J. 1980. The slumping of gravity currents. *J. Fluid Mech.* **99**, 785-799.
- Huq, P. 1996. The role of aspect ratio on entrainment rates of instantaneous, axisymmetric finite volume releases of dense fluid. *J. Hazard. Mater.* **49**, 89-101.
- Klemp J.B., Rotunno R. & Skamarock W.C. 1994. On the dynamics of density currents in a channel. *J. Fluid Mech.* **269**, 169-198.
- Kubat, M., Holte, R. C., & Matwin, S. 1998. Machine learning for the detection of oil spills in satellite radar images. *Machine learning* **30**, 195-215.
- La Rocca M., Adduce C., Sciortino G. & Pinzon A.B. 2008. Experimental and numerical simulation of three-dimensional gravity currents on smooth and rough bottom. *Phys. Fluids* **20**, 106603.

- Lee, H., Ha, M. Y., & Balachandar, S. 2012. Work-based criterion for particle motion and implication for turbulent bed-load transport. *Physics of Fluids*, **24**(11), 116604.
- Lighthill J., *Waves In Fluids* (Cambridge Univ. Press, 1978).Lowe, D. R. 1982. Sediment gravity flows: II Depositional models with special reference to the deposits of high-density turbidity currents. *J. Sed. Res.*, **52** 279-297.
- Lowe R.J., Rottman J.W., Linden P.F. 2005. The non-Boussinesq lock-exchange problem. Part 1. Theory and experiments. *J. Fluid Mech.* **537**,101–24.
- Marino, B. M., Thomas, L. P., & Linden, P. F. 2005. The front condition for gravity currents. *J. Fluid Mech.* **536**, 49-78.
- Maxworthy, T. 1999. The dynamics of sedimenting surface gravity currents. *Journal of Fluid Mechanics*, **392**, 27-44.
- Meiburg E. & Kneller B. 2010. Turbidity currents and their deposits. *Annu. Rev. Fluid Mech.* **42**, 135-156.
- Necker, F., H"artel, C., Kleiser, L. & Meiburg, E. 2002. High-resolution simulations of particle-driven gravity currents. *Intl J. Multiphase Flow* **28**, 279–300.
- Ooi, S. K., Constantinescu, G., & Weber, L. J. 2007. 2D large-eddy simulation of lock-exchange gravity current flows at high Grashof numbers. *J. Hydraulic Eng.* **133**, 1037-1047.
- Paik, J., Eghbalzadeh, A., & Sotiropoulos, F. 2009. Three-dimensional unsteady RANS modeling of discontinuous gravity currents in rectangular domains. *J. Hydraulic Eng.* **135**, 505-521.
- Parker, G., Fukushima, Y., & Pantin, H. M. 1986. Self-accelerating turbidity currents. *Journal of Fluid Mechanics*, **171**, 145-181.
- Quinn, W. R. 1989. On mixing in an elliptic turbulent free jet. *Phys. Fluids A* **1**: 1716-22.
- Ross, A. N., Linden, P. F., & Dalziel, S. B. 2002. A study of three-dimensional gravity currents on a uniform slope. *J. Fluid Mech.***453**, 239-261.
- Rottman, J. W., & Simpson, J. E. 1983. Gravity currents produced by instantaneous releases of a heavy fluid in a rectangular channel. *J. Fluid Mech.* **135**, 95-110.
- Sachdev P.L. 2004. *Shock waves and explosions* (Chapman & Hall/CRC).
- Shields, A. 1936. Application of similarity principles and turbulence research to bed-load movement.

- Shin, J. O., Dalziel, S. B., & Linden, P. F. 2004. Gravity currents produced by lock exchange. *J. Fluid Mech.* **521**, 1-34.
- Shringarpure, M., Cantero, M., & Balachandar, S. 2012. Dynamics of complete turbulence suppression in turbidity currents driven by monodisperse suspensions of sediment. *J. Fluid Mech.* **712**, 384-417.
- Simpson, J. E. 1972. Effects of the lower boundary on the head of a gravity current. *J. Fluid Mech.* **53**, 759-768.
- Simpson, J.E. 1982. Gravity currents in the laboratory, atmosphere and oceans. *Annu. Rev. Fluid Mech* **14**, 213-234.
- Sequeiros, O., Naruse, H., Endo, N., Garcia, M. & Parker, G. 2009. Experimental study on self-accelerating turbidity currents. *J. Geophys. Res.* **114**, C05025.
- Tickle, G. A. 1996. A model of the motion and dilution of a heavy gas cloud released on a uniform slope in calm conditions. *J. Hazard. Mater.* **49**, 29–47.
- Turner, J. S., & Turner, J. S. (1973). *Buoyancy effects in fluids*. Cambridge University Press.
- Ungarish, M. 2007. A shallow-water model for high-Reynolds-number gravity currents for a wide range of density differences and fractional depths. *J. Fluid Mech.* **579**, 373–82.
- Ungarish, M. 2009. An introduction to gravity currents and intrusions, CRC Press.
- Ungarish, M., & Huppert, H. 1998. The effects of rotation on axisymmetric gravity currents. *J. Fluid Mech.* **362**, 17-51.
- Ungarish, M. & Zemach, T. 2005. On the slumping of high Reynolds number gravity currents in two-dimensional and axisymmetric configurations. *Eur. J. Mech. B/Fluids* **24**, 71–90.
- Unverdi S., Tryggvason G. 1992. A front-tracking method for viscous, incompressible multi-fluid flows, *J. Comput. Phys.* **100**, 25–37
- von Karman R. 1940. The engineer grapples with nonlinear problems. *Bull. Am. Math. Soc.* **46**, 615-683.
- Webber, D. M., Jones, S. J., & Martin, D. 1993. A model of the motion of a heavy gas cloud released on a uniform slope. *J. Hazard. Mater.* **33**, 101–122.
- Yalin, M.S., Karahan, E., 1979. Inception of sediment transport. *J. Hydraulics Division* **105** (11), 1433–1443.

- Yarin, A.L. 2006. Drop impact dynamics: splashing, spreading, receding, bouncing... *Annu. Rev. Fluid Mech.*, **38**, 159-192
- Zemach T. & Ungarish M. 2013. Gravity currents in non-rectangular cross-section channels: Analytical and numerical solutions of the one-layer shallow-water model for high-Reynolds-number propagation. *Phys. Fluids* **25**, 026601.
- Zgheib, N., Bonometti, T., & Balachandar, S. 2014. Long-lasting effect of initial configuration in gravitational spreading of material fronts. *Theoretical and Computational Fluid Dynamics*, **28**(5), 521-529.
- Zgheib, N., Bonometti, T., & Balachandar, S. 2015a. Dynamics of non-circular finite release gravity currents. Submitted
- Zgheib, N., Bonometti, T., & Balachandar, S. 2015b. Propagation and deposition of non-circular finite release particle-laden currents. Submitted.
- Zhou, J., Adrian, R., Balachandar, S. & Kendall, T. 1999. Mechanics for generating coherent packets of hairpin vortices. *J. Fluid Mech.* **387**, 353–396.
- Ziskind, G., Fichman, M., Gutfinger, C. 1995. Resuspension of particulates from surfaces to turbulent flows – review and analysis. *J. Aerosol. Sci.* **26**, 613–644.